Highly-Ordered Magnetic Nanostructures on Self-Assembled α-Al_2O_3 and Diblock Copolymer Templates

Dissertation

zur Erlangung des Doktorgrades
des Fachbereichs Physik
der Universität Hamburg

vorgelegt von

DENISE ERB

aus Essen

Hamburg
2014

Gutachter der Dissertation:	Prof. Dr. Ralf Röhlsberger Prof. Dr. Robert Blick
Gutachter der Disputation:	Prof. Dr. Ralf Röhlsberger Prof. Dr. Kornelius Nielsch
Datum der Disputation:	15. Januar 2015
Vorsitzender des Prüfungsausschusses:	Prof. Dr. Michael Rübhausen
Vorsitzende des Promotionsausschusses:	Prof. Dr. Daniela Pfannkuche
Dekan der MIN-Fakultät:	Prof. Dr. Heinrich Graener

Abstract

This thesis shows the preparation of nanostructured systems with a high degree of morphological uniformity and regularity employing exclusively self-assembly processes, and documents the investigation of these systems by means of atomic force microscopy (AFM), grazing incidence small angle x-ray scattering (GISAXS), and nuclear resonant scattering of synchrotron radiation (NRS). Whenever possible, the x-ray scattering methods are applied in-situ and simultaneously in order to monitor and correlate the evolution of structural and magnetic properties of the nanostructured systems.

The following systems are discussed, where highly-ordered magnetic nanostructures are grown on α-Al_2O_3 substrates with topographical surface patterning and on diblock copolymer templates with chemical surface patterning:

- Nanofaceted surfaces of α-Al_2O_3
- Magnetic nanostructures on nanofaceted α-Al_2O_3 substrates
- Thin films of microphase separated diblock copolymers
- Magnetic nanostructures on diblock copolymer thin film templates

The fact that the underlying self-assembly processes can be steered by external factors is utilized to optimize the degree of structural order in the nanostructured systems. The highly-ordered systems are well-suited for investigations with x-ray scattering methods, since due to their uniformity the inherently averaged scattered signal of a sample yields meaningful information on the properties of the contained nanostructures:

By means of an in-situ GISAXS experiment at temperatures above 1000 °C, details on the facet formation on α-Al_2O_3 surfaces are determined. A novel method, merging in-situ GISAXS and NRS, shows the evolution of magnetic states in a system with correlated structural and magnetic inhomogeneity with lateral resolution. The temperature-dependence of the shape of Fe nanodots growing on diblock copolymer templates is revealed by in-situ GISAXS during sputter deposition of Fe. Combining in-situ GISAXS and NRS, the magnetization stabilization process is observed in hexagonal arrays of Fe nanodots during growth.

Zusammenfassung

Diese Dissertation zeigt die Herstellung von nanostrukturierten Systemen mit einem hohen Grad an morphologischer Uniformität und Regularität unter ausschließlicher Verwendung von Selbstorganisationsprozessen und deren Untersuchung mittels Rasterkraftmikroskopie (AFM), Kleinwinkelstreuung von Röntgenstrahlung unter streifendem Einfall (GISAXS) und kernresonanter Streuung von Synchrotronstrahlung (NRS). Wenn möglich, werden die Röntgenstreumethoden in-situ und simultan angewandt, um die Entwicklung struktureller und magnetischer Eigenschaften der nanostrukturierten Systeme während der Selbstorganisation zu verfolgen und zu korrelieren.

Folgende Systeme werden diskutiert, wobei geordnete magnetische Nanostrukturen auf α-Al_2O_3 Substraten mit topographischer Oberflächenstrukturierung und auf Diblock-Copolymer-Dünnfilmen mit chemischer Oberflächenstrukturierung gewachsen werden:

- Nanofacettierte Oberflächen von α-Al_2O_3
- Dünne Filme von mikrophasenseparierten Diblock-Copolymeren
- Magnetische Nanostrukturen auf nanofacettiertem α-Al_2O_3
- Magnetische Nanostrukturen auf Diblock-Copolymer-Dünnfilmen

Die Steuerbarkeit der zugrunde liegenden Selbstorganisationsprozesse durch externe Faktoren wird zur Optimierung des strukturellen Ordnungsgrades der nanostrukturierten Systeme genutzt. Die hochgeordneten Systeme eignen sich besonders zur Untersuchung mit Röntgenstreumethoden, da aufgrund ihrer Uniformität das inhärent gemittelte Streusignal einer Probe aussagekräftige Informationen über die Eigenschaften der in ihr enthaltenen Nanostrukturen liefert:

Mit einem in-situ GISAXS Experiment während der Oberflächenrekonstruktion von α-Al_2O_3 bei über 1000 °C werden Details zur Facettenbildung ermittelt. Eine neue Methode, die in-situ GISAXS und NRS vereint, zeigt ortsaufgelöst die Entwicklung der magnetischen Zustände in einem Fe Film mit korrelierter struktureller und magnetischer Heterogenität während des Filmwachstums. Die Temperaturabhängigkeit der Form von auf Diblock-Copolymer-Dünnfilmen wachsenden Fe Nanodots wird mit einem in-situ GISAXS Experiment während der Sputterdeposition von Fe aufgedeckt. In hexagonalen Anordnungen von Fe Nanodots wird die Stabilisierung der Magnetisierung während des Wachstums mittels der Kombination von in-situ GISAXS und NRS beobachtet.

For Gregor.

Contents

III Results 95

Introduction

Nanometer-sized three-dimensional structures and nanopatterned materials are both of high academic interest and of wide technological applicability. Fundamental questions are to be answered about how and why physical properties and interactions on the nanoscale are different from bulk behavior. Technological applications comprise numerous diversifications of magnetic data storage, sensor devices, and functional surfaces.

Various methods have been developed to manufacture structures on the nanoscale: Top-down methods of nanopatterning such as photolithography [1], e-beam lithography [2], focused ion beam lithography [3], nanoimprint lithography [4], and scanning probe microscope lithography [5] are used to produce nanopatterns with feature sizes down to below 5 nm and pitches of 20 nm. Employing these techniques, patterns of nanoscale structures can be prepared with a very low number of defects. However, nanopatterning large areas is extremely time-consuming with these methods. Moreover, the necessary equipment and infrastructure are complex and expensive.

As alternatives, numerous bottom-up nanopatterning methods based on self-assembly processes of block copolymers [6], colloidal particles [7], or biomolecules [8] have been conceived and are being developed. These methods are parallel, in the sense that all nanostructures form simultaneously due to intrinsic properties and resulting interactions of the self-assembling system [9]. Therefore, large-area patterning with structures is much faster when employing self-assembly (but less perfect structure patterns are achieved compared to using the top-down nanolithography methods listed above). The sizes of resulting structures scale with the sizes of the constituents of the self-assembling system - for block copolymers for example the polymer molecule size is readily controlled in the polymerization process. Thus, structures of even less than 10 nm are not necessarily more difficult to produce than significantly larger structures.

From a technological point of view, bottom-up methods for nanopatterning are especially of interest for large-scale structuring applications, where a certain degree of imperfectness can be tolerated, such as nanoelectronics, display technology, micro-electromechanics, chemical and biological sensing [10], drug delivery and filtration [11–14], or media for catalytic reactions [15].

From an academical point of view the process of self-assembly itself presents an interesting research subject: While for lithography the pattern is encoded externally in a software file controlling the lithography tool, for self-assembly the resulting pattern is encoded in the physical and chemical properties and in the interactions of the material components and can be influenced via external parameters such as temperature, pressure, magnetic or electric field [9]. Moreover, and in clear contrast to lithographical methods, nanostructure fabrication by self-assembly processes allows for in-situ observation, opening the possibility to study for example optical, magnetic, or conductive properties, phase transitions or collective behavior in dependence of nanostructure size and shape or of a pattern order parameter.

This work presents ways of nanopatterning samples with a high degree of structural order using exclusively self-assembly processes, and discusses the in-situ investigation of the development of structural and magnetic properties of the samples by means of synchrotron-based x-ray scattering techniques.

Two preparation routines for metallic nanostructure arrays are considered, as sketched in Figs. 1 and 2. Both are based on nanofaceted α-Al_2O_3 substrates produced by high-temperature annealing of M-plane α-Al_2O_3. Following the first routine, metal atoms are sputter deposited directly on the the nanofaceted substrate. By choosing a non-normal incidence angle for the sputtered atoms, either separated nanowires or continuous films with periodically varying thickness are prepared. In the second routine, the nanofaceted α-Al_2O_3 substrate is coated with a diblock copolymer thin film. Exposure to an appropriate solvent vapor induces microphase separation of the diblock copolymer film into nanometer-sized chemical domains. As the nanofaceted α-Al_2O_3 substrate provides a pronounced preferential direction, this self-assembly process results in a highly regular chemical surface patterning of the diblock copolymer film. Metal atoms sputter deposited onto such a diblock copolymer template can grow into nanostructures reproducing the template pattern due to disparate effective wetting behavior of the metal atoms on the chemically distinct surface domains of the template. Thus, the sizes, shapes, and lateral arrangement of the template surface domains are transferred to an array of uniform three-dimensional metal nanostructures.

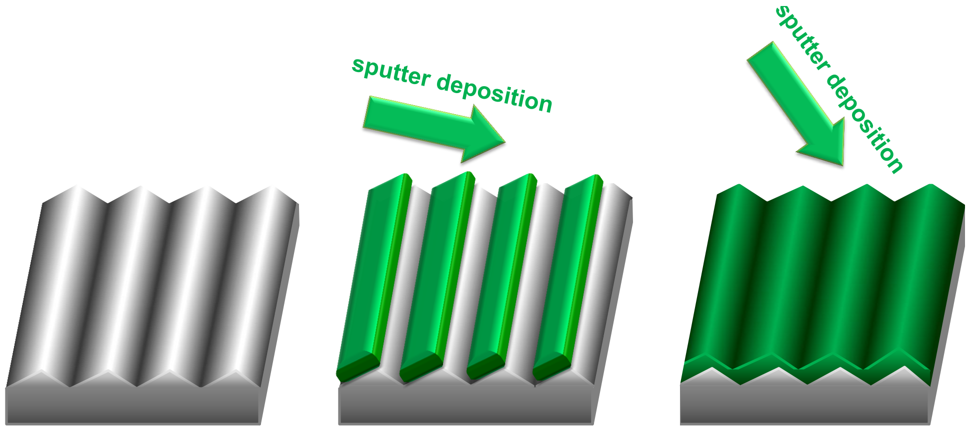

(a) (b) (c)

Figure 1: Sketch of the proposed bottom-up routine for metal nanostructure fabrication using faceted α-Al_2O_3 substrates. a) α-Al_2O_3 substrate, facetted by high-temperature annealing. b) Fabrication of isolated nanostripes by sputter deposition at from a polar angle $\omega \ll 90°$. c) Fabrication of a continuous film with facetted surface and periodically varying thickness by sputter deposition from a polar angle $\omega < 90°$.

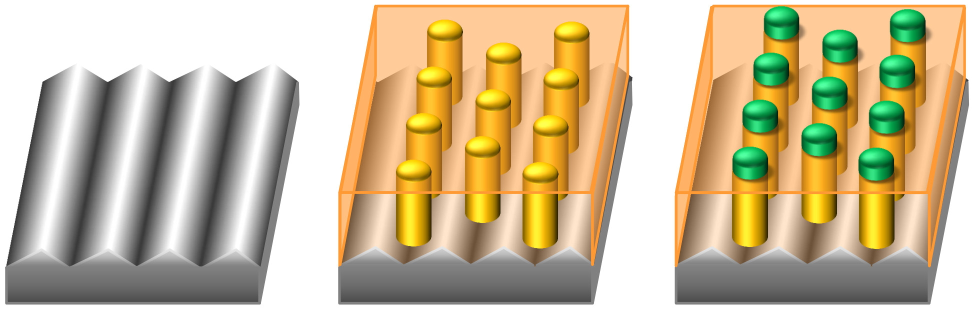

(a) (b) (c)

Figure 2: Sketch of the proposed bottom-up routine for metal nanostructure fabrication using diblock copolymer thin films on faceted α-Al_2O_3 substrates as templates. a) α-Al_2O_3 substrate, facetted by high-temperature annealing. b) Diblock copolymer film on substrate, microphase-separated by solvent vapor annealing, with chemical surface structure. c) Metal nanostructure pattern on diblock copolymer film, reproducing shape and lateral arrangement of the chemically distinct surface domains of the template.

Using self-assembly processes for nanostructure fabrication offers the important advantage of enabling the in-situ observation of the nanostructure properties during their growth: There is no structuring apparatus obstructing access to the sample, and the self-assembly takes places in the entire sample simultaneously providing sufficient sample volume for investigation. The in-situ investigations presented in this work are focused on the development of structural and magnetic sample properties during nanostructure self-assembly. Synchrotron radiation provides a suitable, non-invasive probe for such in-situ studies. The facet formation on α-Al_2O_3 surfaces can be monitored by Grazing Incidence Small Angle Scattering (GISAXS) during high-temperature annealing. By combining Nuclear Resonant Scattering of Synchrotron Radiation (NRS) and GISAXS, complementary information on the evolution of structural and magnetic properties of a sample can be obtained at the same time. This is exemplified by the investigation of ^{57}Fe nanodot arrays growing on diblock copolymer templates. Moreover, NRS and GISAXS have been merged into one single in-situ experiment yielding spatially resolved magnetic information of a sample with periodically heterogeneous structure, as demonstrated by a study on a ^{57}Fe film on a nanofaceted α-Al_2O_3 substrate.

This thesis is to show how the outcome of self-assembly processes can be steered by control over few external parameters (such as substrate annealing temperature, diblock copolymer film thickness, or template temperature during metal deposition) in order to fabricate highly regular magnetic nanostructure arrays. This thesis further aspires to contribute to in-situ approaches for gathering comprehensive and correlated information on the development of nanoscale structure and magnetism in self-assembling systems.

Part I

Fundamentals

1 Crystal Surface Reconstruction

Nanofaceted α-Al_2O_3 substrates are the basis for the majority of sample systems described in this work, and the formation of surface facets in α-Al_2O_3 is investigated as a topic of its own (see chapter 7). It is therefore relevant to understand crystal surface reconstruction as the underlying mechanism for surface faceting in α-Al_2O_3 .

Crystalline solids are characterized by anisotropy. Their anisotropy in surface free energy density for different crystal planes can drive them to assume non-trivial equilibrium shapes: The equilibrium shape is that of minimum free energy, not of minimum surface area. For equilibration, i.e. minimization of the total free energy, it can therefore be necessary to increase the surface area by facet formation, thereby replacing a planar surface of high surface free energy density with facets of low surface free energy density. The length scales of such periodic surface structures are in the nanometer range, while the macroscopic orientation of the surface is preserved during the equilibration process [16]. Their periodic nanoscale topography draws attention to such surfaces for potential uses in non-lithographic nanostructure fabrication and in-situ investigation.

1.1 The equilibrium crystal shape

Every solid or liquid body has an equilibrium shape, in which its total free energy at constant volume and temperature is lowest. A liquid body without contact to a substrate has an isotropic surface free energy density and therefore a spherical equilibrium shape. A solid crystal on the other hand has a highly anisotropic surface free energy density and thus its equilibrium shape is far from trivial.

1.1.1 Basic thermodynamic considerations

Consider a system of N identical particles in which a crystalline solid and a fluid phase coexist. The particle number densities of solid and fluid phase are n_{cs} and n_{fl}, respectively. The volume V of the system is fixed, it is at constant temperature T and pressure P. Assume that the solid is crystalline with defined crystal axes, while the fluid is isotropic. The volume V_{cs} of the solid phase is $V_{cs} = (N - n_{fl}V)/(n_{cs} - n_{fl})$. The entire system has a total free energy of

$$\begin{aligned} F &= F^b_{cs} + F^b_{fl} + F^s \\ &= \gamma^b_{cs}(n_{cs}) \cdot V_{cs} + \gamma^b_{fl}(n_{fl}) \cdot (V - V_{cs}) + \int_{\partial V_{cs}} \gamma^s\left(\boldsymbol{s}(\boldsymbol{r})\right) dS \qquad (1.1) \end{aligned}$$

where γ^b are the free energy densities of the bulk phases and γ^s is the free energy per unit area dS of the surface of the solid phase. $\boldsymbol{s} = \boldsymbol{s}(\boldsymbol{r})$ is the orientation of the surface element dS with respect to the crystal axes of the solid. Among the three summands of the total free energy, only the surface contribution depends on the shape of the solid phase. This shape dependence of the surface free energy arises from the structural anisotropy of the solid – as opposed to the structural isotropy of the surrounding fluid – and results in non-trivial shapes of the solid (in case of coexisting isotropic phases the resulting shapes are trivial spheres, as observed e.g. for vapor bubbles in liquids). Given a constant volume V_{cs}, the equilibrium crystal shape of the solid is the one shape $G(\boldsymbol{g})$, for which the surface free energy F^s is minimized at constant volume [17].

1.1.2 The Wulff construction

The equilibrium crystal shape $G(\boldsymbol{g})$ can be derived geometrically via the Wulff construction, as demonstrated in Fig. 1.1 [18,19]: Begin with a polar plot of the surface free energy density $\gamma^s(\boldsymbol{s})$ (gray curve). A normal (dashed lines) to every orientation $\boldsymbol{s}$ is constructed at its intersection with the surface free energy density curve γ^s. The normals to the orientations $\boldsymbol{s}$ are tangents to the equilibrium crystal shape, so that $G(\boldsymbol{g})$ (black curve) is the inner envelope of these normals.

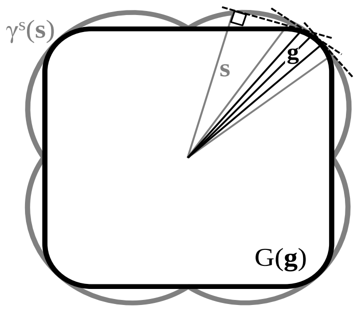

Figure 1.1: Wulff construction of an equilibrium crystal shape.

1.2 Spontaneous faceting of crystal surfaces

1.2.1 The surface free energy for a model crystal

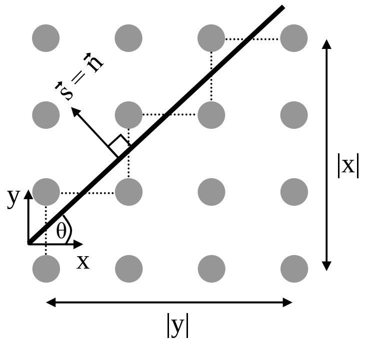

Figure 1.2

A simple example for the determination of the surface free energy in two spatial dimensions shall be given [17]. Consider a plain square lattice at $T = 0\ K$ with a surface cut between two arbitrary points, as shown in Fig. 1.2. The solid line represents a surface unit produced by cutting, the dotted lines indicate the bonds which are severed by the surface unit.

The number of free bonds at this surface unit is $|x| + |y|$, with an energy of ϵ_b each. Thus, the surface free energy density is

$$\gamma^s(\boldsymbol{s}(\boldsymbol{r})) = \frac{(|x| + |y|)}{\sqrt{x^2 + y^2}}\epsilon_b = (|\cos\theta| + |\sin\theta|)\epsilon_b \tag{1.2}$$

Due to the absolute values $|\cos\theta|$ and $|\sin\theta|$ there are cusps in γ^s in the direction of the crystal axes, as seen in Fig. 1.1. Through the Wulff construction, these cusps in the surface free energy density γ^s correspond to extended planes in the equilibrium crystal shape $G(\boldsymbol{g})$.

Real crystals grow under conditions far from equilibrium, and therefore also occur in shapes which strongly deviate from their equilibrium crystal shape. If allowed, e.g. by annealing, such a crystal will approach its equilibrium shape of minimum surface free energy.

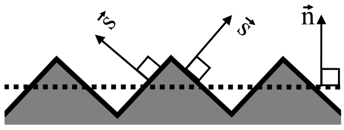

Figure 1.3

Based on the previous deliberations, consider a crystalline solid of fixed volume as before, and with all of its surfaces but the top one being fixed as well. Due to these constraints, the top surface can only rearrange into a hill-and-valley or faceted structure in order to approach the equilibrium crystal shape and thus reduce its surface free energy F^s (see Fig. 1.3, the dotted line represents the initial surface). If the given surface of the crystal is not simultaneously a surface of the equilibrium crystal shape, then such a faceted surface structure is always energetically more favorable than a planar surface [19]. The surface free energy of the faceted surface is

$$F^s(\boldsymbol{s}) = \int \frac{\gamma^s(\boldsymbol{s})}{\boldsymbol{s} \cdot \boldsymbol{n}} \, dS \tag{1.3}$$

As another consequence of the assumed constraints, the average of the surface orientation vectors $\boldsymbol{s}(\boldsymbol{r})$ is the normal vector $\boldsymbol{n}$ of the initial planar surface.

$$\frac{1}{S} \int \boldsymbol{s}(\boldsymbol{r}) \, dS \ = \boldsymbol{n} \tag{1.4}$$

The orientation of the facets can be determined by minimizing the surface free energy Eqn.(1.3) under the constraint of Eqn.(1.4). However, information on the linear scale of the faceted equilibrium surface and thus the description of a possible periodicity of surface facets is beyond the scope of this model. Intrinsic surface stress and capillary effects have to be taken into consideration to account for the formation of periodic surface structures [20].

1.2.2 Periodicity of faceted crystal surfaces

According to the theoretical description devised by Marchenko [21, 22] the surface free energy density γ^s_{facet} of a periodically faceted surface has three contributions: one from the planar surfaces $S1$ and $S2$ of the facets, one from both the concave and convex edges at the intersections of the facets, and one from intrinsic surface stress [20]:

$$\gamma^s_{facet} = \frac{\sin{(\theta_{S2})}\gamma^s_{S1} + \sin{(\theta_{S1})}\gamma^s_{S2}}{\sin{(\theta_{S1} + \theta_{S2})}} + \frac{\eta}{L} - \frac{C\mathcal{T}^2}{YL} \ln\left(\frac{L}{a}\right) \tag{1.5}$$

where θ_{S1} and θ_{S2} are the angles enclosed by the initial planar surface and the facet surfaces $S1$ and $S2$, respectively. η denotes the energy of convex and concave edges, C is a geometric factor related to the elastic anisotropy of the crystal and the symmetry of the intrinsic surface stress tensor $\mathcal{T}$. Furthermore, Y is the Young's modulus, a is the lattice parameter, and L is the period of the facets. An equilibrium period L_0 is reached after extensive annealing, when:

$$\frac{\partial \gamma^s_{facet}}{\partial L} = 0 \quad \Rightarrow \quad L_0 = a \exp\left(\frac{\eta Y}{C\mathcal{T}^2}\right) + 1 \tag{1.6}$$

A correlation length ζ can be introduced to assess the degree of periodicity:

$$\zeta = \frac{L^2}{\sigma_L} \tag{1.7}$$

where σ_L is the standard deviation of the facet period L [23, 24].

1.2.3 Spontaneous faceting of M-plane α-Al_2O_3

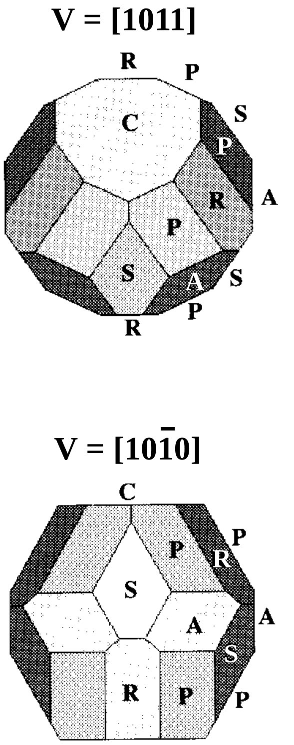

Figure 1.4: Equilibrium crystal shape of α-Al_2O_3. From [25]

α-Al_2O_3 [26, 27] is used in this work to prepare substrates with nanofaceted surfaces. The equilibrium crystal shape of α-Al_2O_3 as derived via the Wulff construction is composed of the crystallographic planes $C\{0001\}$, $R\{1\bar{1}02\}$, $S\{10\bar{1}1\}$, $P\{11\bar{2}3\}$, $A\{11\bar{2}0\}$, and $M\{10\bar{1}0\}$. The associated surface free energy density increases from the first to the last of the listed planes [23]. Figure 1.4 shows the equilibrium crystal shape of α-Al_2O_3 from two directions of view $\boldsymbol{V}$. In this representation, the area of the different faces corresponding to the crystallographic planes is inversely proportional to the respective surface energy density. The M-plane has too high surface energy density to be expressed in the equilibrium shape [23,25]. Cutting an α-Al_2O_3 single crystal along the M-plane thus results in an unstable surface. Extended annealing allows the crystal to minimize its surface free energy (Eqn.(1.5)) by rearranging its unstable high-energy M-plane surface into facets of the more stable low-energy R-plane and S-plane surface orientations [23], as was observed via GISAXS in an in-situ annealing experiment (see chapter 7). The process of equilibration of an α-Al_2O_3 M-plane surface proceeds through five stages, as described below. The driving force in every stage is the reduction of surface free energy [28].

1. Surface smoothing

Mass transport by surface diffusion starts well below the melting temperature of 2053 °C. Heffelfinger and Carter observed a surface smoothing reducing the rms roughness from 2.1 nm to 0.2 nm after short annealing times of about one hour at 1400°C [28] already. However, surface smoothing is not necessarily observed, if the initial polished surface already has very low roughness.

2. Formation and growth of individual facets

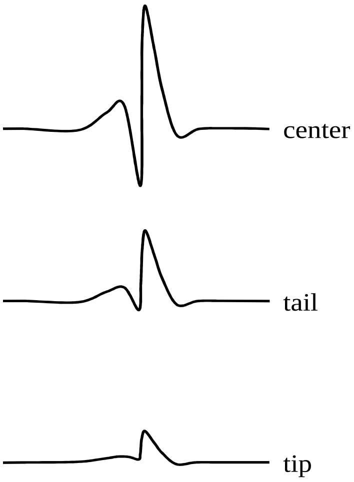

Figure 1.5: Profiles of a facet from center to tip [28].

In M-plane α-Al_2O_3 initial facets nucleate in a heterogeneous manner, i.e. without spatial and temporal correlation to each other. The individual facet has one simple and one complex surface. The simple surface is formed first and conforms to the $\{1\bar{1}02\}$ R-plane orientation, which is at an angle of $\phi_R = 32.4°$ with the $\{10\bar{1}0\}$ M-plane orientation of the initial surface. The complex surface does not conform exactly to any specific crystal orientation of α-Al_2O_3, but is closest to the $\{10\bar{1}1\}$ S-plane. All facets are parallel to the $[11\bar{2}0]$ direction. In relation to the initial surface, a facet consists of a "hill" and a corresponding "valley". The height profile of each facet varies along its length (see Fig. 1.5): The height of the hill decreases and the valley becomes much less pronounced towards the tips of the facet. This indicates mass transport along the facet: The valley provides material for the growth of the hill in both vertical direction and lateral directions [28].

3. Formation of facet groups

Facets cause surface distortions on both of their sides, which increase as the facet grows. These distortions can in turn serve as nucleation sites for successional facets, when the orientation of the distortions becomes more similar to the $\{1\bar{1}02\}$ R-plane orientation than to the $\{10\bar{1}0\}$ M-plane orientation of the initial surface. Thus, groups of facets are formed. The distortions are more pronounced on the side of the simple facet surface (left facet surface in the profiles shown in Fig. 1.5); most successional facets are found to nucleate on this side of an existing facet. The formation of neighboring facets limits the growth of each facet in width. In length, facets can grow until they hit another facet. In this phase, the sample surface features unfaceted areas, single facets, and facet groups.

4. Coalescence of facet groups

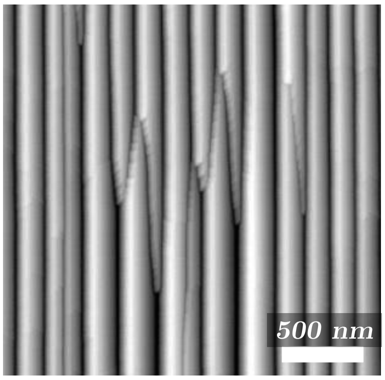

Figure 1.6: Facet junctions formed upon coalescence of facet groups.

The edges of facets in two different facet groups are generally not aligned. Therefore, when two groups of growing facets meet, the facets form junctions, as can be seen in the AFM micrograph in Fig. 1.6 (the nanofaceted α-Al_2O_3 substrates prepared and investigated for this work are discussed in detail in chapter 7). At the end of the coalescence phase the entire sample surface is faceted. The process of faceting up to the completion of the coalescence phase has been found to take 4 hours at 1400°C [28].

5. Facet coarsening

In the first few hours of annealing, the facet period L increases to a constant value (coarsening), while the number density of junctions n_{jcn} decreases to a constant value. Coarsening is thought to be accomplished by motion of junctions along the facets [28]. When two junctions meet and merge, a facet is eliminated. The remaining adjacent facets effectively become wider and deeper. However, the number density of junctions n_{jcn} does not become zero: Junctions must contain other orientations than the preferred $\{1\bar{1}02\}$ R-plane and $\{10\bar{1}1\}$ S-plane orientations. Since according to Eqn.(1.4) the average of all surface orientations must be the orientation of the initial planar surface, the remaining junctions could be necessary to account for any misorientation of the initial surface [28]. In the α-Al_2O_3 samples investigated for this work, the the average facet period was found to range from $L \approx 50 \ldots 200$ nm, with a standard deviation of $\sigma_L \approx 0.25\ L$ (see section 7.2).

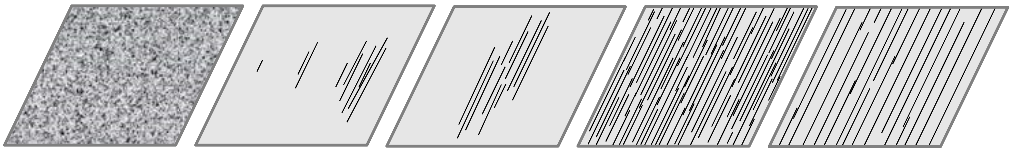

Figure 1.7: Equilibration in M-plane α-Al_2O_3 upon annealing.

2 Diblock Copolymers

Polymers are widely used in industrial applications and contemporary every day life can hardly be imagined without them. This section is only a brief introduction to the field of polymer science - its purpose is to give an idea what polymers are and how their use as templates for producing metallic nanostructures is motivated.

Groundbreaking work leading forward to the modern concept of polymers and to the understanding of their nature was accomplished by Staudinger (macromolecular theory and chain structure of polymer molecules, 1920 [29] - Nobel Prize in 1953), by Flory (thermodynamics, reaction kinetics, and solution theory of polymers, 1953 [30] - Nobel Prize in 1974), and by de Gennes (dynamics of polymers in concentrated solutions and melts, scaling concepts in polymer physics, 1972 [31,32] - Nobel Prize in 1991). Mark (x-ray diffraction on polymers, 1926 [33]), Carothers (polymer synthesis, first synthetic rubber (neoprene) and synthetic silk (nylon), 1930 [34, 35]), and Heeger, MacDiarmid, Shirakawa (electrically conducting and semiconducting polymers, 1977 [36] - Nobel Prize in 2000), among many others, contributed significantly to advancing polymer science to its current state-of-the-art.

Especially diblock copolymers have been the subject of intense research interest. Several reasons can be listed for this: diblock copolymers are produced on industrial scales with high quality and in innumerable variants of molecule composition, size, and architecture. They are able to self-assemble via microphase separation (see section 2.3) and this process can be initiated and controlled by various methods. Size and shape of the resulting nanodomains can be determined by the choice of polymer molecule size and composition. Diblock copolymer nanodomains are uniform in size and shape and can be driven to arrange in patterns with long-range order. With these properties diblock copolymers also lend themselves to exploring their applicability as templates in new methods of metallic nanostructure fabrication.

2.1 Basic concepts of polymer science

2.1.1 General properties of polymers

The polymer molecule

Polymer molecules are molecules of high molecular mass, which are composed of low-mass sub-units (monomer residues) in multiple repetition [37]. Characteristically, polymer molecule structures are based on a main chain (backbone) with side groups pending from it. A monomer residue then comprises one segment of the main chain with the dependent side group(s). By steering the processes of polymer synthesis, polymers can be produced in a variety of molecular architectures, ranging from linear, branched, or star-shaped, to looped or multiply interconnected. The majority of polymers are organic compounds, i.e. covalent compounds of carbon with mainly hydrogen, oxygen, chlorine, fluorine, phosphor, and/or sulfur. There are also some inorganic polymers such as polysilicates or polysulfates [37, 38].

Due to their high molecular mass polymer molecules are classified as macromolecules. Polymer production processes always result in a mixture of molecules of different chain lengths, i.e. different molecular masses. Hence, the properties of a polymer sample reflect the properties of the average polymer molecule, and it is useful to define an average mass of the polymer molecules present in the polymer sample. There are two common alternatives how to define that average mass:

- the number average molecular mass M_n, defined as $M_n = \frac{\sum n_i M_i}{\sum n_i}$
- the weight average molecular mass M_w, defined as $M_w = \frac{\sum n_i M_i^2}{\sum n_i M_i}$

where n_i is the number of polymer molecules of species i, with a specific size/mass M_i. For an ideal polymer sample consisting of identical molecules $M_n = M_w$, for all other $M_n < M_w$. Therefore, the ratio $M_w/M_n \geq 1$ serves as a measure for the polydispersity, i.e. the spread of molecular masses, of the polymer molecules in one sample. The repetition of monomer residues is the characteristic structural feature of a polymer molecule. Its size can therefore not only be defined by its mass but equivalently also by its chain length, i.e. the number of monomer residues it contains – its degree of polymerization N [38]. In homopolymers, all monomer residues are identical in chemical composition. Copolymers on the other hand are composed of chemically distinct species of monomer residues. Depending on the sequence of the different monomer residues, copolymers are further classified as random or block copolymers. Random copolymers usually have physical properties which are intermediate between those of the respective homopolymers.

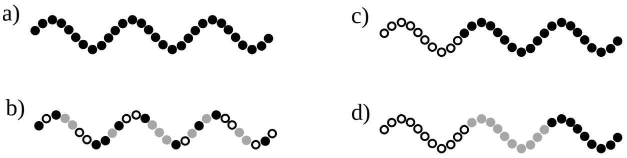

Figure 2.1: Linear polymer molecules: a) homopolymer, b) random coplymer, c) diblock copolymer, d) triblock copolymer.

The majority of pairs of polymers is not miscible - and one can make versatile use of their phase separation behavior. Mixtures of polymers will be considered according to the regular solution model in section 2.2. Block copolymers can be synthesized from immiscible types of monomer residues. They tend to phase separate, but the covalent bonds linking the blocks do not allow for a macroscopic phase separation as in homopolymer mixtures. Instead, in block copolymers a microphase separation takes place and – via self-assembly – leads to a variety of phase morphologies. The concepts introduced for polymer mixtures will be employed to explain the microphase separation of block copolymers in section 2.3).

The glass transition

Polymers primarily occur in one of the following states of aggregation:

- liquid: polymer melts, polymer solutions
- glass: most common state of aggregation for polymers
- semi-crystal: polymers generally fail to crystallize completely, usually very small crystallites are found in an amorphous matrix
- liquid crystal: rigid polymer molecules are able to line up and thus form liquid crystals

The glass transition is a second order phase transition which occurs in amorphous polymers and in the amorphous fraction of crystalline polymers at the glass transition temperature T_g. On the macroscopic scale, the bulk polymer transits from a brittle, glassy state to a ductile, rubbery state upon exceeding the glass transition temperature. Since beyond T_g rotations around single bonds in the polymer molecules become significantly easier, the physical properties which change during glass transition are those depending on the molecules' degrees of freedom in rotation, such as the coefficient of thermal expansion, the heat capacity, or the refractive index. The glass transition temperature T_g of a polymer is determined by those molecular characteristics which condition the intra- and intermolecular mobility of the polymer molecules:

- the presence of side groups pending from the main chain
- covalent or hydrogen bonds between polymer molecules
- the rigidity of the main chain
- molecular mass (for degrees of polymerization below $N = 200$)
- type of tacticity (i.e. sequence of locations of the residues with respect to each other and to the backbone)

During heating from $T < T_g$ to $T > T_m$ a polymer passes through the glass transition of its amorphous fraction at T_g and then – in case of a crystalline polymer – undergoes melting of its crystalline fraction at T_m. The molecular characteristics listed above affect the glass transition temperature and the crystalline melting temperature similarly in their effect on the mobility of the molecules. This is reflected in the relation

$$T_g = (0.66 \pm 0.04)T_m \tag{2.1}$$

found empirically for most polymers [38].

2.1.2 A simple statistical model of polymer molecules

Despite their widely varying properties, all polymers exhibit universal behavior – which facilitates their description tremendously. Much of their behavior is related to the dimensions of polymer molecules, which in turn are determined by the degree of polymerization N. Polymer molecule dimensions and resulting behavior can be described very accurately using a simple model: the ideal self-avoiding random walk, representing a free-jointed polymer chain [39].

An ideal polymer chain

In a first approach, a linear polymer molecule can be modeled by a free-jointed chain of N links. The length and orientation of each chain link is described by a vector $\boldsymbol{a}$, with the orientation of each link being independent of the orientation of the adjoining links. Thus, tracing the model polymer molecule from one end to the other means in fact to follow a self-avoiding random walk with N steps of length a. Given that the sum of all steps $\boldsymbol{a}_i$ is the vector $\boldsymbol{r}$ pointing from one end of the chain to the other,

$$\boldsymbol{r} = \sum_{i}^{N} \boldsymbol{a_i} \tag{2.2}$$

the mean end-to-end distance $\langle \boldsymbol{r}^2 \rangle$ of such a free-jointed chain is the mean sum of all steps

$$\left\langle \boldsymbol{r}^2 \right\rangle = \left\langle \left(\sum_i \boldsymbol{a_i} \right)^2 \right\rangle = \left\langle \sum_i \sum_j \boldsymbol{a_i} \cdot \boldsymbol{a_j} \right\rangle = Na^2 + \left\langle \sum_{i \neq j} \boldsymbol{a_i} \cdot \boldsymbol{a_j} \right\rangle \tag{2.3}$$

In a free-jointed chain there is no correlation between the orientations of the individual links, so that the average of the cross terms in Eqn.(2.3) vanishes. Thus, in this random walk model the mean square end-to-end distance of the polymer molecule is

$$\left\langle \boldsymbol{r}^2 \right\rangle = Na^2 \quad \Leftrightarrow \quad \langle \boldsymbol{r} \rangle = \sqrt{N} a \tag{2.4}$$

For large degrees of polymerization N the possible end-to-end distances obey a Gaussian probability distribution function $P(\boldsymbol{r})$ with

$$P(\boldsymbol{r}) = \left(\frac{2}{3} \pi N a^2 \right)^{-\frac{2}{3}} \cdot \exp\left(-\frac{3}{2} \frac{\boldsymbol{r}^2}{Na^2} \right) \tag{2.5}$$

The conformational entropy $S(\boldsymbol{r})$ of the model polymer chain, i.e. its entropy due to the possible relative locations of its links, can then be expressed as a function of its end-to-end distance:

$$S(\boldsymbol{r}) = k_B \ln\left(P(\boldsymbol{r})\right) = -\frac{3}{2} k_B \frac{\boldsymbol{r}^2}{Na^2} + \text{const.} \tag{2.6}$$

Increasing the end-to-end distance of a polymer molecule by stretching it hence reduces its conformational entropy (there are more coiled random walk conformations than outstretched conformations), thereby increasing its free energy $F(\boldsymbol{r})$ [39]:

$$F(\boldsymbol{r}) = -TS(\boldsymbol{r}) = \frac{3}{2} k_B T \frac{\boldsymbol{r}^2}{Na^2} + \text{const.} \tag{2.7}$$

Real polymer chains

In real polymer chains the orientations of the individual links are not uncorrelated but determined by the precise angles of the respective chemical bonds. Interestingly, even if such a correlation is included into the model introduced above, it retains its random walk characteristics with only the step width a being replaced by an effective value. Given that links can rotate freely around the bonds only at an angle θ, the mean square end-to-end distance of the chain becomes

$$\left\langle \boldsymbol{r}^2 \right\rangle = Na^2 + \left\langle \sum_{i \neq j} \boldsymbol{a}_i \cdot \boldsymbol{a}_j \right\rangle = Na^2 + a^2 \cos^m (\theta) \tag{2.8}$$

where $m = i - j$; $i > j$. Since $\cos(\theta) < 1$, the second term is very small for links which are far away from link i: these correlations have a limited range. The chain can be re-divided into new subunits larger than the correlation range to regain the random walk model. Let the vectors $\boldsymbol{a'}$ specify length and orientation of the newly defined subunits, each of which contains k links. Then a' is the size of the effective monomer (or: statistical segment length) in this refined model of the polymer chain. The mean end-to-end distance of the chain is that of a random walk with N/k steps of width a':

$$\left\langle \boldsymbol{r}^2 \right\rangle = \frac{N}{k} \langle \boldsymbol{a'} \rangle \tag{2.9}$$

The corresponding distribution $Q(\boldsymbol{r}, N)$ of end-to-end distances in the Gaussian limit (i.e. $N \gg 1$) is

$$Q(\boldsymbol{r}, N) = \left(2\pi \frac{Na^2}{3} \right)^{-3/2} \exp\left(-\frac{3\boldsymbol{r}^2}{2Na^2} \right) \tag{2.10}$$

Accordingly, the conformational entropy $S(\boldsymbol{r})$ of a freely jointed chain is

$$S(\boldsymbol{r}) = k_B \ln (Q(\boldsymbol{r})) = -\frac{3k_B \boldsymbol{r}^2}{2Na^2} + const. \tag{2.11}$$

with the extent of chain stretching being expressed in the length of $\boldsymbol{r}$. The principle demonstrated by this example is found everywhere in polymer physics: properties and behavior on the molecular level are universal to all polymers. The distinct chemical features of a specific polymer can be subsumed in statistical parameters like the effective monomer size [32, 39].

2.2 Polymer mixtures

Understanding the behavior of homopolymer mixtures is the first step to understanding the behavior of diblock copolymers – especially the self-assembly by microphase separation observed in these.

2.2.1 The free energy and the Flory-Huggins interaction parameter

The free energy of mixing is a central term in describing mixing or separation behavior. For homopolymer mixtures, it is derived within the regular solution model (valid for minor deviations from the ideal solution) [40] by first considering a system Ω of two species of monomers A and B, which can be found in a state of two unmixed liquids (state 0) or as a liquid mixture (state 1). The difference in free energy of the two possible state is the free energy of mixing F_{mix}. It expresses the change in the balance of energy and entropy when changing from one state to the other:

$$F_1 - F_0 \;=\; F_{mix} \;=\; U_{mix} - TS_{mix} \;=\; (U_1 - U_0) - T(S_1 - S_0) \tag{2.12}$$

Knowing the dependence of F_{mix} on temperature T and on the composition of the mixture (volume fractions f_A and f_B) is sufficient to characterize the phase behavior of the system. In order to find the relevant expression for F_{mix}, the energy of mixing U_{mix} and the entropy of mixing S_{mix} have to be deduced. For deriving the entropy of mixing, the following definitions and assumptions concerning structure and composition of the system are required:

- mean field assumption: every monomer molecule can be assigned to a site with z nearest neighbors, and the occupation of a site with species A or B is independent of how the neighboring sites are occupied
- incompressibility assumption: all monomer molecules are of the same size and the total liquid volume is constant
- definition of composition: the volume fractions for the two species are $f_{A,B} = V_{A,B}/(V_A + V_B)$, with $f_A + f_B = 1$.

The Boltzmann formula for the entropy per site – summing over all possible states i, each with probability p – becomes very simple in this system. There are only two possible states to consider: Each site is occupied by either species A or species B, and the corresponding probabilities are equal to the respective volume fraction. Thus the entropy of mixing per site is:

$$S_{mix} \;=\; -k_B \sum_i p_i \ln{(p_i)} = -k_B(f_A \ln{(f_A)} + f_B \ln{(f_B)}) \tag{2.13}$$

Deriving the energy of mixing requires assumptions concerning the interactions among the monomer molecules in the system:

- monomer molecules interact with their nearest neighbors only
- the interaction energies (ϵ_{AA}, ϵ_{BB}, ϵ_{AB}) depend on the interacting species

According to the mean field assumption, each site has zf_A nearest neighbors of species A and zf_B nearest neighbors of species B. Thus, the interaction energies per site for the two states of the system are:

$$U_0 \;=\; \frac{z}{2}(f_A\epsilon_{AA} + f_B\epsilon_{BB}) \tag{2.14a}$$

$$U_1 \;=\; \frac{z}{2}(f_A^2\epsilon_{AA} + 2f_Af_B\epsilon_{AB} + f_B^2\epsilon_{BB}) \tag{2.14b}$$

Consequently, the energy of mixing is

$$\begin{aligned} U_{mix} \;=\; U_1 - U_0 \;&=\; \frac{z}{2}\Big((f_A^2 - f_A)\epsilon_{AA} + 2f_Af_B\epsilon_{AB}(f_B^2 - f_B)\epsilon_{BB}\Big) \\ &=\; \frac{z}{2}f_Af_B(\epsilon_{AB} - \epsilon_{AA} - \epsilon_{BB}) \end{aligned} \tag{2.15}$$

From the energy of mixing an interaction parameter χ can be defined:

$$\chi \;=\; \frac{z}{2k_BT}(2\epsilon_{AB} - \epsilon_{AA} - \epsilon_{BB}) \tag{2.16}$$

so that

$$\frac{U_{mix}}{k_BT} \;=\; \chi f_A f_B \tag{2.17}$$

The Flory-Huggins interaction parameter χ expresses the strength of the interaction between monomer species A and B in relation to the strength of their respective intra-species interactions. Then, with Eqns.(2.17) and (2.13), the free energy of mixing per site in units of k_BT is [30, 39]

$$\frac{F_{mix}}{k_BT} \;=\; \underbrace{\chi f_A f_B}_{\text{energy of mixing}} \;+\; \underbrace{f_A \ln{(f_A)} + f_B \ln{(f_B)}}_{\text{entropy of mixing}} \tag{2.18}$$

2.2.2 Stability of mixtures

The significance of the interaction parameter χ becomes apparent when plotting the free energy of mixing F_{mix}/k_BT as a function of the composition, described by the volume fraction f ($f = f_A$, $f_B = 1 - f$), for several values of χ (see Fig. 2.2). The shape of the curve $F_{mix}(f)/k_BT$ changes qualitatively with the value of the interaction parameter: for $\chi < 2$ there is a single minimum at $f = 0.5$, for $\chi > 2$ there are one maximum at $f = 0.5$ and two minima.

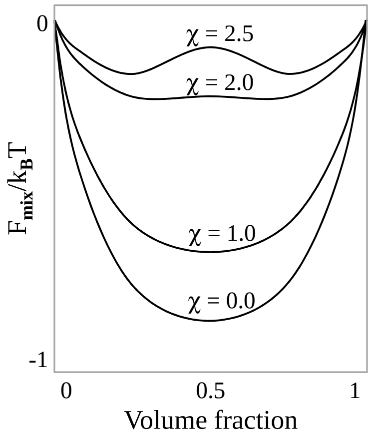

Figure 2.2

For interpreting the physical difference between these cases, two further energy terms have to be taken into account: the total free energy F_Ω of the system Ω in mixed state and the total free energy $F_{\Omega1\Omega2}$ of the system separated into two subsystems $\Omega1$ and $\Omega2$. Both F_Ω and $F_{\Omega1\Omega2}$ can be read from the plot of F_{mix}/k_BT as function of the volume fraction f, as shown in Fig. 2.3. For $\chi < 2$, the free energy of the separated system, $F_{\Omega1\Omega2}$, is always larger than the free energy of the non-separated system, F_Ω. Therefore, a monomer mixture with $\chi \leq 2$ is stable and will not phase separate. For $\chi > 2$, there are compositions for which $F_{\Omega1\Omega2}$ is less than F_Ω. Such monomer mixtures can separate into subsystems, or phases, $\Omega1$, $\Omega2$ with compositions $f_{\Omega1}$ and $f_{\Omega2}$.

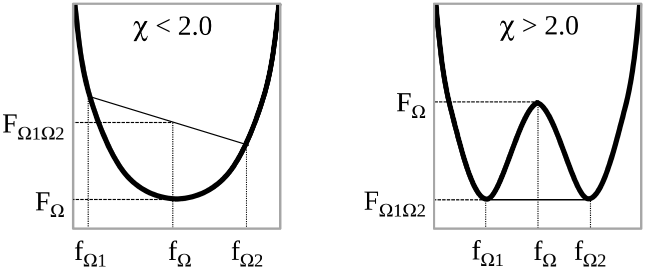

Figure 2.3: The free energy of mixing F_{mix}/k_BT as a function of the volume fraction f. Graphical determination of F_Ω and $F_{\Omega1\Omega2}$.

In order to describe mixtures of polymers, i.e. with the monomer residues being joined to chain-like polymer molecules, Eqn.(2.18) has to be adapted accordingly. Given that a polymer molecule consists of N monomer residues, the interaction parameter χ per site (i.e. per monomer residue) and thus the energy of mixing U_{mix} have to be multiplied by N. The entropy of mixing S_{mix} remains unchanged, so that

$$\frac{F_{mix}}{k_B T} = f_A \ln(f_A) + f_B \ln(f_B) + \chi N f_A f_B \tag{2.19a}$$

$$\frac{F_{mix}}{N k_B T} = \frac{f_A}{N} \ln(f_A) + \frac{f_B}{N} \ln(f_B) + \chi f_A f_B \tag{2.19b}$$

Eqn.(2.19a) defines the free energy of mixing F_{mix} per molecule, and Eqn. (2.19b) defines the free energy of mixing F_{mix} per monomer residue for a polymer mixture. The latter is commonly known as the Flory-Huggins free energy [39]. By substituting the interaction parameter χ with χN, other results of the previous section can be transferred to polymer molecules as well. Consider the stability of mixtures: For monomer mixtures, the critical interaction parameter is $\chi_c = 2$. Thus, with χ replaced by χN, the critical interaction parameter for polymer mixtures is $\chi_c = 2/N$, resulting in

- homogeneous mixture for $\chi < 2/N$
- phase separation for $\chi > 2/N$

Typical values of χ for polymer pairs range from 0.01 to 0.1. Since $\chi_c \propto 1/N$, the critical value is already exceeded for comparatively low degrees of polymerization of $N = 20 ... 200$. Hence, the vast majority of polymers will not form single-phase mixtures with each other, but rather phase separate [39].

2.3 Self-assembly in diblock copolymers

Self-assembly in diblock copolymers means a phase separation process on the nanoscale: A diblock copolymer molecule consists of two subchains with chemically distinct monomer residues, with the subchains being connected by a covalent bond. Since most polymers do not form stable mixtures (see section 2.2.2), also the subchains of most diblock copolymer molecules tend to separate from each other. Consequently, in diblock copolymers with incompatible constituents there are two counteracting phenomena:

- short-range attractive interaction imposed by the covalent bonds attaching the blocks of a molecule to each other
- long-range repulsive interactions given by the immiscibility of incompatible blocks

In homopolymer mixtures of incompatible components the interfacial energy is minimized by macroscopic phase separation. However, in diblock copolymers macrophase separation is inhibited by the covalent bonds connecting the blocks. The competition of attractive and repulsive interactions is settled by the diblock copolymer undergoing microphase separation into nanoscale phase domains.

2.3.1 Microphase separation

A diblock copolymer with blocks A and B is characterized by

- the overall degree of polymerization N of the diblock copolymer molecules
- the composition, given by the volume fraction f
- the constraint given by the architecture of the molecules
- the Flory-Huggins interaction parameter χ

The overall degree of polymerization and the architectural constraint are given by the polymerization process. These factors determine the translational and conformational entropy. The Flory-Huggins interaction parameter χ (see section 2.2.1) depends on the choice of the distinct diblock copolymer blocks A and B. It is inversely proportional to temperature: $\chi = \alpha T^{-1} + \beta$, where α and β are material specific constants for given architectural constraints and volume fractions. Since the volume fractions of the two blocks and the architectural constraints of the copolymer molecules are contained in the Flory-Huggins interaction parameter, it is sufficient to consider the morphological phase state of a diblock copolymer in dependence of the two factors χ and N. When entropic contributions dominate, i.e. for high temperatures and/or short chains, χ and/or N are small, so that $\chi N = \mathcal{O}(1)$. When energetic contributions dominate, i.e. for low temperatures and/or long chains, χ and/or N are large, so that $\chi N = \mathcal{O}(100)$.

Diblock copolymers in the strong segregation limit

The local composition $f(r)$ behaves quite differently in the two limits of weak segregation with $\chi N \ll 1$ and strong segregation with $\chi N \gg 10$: In the weak segregation limit (WSL), f varies only slightly with the distance r from an arbitrary molecule (see the blue curve in Fig. 2.4); fluctuations in composition appear with a period D_0^{WSL} which is proportional to the gyration radius R_g of the diblock copolymer molecules: $D_0^{WSL} \propto R_g \propto a\sqrt{N}$. In the strong segregation limit (SSL), the composition profile $f(r)$ exhibits domains containing almost exclusively one block of the diblock copolymer molecules with sharp interfaces between those regions of different local volume fraction (see the red curve in Fig. 2.4).

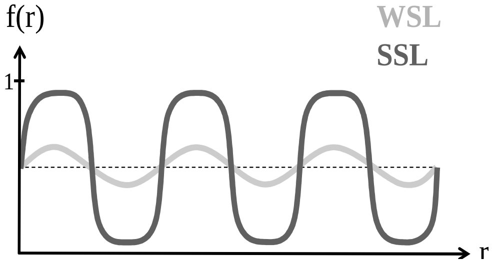

Figure 2.4: The local volume fraction $f(r)$ in the weak and strong segregation limit.

Obviously, in the weak segregation limit (WSL) there is no compositionally ordered structure, while in the strong segregation limit (SSL) the diblock copolymer is separated into microdomains with sharp interfaces, containing only one of the blocks each [41]. There is a transition between ordered and disordered phases (order-disorder-transition, ODT) at $\chi N = \mathcal{O}(10)$ for $f = 0.5$ [42].

A variety of different domain morphologies can be observed in compositionally ordered (i.e. microphase separated) diblock copolymers in the strong segregation limit (see Fig. 2.5), depending on the volume fractions of the blocks A and B and on the degree of segregation χN:

- for no compositional asymmetry:
  lamellae L (stable)
- for low compositional asymmetry:
  perforated lamellae PL (metastable)
  gyriod G (stable)
  ordered bicontinuos double diamond DD (unstable)
- for intermediate compositional asymmetry:
  hexagonal cylinders C (stable)
- for high compositional asymmetry:
  body-centered cubic spheres S (stable)

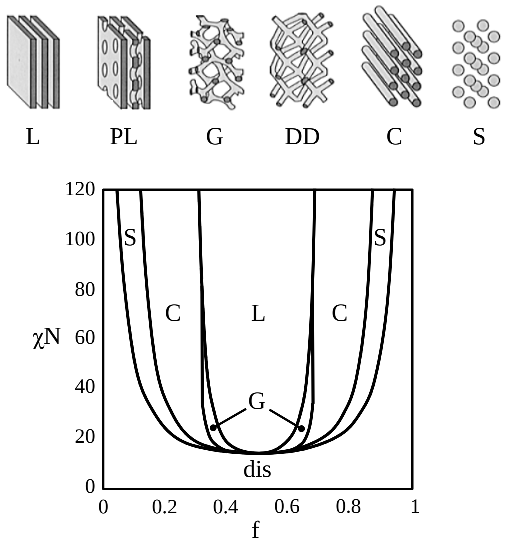

Figure 2.5: Top: Sketches of domain morphologies in microphase separated diblock copolymers with compositional asymmetry increasing from left to right [43]. Bottom: Phase diagram for stable morphological phases of diblock copolymers, after [44].

Among the efforts to describe the phase behavior of diblock copolymers in the strong segregation limit, some theoretical works are standing out [41]: Helfand and Wasserman [45] worked out a self-consistent field theory, which allows for quantitative predictions about free energies, chain conformations, and composition profiles. They conclude that the most important factors in the free energy in the strong segregation limit are the contact enthalpy at block interfaces, the entropy loss due to chain stretching and the confinement entropy from the covalent bond in each diblock copolymer molecules being localized at a block interface. Moreover, they devised numerical procedures for calculating the phase diagram for the compositionally ordered phases in the strong segregation limit, and noticed that the boundary compositions were temperature independent. From their theory, a characteristic interface width of $w \propto a/\sqrt{\chi}$ and a domain size of $D \propto aN^{\delta}\chi^{\mu}$ with $\delta \approx 9/14$ and $\mu \approx 1/7$ for $N \to \infty$ are deduced. Semenov [46] found analytical techniques for an estimation of the free energy (for $N \to \infty$) by analogy to classical mechanics. This theory is considerably less complex than Helfand's and Wasserman's approach, but only valid for strong chain stretching. It implies that the diblock copolymer molecules are not evenly stretched, and that chain ends are preferably found in the domain interior. According to Semenov's theory, the domain size is $D \propto aN^{\delta}\chi^{\mu}$ with $\delta = 2/3$ and $\mu = 1/6$. It allows for estimates of the phase boundary compositions as well and also predicts that they are independent of temperature. Discrepancies between

Semenov's and Helfand's and Wasserman's results can be attributed to the fact that their numerical procedures were only executed up to $D/(a\sqrt{N}) \approx 3$; for $D/(a\sqrt{N}) \to \infty$ these discrepancies would have vanished [41]. Ohta and Kawasaki [47,48] proposed an alternative, strongly simplified field-theoretical approach. They considered diblock copolymers with symmetric and asymmetric composition and yielded results quite similar to those of Semenov, Helfand and Wasserman. However, for the sake of simplicity they did not include effects resulting from non-uniform chain end placement. Anderson and Thomas [49] developed the first theory to include the so-called ordered bicontinuous double diamond phase (see DD phase in Fig. 2.5). The others had not considered this phase, since it had not been experimentally observed by the time. Matsen and Bates [44] unified theories for the strong and the weak segregation limit. They calculated the complete phase diagram for all degrees of segregation, including quantitative coordinates for the phase boundaries.

Symmetric diblock copolymers

The simplest way to consider a microphase separated state is by studying a compositionally symmetric diblock copolymer, with the same volume fraction f and same length a of monomer residues for both subchains. A symmetric diblock copolymer will express lamellar nanodomains - layerlike domains of each monomer species in alternation (see L phase in Fig. 2.5) - AB interfaces have to form at the domain boundaries and chains have to stretch. The equilibrium period D_0 of the lamellae is determined by interface energy and chain configuration entropy: Interface energy decreases with increasing lamellae width i.e. diminishing interface. Entropy increases with decreasing lamellae width, i.e. less stretched subchains having more possible positional configurations of their monomer residues. For a phenomenologial deduction [39,47], consider a sample unit volume a^3 containing $n = 1/Na^3$ diblock copolymer molecules in strong segregation limit. The energy increase per unit volume and chain due to the formation of interfaces between A domains and B domains at a period of D is

$$\frac{\gamma}{nD} = \frac{\gamma N a^3}{D} = k_B T \sqrt{\chi} \frac{N a^3}{D} \tag{2.20}$$

where $\gamma = k_B T \sqrt{\chi}/a^2$ is the surface energy density. The entropy decrease due to the necessary chain stretching (see Eqn.(2.11)) is

$$k_B \ln Q = -\frac{3k_B\boldsymbol{r}^2}{Na^2} = -\frac{3k_B D^2}{Na^2} \tag{2.21}$$

where Q is the distribution of end-to-end distances for a freely jointed chain in Gaussian limit ($N \gg 1$), Eqn.(2.10) and $r = D/2$. Summing Eqns. (2.20) and (2.21) results in the free energy associated with microphase separation:

$$\frac{F_{sep}}{k_B T} = \sqrt{\chi}\frac{Na}{D} + \frac{3}{8}\frac{D^2}{Na^2} \tag{2.22}$$

Minimizing this sum with respect to the period D, yields the equilibrium bulk lamellae period

$$D_0 = \left(\tfrac{3}{4}\right)^{1/3} \chi^{1/6} N^{2/3} a \tag{2.23}$$

Asymmetric diblock copolymers

For compositionally asymmetric diblock copolymers in the phase separated state nanodomain morphologies involving strongly curved interfaces are more favorable [43]: by curving the interfaces the degrees of chain stretching in the two blocks can be equalized. The area-average of the mean interface curvature increases with the composition becoming more asymmetric. It is expected to dictate the sequence of domain morphologies with increasing compositional asymmetry as follows: $L \rightarrow PL \rightarrow G \rightarrow DD \rightarrow C \rightarrow S \rightarrow$ *disordered*. In fact, however, the domain morphologies PL and DD are not experimentally observed. It turns out, that the standard deviation of the mean curvature σ_H determines the stability of possible morphological phases, and thereby decides which phases are actually adopted by the diblock copolymer. The value of σ_H results from the interplay of two factors: On the one hand, due to interface tension block copolymers are preferably forming domains of minimum interface area and constant mean curvature, i.e. ideally $\sigma_H = 0$. On the other hand, in order to avoid strong chain stretching and packing frustration block copolymers tend to form domains of uniform thickness, i.e. $\sigma_H > 0$. As an example, consider a morphology of type C, hexagonally packed cylinders of block A in a matrix of block B. A cross-section through a cylindrical domain is generally not circular, but has hexagonal symmetry [50] with a deviation Δ from a constant mean curvature. The minority component A favors $\Delta = 0$ for reasons of minimizing interface tension. The majority component B favors $\Delta > 0$ for reasons of avoiding packing frustration by uniform domain thickness. The preferences of both components have to be balanced. In the so-called classical phases L, C, and S this can easily be accomplished by just slightly increasing Δ to $\Delta \gtrsim 0$, because in these phases molecules can inherently pack with little frustration. However, in strong segregation the molecule chains are strongly stretched, which increases packing frustration and requires larger deviations from a constant mean curvature to accommodate the molecules. The so-called complex phases PL, G, and DD inherently present higher packing frustration than the classical phases, resulting in larger σ_H. Reversely, σ_H is an indicator for the ability of a block copolymer in a given ordered morphology to satisfy conditions of minimum interface area and minimum packing frustration: The larger σ_H, the less favorable is the morphology. Therefore, the phases PL and DD are not stable and the phase G exists only for lower degrees of segregation.

2.3.2 Thin films of diblock copolymers

In bulk diblock copolymers the chemical domains resulting from microphase separation are arranged in randomly oriented grains. In contrast, thin films of diblock copolymers exhibit a high degree of uniform orientation of the chemical domains with respect to the interfaces of the film. The chemical phase morphology of diblock copolymer films is determined by boundary conditions at the film interfaces and by the relation between diblock copolymer domain period and film thickness. There are two different interface boundary conditions for diblock copolymers: Symmetric wetting conditions, where the same block is preferred for both the air interface / free surface and the substrate interface. Anti-symmetric wetting conditions, where one of the blocks is preferred for the substrate interface and the other block is preferred for the free surface. In addition, the domain orientation changes as a function of the film thickness: Surface-parallel orientations are found, when the film thickness d is commensurate with the equilibrium period D_0. Surface-perpendicular domain orientations are observed, when the film thickness is incommensurate with the equilibrium period – especially for $d < D_0$ [51][1]. A surface-perpendicular domain orientation results in a chemical patterning of the free film surface, which will exhibit a pronounced regularity governed by the domain period D given by the size of the diblock copolymer molecules. Thus, suitable templates for fabricating nanostructure arrays can be prepared from diblock copolymer thin films.

---

[1] See also references therein.

Thin films of symmetric diblock copolymers

Consider first a compositionally symmetric AB diblock copolymer film with $f = 0.5$ and $\gamma_A \neq \gamma_B$. The presence of a substrate supporting the film or of a free surface requires the block with lowest respective surface energy density to be located at the corresponding film interface. Moreover, surface-parallel lamellae have the lowest AB interface area for any given domain period D_0.

In films of thickness $d \geq D_0$ this leads to surface-parallel lamellar morphologies s-L$^{\parallel}$ and a-L$^{\parallel}$ for symmetric and antisymmetric wetting conditions, respectively, as shown in Fig. 2.6. In this way, both the interface boundary conditions are fulfilled and the bulk equilibrium period D_0 resulting from the spontaneous ordering is maintained. The symmetric morphology s-L$^{\parallel}$ is stable at $d = nD_0$ for symmetric wetting conditions, and the antisymmetric morphology a-L$^{\parallel}$ is stable at $d = (n + \frac{1}{2})D_0$ for antisymmetric wetting conditions ($n \geq 1$) [52]. For film thicknesses $d \leq D_0$, however, a surface-parallel morphology is unfavorable, because it would require domains with $D < D_0$, i.e. to compress the polymer chains. It can therefore be more favorable for the domains to be oriented in a surface-perpendicular way, so that the equilibrium period D_0 can be maintained laterally within the film. Consequently, additional stable surface-perpendicular lamellae and hybrid structures have been predicted and observed [51, 53, 54]: The anti-symmetric hybrid structure a-H, antisymmetric surface-parallel half lamellae a-hL$^{\parallel}$, symmetric hybrid structure s-H, and symmetric surface-perpendicular lamellae s-L$^{\perp}$ are depicted in Fig. 2.7. These result in chemically patterned free film surfaces which are highly interesting for further applications.

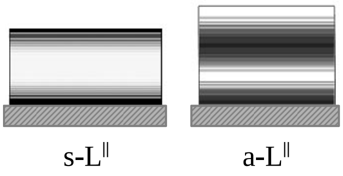

Figure 2.6: Morphologies for $d \geq D_0$. Adapted from [52].

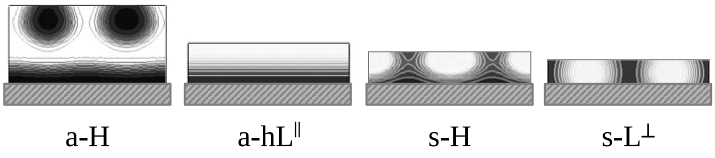

Figure 2.7: Morphologies for $d \leq D_0$. Adapted from [52].

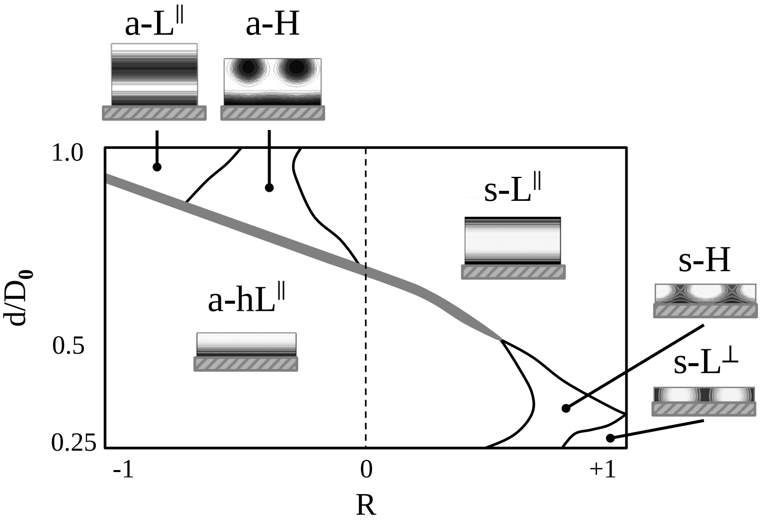

Figure 2.8: Phase diagram of morphologies for compositionally symmetric ($f = 0.5$) supported diblock copolymer thin films. d/D_0 is the ratio of film thickness d to equilibrium domain period D_0. R is a parameter describing the wetting conditions: wetting conditions are anti-symmetric for $R < 0$, symmetric for $R > 0$. The gray area is the phase field for metastability of the symmetric hybrid structure s-H. Adapted from [52].

Fasolka and coworkers [51, 52] have developed a theoretical phase diagram of these morphologies for supported thin films of diblock copolymers with $f = 0.5$ in dependence of the film thickness d and the wetting conditions (described by the parameter R); it is shown in Fig. 2.8. The left half of the diagram comprises anti-symmetric wetting conditions ($R < 1$), the right half comprises symmetric wetting conditions ($R > 1$). It becomes apparent, that the two hybrid structures a-H and s-H can be regarded as intermediate states: When wetting conditions are reversed, a-H is intermediate in between the anti-symmetric and the symmetric surface-parallel lamellae morphologies a-L$^{\parallel}$ and s-L$^{\parallel}$. Then s-H is intermediate in between the anti-symmetric surface-parallel half lamellae a-hL$^{\parallel}$ and the symmetric surface-perpendicular lamellae s-L$^{\perp}$. When the film thickness is changed, for distinct wetting conditions a-H can be the transition state between anti-symmetric surface-parallel full lamellae a-L$^{\parallel}$ and surface-parallel half lamellae a-hL$^{\parallel}$, and s-H can be the transition state between symmetric surface-parallel full lamellae s-L$^{\parallel}$ and perpendicular lamellae s-L$^{\perp}$. Notably, under anti-symmetric wetting conditions, the surface-perpendicular phase (a-H) is only stable for film thicknesses above $d = 0.5D_0$, while under symmetric wetting conditions, surface-perpendicular phases (s-H and s-L$^{\perp}$) are only stable for film thicknesses below $d = 0.5D_0$. Surface parallel lamellae morphologies are stable at $d = 0.5D_0$ under anti-symmetric wetting conditions, and stable at $d = D_0$ under symmetric wetting conditions (see Fig. 2.8).

The fact that a free surface is not a rigid confinement is often disregarded in theory, but has noteworthy consequences in practice. Assume a diblock copolymer film on a substrate under symmetric wetting conditions, with film thickness $nD_0 < d < (n+1)D_0$. There is a mismatch between the thickness at which the film can adopt a stable morphology and its actual thickness. Upon annealing however, the film will express regions of different thickness, each conforming with the equilibrium domain period, i.e. either $d = nD_0$ or $d = (n+1)D_0$). The area ratio of regions of different thickness will be such, that the initial thickness is retained on average. In a flat film, these regions form as holes or islands, respectively; in a wedge-shaped film they form as terraces of height difference D_0 [52]. In a confined film, the mismatch between equilibrium bulk period D_0 and actual film thickness d must be compensated by a deviating period D as compared to D_0 [55–57] or by domain reorientation from surface-parallel to surface-perpendicular [53].

Thin films of asymmetric diblock copolymers

Thin films of diblock copolymers with asymmetric composition $f \neq 0.5$ have been studied more rarely in theory, since their curved interfaces introduce more complexity into descriptions of their morphological behavior. Huinink and coworkers [58] have executed dynamic density functional theory calculations for a diblock copolymer with composition $f = 1/3$ in a film confined between two identical rigid surfaces. The morphology of the confined film was calculated for different film thicknesses and surface interactions. In bulk, a diblock copolymer with $f = 1/3$ is expected to express hexagonally packed cylinders of the minority block in a matrix of the majority block. For a confined thin film of this diblock copolymer, several different phases are predicted: surface-parallel cylinders $\mathrm{C}^{\parallel}$, surface-perpendicular cylinders $\mathrm{C}^{\perp}$, surface-parallel lamellae $\mathrm{L}^{\parallel}$, and surface-parallel perforated lamellae $\mathrm{PL}^{\parallel}$. It turns out, that besides film thickness also (effective) surface selectivity plays a crucial role in determining the stable morphology under the given conditions: If the confining surfaces are selective, i.e. if one of the blocks preferentially wets the confining surfaces (comparable to symmetric wetting conditions for a thin film supported on a substrate), surface-parallel morphologies are more favorable. Selectivity is caused by a difference in surface energy densities $\Delta\gamma$ of the two blocks, but can also occur for $\Delta\gamma = 0$: In asymmetric diblock copolymers the shorter block is entropically preferred for wetting the confining surface – the reasons have not yet been clarified. For (effectively) selective confining surfaces, surface-perpendicular cylinders are predicted to be stable only for distinct film thicknesses, when the energy increase due to domain reorientation is less than the entropic penalty due to the extreme chain stretching or compression which would be required to fit an integer number of domains into the given film thickness. This appears to be an effect of confinement by rigid surfaces: The $C^{\perp}$ phase for selective confining surfaces was not observed experimentally, where the film usually has at least one free surface which can restructure to make the local film thickness conform with the bulk equilibrium period D_0. If the confining surfaces are (effectively) non-selective, i.e. none of the blocks is preferably wetting the confining surfaces, surface-perpendicular cylinders are stable for all film thicknesses. Effective non-selectivity for asymmetric diblock copolymers is achieved, when an energetic preference for the larger block is canceled out by the entropic preference for the smaller block.

Diblock copolymer thin films in practice

In practice, diblock copolymer thin films are prepared by casting from a solution, e.g. by spin coating (see section 5.2). Generally, this procedure leaves the diblock copolymer film in a non-equilibrium state. Microphase separation to a certain degree may take place during film deposition, but the chemical nanodomains are not found in a well-ordered morphology or even in a long-range order of lateral positioning. In order to bring about this high degree of ordering, the diblock copolymer film has to be annealed either thermally or by exposure to solvent vapor. Section 5.3 describes the process of solvent vapor annealing and names the important parameters for obtaining optimum results in ordering the diblock copolymer domains.

3 Magnetic Nanostructures

Both the nanofaceted α-Al_2O_3 substrates and the microphase-separated diblock copolymer films described in sections 1.2.3 and 2.3.2 will serve as templates for the fabrication of self-assembled metallic, especially magnetic, nanostructures in this work. For the explanation of basic terms and phenomena in magnetism the reader is kindly referred to standard textbooks [59–62]. This chapter briefly outlines specific magnetic properties of nanostructures, especially nanoparticles and thin films. The magnetic properties of one exemplary system - a Fe thin film of uniaxially uniaxially corrugated shape - are discussed in more detail. An experiment on such a system will be presented in section 8.2, proposing to merge Grazing Incidence Small Angle X-ray Scattering and Nuclear Resonant Scattering in GINSAXS (Grazing Incidence Nuclear Small Angle X-Ray Scattering).

3.1 The single-domain state in nanostructures

In nanostructures - as in macroscopic objects - domains of different magnetization orientations are formed to minimize stray field energy. The exact domain pattern in a sample depends on its size, shape, magnetic anisotropy, and magnetization history [63, 64]. Retaining domain walls becomes energetically unfavorable, if the size d of the magnetic object is reduced into the sub-μm regime [62]. There is a critical size d_c, i.e. surface-to-volume relation, at which the stray field or demagnetization energy (which scales with d^3) saved by the presence of domain walls is exceeded by the energy cost for retaining domain walls (which scales with d^2). Then the total energy is minimized, if the object contains only one single magnetic domain and no domain walls [61]. Both calculations and experimental studies show that the critical diameter for a spherical or cylindrical nanoparticle is on the order of 10^2 nm [61, 65, 66]. The magnetic nanodots described in chapter 10 can therefore be assumed to be single-domain nanoparticles.

3.2 Magnetic anisotropy in nanostructures

If for a sample there is an orientation in space along which a lower external magnetic field strength H is required to achieve saturation magnetization M_s than along the other orientations, the sample is said to exhibit magnetic anisotropy and the aforementioned orientation is called the easy axis of magnetization. Easy and hard axes of magnetization can for example be given by the crystal structure or texture orientation, by the shape of the magnetic body, or by asymmetric conditions at surfaces and interfaces. Anisotropy constants K_i can be defined to quantify the strength of the respective anisotropy contribution. The contributions E_{K_i} to the energy density associated with magnetic anisotropies are expressed in terms of the orientation of the magnetization with respect to the easy axis of magnetization. This holds for macroscopic magnetic samples as well as for magnetic nanostructures. However, volume-, surface-, and shape-related anisotropy energies scale differently with the object size. Therefore, the (relative) magnitudes of the possible contributions to the total magnetic anisotropy energy differ from macroscopic bodies to nanostructures and also among nanostructures of different geometries.

The magnetic anisotropy dictates how the net magnetization $\boldsymbol{M}$ of a magnetic body behaves in an external magnetic field $\boldsymbol{H}$. In general, the magnetization always lies within the plane spanned by the external field $\boldsymbol{H}$ and the easy axis of magnetization. In the absence of any anisotropy, the magnetization $\boldsymbol{M}$ is always parallel to a given external magnetic field $\boldsymbol{H}$.

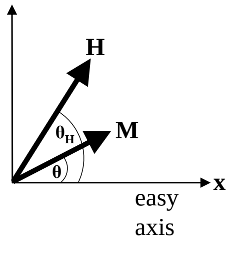

Consider a nanostructure with uniaxial anisotropy, i.e. one easy axis of magnetization, in an external magnetic field: The strength of the anisotropy is quantified by an effective anisotropy constant K. The easy axis of magnetization is parallel to the unit vector $\boldsymbol{e}_x$ of the coordinate axis x and the external magnetic field vector $\boldsymbol{H}$ encloses a fixed angle θ_H with the easy axis of magnetization. For simplicity, let all vectors lie in the x-y-plane. The energy density of the structure with uniaxial anisotropy in the external magnetic field is

$$
\begin{aligned}
E &= E_K + E_H = K\sin^2(\theta) - \mu_0 \boldsymbol{H}\boldsymbol{M} \\
&= K\sin^2(\theta) - \mu_0 H M \cos(\theta_H - \theta) \\
&= K\sin^2(\theta) - \mu_0 H_x M \cos(\theta) - \mu_0 H_y M \sin(\theta)
\end{aligned} \tag{3.1}
$$

It is minimized when the angle between the magnetization and the easy axis is $\theta = \theta_0$, fulfilling

$$
\frac{dE}{d\theta} = 2K\sin\theta\cos\theta + \mu_0 H_x M \sin\theta - \mu_0 H_y M \cos\theta = 0 \tag{3.2}
$$

or equivalently

$$
\frac{H_y}{\sin\theta} - \frac{H_x}{\cos\theta} = \kappa \qquad \text{with} \qquad \kappa = \frac{2K}{\mu_0 M} \tag{3.3}
$$

Depending on the magnitude of H, Eqn. (3.3) has two or four real solutions [62]. In case of two solutions, $\frac{1}{K}E(\theta)$ has one minimum, so that the magnetization has one equilibrium orientation θ_0. In case of four solutions, $\frac{1}{K}E(\theta)$ has two minima, so that the magnetization has two possible equilibrium orientations θ_0. Resulting $M(H)$ behavior for different orientations of the external magnetic field with respect to the easy axis of magnetization is shown in Fig. 3.1.

If the external magnetic field is parallel to the easy axis of magnetization ($H_x = H, \quad H_y = 0, \quad \theta_H = 0°$), Eqn. (3.3) becomes $\kappa\cos\theta + H = 0$. There are two real solutions for $|H/\kappa| \leq 1$ and one real solution for $|H/\kappa| > 1$. When reducing H, the magnetization is retained in the beginning. When reducing H further and then increasing in the opposite direction, $\boldsymbol{M}$ is retained until $H = \kappa$ and $\frac{dE}{d\theta}$ changes its sign: Then the magnetization suddenly switches into the direction of $\boldsymbol{H}$. The resulting $M(H)$ behavior is hysteretic, i.e. irreversible.

If the external magnetic field is perpendicular to the easy axis of magnetization, ($H_x = 0, \quad H_y = H, \quad \theta_H = 90°$), Eqn. (3.3) becomes $\kappa\sin\theta - H = 0$. For a linear material, the y-component of the magnetization depends linearly on $H = H_y$. When $H = \kappa$, then $M = M_s$ and remains constant. The resulting $M(H)$ behavior is completely reversible.

If the external magnetic field is at an arbitrary angle with respect to the easy axis of magnetization, the resulting $M(H)$ behavior of the nanostructure is partly hysteretic, partly reversible.

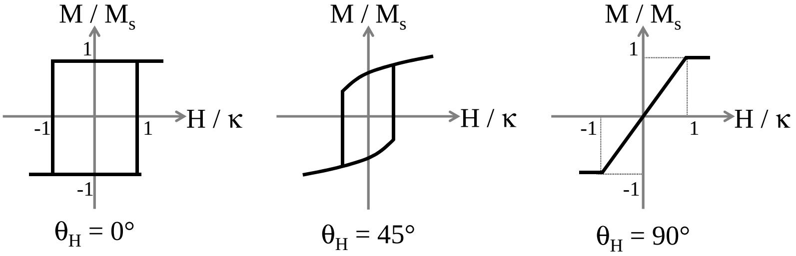

Figure 3.1: Magnetization curves of single-domain nanostructures exhibiting uniaxial magnetic anisotropy, with the external magnetic field being parallel, perpendicular, or at 45° to the easy axis of magnetization.

3.3 Superparamagnetism in nanoparticles

Within this work, superparamagnetism is explicitly observed in ^{57}Fe dot-shaped nanoparticles growing on diblock copolymer templates (see section 10.3.3). Therefore, a basic description of this behavior of magnetic nanoparticles shall be given here.

The anisotropy energy density E_K is a function of the angle θ enclosed by the magnetization $\boldsymbol{M}$ and the easy axis of magnetization, as depicted in Fig. 3.2. Consider a single-domain nanoparticle with uniaxial anisotropy and volume V. Let ΔE_K be the difference between minimum and maximum value of $E_K(\theta)$ for this particle. Then the product $V\Delta E_K$ is the magnetic anisotropy energy of this nanoparticle: an activation energy equal to $V\Delta E_K$ is required to flip its magnetization orientation from $\theta_H = \pi$ to $\theta_H = 2\pi$.

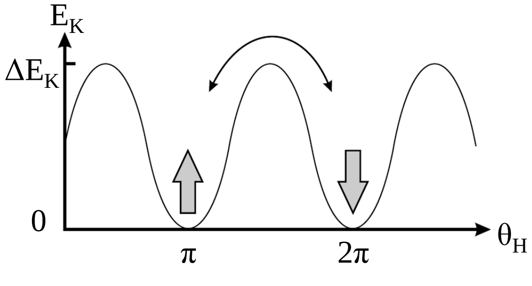

Figure 3.2: The anisotropy energy density $E_K(\theta)$. Reversing the magnetization orientation requires to overcome the energy barrier $V\Delta E_K$. From [62].

For $V\Delta E_K \gg k_B T$ thermal excitations are negligible on experimentally relevant timescales. The magnetization of the particle is stable and the $M(H)$ dependence behaves as described in section 3.2. However, if $V\Delta E_K < k_B T$, thermal excitations cause the magnetization of the nanoparticle to fluctuate between different minimum energy states.

An ensemble of such nanoparticles then behaves like an ensemble of paramagnetic atoms and shows no hysteretic $M(H)$ behavior. In the presence of an external magnetic field, the magnetization of the nanoparticle ensemble depends linearly on the magnetic induction and is completely reversible. In the absence of an external magnetic field, the net magnetization of the ensemble is approximately zero. The fluctuation frequency of the magnetization is

$$\nu = \nu_0 \exp\left(-\frac{V\Delta E_K}{k_B T}\right) \tag{3.4}$$

Decreasing the temperature decreases the fluctuation frequency, so that the magnetization orientation of the nanoparticles becomes stable for temperatures below $T_b = \frac{V\Delta E_K}{k_B}$, the blocking temperature. Increasing the nanoparticle volume decreases the fluctuation frequency, too [61]. Fluctuation frequencies of $\nu \approx 3 \cdot 10^{-8}$ (one fluctuation in ten years) at room temperature, allowing for technological applications e.g. in data storage, are achieved for nanoparticles containing at least about 5500 atoms. This corresponds to a nanoparticle size of roughly 5 nm and a storage density of around 10 Tbit/inch^2 [62]. While the number density of bits in commercially available magnetic data storage devices is about 0.1 Tbit/inch^2, a number density of 10 Tbit/inch^2 has been accomplished in nanostructure patterns fabricated from self-assembled diblock copolymers [67].

3.4 An example: Self-assembled Fe thin films on corrugated oxide surfaces

One example of magnetism in nanostructures shall be discussed in more detail: Sugawara, Shiratsuchi, Fukunaga and their respective coworkers have investigated the growth and the magnetic properties of Fe thin films on uniaxially corrugated (i.e. stepped and faceted) surfaces and found correlations between shape, microstructure, and magnetism of the films [68–74]. Their results on uniaxially corrugated Fe thin films described below can serve as references for the in-situ GINSAXS experiment performed on a Fe thin film growing on nanofaceted α-Al_2O_3 (see section 8.2).

3.4.1 Growth of Fe nanowires and thin films on corrugated oxide surfaces

The growth mechanism and resulting morphology of Fe deposited on substrate surfaces with nanoscale topographic corrugations (facets or steps) is influenced by the substrate temperature, the dimensions of substrate surface corrugations, and the polar incidence angle of Fe atoms on the substrate [68]. Depending on the polar incidence angle, different areas of the substrate surface are exposed to the beam of Fe atoms, and the deposition process results in separated nanostripes or in a continuous corrugated thin film, respectively, as sketched in Fig. 3.3.

Generally, Fe is found to grow via particle nucleation and coalescence on oxide surfaces. The resulting morphology is smoother for lower substrate temperatures and more granular for higher substrate temperatures (compare Fig. 3.4 (a) and (b)) [68,69,71,75]. Near room temperature, diffusion lengths are short and small particles (diameter < 2 nm) are formed, which are densely packed on the oxide substrate surface.

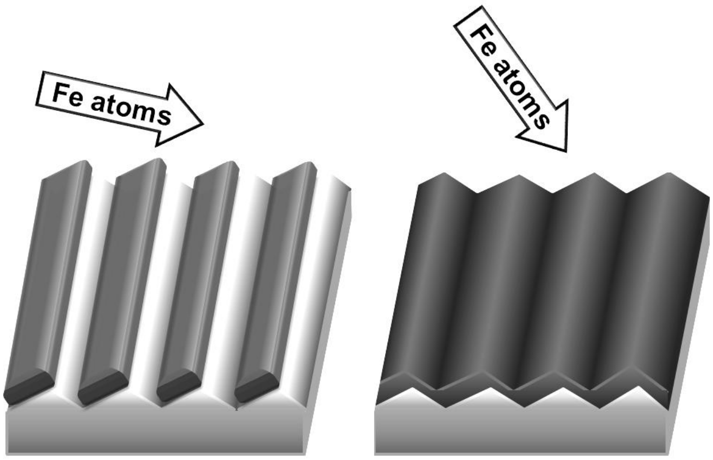

Figure 3.3: Left: Separated Fe nanostripes are grown at oblique incidence of the Fe atoms with respect to the macroscopic substrate surface. Right: For larger incidence angles of the Fe atoms a continuous film is grown, which reproduces the uniaxial corrugation of the substrate surface.

Upon further deposition, the Fe particles grow and touch (without coalescing to bigger spherical particles due to the low diffusivity) and gaps in between particles are filled. Fe grows on the corrugated surface in a polycrystalline manner with particles of isotropic shape and without any texture orientation, as can be seen in the transmission electron microscopy data of Fe films on uniaxially corrugated substrates shown in Fig. 3.4 [68]. Moreover, the substrate corrugation propagates through the entire Fe film, as shown in Fig. 3.5 [74].

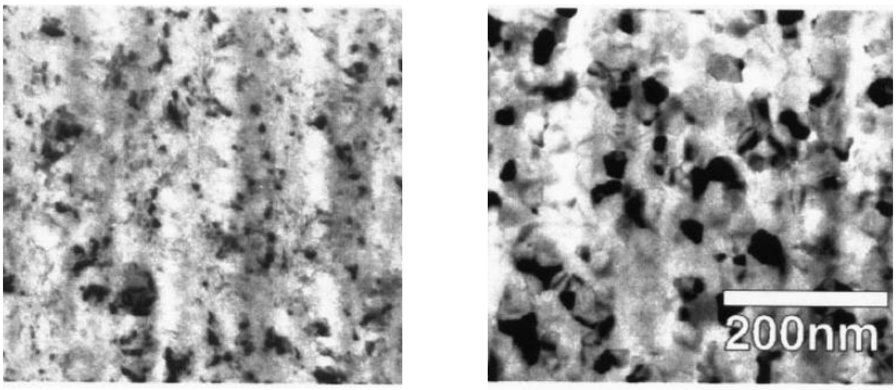

(a) grown at room temperature

(b) grown at 190 °C

Figure 3.4: Bright field transmission electron micrographs of continuous Fe particle film grown at room temperature and at 190 °C substrate temperature, respectively, on a faceted NaCl surface coated with SiO_x. The particles are densely packed and isotropically shaped. A higher substrate temperature during deposition results in a film composed of larger Fe particles. From [68]. The scale is identical for both images.

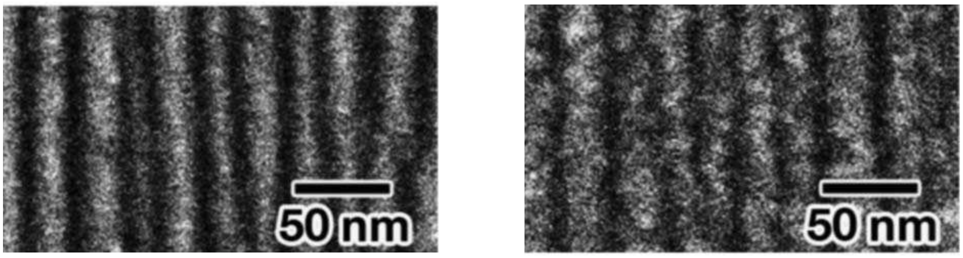

(a) substrate side

(b) growth front side

Figure 3.5: Scanning electron micrographs of a $\mathrm{SiO_x}$ /Fe(20nm)/$\mathrm{SiO_x}$ trilayer floated off its faceted NaCl substrate. The corrugations induced by the faceted substrate are present on both sides of the trilayer, confirming that the corrugations propagates through the entire stack. From [74].

3.4.2 Magnetism of Fe thin films on corrugated oxide surfaces

A continuous Fe film which reproduces the uniaxial corrugation of the substrate can be prepared under suitable deposition conditions, as described above. Due to the uniaxially corrugated film shape, the magnetism of such Fe films can differ markedly from that of planar films. Especially, this film shape induces an additional uniaxial in-plane magnetic anisotropy, which is not present in planar films [73, 76].

Dependence of the magnetic phase on the film thickness

The GINSAXS experiment presented in section 8.2 investigates the evolution of magnetic states of a uniaxially corrugated Fe film in-situ during deposition of the film. As a reference, the results of former ex-situ studies on the thickness dependence of the magnetic phase of Fe films shall be outlined briefly. The following results hold for Fe film on both planar and uniaxially corrugated substrates [69–71]. Fig. 3.6 shows the $M(H)$ curves for Fe thin films grown on corrugated substrates. In all cases, the external magnetic field was applied parallel to the orientation of the corrugation edges.

For a thickness of 1.0 nm the iron film is in a superparamagnetic state. Measurements of the magnetization as a function of an externally applied magnetic field at room temperature show that the saturation magnetization is not reached for an external field strength of 4.5 kOe and that the films exhibit neither remanence nor coercivity. The shape of the $M(H)$ curves is characteristic of paramagnetic behavior, i.e. given by a Langevin function. Characteristic blocking phenomena can be deduced from comparing measurements of the magnetization as a function of temperature during field cooling and zero-field cooling.

At 2.0 nm film thickness superparamagnetic and ferromagnetic phase coexist within the film. Characteristic differences in the temperature dependence of the magnetization during field cooling and zero-field cooling (blocking) evidence the presence of a superparamagnetic fraction. $M(H)$ curves exhibit remanent magnetization and coercivity, thus evidencing the presence of a ferromagnetic fraction. However, the saturation magnetization can still not be reached.

Films thicker than 3.0 nm are purely ferromagnetic. Characteristic hysteresis curves are found in measurements of the magnetization as a function of an externally applied magnetic field.

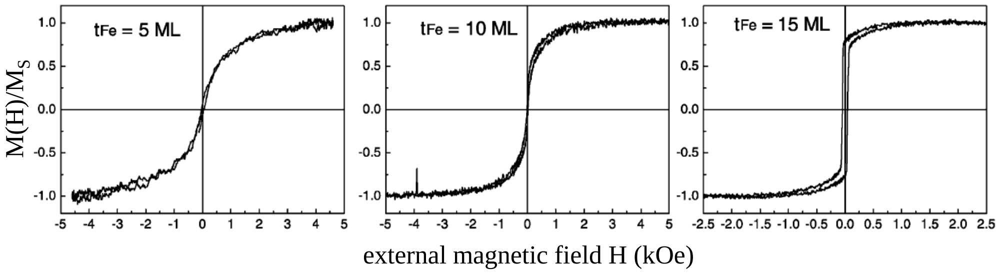

Figure 3.6: The relative magnetization $M(H)/M_s$ of Fe thin films on stepped α-Al_2O_3 (0001) as a function of an external magnetic field H applied parallel to the substrate step edges. The magnetization stabilization from the superparamagnetic phase to the ferromagnetic phase proceeds via a coexistence phase. t_{Fe} is the nominal film thickness in units of monolayers; 5 ML = 1 nm. From [70].

In the superparamagnetic phase magnetic inter-particle interactions determine the magnetic behavior of the sample. These interactions are relevant due to the small sizes and distances of the particles forming the Fe film grown near room temperature. Several indications for the presence and significant influence of magnetic interparticle interactions in Fe films of 1.0 nm thickness on planar substrates were found (see [69] and references therein). One of them is the fact that the magnetization of the Fe particle film lies in-plane. A film of non-interacting isotropic particles would exhibit no magnetic anisotropy. The ratio of ferromagnetic to superparamagnetic fraction in the intermediate phase depends on whether or not the substrate is corrugated and on the substrate temperature during Fe deposition [71, 72]. Two effects were observed for Fe films of 2 nm thickness grown at room temperature: The ferromagnetic fraction is larger in uniaxially corrugated films on corrugated substrates than in planar films. For uniaxially corrugated Fe films, the ferromagnetic fraction decreases monotonously with increasing temperature during growth. These findings can be explained in terms of an in-plane magnetic anisotropy: An in-plane magnetic anisotropy would magnetically stabilize a thin Fe film, i.e. increase the ferromagnetic fraction. A uniaxially corrugated substrate surface causes a correspondingly uniaxially corrugated shape of the film, thereby inducing a uniaxial in-plane magnetic anisotropy with the easy axis of magnetization parallel to the substrate corrugation edges (see next section), and thus augmenting the ferromagnetic fraction as compared to a planar film of the same thickness. On the other hand, film growth at higher temperatures leads to monotonously increasing roughness of the film surfaces, washing out the uniaxially corrugated film shape with ideally parallel film/substrate and film/vacuum interfaces. This reduces the uniaxial magnetic anisotropy energy (see also Fig. 3.8) and thereby reduces the ferromagnetic fraction in comparison to films grown at lower temperatures.

Magnetic anisotropy in uniaxially corrugated Fe films

Thin Fe films grown by normal-incidence deposition on a planar surface exhibit no in-plane magnetic anisotropy [70]. Fe films on grown on uniaxially corrugated surfaces, however, were found to have a uniaxial in-plane magnetic anisotropy with the easy axis of magnetization parallel to the corrugation edges and the hard axis of magnetization perpendicular to the corrugation edges, as becomes apparent by comparing the hysteresis curves in Fig. 3.7 [70]: Subfigure (a) shows magneto-optical Kerr effect measurements of $M(H)$ curves of a planar Fe film in the ferromagnetic phase with the external magnetic field applied parallel and perpendicular to the substrate crystallographic orientation corresponding to the orientation of the corrugation edges in the corrugated sample. The curves are identical, there is no in-plane magnetic anisotropy. Subfigure (b) shows analogous measurements for an uniaxially corrugated film on a corrugated substrate, exhibiting pronounced in-plane magnetic anisotropy. The $M(H)$ curve for the applied magnetic field parallel to the corrugation edges is hysteretic, characterizing an easy axis of magnetization, while the curve for the applied magnetic field perpendicular to the corrugation edges is almost reversible, characterizing a hard axis of magnetization.
The uniaxial in-plane magnetic anisotropy is already observed for samples in the intermediate phase (Fe film thickness of 2.0 nm), where superparamagnetism and ferromagnetism coexist. For a film thickness of 2.0 nm it is one order of magnitude larger than the magnetocrystalline anisotropy energy for bulk α-Fe. The uniaxial magnetic anisotropy energy decreases with increasing particle size, i.e. film roughness or graininess, at higher deposition temperatures (see Fig. 3.8) [68, 73]. These findings on the correlation between the particle size / film roughness and the uniaxial in-plane magnetic anisotropy energy are consistent with the argumentation concerning the size of the superparamagnetic fraction in the intermediate state [71, 72].

There are several possible origins of this uniaxial in-plane magnetic anisotropy: The most common contributions to the total anisotropy of a sample are magneto-crystalline, magneto-elastic, and shape anisotropy. The contribution of magneto-crystalline anisotropy to any magnetic anisotropy of the films is negligible in case of the polycrystalline, non-textured growth of Fe at room temperature [68]. A magneto-elastic contribution is ruled out for uniaxially corrugated thin films, too [76]. Due to the exponential decrease of the uniaxial in-plane magnetic anisotropy energy with increasing Fe film thickness, surface anisotropy is excluded as the reason for the observed uniaxial in-plane magnetic anisotropy [70, 73].

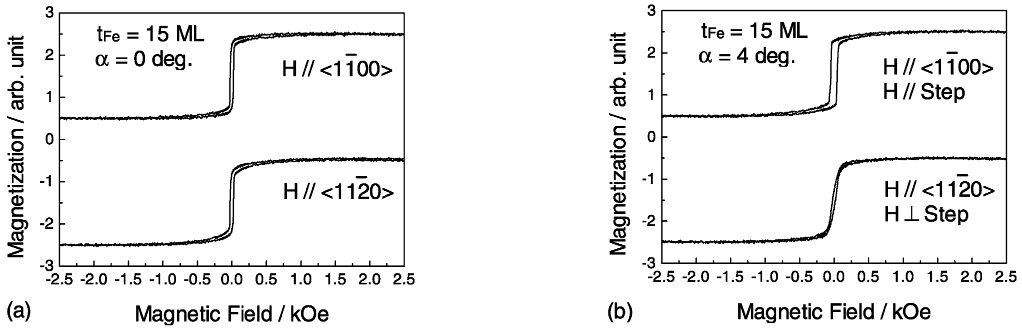

Figure 3.7: Comparison of the in-plane magnetic anisotropy (a) in a flat Fe film on a planar α-Al$_2$O$_3$ (0001) substrate and (b) in a uniaxially corrugated Fe film on a stepped α-Al$_2$O$_3$ (0001) substrate: Measurement of the magnetization as a function of the external magnetic field strength, with the external magnetic field applied perpendicular to the orientation of the step edges in miscut α-Al$_2$O$_3$ (0001). The curves were shifted along the magnetization axis for clarity. t_{Fe} is the Fe film thickness in monolayers; α is the miscut angle of the substrate. From [70].

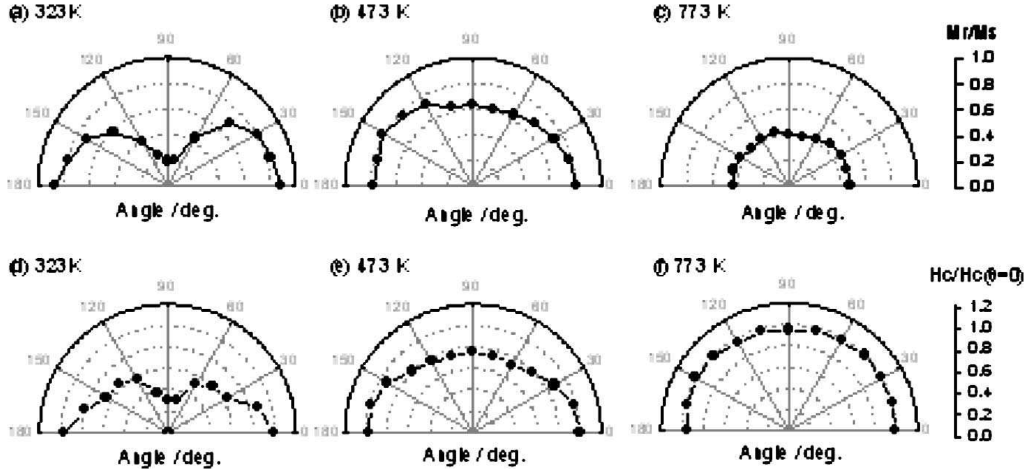

Figure 3.8: The ratio of remanent magnetization M_r to saturation magnetization M_s and the coercivity H_c of uniaxially corrugated Fe films on stepped α-Al$_2$O$_3$ (0001) as functions of the orientation of an external magnetic field with respect to the step edges. The films were grown at the indicated substrate temperatures. The uniaxially corrugated film grown at 323 K exhibits pronounced uniaxial in-plane magnetic anisotropy as evidenced by the two-fold symmetry of the polar plots. The uniaxial in-plane magnetic anisotropy is diminished with increasing deposition temperature. From [73].

Thus, the uniaxially corrugated shape of the Fe film is most likely to cause the uniaxial in-plane magnetic anisotropy. At first sight, the large aspect ratio of the stripe-like film regions on the step or facet surfaces may appear as the origin of the pronounced anisotropy. However, this is not consistent with a strong correlation between the uniaxial in-plane magnetic anisotropy energy and the Fe film thickness [70]. Moreover, the increasing graininess of the film with increasing deposition temperature is not expected to change the aspect ratio of the stripe-like regions enough as to explain the drastic effects depicted in Fig. 3.8.

The mechanism by which the film shape causes magnetic anisotropy in the case of uniaxially corrugated films is somewhat more subtle [70, 73, 76] (see also Fig. 3.9): Consider an absolutely planar film, infinitely extended in the lateral directions. For any in-plane orientation of the magnetization, the magnetization is parallel to the film interfaces at every point. Therefore, there is no divergence of the magnetization at the film interfaces, thus no demagnetizing field. Consider now a film with uniaxial in-plane corrugation: If the magnetization is in-plane and parallel to the edges of these corrugations, it is also parallel to the interfaces of the film at every point. Therefore, there is no divergence of the magnetization at the film interfaces and no demagnetizing field. If, however, the magnetization is in-plane and perpendicular to the corrugation edges, the magnetization is not parallel to the film interfaces anymore. It diverges at the film interfaces, resulting in a demagnetizing field. The energy associated with this demagnetizing field is the origin of the uniaxial in-plane magnetic anisotropy. The anisotropy contribution due to the uniaxially corrugated film shape is independent of the film material. However, this film shape is too complex for an analytical calculation of the demagnetizing field [76].

This mechanism can only be the origin of uniaxial in-plane magnetic anisotropy, if the film surface is smooth and parallel to the substrate surface, reproducing its well-oriented corrugations. This is the case for low substrate temperatures during deposition where a smooth film is produced, not for high substrate temperatures where a rough film is produced. The demagnetizing field decreases with increasing film roughness, and so does the uniaxial anisotropy energy. Thus the assumption of a demagnetizing field is consistent with the observed dependence of the uniaxial in-plane magnetic anisotropy energy on the substrate temperature during film deposition [73].

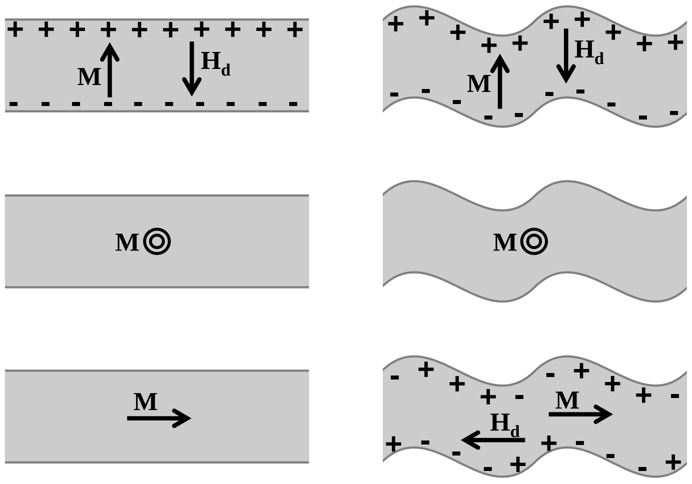

Figure 3.9: Cross-section sketches of a planar film (left) and a uniaxially corrugated film (right): The films are assumed to be infinitely extended in the lateral dimensions. The corrugated film is seen along the edges of the corrugations. The individual subfigures consider different orientations of the magnetization $\boldsymbol{M}$ in both films. If the magnetization is not parallel to the film interfaces $\boldsymbol{M}$, it diverges at the interfaces, resulting in a demagnetizing field $\boldsymbol{H_d}$. This can be pictured by magnetic charges (+, -) being present at the interfaces and acting as sources and drains of the demagnetizing field. In both the planar and the corrugated film there is a demagnetization field in case of the magnetization being oriented out of the film plane (top). For the magnetization being within the film plane, there is no demagnetzation field in the planar film (left, middle and bottom). However, for the corrugated film, it depends on the orientation of the magnetization with respect to the corrugation edges, whether or not a demagnetizing field is present (compare right, middle and bottom). The energy associated with the demagnetizing field is the origin of the unidirectional in-plane magnetic anisotropy in corrugated films.

4 Synchrotron Radiation

Synchrotron radiation possesses two qualities, which are essential for the studies described in this work, and which are not provided by radiation from an x-ray tube: On the one hand, the high spectral brilliance of synchrotron radiation makes scattering experiments on nanostructures, i.e. on samples with very small volumes of the structures of interest, feasible. On the other hand, the method of Nuclear Resonant Scattering (NRS) fundamentally relies on the time structure of synchrotron radiation (see section 6.3).

Synchrotron radiation was first observed as a byproduct in storage rings built for particle physics experiments. After its usefulness for spectroscopy and diffraction experiments had been recognized, designated synchrotron radiation sources were developed based on storage ring designs.

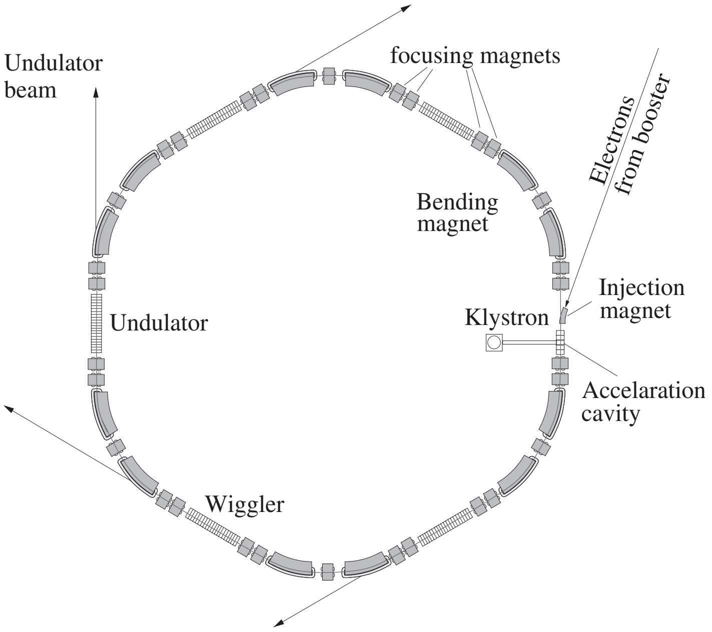

Figure 4.1: Generic layout of a third-generation synchrotron radiation source. From [77].

4.1 Production of synchrotron radiation

The very basic working principle of a synchrotron radiation source is the following: A beam of electrons (or positrons) is produced, pre-accelerated and pulsed. These electron pulses are injected into the toroidal vacuum chamber enclosing the designated trajectory of the particles (this vacuum chamber is not explicitly depicted in Fig. 4.1). A magnetic guide field generated by dipole bending magnets distributed along the circumference of the vacuum chamber forces the electrons onto a closed path within the vacuum chamber - thus the electron pulse is stored. The guide field also focuses the electrons onto their designated trajectory in radial direction and in direction perpendicular to the plane of the storage ring. Each time the electron trajectory is bent by the guide field, the electrons are accelerated orthogonally to their initial direction of motion, causing them to emit electromagnetic radiation and lose some of their energy. This energy loss is compensated for when the electrons pass the RF-cavity. Here, they are re-accelerated by a radio-frequency electric field, which also serves to gather the electrons into bunches [78]. In order to synchronize the oscillation of the re-acceleration field with the orbiting motion of the electron bunches, the cavity frequency f_{RF} must be an integer multiple of the electron orbiting frequency f_e: $f_{RF} = mf_e$. m is then the number of so-called buckets, i.e. possible locations of electron bunches along the designated trajectory. Quadrupole magnets serve to improve the focusing by the guide field. Hexapole magnets are used for dispersion correction, since not all electrons in one bunch have exactly the same energy and thus are deflected differently by the dipole bending magnets.

The stored electrons move at velocities close to the velocity of light, so that relativistic effects determine their radiation characteristics (see Fig. 4.2). In the rest frame of the electron its radiation pattern is that of a non-relativistic dipole. In the rest frame of an observer, however, the radiation pattern of the moving electron resembles a very narrow cone (opening angle of $2/\gamma$, $\gamma = E/m_0c^2$) directed along the tangential component of the electron motion.

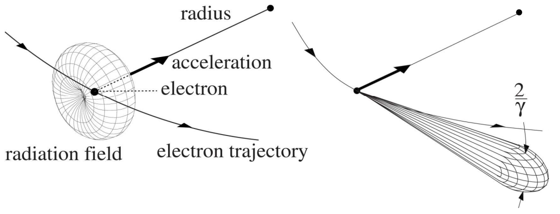

Figure 4.2: The radiation pattern of an electron at relativistic velocity a) in the rest frame of the electron and b) in the rest frame of an observer. From [77]

Synchrotron radiation can be extracted at the bending magnets or at the so-called insertion devices – wigglers or undulators, which are placed in the unbent, straight sections of the electron trajectory. While the field of a dipole bending magnet is fixed to maintain its guiding properties, the field of an insertion device can be adjusted in order to optimize the properties of the produced radiation.

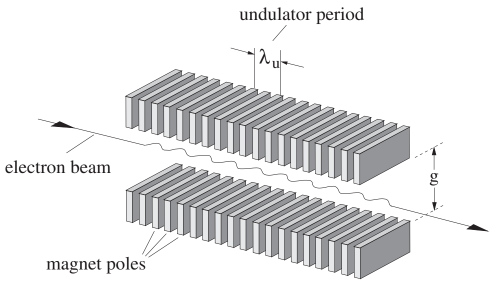

Figure 4.3: From [77].

Wigglers and undulators are composed of two opposed rows of each n dipole magnets above and below the electron trajectory. The individual dipole magnets alternate in orientation and thereby cause the electrons to follow a sinusoidal path along the length of the insertion device in the plane of the storage ring. For a wiggler, the radiation emitted from the electrons at each left or right bend on their sinusoidal path is superposed incoherently. The radiation from a wiggler has a comparatively wide angular spread and the radiation flux obtained from a wiggler is n-times higher than the flux obtained from a single dipole bending magnet. For an undulator, the radiation emitted at the bends of the sinusoidal electron path is superposed coherently, leading to a well-collimated radiation from the undulator, with a flux n^2-times as compared to that of one dipole bending magnet. A synchrotron radiation source has an energy spectrum ranging from infrared to hard x-rays. [77, 79]

4.2 Properties of synchrotron radiation

Synchrotron radiation differs from radiation produced by other x-ray light sources in three important aspects [77, 79]:

- **Spectral brilliance**:
  In a given energy bandwidth, the number of photons produced by a third generation synchrotron radiation source per second, unit area of the source, and solid angle is about ten orders of magnitude higher than for a laboratory x-ray tube.
- **Polarization**:
  Radiation emitted exactly in the plane of the synchrotron source is fully

linearly polarized in this plane (usually labeled as σ-polarization). Radiation emitted out of the storage ring plane has a circular polarization component, thus in total an elliptical polarization. Unwanted polarization components can be filtered out.

– **Time structure**:
Due to the fact that the stored electrons gather in bunches, a synchrotron radiation source emits photon pulses, not as continuous radiation. The duration and temporal separation of these pulses are given by the length of the bunches and their spatial separation. Typically, the pulse length is 30 ps to 100 ps, the pulse separation is 2 ns to 3 ns.

The high spectral brilliance makes experiments with very small sample volumes feasible. The polarization of synchrotron radiation provides additional information about sample systems which e.g. change the polarization of radiation scattered from them, or in which the scattered intensity depends on the polarization of the incident radiation. The time structure of synchrotron radiation allows for NRS and pump-probe experiments.

4.3 Synchrotron radiation sources and beamlines

The x-ray scattering experiments discussed in this work were conducted at experimental stations at three different synchrotron radiation sources: DORIS III and PETRA III at DESY (Hamburg, Germany), and ESRF (Grenoble, France). Table 4.1 lists some characteristics of theses sources [80–82]. The order of magnitude of the spectral brilliance is given for photon energies of 8 to 15 keV. The particle beam size varies along the storage ring circumference; it is given for the beamlines BW4 (DORIS III), P01 (PETRA III), and ID18 (ESRF).

The beamline BW4 at the DORIS III synchrotron radiation source (shut down in October 2012) was dedicated to Small Angle X-Ray Scattering. Its insertion device was a 2.7 m long wiggler, providing a flux in the range of 10^{09} photons per second at energies from 6 to 14 keV [80]. The standard photon beam size after focusing was 400 mic × 400 μm. Structures with period lengths of 3 to 300 nm could be resolved at BW4 [83].
The beamline P01 at PETRA III is dedicated to nuclear resonant scattering and inelastic x-ray scattering experiments. The insertion device of P01 consists of two 5 m long undulators and provides a maximum flux at the sample

parameter / units	DORIS III	PETRA III	ESRF
generation	2nd	3rd	3rd
circumference m	289	2300	844
particle energy GeV	4.45	6	6
particle beam current mA	120	100	200
particle beam size μm × μm (hor × ver)	1300 × 300	141.6 × 6.6	402 × 7.9
rms particle beam emittance nmrad × nmrad (hor × ver)	410 × 12	1 × 0.01	48 × 0.048
spectral brilliance photons/(s $\cdot$ mm^{2}mrad^{2}0.1%BW)	10^{15}	10^{21}	10^{20}

Table 4.1: Some characteristic parameters of the synchrotron radiation sources DORIS III, PETRA III, and ESRF, at which the experiments described in this thesis were conducted. Data compiled from [80–82].

position of 7×10^{13} photons per second at 14.4 keV; with all components for experiments in grazing incidence geometry installed, the flux at the sample position is in the range of 10^6 to 10^7 photons per second (saturation of the detectors is a limiting factor here). The energy resolution ensured by a specialized high-resolution monochromator at this energy (the nuclear resonance of ^{57}Fe) is 1 meV. Special electronics and detectors provide sub-nm time resolution. P01 can provide a low-divergence photon beam, using a set of Lengeler lenses with a focal length of 25 m, which makes it a well-suited beamline for GISAXS experiments, too. The beam can be focused from 3 mm × 1 mm to 7 μm × 7 μm [81].

The beamline ID18 at ESRF is also dedicated to nuclear resonant experiments. It provides optimized flux for photon energies at the nuclear resonances between 6 keV and 30 keV. At the ^{57}Fe nuclear resonance flux and energy resolution can be varied from 1.4×10^{10} photons/s at 6.4 meV resolution to 5.5×10^{08} photons/s at 0.47 meV resolution, depending on the Bragg reflections chosen for the Si crystals of the high resolution monochromator. Special electronics and detectors provide sub-ns time resolution. The photon beam can be focused to 100 μm × 100 μm using lenses and a bent Si crystal, and focused to 10 μm × 10 μm using multilayer mirrors [82].

For more information on the components and layout of nuclear resonant scattering beamlines at synchrotron radiation sources, see section 6.3.4.

Part II

Methods

5 Sample Preparation

5.1 Surface faceting of M-plane α-Al_2O_3 by high-temperature annealing

A facetted α-Al_2O_3 surface can be prepared by annealing M-plane α-Al_2O_3 at high temperatures. The M-plane of α-Al_2O_3 has the highest surface energy density of all crystal planes present in α-Al_2O_3. Upon annealing it will therefore reconstruct into facets in order to minimize its surface energy (see section 1.2.3).

Figure 5.1

The annealing procedure can readily be carried out using commercially available high-temperature furnaces, e.g. a chamber furnace as shown in Fig. 5.1 or a horizontal tube furnace as shown in Fig. 5.2[1]. The chamber furnace provides easy access to the heated volume and allows to anneal larger quantities of wafers simultaneously. The samples are protected against dirt (especially particles flaking off from the insulation of the heated volume or from the oxidized surface of the heating elements) by covering with an alumina half-pipe.

---

[1] Figures 5.1 and 5.2 from producers' homepages.

The tube furnace has two openings and can thus be employed in Grazing Incidence Small Angle X-Ray Scattering (GISAXS, see section 6.2) measurements. Using this method, the formation of surface facets can be studied in-situ during annealing (see sections 7.1). The samples are positioned in the center of the furnace tube using a custom-made alumina sample holder.

Figure 5.2

5.2 Preparation of diblock copolymer thin films by spin coating

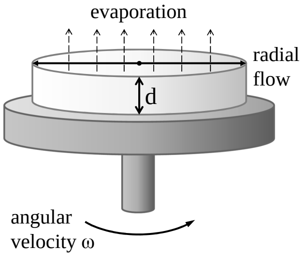

Figure 5.3

Spin coating is a method to produce thin polymer films from solutions. An amount of polymer solution is deposited on a substrate, which is fixed on a rotatable disk. The disk is then accelerated and rotated at high angular velocity. The solution flows radially due to centrifugal forces and adhesion to the substrate. Most of the deposited solution is cast off the disk. As the solvent evaporates, the viscosity of the solution increases due to the increasing relative polymer content, and the film thickness decreases. The result of this process is a solid film of polymer molecules on the substrate [84].

The first theoretical description by Emslie and coworkers [85] employed a very rough model neglecting many crucial factors, such as viscosity or concentration gradients. More refined theories have been developed by now, e.g. by Lawrence [86].

It is known from experiment, that the resulting film thickness d depends on the angular velocity ω, the solution concentration c and viscosity η. Other process parameters, such as the amount of deposited solution, the solution deposition rate, or the total spinning time, have been found to have little or no effect on the resulting film thickness [84]. Theoretical elaborations and experimental observations agree upon the general relation

$$d = \frac{k_1}{\sqrt{\omega}} \tag{5.1}$$

where k_1 is a specific constant for the given system of polymer, solvent, and substrate. k_1 is proportional to the initial solution viscosity η_0: $k_1 = k_2 \eta_0^\beta$, where $\beta = 0.29 \ldots 0.39$ for most polymer solutions. Thus,

$$d = \frac{k_2 \eta_0^\beta}{\sqrt{\omega}} \tag{5.2}$$

k_2 describes the effect of properties such as the average solvent evaporation rate, latent heat of evaporation and solvent heat capacity, or solvent diffusivity. It is a matter of debate, whether the weight average molecular mass M_w (see section 2.1.1) or an effective, so-called viscosity average molecular mass M_η determines the resulting film thickness [87, 88]. The minimum film thickness (i.e. the thickness of a continuous monolayer of polymer molecules) is determined by the respective radius of gyration of the polymer molecules.

In practice, the resulting film thickness d can readily be determined via the solution concentration c and the angular velocity ω. Solutions of two types of diblock copolymers (PS-b-PMMA(203/203) and PS-b-PMMA(63/142)) solved in toluene at various concentrations were frequently used in this work. The following specific relations were found (see appendix A.3.1), where d is measured in nm, c in mg/ml and ω in rad/s:

- $d \approx 1770\ c/\sqrt{\omega}$ for PS-b-PMMA(203/203)
- $d \approx 1530\ c/\sqrt{\omega}$ for PS-b-PMMA(63/142)

The uniformity in thickness of the resulting polymer film depends on the solvent volatility and on the compatibility of polymer and solvent. The most uniform films are produced using solvents of high compatibility and low volatility [87]. One has to be aware though, that the outcome of a spin coating process can also be influenced by extrinsic factors such as temperature, air flow, or humidity [84].

5.3 Solvent vapor annealing of diblock copolymer films

Thin films of diblock copolymers are prepared by casting from a solvent, e.g. by spin coating (see section 5.2), and are then kinetically trapped in a non-equilibrium state. Microphase separation (see section 2.3.1) to some degree can occur during film preparation, but the resulting chemical domain morphology is in general not well ordered - the chemical nanodomains lack long-range positional order and can be distorted. Equilibration requires mobility of the diblock copolymer molecules to bring about the formation of regular structures. There are two alternative ways for mobilizing the copolymer molecules: thermal annealing and solvent vapor annealing. Thermal annealing at temperatures above the glass transition temperature T_g provides the molecules with sufficient mobility for microphase separation and long-range ordering. In contrast, in solvent vapor annealing the glass transition temperature T_g is reduced to values below room temperature by swelling the diblock copolymer film with a solvent, making the molecules sufficiently mobile at ambient temperatures. Thermal annealing is not very effective for diblock copolymers of high molecular weight, which demand very long annealing times of typically several days for the required chain diffusion to take place. The effect of solvent vapor annealing concerning an improvement of long-range lateral order in the copolymer nanodomains was observed to be comparable to that of thermal annealing, but to be achieved in much shorter time [89].

Solvent vapor annealing aims at producing a diblock copolymer film which exhibits well-ordered chemical phase domains after solvent removal. There is no standardized routine for solvent vapor annealing, and experimental setups range from most basic to highly sophisticated. The basic process can be subdivided into three phases:

- The diblock copolymer film is exposed to solvent vapor; solvent molecules begin to diffuse into the polymer film and thus swell it.

- Swelling is completed; the system of diblock copolymer film and solvent is in a steady state.

- The solvent is evaporated from the diblock copolymer film; the polymer film de-swells.

Swelling of the diblock copolymer film with solvent occurs, because in comparison to the non-swollen state mixing of solvent and diblock copolymer is entropically preferable and dilution of the unfavorable AB contacts by favorable polymer-solvent contacts is energetically preferable. The swollen diblock copolymer film can be considered as a concentrated solution and characterized by the diblock copolymer content. The thickness of the swollen film increases with increasing solvent content, i.e. with decreasing polymer content. The swelling stops, when the solvent volume fraction in the film reaches its equilibrium value, so that the osmotic pressure is relaxed to zero [90]. When the swelling is completed, the system is in a steady state with constant film thickness, which is directly related to the polymer concentration (or solvent content, respectively) of the swollen film. If the degree of swelling is sufficient, the diblock copolymers are mobilized effectively and can reorganize into equilibrium chemical domain morphologies. The structures which are formed then can - in a first approximation - be compared to the structures formed by block polymers in solution [91]. By rapid solvent removal, i.e. by rapidly raising the glass transition temperature T_g to values far above room temperature, these morphologies can be frozen in, so that they remain stable even if the solvent is not present anymore.

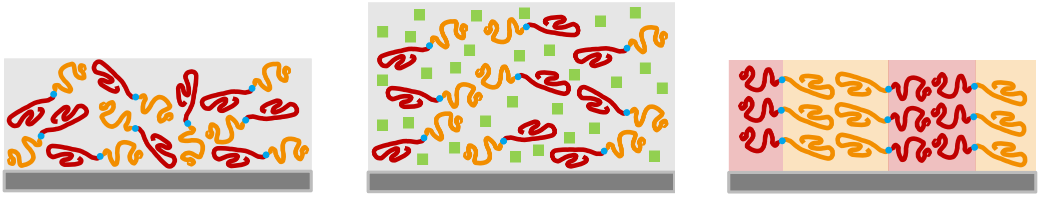
(a) (b) (c)

Figure 5.4: Sketch of the microphase separation in an AB diblock copolymer film during solvent vapor annealing. (a) After deposition the diblock copolymer molecules (block A: red subchain, block B: yellow subchain, covalent bond: blue link) are kinetically trapped in a chemically disordered non-equilibrium state. Depending on the combination of substrate and diblock copolymer, one block may preferably tend to be located at the substrate. (b) Upon exposure to a solvent vapor, solvent molecules (green) diffuse into the polymer film and swell it. The diblock copolymer molecules are mobilized and can rearrange into a favorable microphase separated state, in which both the number of number of AB contacts is minimized and the wetting conditions at the film interfaces in the presence of the solvent are satisfied. (c) A surface-perpendicular orientation of the chemical domains in the microphase separated state is preferred in film with thicknesses below the equilibrium period of the chemical domains. The chemically ordered state is preserved by rapid removal of the solvent.

5.3.1 Factors determining the resulting morphology

A multitude of factors determine the morphology of the diblock copolymer film after the solvent annealing process. Thus, this method – though readily implemented – features complex (inter)dependencies between various parameters of the sample and conditions of the procedure. Consider as an example a system, with which this work will be concerned: a film of symmetric PS-b-PMMA (a diblock copolymer consisting of Poly(Styrene) and Poly(Methyl MethAcrylate) with composition $f = 0.5$) on a silicon substrate with natural oxide layer. Since only surface-perpendicular orientations of the chemical domains resulting from microphase separation (see section 2.3.2) are relevant for this work, only films with a thickness smaller than the equilibrium domain period are considered here.

Intrinsic properties of the diblock copolymer

Several intrinsic properties of diblock copolymers are of significance for their behavior under solvent vapor exposure: Diblock copolymers with strong segregation (high value of $\chi_{AB}N$, see section 2.3.1) and high molecular mass M_{A+B} equilibrate more slowly compared to diblock copolymer with low $\chi_{AB}N$ and M_{A+B}, since the necessary diffusion of their long chains takes more time. Consequently, the solvent vapor annealing procedure has to last longer for such systems. It depends on the Flory-Huggins interaction parameters χ_{AS} and χ_{BS} for the two constituents of the copolymer and a solvent, whether the solvent is suitable for annealing and whether it is selective or non-selective with respect to the two blocks. The composition f determines, which domain morphologies (see figure 2.5) can result from the solvent annealing procedure for a given degree of segregation $\chi_{AB}N$. The values of the glass transition temperatures T_g^A, T_g^B have to be such, that solvent vapor annealing can lower them sufficiently: The sample can additionally be heated, but the solvent boiling point or possible flammability have to be kept in mind.

Recall the example system of PS-b-PMMA on $\mathrm{SiO_x}$. On the one hand, the surface energy density of PS is lower than that of PMMA. Therefore, PS is preferentially located at the film free surface. On the other hand, PMMA can form hydrogen bonds with the oxide layer on the Si substrate and therefore preferentially wets the substrate. These anti-symmetric wetting conditions result in an as-cast film of PS-b-PMMA on a $\mathrm{SiO_x}$ substrate in air exhibiting a continuous PS layer at the free surface and a continuous PMMA layer at the substrate interface [51,92,93]. This situation conforms to the a-hL$^{\parallel}$ structure (see section 2.3.2; black component corresponds to PMMA, white component to PS). This will be relevant for the choice of solvent, as explained below.

Choice of solvent

Exposing the as-cast PS-b-PMMA film to a PS-selective solvent does not qualitatively alter the antisymmetric wetting conditions for the polymer film: The PS block still prefers to be located at the surface, while the PMMA block preferentially wets the substrate. The number of unfavorable AB contacts is already minimized in this situation, so there is no driving force for rearrangement of the molecules. After solvent annealing in a PS-selective solvent, there will still be exclusively PS subchains at the sample surface [94].

If the film is exposed to a PMMA-selective solvent, the wetting conditions change from antisymmetric to symmetric: PMMA is then preferred at both the free surface and the substrate interface. Contacts between the solvent and PMMA are more favorable than contacts between the solvent and PS. Therefore, PMMA will migrate toward the sample surface and the film morphology is altered in consequence [94]. The resulting chemical structures correspond to the morphologies s-L$^{\parallel}$, s-H, or s-L$^{\perp}$, depending on the sample thickness (see section 2.3.2), which are stable at symmetric wetting conditions.

Duration of annealing

The restructuring of the film induced by the presence of a PMMA-selective solvent happens on a timescale of hours. Depending on when the solvent annealing is stopped by removing the solvent, different morphologies representing different stages in the restructuring process can be observed. It is important to note that these morphologies are conserved by rapid solvent removal: They are stabilized at ambient conditions, because removing the solvent quickly means rapidly increasing the glass transition temperature T_g so that the structures present in the swollen state at the time of solvent removal are "frozen-in" and preserved in the dried state. During solvent vapor annealing of a compositionally symmetric PS-b-PMMA film with $d < 0.5D_0$, Xuan and coworkers have observed six stages of restructuring with increasing PMMA content at the free surface of the film to satisfy the attractive interaction between solvent and PMMA, as depicted in 5.5 [94]:

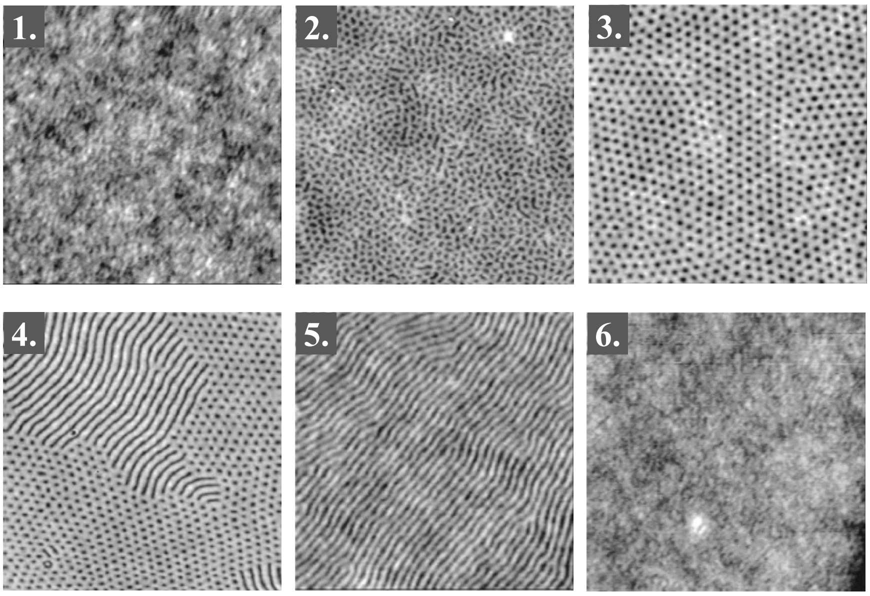

Figure 5.5: PS-b-PMMA film on SiO_x restructuring upon solvent vapor annealing. From [94].

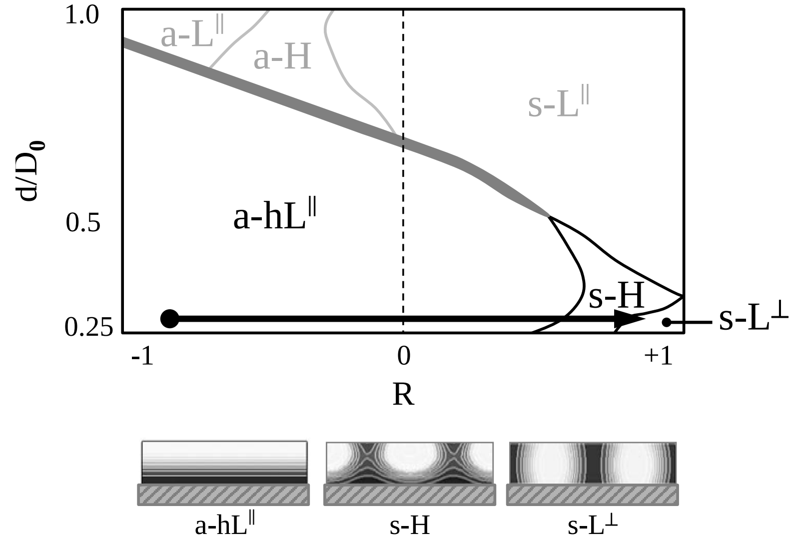

Figure 5.6: Morphological transition of a compositionally symmetric PS-b-PMMA diblock copolymer thin film with $d/D_0 < 0.5$ on SiO_x upon solvent vapor annealing in a PMMA-selective solvent. Graphic uses elements from [52].

1. In the as-cast film PS is expressed at the featureless surface.
2. PMMA protrusions of irregular horizontal cross-section form.
3. The PMMA protrusions assume circular cross-sections and regular hexagonal arrangements on a short scale.
4. The PMMA protrusions coalesce to form surface-perpendicular lamellar domains.
5. The film is entirely structured by surface-perpendicular lamellar domains.
6. After extensive annealing: PMMA is expressed at the featureless surface.

The conditions under which solvent vapor annealing is performed may strongly influence the time scale on which the restructuring process takes place. The sample prepared by Xuan and coworkers required 100 h to reach stage 5. In the samples prepared for the present work, complete restructuring into surface perpendicular lamellar domains was achieved within 3 h, and the domain regularity was significantly deteriorated already after 6 h as the samples approached stage 6 (see section 9.1.1). Reproduction of the individual stages of this morphological transition is not part of this work.

Referring to the phase diagram of morphologies developed by Fasolka and coworkers, the restructuring process upon solvent annealing up to stage 5 corresponds to a transition at constant film thickness from the a-hL$^{\|}$ morphology via the s-H phase to the s-L$^{\|}$ as indicated in Fig. 5.6. This transition takes place, because the wetting conditions are changed from antisymmetric (PMMA preferred at substrate interface, PS preferred at free surface of film) to symmetric (PMMA preferred at both substrate interface and free surface), when a PMMA-selective solvent is present.

If the restructuring process is stopped in stage 5 by rapid removal of the solvent, regularly chemically patterned film surfaces are obtained (see chapter 9). As self-assembly processes, the microphase separation and restructuring are intrinsically independent of the surface area of the diblock copolymer film. Thus, diblock copolymer self-assembly is a quick and easy way to produce large-area templates with regular nanoscale chemical surface patterning for further nanostructure growth (see chapter 10).

5.4 Sputter deposition

Having prepared a faceted α-Al$_2$O$_3$ substrate or a chemically patterned diblock copolymer template, metallic nanostructures can be grown on these by sputter deposition (see chapters 8 and 10). Sputtering means the erosion of a solid target surface by bombardment with ions of high kinetic energy. The accretion of the sputtered target atoms on a substrate is called sputter deposition, and is a means to produce films of the target material. The first report on a sputtering process was given by Grove in 1852 [95].

A basic sputter setup consists of a process chamber filled with a working gas (usually a noble gas to avoid chemical reactions with target or substrate) at low pressure, and containing opposed anode and cathode. The target is placed on top of the cathode, and the substrate is placed on top the the anode. The mentioned high-energy ions are produced in a plasma of the working gas and are accelerated toward the target by an applied electric field. The sputtered target particles are electrically neutral atoms, which deposit all over the inside of the process chamber. For sputter deposition and other technological applications, low-pressure non-thermal plasmas are used [96, 97].

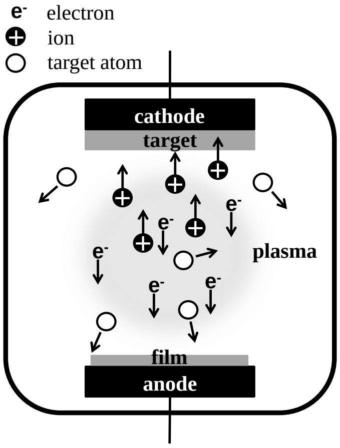

Figure 5.7

5.4.1 Sputter methods

DC sputtering and RF sputtering

In DC sputtering [96,97], the anode and cathode are supplied with direct current (DC), so that a static electric field is generated between them. The electric field accelerates ions initially present in the working gas (e.g. produced by cosmic radiation); by collision with neutral gas atoms or with the cathode/target, further charged particles are produced. Ionization avalanches then rapidly increase the number of charged particles until the plasma becomes self-sustaining. In a self-sustained non-thermal plasma, the fraction of ionized gas atoms is typically about 0.01%. This degree of ionization is limited by the increasing current between cathode and anode with increasing number of electrons: Increasing current decreases the charge on anode and cathode (at constant voltage) and thereby the electric field strength, so that charged particles are supplied with less kinetic energy required for ionization. Since the electrons are repelled by the cathode, a positive space-charge region forms in front of the cathode. Following the applied electric field, all ions in this space-charge region impinge onto the target surface at normal incidence. The kinetic energy of the ions upon their collision with the target is proportional to the voltage drop over the width of the positive space-charge region, in addition to the ions' initial kinetic energy. Due to the low degree of ionization in a low-pressure non-thermal plasma, the sputtering rate in DC setups is low. It can be enhanced by applying a radiofrequency alternating current to anode and cathode: The ions are too inertial to follow the alternating direction of the electric field, while the electrons begin to oscillate. This prolongs the trajectory of the electrons, thus increases the probability for collisions and thereby augments the degree of ionization. Consequently, the working gas pressure can be reduced, so that loss of target atoms due to collisions with the working gas is decreased and the sputter yield is increased.

Magnetron sputtering

In magnetron sputtering [96, 97] the cathode is combined with a magnet arrangement. This produces a magnetic field which keeps electrons from the plasma moving on a closed trajectory parallel to the target surface plane due to the Lorentz force. The controlled electron motion reduces the number of collisions between electrons and ions (recombination), thus increases the mean free path length of the electrons. Thereby, the probability of collisions between electrons and neutral gas atoms, and thus the ionization rate, is augmented. This leads to an increased plasma density near the target, resulting in a higher sputter yield. Magnetron sputtering has the highest efficiency of all sputter methods, and is therefore the method most commonly applied in industry. However, targets for magnetron sputtering are chosen to be comparatively thin, since the strength of the magnetron field at the target surface decreases with increasing target thickness (i.e. distance of the target surface from the cathode), and must consequently be replaced more frequently.

5.4.2 The sputter process

Sputtering happens by collisions, i.e. by momentum transfer, especially momentum reversal. The main factor in this process therefore is the kinetic energy E_{kin} of the ions impinging on the target surface [96]: If E_{kin} is lower than the surface binding energy E_B of the target atoms, the ions are adsorbed or reflected. For $E_{kin} \gtrsim E_B$, the impinging ions cause target atoms to dislocate within the target surface. Sputtering occurs if $E_{kin} \geq 4E_B$. When $E_{kin} \gtrsim 4E_B$, sputtering is a complex process involving several collisions among target surface atoms before a target atom is released. The sputter yield is consequently low, about 10^{-5} atoms/ion. For $E_{kin} \gtrsim 8E_B$, sputtering is actually a two-particle collision process and the sputter yield increases proportionally to E_{kin} up to a yield of 1 atom/ion. The sputter yield does not increase anymore for very high ion energies (>50 keV), since ions are then rather implanted into the target than releasing target atoms.

Gas kinetics

The residual gas pressure is one of the main factors in sputter deposition for two reasons [10]:

- possible collisions between residual and sputtered atoms, quantified via the mean free path length l for particles of diameter d

$$l = \frac{k_B T}{\sqrt{2}\pi d^2 p} \tag{5.3}$$

- condensation of residual gas particles on the growing surface, quantified by the number N of incorporated gas particles with mass m

$$N = p\sqrt{\frac{1}{2\pi k_B m T}} \tag{5.4}$$

The mean free path length l exceeds the typical distances of a few centimeters or decimeters between sputtering source and substrate already for moderate vacua of $p > 10^{-6}$ mbar [10]. However, the incorporation rate of residual gas atoms can be high in comparison to the typical deposition rate of the sputtered atoms, thus making ultra-high vacua a necessity for producing pure films.

Film growth

Sputtered atoms have a much higher mean kinetic energy of about 1 eV to 100 eV as compared to evaporated atoms with a kinetic energy of about 0.1 eV. This results in different microstructures of sputtered deposited and vapor deposited films. Some general statements can be made about the factors which influence the microstructure of sputter-deposited films [96]:

- Target atoms with higher kinetic energy produce more compact films.
- Increasing the deposition rate decreases the effects of surface diffusion.
- Surface diffusion is enhanced by increasing the substrate temperature.
- High working gas pressure (i.e. high number of collisions between sputtered atoms and working gas ions) reduces the kinetic energy of sputtered atoms and increases the spread of directions from which they impinge onto the substrate.

Thornton's zone diagram (see Fig. 5.8) [98] can be a rough guide to envisage the resulting microstructures: For low substrate temperatures the gas pressure determines, whether a porous film consisting of separated fibrous grains (zone I) or a compact film consisting of densely packed fibrous grains (zone T) is formed. For moderate substrate temperatures (zone II), the film is characterized by close-packed columnar grains. For high substrate temperature the film has a recrystallized large-grained structure (zone III).

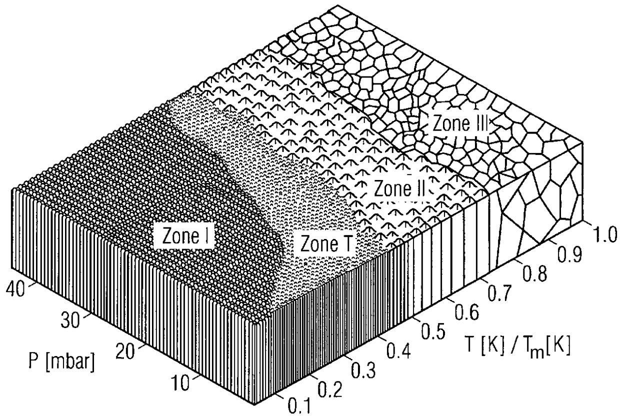

Figure 5.8: Zone diagram according to Thornton [98] depicting the dependence of the microstructure of a sputter deposited film on the working gas pressure P and the temperature T in units of the melting temperature T_m of the film material. From [99].

5.5 Experimental setups, materials, and procedures

A main aim of this work is to fabricate highly ordered nanostructure arrays – based exclusively on self-assembly processes and not including any lithographical procedures. Two main routes are followed here - both are based on substrates of α-Al_2O_3 which are faceted by high temperature annealing. Metals can be sputter deposited directly onto a faceted substrate from a direction which is normal to the orientation of the facets but not normal to the substrate surface. Depending on the angle of the sputter source with respect to the substrate surface, this results either in separated stripes of the metal on the facet faces facing the sputtering source or in a continuous film exhibiting stripe-like regions of alternating thickness on the two different faces of the substrate facets. This routing is schematically represented in Fig. 5.9.

Alternatively, copolymer thin films can be deposited on the faceted substrates. They are subjected to solvent vapor annealing to induce microphase separation and thus produce a topographically flat, but chemically patterned surface. Here, the faceted substrate surface provides a preferential direction for the arrangement of the chemical domains within the diblock copolymer film. Nanostructure arrays are then prepared by sputter deposition onto these templates, making use of the selective wetting properties of the sputtered material on the polymeric surface. This routine is schematically represented in Fig. 5.10.

Procedural details or parameters deviating from the standards described above will be mentioned explicitly in the respective sections in part III.

α-Al_2O_3 substrates

M-plane α-Al_2O_3 wafers were purchased from Crystec GmbH, Germany, and cut into samples of 10 x 10 mm^2 or 15 x 15 mm^2. Annealing was carried out in air – in a chamber furnace for regular substrate production and in a tube furnace for in-situ GISAXS investigation of the faceting process. Typical temperatures ranged from 1300°C to 1500°C, while the duration of annealing was varied from 2 to 48 hours. After annealing the furnace heating elements were completely switched off - this allowed for the fastest cooling, given that the samples could not be actively cooled in the furnaces.

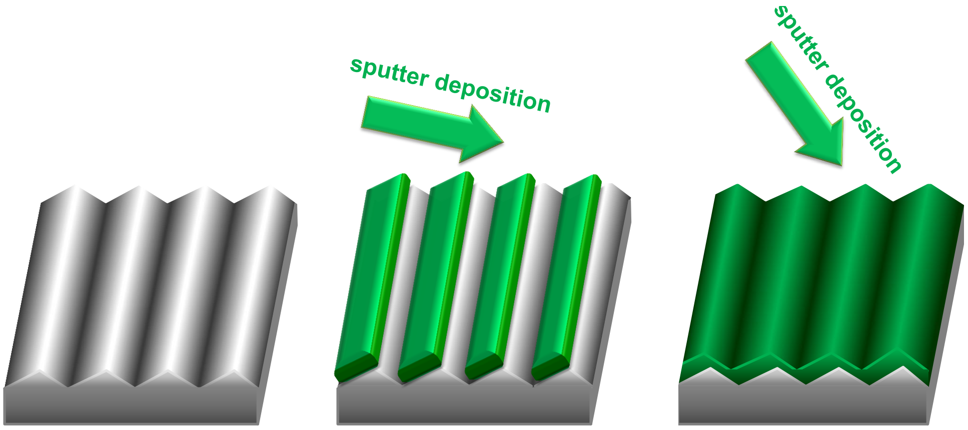

(a) (b) (c)

Figure 5.9: Sketch of the proposed bottom-up routine for metal nanostructure fabrication using faceted α-Al_2O_3 substrates. a) α-Al_2O_3 substrate, facetted by high-temperature annealing. b) Fabrication of isolated nanostripes by sputter deposition at from a polar angle $\omega \ll 90°$. c) Fabrication of a continuous film with facetted surface and periodically varying thickness by sputter deposition from a polar angle $\omega < 90°$.

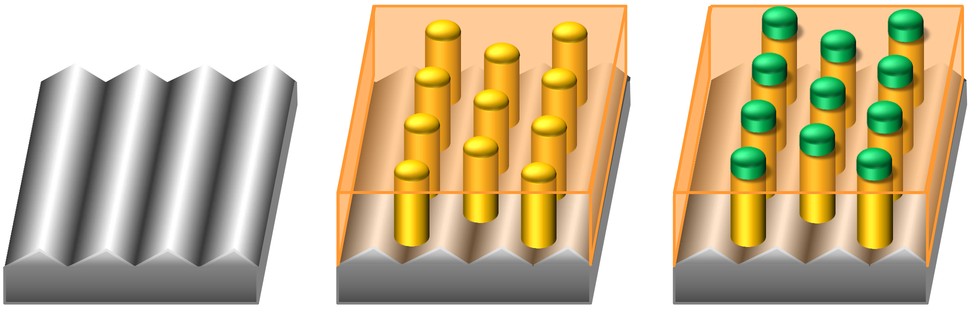

(a) (b) (c)

Figure 5.10: Sketch of the proposed bottom-up routine for metal nanostructure fabrication using diblock copolymer thin films on faceted α-Al_2O_3 substrates as templates. a) α-Al_2O_3 substrate, facetted by high-temperature annealing. b) Diblock copolymer film on substrate, microphase-separated by solvent vapor annealing, with chemical surface structure. c) Metal nanostructure pattern on diblock copolymer film, reproducing shape and lateral arrangement of the chemically distinct surface domains of the template.

PS-b-PMMA diblock copolymers

Three different PS-b-PMMA copolymers are discussed in this work – two symmetric copolymers and one asymmetric copolymer:

- PS-b-PMMA(203/203) :
  $M_{\mathrm{PS}} = 203.5$ kg/mol, $M_{\mathrm{PMMA}} = 203.5$ kg/mol
  $M_w/M_n = 1.10$
  $f_{\mathrm{PS}} = 0.50$, $\chi\mathrm{N} = 163$, $D_0 = 103$ nm
- PS-b-PMMA(47/53) :
  $M_{\mathrm{PS}} = 47$ kg/mol, $M_{\mathrm{PMMA}} = 53$ kg/mol
  $M_w/M_n = 1.12$
  $f_{\mathrm{PS}} = 0.47$, $\chi\mathrm{N} = 40$, $D_0 = 41$ nm
- PS-b-PMMA(63/142) :
  $M_{\mathrm{PS}} = 63$ kg/mol, $M_{\mathrm{PMMA}} = 142$ kg/mol
  $M_w/M_n = 1.08$
  $f_{\mathrm{PS}} = 0.31$, $\chi\mathrm{N} = 83$

These diblock copolymers were purchased in powder form from Polymer Standards Service, Germany ((203/203)) and from Polymer Source Inc., Canada ((47/53), (63/142)).

In the phase diagram for stable chemical domain morphologies in bulk diblock copolymers (see section 2.3.1), these are located as shown in Fig. 5.11. The bulk equilibrium periods D_0 were calculated from Eq.(2.23), assuming the Flory-Huggins interaction parameter $\chi = 0.04$ [100–102], the monomer molecular masses $M_{0,PS} = 104.15$ g/mol and $M_{0,PMMA} = 100.12$ g/mol, and the statistical segment length $a = 0.64$ nm [51]. Note, that Eq.(2.23) was derived for symmetric diblock copolymers of composition $f = 0.5$.

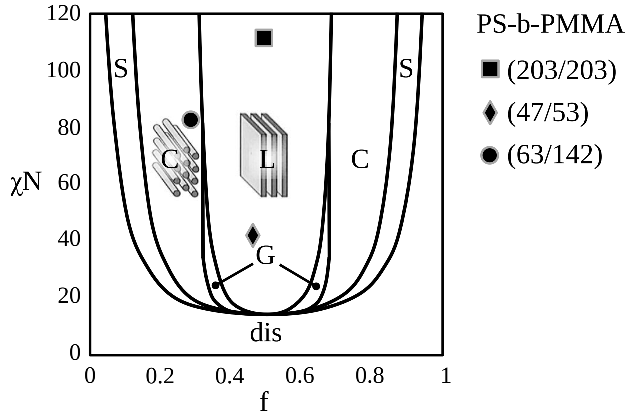

Figure 5.11: Location of the employed PS-b-PMMA diblock copolymers in the domain morphology phase diagram, after [44]. The product of the Flory-Huggins interaction parameter χ and the degree of polymerization N is the degree of segregation of the two blocks. f denotes the volume fraction of one block.

Solutions of PS-b-PMMA are prepared by weighing an amount of PS-b-PMMA and adding the corresponding amount of toluene to obtain the required solution concentration. After sealing the vessel, this mixture was shaken for two hours and then filtered into a fresh vessel. Prepared solutions were stored in tight vessels in a refrigerator. Prior to coating, the substrates were cleaned using isopropanol and acetone: Silicon Si(110) substrates with natural oxide layer were scrubbed thoroughly with isopropanol, then immersed in acetone at 50°C for about 20 seconds. α-Al_2O_3 substrates were cleaned in an ultra-sonic bath of acetone at 50°C for 15 minutes prior to high-temperature annealing. All spin coating was carried out using the same apparatus under a fume hood in a climate-controlled laboratory. The employed spin coating apparatus allows to control the disk acceleration and deceleration, the final angular velocity, and the duration of spinning at this velocity. An amount of polymer solution sufficient to cover the entire substrate surface with one large drop was applied to the substrate, then the spinning was started. Typical angular velocities ranged from 2000 to 4000 rotations per minute. All substrates were spun for 30 s and the initial acceleration and final deceleration always were 1000 rpm/s, since this proved to produce films of best thickness homogeneity in preliminary tests. The polymer film thickness was varied either by using solutions with different concentrations or by changing the angular velocity (to produce films of different thicknesses from the same solution). Solutions with concentrations of 8 mg/ml, 10 mg/ml, or 12 mg/ml were most frequently used.

After spin coating the solutions the samples were generally dried for 2.5 hours at 50 °C in air to remove residual toluene. Solvent vapor annealing of the samples was carried out in a climate-controlled clean room with no direct solar irradiation of the samples. For annealing, each sample was placed on a metal post in an individual glass vessel, solvent was added near the bottom of the vessel, then the vessel was closed tightly with a sealed screw cap. 1.67 μl of acetone were applied per 1 ml of vessel volume, which resulted in a saturated acetone vapor inside the vessel. The samples were annealed for few hours at room temperature, depending on the type of polymer. During annealing, the interference color of the polymer film on the substrate changed due to the increase in thickness brought about by the swelling of the film with the solvent. After annealing, the vessels are unscrewed quickly and the samples were removed from the vessels. It was observed that the interference color of the polymer film changed back to its initial tone within split-seconds as the polymer film de-swelled due to the pressure drop in the vessel dropped upon unscrewing the cap – which indicates a rapid solvent removal from the polymer film upon opening the vessel.

Metal nanostructures

Both faceted α-Al_2O_3 substrates and chemically phase separated, well-ordered diblock copolymer films on substrates were used as templates for fabricating metallic nanostructures by sputter deposition. The employed custom-made UHV sputter deposition chamber depicted in Fig. 5.12 features four possible positions for the sputtering source(s) at angles of 90°, 45°, 30°, and 10° with respect to the sample surface. Base pressures are in the range of 10^{-7} mbar to 10^{-6} mbar; pressures of the working gas Ar are in the range of 10^{-3} mbar to 10^{-2} mbar for sputter deposition. The samples can be rotated and heated, and a magnetic field of up to 75 mT can be applied. Furthermore, the deposition chamber can be set up at synchrotron beamlines for in-situ characterization of growing nanostructures by x-ray scattering techniques. Nanostructures on diblock copolymer templates were usually prepared with the sputtering source at 90° with respect to the sample surface. Nanowires and nanopatterned continuous films on faceted α-Al_2O_3 were produced with the sputtering source at shallower angles.

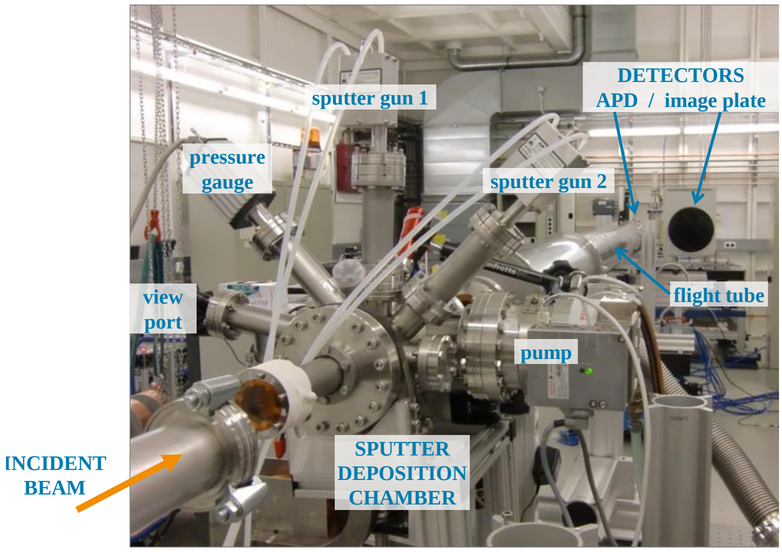

Figure 5.12: The UHV sputter deposition chamber set up at the beamline P01 at the PETRA III synchrotron.

6 Sample Characterization

6.1 Atomic Force Microscopy

Advanced microscopy techniques allow real space imaging even of nm-sized topographical features. For the faceted α-Al_2O_3 substrates, the diblock copolymer templates, and the metal nanostructure arrays presented in this work, atomic force microscopy was applied to visualize the nanostructured sample surface.

Atomic force microscopy (AFM) is a method for imaging the local topography of a sample by scanning a force-sensitive probe over the sample surface. AFM has been developed in the mid 1980s by Binnig and coworkers on the basis of combining the principles of scanning tunneling microscopy and stylus profilometry [103]. The novel probe concept employed in the AFM setup was to mount the measuring tip to an ultralight spring with low spring constant, which would respond to extremely small forces of about 10^{-18} N acting on it. In contrast to scanning tunneling microscopy, an AFM instrument measures the forces, not the tunneling current, between a tip and a sample to reconstruct the surface topography. Therefore, AFM allows for measuring surface profiles not only of conductors, but of insulators as well. Also, AFM does not damage the sample as stylus profilometry does, while exceeding the resolution of stylus profilometry both laterally and vertically. Three-dimensional objects with feature sizes larger than the apex curvature radius of the tip can be resolved without complications: A lateral resolution of about 10 nm can be readily achieved. On flat surfaces, even true atomic resolution has been demonstrated [104].

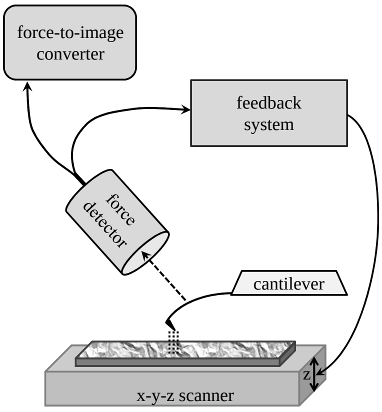

Figure 6.1

Some key components are essential to all force microscopes [105]:

- probe: a very sharp tip fixed to a very small flat spring (cantilever)
- precision scanning device for moving sample and tip relative to each other
- detection system for the response of the cantilever to forces acting on it
- feedback system for controlling the force affecting on the cantilever
- conversion from the measured signal to the image of the sample surface

There are several different modes for operating an atomic force microscope (see for example [106] and references therein). However, the following sections will mainly cover the so-called constant-force non-contact AFM mode, since this mode was employed for all AFM measurements in the present work. The basic principle of constant-force non-contact atomic force microscopy is to bring the sharp tip fixed to a flat spring (the so-called cantilever) very close to the sample and detect the force acting between probe and sample as a measure of the tip-to-sample distance. The flat spring cantilever is driven to oscillate at its resonance frequency, so that the force can be detected by the effect it has on the behavior of the cantilever. A feedback system keeps the force constant by regulating the tip-to-sample distance, so that the tip traces the topographical profile of the sample at a constant distance when scanned across its surface. The surface topography is reconstructed from the feedback signal at every point of measurement [103]. Piezoelectric elements are commonly used for both driving the cantilever oscillation and scanning the sample with high precision.

6.1.1 Forces between probe and sample

Both long-range and short-range forces contribute to the interaction of probe and sample in AFM. Chemical short-range forces dominate, when the tip is so close to the sample that atom orbitals of tip and sample overlap, i.e. for distances less than about 1 nm. Long-range magnetic, electrostatic and resultant van-der-Waals forces determine the probe-sample interaction at larger distances of up to 100 nm. They originate from the entire interaction volume of sample and tip and depend strongly on the tip shape. Additionally, capillary forces due to adsorbed water layers on tip and sample can occur under ambient conditions.

In non-contact AFM, the distance z_{ps} between tip and sample is about 10 to 100 nm. Consequently, this AFM mode is sensitive to magnetic, electrostatic, or van-der-Waals forces rather than to the short-range interatomic forces [105]. The overall force experienced by the cantilever in this distance range is weakly attractive.

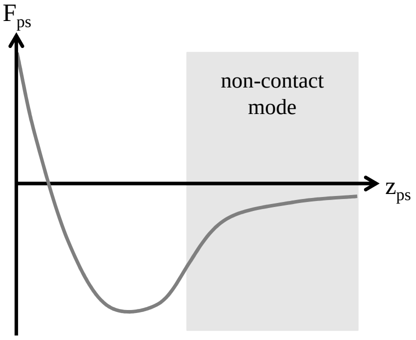

Figure 6.2

For a general potential energy E_{ps}, subsuming all interactions between probe and sample, the corresponding probe-sample force F_{ps} is given by Eqn.(6.1). The second derivative of the potential energy E_{ps} can be interpreted as a probe-sample force constant k_{ps}, given by Eqn.(6.2):

$$F_{ps}(z) = -\frac{\partial E_{ps}(z)}{\partial z} \qquad (6.1) \qquad\qquad k_{ps}(z) = -\frac{\partial F_{ps}(z)}{\partial z} \qquad (6.2)$$

The magnitudes of electrostatic and van-der-Waals forces for spherical tips with typical radii in common measurement distances to the sample are $F_{ps} \sim 10^{-10}$ N to 10^{-9} N [106].

6.1.2 Properties of the cantilever and detection of the probe-sample force

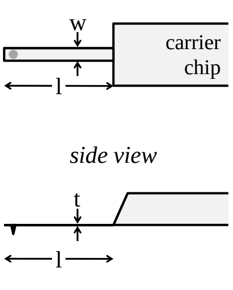

The force sensor of an atomic force microscope is a spring, namely the cantilever to which the measuring tip is mounted. For effectively sensing forces in z-direction, the cantilever has to be soft in this direction and hard in the others. Therefore, AFM force sensors are typically flat springs, with proportions resembling those of a diving board. Such a rectangular cantilever with width w, thickness t, and length l has a spring constant of $k_0 = (Ywt^2)/(4l^3)$, where Y is the Young's modulus of the cantilever material. For a given force, the cantilever with lowest spring constant will show the maximum response, i.e. produce the largest signal. However, the cantilever with highest spring constant will have the lowest sensitivity to noise (e.g. vibrations of the laboratory building of about 100 Hz). As a compromise rule of thumb – also taking into account what is feasible in microfabrication – the spring constant should be larger than several hundred N/m [106, 107].

A force between tip and sample is detected via the deflection of the cantilever. There are several ways to measure the cantilever deflection [107], the most robust and simple method is light reflection [108]. Here, a beam of light is directed at the backside of the cantilever and reflected onto a position-sensitive photodetector. For a lever as short as an AFM cantilever a small deflection results in a large change in the angle with respect to the light beam, i.e. in a large change of the position of the reflected light spot on the photodetector. The amplitude, frequency, and phase of the cantilever oscillation can be detected and used as input signal for the feedback system.

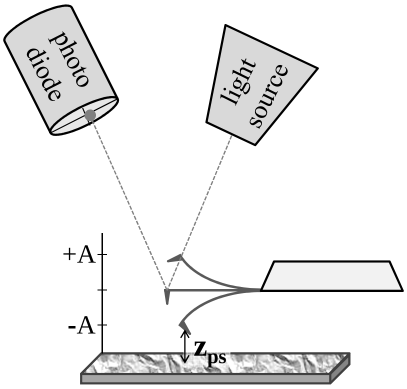

Figure 6.3

6.1.3 Non-contact constant-force AFM

Non-contact constant-force atomic force microscopy shall be discussed here as the AFM operating mode employed for the measurements presented in this work. When brought close to the sample, so that the probe-sample force becomes relevant, the unperturbed values of spring constant k_0 and resonant frequency ω_0 of the cantilever have to be replaced by respective effective values. In the non-contact constant-force mode, the cantilever oscillation is driven by an actuator with frequency ω_d close to but not equal to the effective resonant frequency ω_0^* of the cantilever. Changes in the probe-sample force constant k_{ps} are detected as changes in the oscillation amplitude of the cantilever. Using a positive feedback, the probe-to-sample distance is regulated so that the cantilever oscillates with a constant setpoint amplitude.

The effective resonant frequency ω_0^* of the cantilever under influence of the probe-sample force F_{ps} is given by Eqn.(6.3), where m is the effective mass of the cantilever. In the presence of a probe-sample force, the effective cantilever spring constant k_0^* is given by Eqn.(6.4):

$$\omega_0^* = \sqrt{\frac{k_0^*}{m}} \qquad (6.3) \qquad\qquad k_0^* = k_0 + k_{ps} = k_0 + \frac{\partial F_{ps}}{\partial z} \qquad (6.4)$$

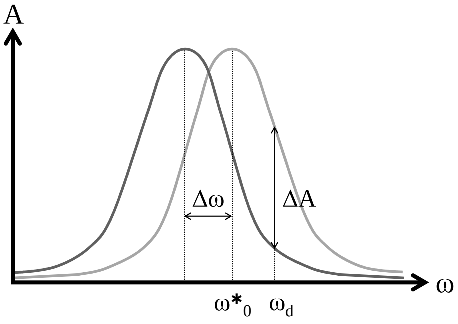

Figure 6.4

Thus, a change in the probe-sample force constant $k_{ps} = k_{ps}(z)$ due to changing tip-sample distance along a scan line alters the effective resonant frequency by $\Delta\omega$. Consequently, the oscillation amplitude at the driving frequency ω_d of the actuator changes by ΔA, as depicted in Fig. 6.4.

The amplitude shift ΔA is registered by the photodetector and passed to the feedback system. The feedback system outputs a correction for the tip-to-sample distance, so that the cantilever oscillation amplitude is kept constant. Fig. 6.5 illustrates the working principle of non-contact constant-force atomic force microscopy.

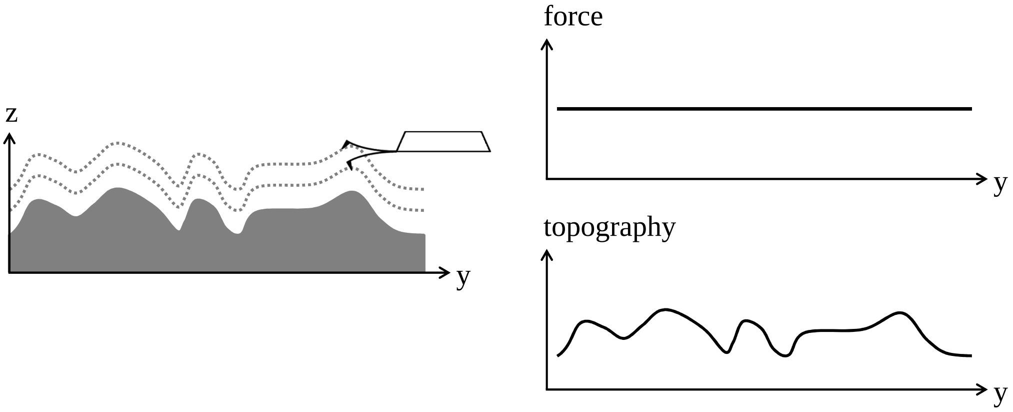

Figure 6.5: Sketch of the working principle of constant-force non-contact AFM

6.1.4 Limitations and alternatives

Considerable advantages of AFM are the affordability of good microscopes, the high-resolution imaging in real space, and the minimum damage done to the sample. However, the exactness of measurements of lateral and vertical dimensions is intrinsically limited by the finite sizes of the tip and the sample surface features: If the interaction area of tip and sample is larger than the size of the feature to be measured, then the measured height is a convolution of the feature height and the height level of the surrounding surface. Consequently, in most cases the measured height of a protruding surface feature is smaller than its actual height. This effect is independent of the AFM operating mode. [109]. Furthermore, contrast inversion of height and phase images can occur, but can be recognized in known sample systems [110].

AFM can only depict the local surface topography of a sample. Nanotomography has been proposed for local real space 3D imaging of the sample interior. Here, the sample is alternatingly imaged by Scanning Force Microscopy and eroded layer by layer. Afterwards, a 3D volume image of the sample interior can be reconstructed from the 2D topography images [111]. Since the individual topography images have to be correlated, this procedure is very complicated if the sample cannot be eroded without being removed from the microscope. Additionally, the sample obviously becomes seriously damaged or completely destroyed. X-Ray scattering techniques (see section 6.2) on the other hand provide element specific structural information on the entire sample surface and volume - in reciprocal space.

6.2 Grazing-Incidence Small-Angle X-Ray Scattering

Grazing-Incidence Small-Angle X-ray Scattering (GISAXS) is a method for structural characterization of discontinuous surfaces and inhomogeneous thin films. It was introduced in the late 1980s as an alternative to microscopic methods such as Transmission Electron Microscopy (TEM) or Scanning Tunneling Microscopy (STM) and as an advancement of Small-Angle X-ray Scattering (SAXS) [112]. TEM or STM require conductive or very thin samples, respectively. Also, just as AFM, these techniques can only probe the sample locally. SAXS is performed in beam transmission geometry and therefore the scattering contribution from the substrate can easily outweigh the scattering contribution of the actual objects of interest. GISAXS can overcome the disadvantages of these techniques: It does not pose any specific sample requirements. GISAXS makes use of a beam reflection geometry with grazing angle of incidence, in which the penetration depth of x-rays into the sample is small, and therefore the bulk scattering contribution is reduced. Depending on the incident angle, the measurement can be sensitive to the very surface or to the interior of a supported layer. Further, the sample is not damaged by GISAXS, as long as it is resistant to hard x-rays. GISAXS is an averaging method, providing statistical information about the sample structure at length scales from several nm to a few μm. Moreover, the technique is well-suited for in-situ studies and is compatible with various sample environments. However, there are some drawbacks: Data are not acquired directly in real space but in reciprocal space, and the analysis of scattering patterns is complicated by the occurrence of multiple photon-matter interactions. Synchrotron radiation will be required for most experiments, because the samples commonly studied with GISAXS, such as discontinuous thin films, nanoparticles, or polymers, are small in volume or of low scattering strength. As GISAXS is not a local probe, it cannot provide any information on an individual structural feature of a sample [112, 113].

6.2.1 Basic concepts of GISAXS

The scattering geometry

The GISAXS scattering geometry and commonly used labels for the relevant quantities are shown in Fig. 6.6.

incident wave vector:	$\boldsymbol{k}_i$
scattered wave vector:	$\boldsymbol{k}_f$
incident angle:	α_i
scattered angle (out-of-plane):	α_f
scattered angle (in-plane):	$2\theta_f$
components of the wave vector transfer $\boldsymbol{q}$:	q_y, q_z

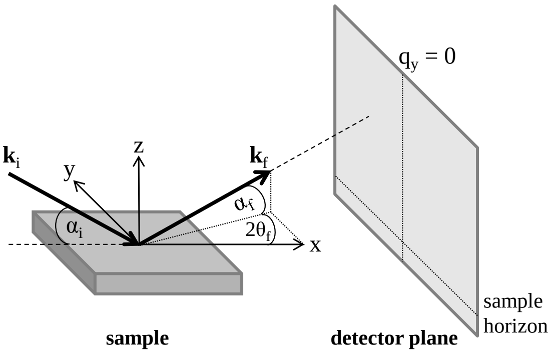

Figure 6.6

In GISAXS, the sample is irradiated with x-rays at an incident angle close to the critical angle $\alpha_i \approx \alpha_c$. The incident angle is fixed and the scattered intensity is recorded using an area detector. The wave vector transfer or scattering vector $\boldsymbol{q}$ is defined as the difference of scattered and incident wave vector:

$$\begin{aligned} \boldsymbol{q} = \boldsymbol{k}_f - \boldsymbol{k}_i &= k_0 \begin{pmatrix} \cos(2\theta_f)\cos(\alpha_f) \\ \sin(2\theta_f)\cos(\alpha_f) \\ \sin(\alpha_f) \end{pmatrix} - k_0 \begin{pmatrix} \cos(\alpha_i) \\ 0 \\ -\sin(\alpha_i) \end{pmatrix} \\ &= k_0 \begin{pmatrix} \cos(2\theta_f)\cos(\alpha_f) - \cos(\alpha_i) \\ \sin(2\theta_f)\cos(\alpha_f) \\ \sin(\alpha_f) + \sin(\alpha_i) \end{pmatrix} \end{aligned} \tag{6.5}$$

with the wave vector norm $k_0 = |\boldsymbol{k}_i| = |\boldsymbol{k}_f| = 2\pi/\lambda$. The scattering vector $\boldsymbol{q}$ is expressed in terms of its surface-parallel component $\boldsymbol{q}_{\|} = (q_x, q_y)$ (q_x is not detected) and its surface-perpendicular component $q_{\perp} = q_z$.

The coherently scattered intensity $I(\boldsymbol{q})$ is proportional to the product of the squared absolute value of the form factor $F(\boldsymbol{q})$ and the interference function or structure factor $S(\boldsymbol{q}_{\|})$:

$$I(\boldsymbol{q}) = I_0 \left|F(\boldsymbol{q})\right|^2 S(\boldsymbol{q}_{\|}) \tag{6.6}$$

The form factor $F(\boldsymbol{q})$ describes the shape of the objects of interest, e.g. supported nanoparticles or holes in a layer, and includes a weighting of the possible photon-matter interaction channels. The structure factor or interference function $S(\boldsymbol{q}_{\|})$ is given by the relative arrangement of the objects of interest (see section 6.2.2). If the sample exhibits structural regularity in-plane (i.e. objects of identical diameter or a periodic arrangement of scattering objects), peaks in the scattered intensity $I(\boldsymbol{q}_{\|})$ are detected at the corresponding value of the surface-parallel wave vector transfer component $\boldsymbol{q}_{\|}$. If the sample presents structural correlations in the vertical, out-of-plane direction (e.g. layer thicknesses, nanoparticle heights) corresponding modulations of the scattered intensity $I(\boldsymbol{q}_z)$ are observed. $I(\boldsymbol{q}_z)$ is comparable to the result of an out-of-plane point-detector scan in diffuse reflectivity measurements [114]. Thus, information about in-plane and out-of-plane structural correlations can be obtained from a GISAXS pattern:

- diameter of nanostructures and the distances between them
- height of nanostructures and layer thicknesses
- distributions of these parameters

The refractive index and penetration depth for x-rays

The scattering geometry employed in GISAXS allows for the x-rays to interact with the objects of interest without having to pass through the supporting substrate as in SAXS. In this way GISAXS exploits the refraction and reflection of x-rays by matter. The refractive index is

$$n = 1 - \delta + \mathrm{i}\beta \tag{6.7}$$

with $\delta = \alpha_c^2/2 = \frac{\lambda^2}{2\pi}\rho_e r_0$ and $\beta = \mu\lambda/4\pi$, where α_c is the critical angle for total external reflection, ρ_e is the number density of electrons, r_0 is the Thomson scattering length, and μ is the material-specific absorption coefficient. δ and β are related to scattering and absorption properties of the material, respectively [115]. For x-rays in matter $n < 1$. Consequently – as according to Snell's law, $\cos(\alpha_i) = n\cos(\alpha_t)$ holds for the situation depicted in Fig. 6.7 – an x-ray beam in matter is refracted towards the vacuum/matter interface. This allows for total external reflection of the incident x-ray beam for angles $\alpha_i \leq \alpha_c$. In this case, only an evanescent wave penetrates into the matter, which makes x-rays a surface-sensitive probe.

Since the refractive index is a complex number, the angle α_t as derived from Snell's law is a complex number, too. The penetration depth Λ is given via the imaginary part of α_t: $\Lambda = (\frac{4\pi}{\lambda}\Im(\alpha_t))^{-1}$. As an example, for $(\mu\lambda)/(4\pi\alpha_c^2) = 0.01$:

$\alpha_i \ll \alpha_c$: $\Lambda \approx 1$ nm

$\alpha_i \approx \alpha_c$: $\Lambda \approx 10$ nm

$\alpha_i \gg \alpha_c$: $\Lambda > 100$ nm [115]

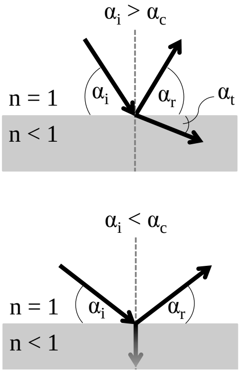

Figure 6.7

GISAXS from tilted and faceted surfaces

The GISAXS pattern of a planar surface with uncorrelated roughness features merely one central rod of scattered intensity along $(0, 0, q_z)$ resulting from the fact that the sample is not infinitely extended in z-direction (crystal truncation rod; see e.g. [116]). This central scattering rod is always perpendicular to the surface off which the incident beam was scattered: If the flat surface is rotated around the $x-$axis, the central scattering rod is tilted away from the vertical direction by the same angle [113, 117], as depicted in Fig. 6.8. A faceted surface, such as the α-Al_2O_3 surfaces described in section

1.2.3, essentially consists of two sets of surface fractions, alternatingly tilted in opposite sense around the same axis. The GISAXS pattern of a faceted surface (with the facets aligned along the $x-$axis) therefore consists of two scattering rods, one to each side of the vertical, as can be seen in Fig. 6.9. Both scattering rods are rotated away from the vertical direction by the corresponding tilt angle of the facet faces with respect to the horizontal sample plane.

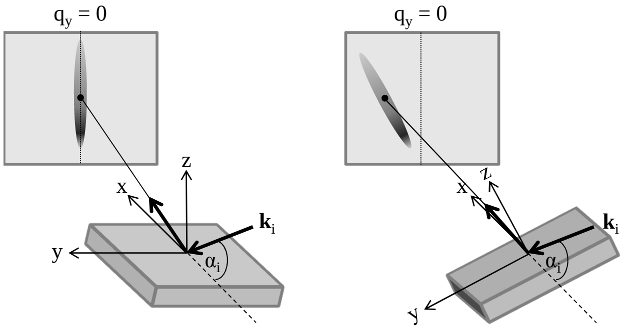

Figure 6.8: GISAXS patterns of a horizontal and a tilted planar surface.

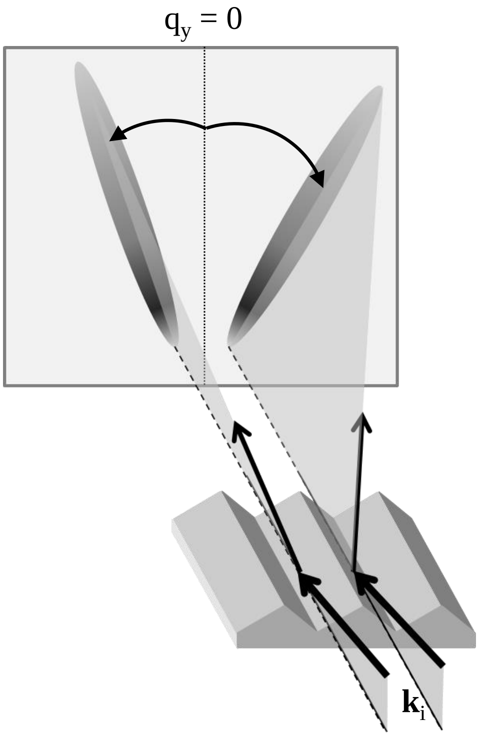

Figure 6.9: The GISAXS pattern of a faceted surface is characterized by two tilted scattering rods.

6.2.2 Theoretical background of GISAXS

In the following, the basic theoretical background of treating GISAXS within the so-called distorted wave Born approximation (DWBA) will be outlined. Only the type of sample system which is relevant for this work will be considered. A comprehensive elaboration can be found in reference [113].

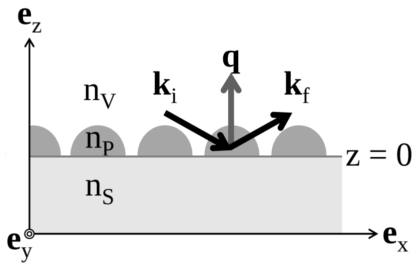

Figure 6.10

Consider the following sample system, typically investigated by GISAXS and sketched in Fig. 6.10: Nanoparticles of refractive index n_P are supported by a homogeneous, semi-infinite substrate of refractive index n_S. The sample is surrounded by vacuum with refractive index $n_V = 1$ and irradiated with hard x-rays at an incident angle $\alpha_i < \alpha_c$.

The Born approximation (BA) is not applicable to such a situation, because it considers only single scattering events and neglects multiple photon-matter interaction events including reflection, refraction and scattering. The distorted wave Born approximation (DWBA) was devised to take into account the interplay of refraction, reflection, and scattering encountered for the small scattering angles in grazing incidence geometry. The DWBA should be used for small incident angles $\alpha_i \lesssim \alpha_c$ and in case of high substrate reflectivity. In the DWBA, nanoparticles on a substrate are described by their effect of causing perturbations in a reference refractive index $n_0(z)$ of the sample system [113, 118]. The reference refractive index is defined as

$$n_0(z) = \begin{cases} n_V & \text{for } z > 0 \\ n_S & \text{for } z < 0 \end{cases} \tag{6.8}$$

The refractive index of the entire system including nanoparticles is

$$n(\boldsymbol{r}) = \left(n_0^2(z) + (1 - n_P^2)\tilde{F}(\boldsymbol{r})\right)^{1/2} \tag{6.9}$$

Here, $\tilde{F}(\boldsymbol{r})$ is the nanoparticle shape with

$$\tilde{F}(\boldsymbol{r}) = \begin{cases} 1 & \text{inside a nanoparticle} \\ 0 & \text{outside of nanoparticles} \end{cases} \tag{6.10}$$

For hard x-rays, the refractive index is $n \approx 1$ (with $1 - n < \mathcal{O}(10^{-6})$) and polarization effects (polarization of the electron distributions by the electric field of the radiation) are negligible [113, 118]. In this case, the propagation equation for the amplitude $A(\boldsymbol{r})$ of the electromagnetic wave is reduced to the stationary wave equation

$$\left[\nabla^2 + n^2(\boldsymbol{r})k_0^2\right] A(\boldsymbol{r}) = 0 \tag{6.11}$$

In the absence of nanoparticles supported on the substrate, i.e. for $n(\boldsymbol{r}) = n_0(z)$, Eqn. (6.11) is satisfied by the unperturbed field amplitude $A(\boldsymbol{r}, \boldsymbol{k}) = A^0(\boldsymbol{r}, \boldsymbol{k})$, given by the Fresnel function

$$A^0(\boldsymbol{r}, \boldsymbol{k}) = \exp\left(\mathrm{i}\boldsymbol{k}_\parallel \cdot \boldsymbol{r}_\parallel\right) \cdot \begin{cases} \exp\left(\mathrm{i}k_{i,z}z\right) + R\exp\left(-\mathrm{i}k_{f,z}\right) & \text{for } z > 0 \\ T\exp\left(\mathrm{i}k_{t,z}z\right) & \text{for } z < 0 \end{cases} \tag{6.12}$$

where $\boldsymbol{r}_\parallel = (x, y)$, $\boldsymbol{k}_\parallel = (k_x, k_y)$, and

$$k_{i,z} = k_{f,z} = -\sqrt{k_0^2 - |\boldsymbol{k}_\parallel|^2} \quad , \quad k_{t,z} = -\sqrt{n_S^2 k_0^2 - |\boldsymbol{k}_\parallel|^2} \tag{6.13}$$

The Fresnel coefficients for reflection and transmission are

$$T = \frac{2k_{i,z}}{k_{i,z} + k_{t,z}} \quad , \quad R = \frac{k_{i,z} - k_{t,z}}{k_{i,z} + k_{t,z}} \tag{6.14}$$

The DWBA form factor

Consider now supported nanoparticles on the substrate surface. Transmission through the substrate is assumed to be negligible and the field amplitude $A(\boldsymbol{r}, \boldsymbol{k})$ is evaluated only for $z > 0$. In this case, there are four channels of photon-matter interaction [113, 118] as sketched in Fig. 6.11:

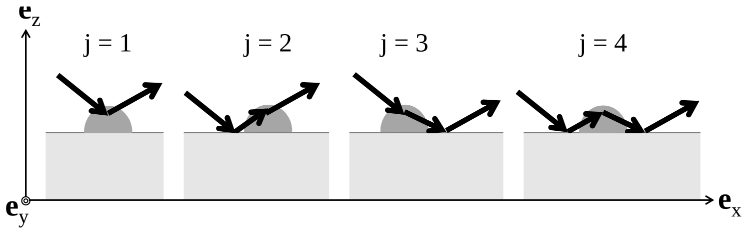

Figure 6.11: The four possible photon-matter interaction channels covered by the DWBA formalism.

- scattering of the incident wave by a nanoparticle ($j = 1$)
- scattering of the incident wave by a nanoparticle and reflection of the scattered wave by the substrate ($j = 2$)
- reflection of the incident wave by the substrate and scattering of the reflected wave by a nanoparticle ($j = 3$)
- reflection of the incident wave by the substrate, scattering of the reflected wave from a nanoparticle, and reflection of the scattered wave by the substrate ($j = 4$)

This is expressed in the field amplitude $A(\boldsymbol{r})$ as described in the DWBA: When supported nanoparticles are taken into consideration as perturbations in the system's refractive index, the field amplitude satisfying Eqn. (6.11) is (in first order) [118, 119]:

$$\begin{aligned} A(\boldsymbol{r}) = &-\frac{k_0}{4\pi r}\left(1 - n_P^2\right)\exp\left(\mathrm{i}k_0 r\right) \\ &\cdot \int A^0(\boldsymbol{r'}, -\boldsymbol{k}_f) F(\boldsymbol{r'}) A^0(\boldsymbol{r'}, \boldsymbol{k}_i) d\boldsymbol{r'} \end{aligned} \tag{6.15}$$

According to Eqn. (6.12) for $z > 0$, both $A^0(\boldsymbol{r'}, -\boldsymbol{k}_f)$ and $A^0(\boldsymbol{r'}, \boldsymbol{k}_i)$ are superpositions of two plane waves:

$$\begin{aligned} A^0(\boldsymbol{r'}, -\boldsymbol{k}_f) &= A^0_1(\boldsymbol{r'}, -\boldsymbol{k}_f) + A^0_2(\boldsymbol{r'}, -\boldsymbol{k}_f) \\ &= \exp\left(-\boldsymbol{k}_{f,\parallel} \cdot \boldsymbol{r'}_{\parallel}\right)\exp\left(-\mathrm{i}k_{f,z}z\right) + \exp\left(-\boldsymbol{k}_{f,\parallel} \cdot \boldsymbol{r'}_{\parallel}\right)R_f \exp\left(+\mathrm{i}k_{f,z}z\right) \\ A^0(\boldsymbol{r'}, +\boldsymbol{k}_i) &= A^0_1(\boldsymbol{r'}, \boldsymbol{k}_i) + A^0_2(\boldsymbol{r'}, \boldsymbol{k}_i) \\ &= \exp\left(+\boldsymbol{k}_{i,\parallel} \cdot \boldsymbol{r'}_{\parallel}\right)\exp\left(+\mathrm{i}k_{i,z}z\right) + \exp\left(+\boldsymbol{k}_{i,\parallel} \cdot \boldsymbol{r'}_{\parallel}\right)R_i \exp\left(-\mathrm{i}k_{i,z}z\right) \end{aligned} \tag{6.16}$$

Since $(a+b)(c+d) = ac+ad+bc+bd$, the integral in Eqn. (6.15) is actually an integral over a sum of four products (i.e. the sum of four integrals over one product each). With Eqn. (6.16) and $\boldsymbol{k}^f_{\parallel} - \boldsymbol{k}^i_{\parallel} = \boldsymbol{q}_{\parallel}$, one yields via rearrangement of the exponential functions (subsuming surface-parallel and surface-perpendicular components in the arguments)

$$
\begin{aligned}
A(\boldsymbol{r}) = &-\frac{k_0}{4\pi r}\left(1-n_P^2\right)\exp\left(\mathrm{i}k_0 r\right)\\
&\cdot\Bigg[\int A_1^0(\boldsymbol{r'},-\boldsymbol{k}_f)A_1^0(\boldsymbol{r'},\boldsymbol{k}_i)\tilde{F}(\boldsymbol{r'})d\boldsymbol{r'}\\
&+\int A_1^0(\boldsymbol{r'},-\boldsymbol{k}_f)A_2^0(\boldsymbol{r'},\boldsymbol{k}_i)\tilde{F}(\boldsymbol{r'})d\boldsymbol{r'}\\
&+\int A_2^0(\boldsymbol{r'},-\boldsymbol{k}_f)A_1^0(\boldsymbol{r'},\boldsymbol{k}_i)\tilde{F}(\boldsymbol{r'})d\boldsymbol{r'}\\
&+\int A_2^0(\boldsymbol{r'},-\boldsymbol{k}_f)A_2^0(\boldsymbol{r'},\boldsymbol{k}_i)\tilde{F}(\boldsymbol{r'})d\boldsymbol{r'}\Bigg]\\
\\
=&-\frac{k_0}{4\pi r}\left(1-n_P^2\right)\exp\left(\mathrm{i}k_0 r\right)\\
&\cdot\Bigg[\int \exp\left(-\mathrm{i}\boldsymbol{q}_\parallel\cdot\boldsymbol{r}_\parallel\right)\exp\left(-\mathrm{i}(k_{f,z}-k_{i,z})z\right)\tilde{F}(\boldsymbol{r'})d\boldsymbol{r'}\\
&+R_i\int \exp\left(-\mathrm{i}\boldsymbol{q}_\parallel\cdot\boldsymbol{r}_\parallel\right)\exp\left(-\mathrm{i}(k_{f,z}+k_{i,z})z\right)\tilde{F}(\boldsymbol{r'})d\boldsymbol{r'}\\
&+R_f\int \exp\left(-\mathrm{i}\boldsymbol{q}_\parallel\cdot\boldsymbol{r}_\parallel\right)\exp\left(-\mathrm{i}(-k_{f,z}-k_{i,z})z\right)\tilde{F}(\boldsymbol{r'})d\boldsymbol{r'}\\
&+R_iR_f\int \exp\left(-\mathrm{i}\boldsymbol{q}_\parallel\cdot\boldsymbol{r}_\parallel\right)\exp\left(-\mathrm{i}(-k_{f,z}+k_{i,z})z\right)\tilde{F}(\boldsymbol{r'})d\boldsymbol{r'}\Bigg]\\
\\
=&-\frac{k_0}{4\pi r}\left(1-n_P^2\right)\exp\left(\mathrm{i}k_0 r\right)\\
&\cdot\left[F_1(\boldsymbol{q}_\parallel,k_{f,z}-k_{i,z})\right.\\
&+R_iF_2(\boldsymbol{q}_\parallel,k_{f,z}+k_{i,z})\\
&+R_fF_3(\boldsymbol{q}_\parallel,-k_{f,z}-k_{i,z})\\
&\left.+R_iR_fF_4(\boldsymbol{q}_\parallel,-k_{f,z}+k_{i,z})\ \right]
\end{aligned}
\tag{6.17}
$$

The functions $F_j(\boldsymbol{q}_\parallel,q_{z,j})$ defined by Eqn. (6.17) constitute the form factor $F(\boldsymbol{q})$ in DWBA - there is one contribution to the DWBA form factor for every interaction channel. Each contribution $F_j(\boldsymbol{q}_\parallel,q_{z,j})$ is characterized by a specific perpendicular scattering vector component $q_{z,j}$ and is weighted by the Fresnel coefficient(s) for reflection corresponding to the respective photon-matter interaction channel [113,118]. The four DWBA form factor contributions $F_j(\boldsymbol{q}_\parallel,q_{z,j})$ to the scattered amplitude $A_f(\boldsymbol{r})$ are plotted in Fig. 6.12 for different incident angles α_i. $F_1(\boldsymbol{q}_\parallel,q_{z,1})$ and $F_2(\boldsymbol{q}_\parallel,q_{z,2})$ dominate for $\alpha_f > \alpha_c$,

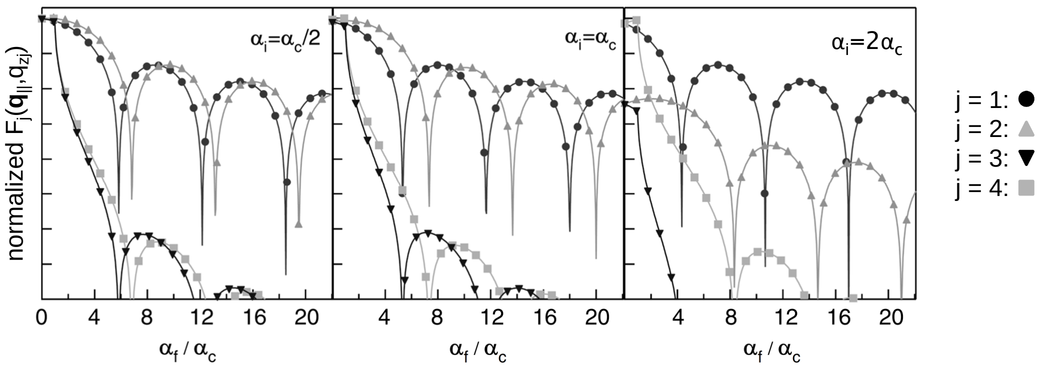

Figure 6.12: The four form factors in the distorted wave Born approximation (Eqn. (6.17)) for different incident angles. Adapted from [113].

while $F_3(\boldsymbol{q}_{\|}, q_{z,3})$ and $F_4(\boldsymbol{q}_{\|}, q_{z,4})$ become relevant for $\alpha_f \leq \alpha_c$. The wave vector shift of $+2k_z^i$ for $F_3(\boldsymbol{q}_{\|}, q_{z,3})$ and $F_4(\boldsymbol{q}_{\|}, q_{z,4})$ relative to $F_1(\boldsymbol{q}_{\|}, q_{z,1})$ and $F_2(\boldsymbol{q}_{\|}, q_{z,2})$ smooths the sharp minima in the resulting curve progression of the resulting form factor $F(\boldsymbol{q})$ [113].

For dense arrangements of nanoparticles, the fact has to be taken into account, that scattered waves can not only be reflected by the substrate (as for $j = 3; 4$) but can also be scattered again by another nanoparticle. In this case, the DWBA form factor is still valid conceptually, but takes a more complicated form to account for multiple scattering [113].

The structure factor

An ordered arrangement (lattice) of scatterers is described by a real space lattice vector $\boldsymbol{R}$, which defines any lattice point in the arrangement of scattering objects via the lattice basis vectors $\boldsymbol{a}_j$. In two dimensions, e.g. for a lattice of nanoparticles on a substrate surface, the real space lattice vector is

$$\boldsymbol{R}_{\|} = b_1\boldsymbol{a}_1 + b_2\boldsymbol{a}_2 \tag{6.18}$$

where b_j are integers. The corresponding 2D reciprocal lattice vector $\boldsymbol{G}_{\|}$ is defined as

$$\boldsymbol{G}_{\|} = h\boldsymbol{a}_1^* + k\boldsymbol{a}_2^* \tag{6.19}$$

where h, k are integers. With $\boldsymbol{a}_3$ being the surface normal unit vector, the basis vectors of the reciprocal lattice are given by [113, 115]

$$\boldsymbol{a}_1^* = 2\pi\frac{\boldsymbol{a}_2 \times \boldsymbol{a}_3}{\boldsymbol{a}_1 \cdot (\boldsymbol{a}_2 \times \boldsymbol{a}_3)}, \quad \boldsymbol{a}_2^* = 2\pi\frac{\boldsymbol{a}_3 \times \boldsymbol{a}_1}{\boldsymbol{a}_2 \cdot (\boldsymbol{a}_3 \times \boldsymbol{a}_1)}$$

The structure factor $S(\boldsymbol{q}_{\|})$ for a two-dimensional lattice is given by

$$S(\boldsymbol{q}_{\|}) = \sum_{h} \sum_{k} \mathcal{S}(\boldsymbol{q}_{\|} - \boldsymbol{G}_{\|}) = \sum_{h} \sum_{k} \mathcal{S}(\boldsymbol{q}_{\|} - h\boldsymbol{a}_1^* - k\boldsymbol{a}_2^*) \tag{6.20}$$

For a perfect lattice, $\mathcal{S}(\boldsymbol{q}_{\|} - \boldsymbol{G}_{\|})$ is a Dirac delta function. Therefore, maxima – so-called Bragg scattering rods or crystal truncation rods – in the distribution of scattered intensity $I(\boldsymbol{q}) \propto S(\boldsymbol{q}_{\|})$ are observed for $\boldsymbol{q}_{\|} = \boldsymbol{G}_{\|}$. It has to be taken into account though, that peaks in the structure factor $S(\boldsymbol{q}_{\|})$ can appear shifted in the scattered intensity $I(\boldsymbol{q})$ (see Eqn. (6.6)) due to the curve progression of the form factor $F(\boldsymbol{q})$. For an imperfect lattice, $\mathcal{S}(\boldsymbol{q}_{\|} - \boldsymbol{G}_{\|})$ (also called the rod shape) is broadened, depending on the type and degree of disorder. The lattice coherence length can be measured by the inverse width of the scattering rods [113]. In disordered systems, $S(\boldsymbol{q}_{\|}) \to 1$ for increasing norm of $\boldsymbol{q}_{\|}$. The distribution of scattered intensity $I(\boldsymbol{q})$ is then determined by the form factor $F(\boldsymbol{q})$ alone [113].

All in all, GISAXS provides comprehensive structural information about a sample, but the quantitative analysis according to the DWBA formalism is far from trivial. Programs for simulating GISAXS patterns, e.g. *IsGISAXS* [117] or *FitGISAXS* [120], have been developed on the basis of the DWBA. Using such a simulation program simplifies the task to extract information on in-plane and out-of-plane structural correlations from a GISAXS pattern and to combine them into a three-dimensional picture of the sample structure.

6.3 Nuclear Resonant Scattering

Magnetic properties of the nanostructure samples presented in this work are investigated using coherent elastic nuclear resonant scattering of synchrotron radiation (NRS)[1]. NRS is a highly sensitive method for determining the strength and orientation of magnetic hyperfine fields at resonant nuclei, which are in good approximation proportional to the atomic magnetic moments. The relevant time scale for NRS is the lifetime of the nuclear excitation; thus it is suited for studying magnetization dynamics on the time scale of nanoseconds (see section 10.3.3). Furthermore, the spatially coherent nature of this scattering process allow for deducing spatially resolved magnetic information from the distribution of scattered intensity in space (see section 8.2). This section (with appendix A.1) may provide a short introduction to the principles of this method. A comprehensive description was elaborated by Röhlsberger [77].

NRS relies on the absorption and delayed re-emission of pulsed radiation by atomic nuclei at specific resonance energies. In a nuclear resonant scattering process, radiation with the resonant energy of the scattering material is absorbed by a nucleus and excites a transition of the nucleus from a ground state level to an excited state level. Upon decay of the excited state, a photon is re-emitted. In the coherent elastic scattering process considered here, the nucleus returns to its initial ground state level and the emitted photon has the same energy as the incident photon. The time scale of the scattering process is given by the lifetime $\tau_0 = \hbar/\Gamma_0$ of the excited state, where Γ_0 is the natural linewidth of the resonance, i.e. the full energy width at half maximum at the resonance energy. The lifetime τ_0 of an excited nuclear state is typically of the order of several nanoseconds ($\sim 10^{-09}$ s) to few microseconds ($\sim 10^{-06}$ s), while scattering by electrons proceeds within some femtoseconds ($\sim 10^{-15}$ s). A resonantly scattered photon will therefore arrive at a detector with a measurable delay with respect to photons which were non-resonantly scattered by electrons. Using a pulsed radiation source with sufficient pulse separation thus allows to distinguish resonantly and non-resonantly scattered photons and to detect them separately.

---

[1] Resonant scattering of photons by atomic nuclei involves different nuclear scattering processes – coherent and incoherent, elastic and inelastic – which are exploited in different experimental techniques. Here, the case of coherent elastic nuclear resonant scattering of synchrotron radiation in grazing incidence geometry will be discussed. Whenever the acronym NRS is used in this work, it refers to this case.

For this work, the iron isotope ^{57}Fe was used as resonant atom. The nuclear ground state of ^{57}Fe has a nuclear spin of $I_g = 1/2$ and magnetic moment of $\mu_g = 0.091\ \mu_N$, while the excited state has a nuclear spin of $I_e = 3/2$ and magnetic moment of $\mu_e = -0.153\ \mu_N$[2]. The natural lifetime of the excited state is $\tau_0 = 141$ ns. In ferromagnetic α-^{57}Fe, the spin polarization of s-electrons and minor contributions from e.g. itinerant electrons result in an internal magnetic field which has a maximum strength of $B_{hf} = 33.3$ T at the position of the nucleus at room temperature [121]. This internal magnetic field, the so-called magnetic hyperfine field, is oriented oppositely to the external magnetization of the sample [122].

Due to the magnetic hyperfine field the nuclear energy levels are subject to Zeeman splitting. Fig. 6.13 depicts the energy levels and allowed dipole transitions for α-^{57}Fe with a hyperfine field strength of $B_{hf} = 33.3$ T. According to the dipole selection rule $M = m_e - m_g = [0; \pm 1]$, there are six allowed transitions from the ground state levels to the exited state levels, thus six resonance sub-lines at six energies. These resonance energies can be expressed in terms of the magnetic moments, and magnetic and spin quantum numbers of the respective levels, or in terms of magnetic quantum numbers and g-factors (see Eqn. (6.21)). The energy differences between the levels are $\Delta E_g = 190.25$ neV for the ground states and $\Delta E_e = 108.70$ neV for the excited states [77].

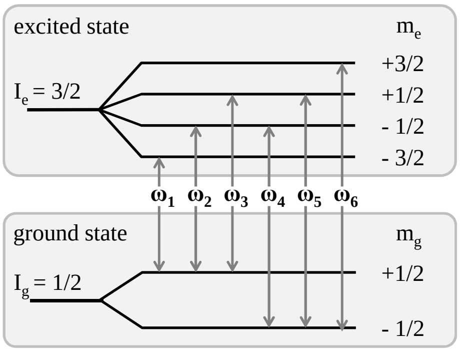

Figure 6.13

$$
\begin{aligned}
E &= E_0 - \left(\mu_e \frac{m_e}{I_e} - \mu_g \frac{m_g}{I_g} \right) B_{hf} \\
&= E_0 - (m_e g_e - m_g g_g) B_{hf} \qquad (6.21)
\end{aligned}
$$

A synchrotron radiation pulse is energetically broad enough to cover the resonance energies of all allowed transitions and thus to excite nuclei to all allowed states. Thus, upon de-excitation the nuclei re-emit photons with several slightly different frequencies ω_j corresponding to the respective resonance energies. The superposition of these photons results in a temporal beating pattern, the quantum beats, in the scattered intensity. The resonantly scat-

---

[2] The nuclear magneton is $\mu_N = e\hbar/2m_p$, where m_p is the rest mass of the proton.

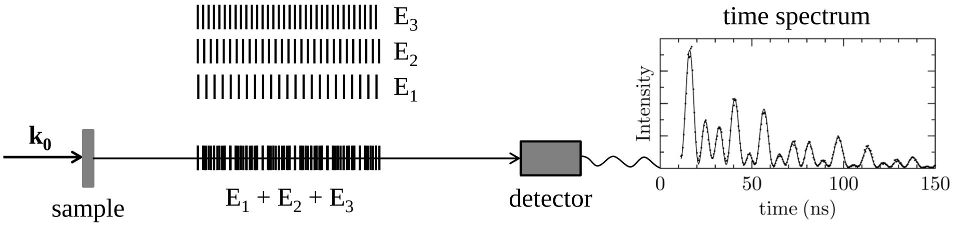

Figure 6.14: A basic NRS experiment. Quantum beats in the recorded time spectrum result from the superposition of photons emitted upon the decay of states with different resonance energies E_j. Adapted from [77].

tered intensity is recorded as a function of delay time, $I(t)$, in a so-called time spectrum. This principle is sketched in Fig. 6.14 [77]. The shape of such a time spectrum sensitively depends on the presence of ferromagnetic ordering in the sample and on the orientation of the magnetic quantization axis with respect to the orientations of the wave vector and the polarization vectors of incident radiation. The magnetic state of the sample can therefore be characterized by evaluation of its time spectrum (see e.g. [121, 123]).

The model of the time-dependence of resonantly forward scattered intensity outlined here is based on the assumption of coherent resonant forward scattering. Assuming coherent scattering leads to a macroscopic refractive index $\boldsymbol{n}(\omega)$ of the sample, which is related to the forward scattering amplitude $\boldsymbol{f}(\omega)$ of the sample as given in Eqn. (6.22). It is implied, that all features of the resonantly scattered intensity, which can be derived from this assumption and have been observed in numerous experiments, are consequences of the coherent nature of the nuclear scattering process [77, 124].

The relation between refractive index $\boldsymbol{n}(\omega)$ and scattering amplitude $\boldsymbol{f}(\omega)$ for a sample consisting of atomic species j with number density ρ_j is expressed as

$$\boldsymbol{n}(\omega) = \mathbf{1} + \frac{1}{k_0}\boldsymbol{f}(\omega) = \mathbf{1} + \frac{2\pi}{k_0^2}\sum_j \rho_j \boldsymbol{M}_j \tag{6.22}$$

The scattering amplitude $\boldsymbol{f}(\omega)$ is determined by the scattering length $\boldsymbol{M}(\omega) = \boldsymbol{E}(\omega) + \boldsymbol{N}(\omega)$, which is the sum of a non-resonant component $\boldsymbol{E}(\omega)$, accounting for the prompt scattering by electrons, and a resonant component $\boldsymbol{N}(\omega)$, describing the delayed nuclear resonant scattering.

6.3.1 Description of NRS in the matrix formalism

Forward scattering by nuclear resonant samples is effectively described within a formalism [77] based on the propagation matrix $\boldsymbol{F}(\omega)$, which relates the amplitude $\boldsymbol{A}(\omega)$ at the position x to the incident amplitude $\boldsymbol{A}_i$ at the surface of the sample ($x = 0$) as

$$\boldsymbol{A}(\omega) = \exp\Big(\mathrm{i}\boldsymbol{F}(\omega)x\Big)\boldsymbol{A}_i \tag{6.23}$$

The resonantly scattered intensity as a function of time – i.e. the time spectrum $I(t)$ – is derived in four steps [77, 124, 125]: The amplitude in the energy domain $\boldsymbol{A}(\omega)$ is determined from the incident amplitude $\boldsymbol{A}_i$ via the exponential $\exp(\mathrm{i}\boldsymbol{F}(\omega)x)$. Then, a Fourier transform is performed on the amplitude $\boldsymbol{A}(\omega)$ to obtain the amplitude in the time domain, $\boldsymbol{A}(t)$. Finally, the resonantly scattered intensity as a function of time, $I(t)$, is calculated from the amplitude $\boldsymbol{A}(t)$. The crucial task here is to calculate the exponential $\exp(\mathrm{i}\boldsymbol{F}(\omega)x)$.

In general, $\boldsymbol{F}(\omega)$ is a multi-dimensional matrix. The dimensionality of the propagation matrix depends on the scattering geometry, i.e. on the number of possible scattering channels. There are two cases with only one possible scattering channel: In transmission geometry there is no reflection channel. In grazing incidence geometry the transmission channel can be neglected for sufficiently small incident angles. In these cases, the propagation matrix is reduced to

$$\boldsymbol{F}(\omega) = \boldsymbol{k_0} + \boldsymbol{f}(\omega) = k_0\boldsymbol{n}(\omega) \tag{6.24}$$

where for the grazing incidence case the wave vector component in x-direction has been approximated as $k_{0,x} = k_0$ [77].

6.3.2 Resonant reflection from a thin layer

Consider first scattering in transmission geometry, with the wavevector of the incident radiation being parallel to the x-direction and the incident surface of the sample being located at $x = 0$, as shown in Fig. 6.15[3]. In the energy domain, the transmitted amplitude is then given by

---

[3] The same orientation of the coordinate system as in section 6.2 is used.

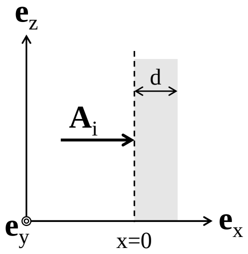

Figure 6.15

$$\begin{aligned}\boldsymbol{A}(\omega) &= \exp\left(\mathrm{i}\boldsymbol{F}(\omega)x\right)\boldsymbol{A}_i \\ &= \exp\left(\mathrm{i}k_0\boldsymbol{n}(\omega)x\right)\boldsymbol{A}_i \\ &= \exp\left(\mathrm{i}k_0x\right)\exp\left(\mathrm{i}\boldsymbol{f}(\omega)x\right)\boldsymbol{A}_i\end{aligned} \tag{6.25}$$

The phase factor $\exp(\mathrm{i}k_0x)$ can be dropped for convenience [77]. Eqn. (6.25) then reads

$$\boldsymbol{A}(\omega) = \exp\left(\mathrm{i}\boldsymbol{f}(\omega)x\right)\boldsymbol{A}_i \tag{6.26}$$

Often, however, samples such as thin films or the supported nanostructures in this work cannot be studied in transmission, but only in reflection. Conveniently, resonant reflection from a single thin layer of thickness d at a grazing incidence angle α_i can be treated analogously to resonant forward scattering in transmission, if two factors are accounted for [121, 123]:

- the beam path through the layer
- the standing wave resulting from interference of incident and reflected wave

Effectively, this means to replace the actual sample thickness d by

$$d' = |T_{VS}|^2 \frac{d}{\sin(\alpha_i)} \approx |T_{VS}|^2 \frac{d}{\alpha_i} \tag{6.27}$$

The beam path through the layer is taken into account by including the factor $1/\sin(\alpha_i) \approx 1/\alpha_i$. The amplitude of the standing wave is $A_s = (1+R_{VS})A_i = T_{VS}A_i$, where T_{VS} and R_{VS} are the Fresnel coefficients for transmission and reflection, respectively, at the interface between vacuum and the substrate. Its effect of enhancing the interaction between radiation and resonant matter is accounted for by a factor of $|T_{VS}|^2$ (the relative intensity at the substrate surface).

$|T_{VS}|^2$ has its maximum value at the critical angle α_c of the substrate. Here, the contribution of resonant scattering events to the total scattering process is highest [77, 123]. Fig.6.16 shows the nuclear and the electronic part of the reflected intensities as functions of incident angle for a ^{57}Fe surface and a ^{57}Fe thin film on a Si substrate.

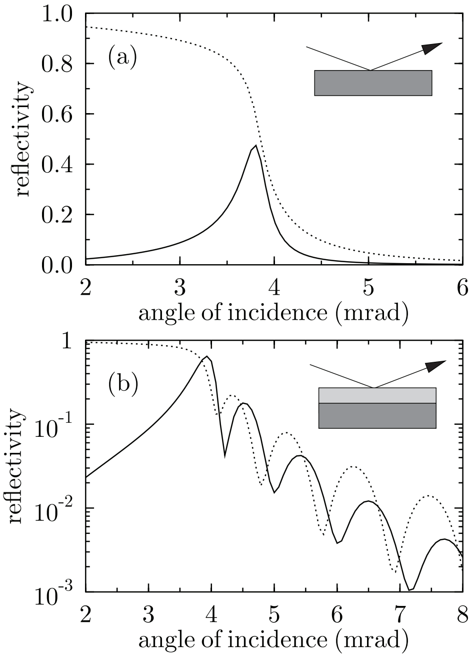

Figure 6.16: Calculated nuclear resonant reflectivities (solid lines) and electronic reflectivities (dotted lines) for (a) an ^{57}Fe surface and (b) an ^{57}Fe film of thickness d =30 nm on a Si substrate. From [77].

In the energy domain, the amplitude reflected by the layer is given by (compare to Eqn. (6.26))

$$\boldsymbol{A}_r(\omega) \approx \exp\left(\mathrm{i}\boldsymbol{f}(\omega)d'\right) R_{VS}\boldsymbol{A}_i = \exp\left(\mathrm{i}\boldsymbol{f}(\omega)\left|T_{VS}\right|^2 \frac{d}{\alpha_i}\right) R_{VS}\boldsymbol{A}_i \tag{6.28}$$

The Fourier transform of Eqn. (6.28) yields the reflected amplitude in the time domain:

$$\boldsymbol{A}_r(t) \approx \left(\delta(t) - \tilde{\boldsymbol{f}}(t)\frac{\chi'}{\tau_0}\exp\left(-\chi'\frac{t}{2\tau_0}\right)\right) R_{VS}\boldsymbol{A}_i \tag{6.29}$$

with $\chi' = \frac{1}{4}\sigma_0 f_{LM}\rho_n d'$, where σ_0 is the nuclear photon absorption cross-section at resonance, f_{LM} is the Lamb-Mössbauer factor, and ρ_n is the number density of resonant nuclei. χ' is often referred to as the "effective" thickness of the sample [77,126]. $\tilde{\boldsymbol{f}}(t)$ denotes the Fourier transform of $\boldsymbol{f}(\omega)$. This expression for the reflected amplitude is analogous to the expression for the outgoing amplitude in transmission geometry (see Eqns. (A.1) and (A.2) in apendix A.1) [77]. The corresponding reflected intensity is given by

$$\begin{aligned} I(t) = {} & \frac{1}{2}(1+\xi)\left(\left|A_{r,\sigma\sigma}(t)\right|^2 + \left|A_{r,\sigma\pi}(t)\right|^2\right) \\ & + \frac{1}{2}(1-\xi)\left(\left|A_{r,\pi\sigma}(t)\right|^2 + \left|A_{r,\pi\pi}(t)\right|^2\right) \end{aligned} \tag{6.30}$$

where $A_{r,ij}(t)$ are matrix elements of the reflected amplitude $\boldsymbol{A}_r(t)$ [77]. In the following, pure $\boldsymbol{\sigma}$-polarization of the incident radiation and polarization-insensitive detection will be assumed (this situation is encountered in many NRS experiments with synchrotron radiation). In this case, $\xi = +1$ and

$$I(t) = |A_{r,\sigma\sigma}(t)|^2 + |A_{r,\sigma\pi}(t)|^2 \tag{6.31}$$

Neglecting the promptly scattered part $\delta(t)$ of the reflected intensity, this becomes

$$I(t) = \left(\left|\tilde{f}_{\sigma\sigma}(t)\right|^2 + \left|\tilde{f}_{\sigma\pi}(t)\right|^2\right) \frac{\chi'^2}{\tau_0^2} \exp\left(-\chi' \frac{t}{\tau_0}\right) \tag{6.32}$$

where $\tilde{f}_{\sigma\sigma}(t)$ and $\tilde{f}_{\sigma\pi}(t)$ are matrix elements of the Fourier transform of the scattering amplitude matrix $\tilde{\boldsymbol{f}}(t)$. The envelope of the time-dependence of the reflected intensity given in Eqn. (6.31) can be approximated as

$$I_{en}(t) = \frac{\chi'^2}{\tau_0^2} \exp\left(-(1+\chi')\frac{t}{\tau_0}\right) \tag{6.33}$$

which exhibits the so-called speed-up – an effect of coherent resonant scattering from an ensemble of nuclei – analogous to Eqn. (A.4) for the transmission geometry (see appendix A.1.1) [77].

6.3.3 Quantum beats

Consider now a sample exhibiting hyperfine splitting of the energy levels, i.e. more than one resonance line. If several energetically different transitions are excited, the decaying nuclei will re-emit photons of different energies, i.e. different frequencies. The interference of these photons causes a beating in the time-dependence of the resonantly scattered intensity $I(t)$, the so-called quantum beats. For a sample with two allowed transition, i.e. two resonance frequencies $\omega_1 > \omega_2$, the quantum beat frequency is simply the frequency difference $\Omega = \omega_1 - \omega_2$ [124]. Ferromagnetic α-^{57}Fe, however, exhibits hyperfine splitting of nuclear levels with six allowed transitions between the sublevels and is best treated in terms of the matrix formalism introduced above. Thus, in order to calculate the scattered amplitude $\boldsymbol{A}(\omega)$ according to Eqn. (6.26), the scattering amplitude matrix $\boldsymbol{f}(\omega)$ has to be determined. Recall, that

$$\boldsymbol{f}(\omega) = \frac{2\pi}{k_0^2} \sum_j \rho_j \boldsymbol{M}_j(\omega) = \frac{2\pi}{k_0^2} \sum_j \rho_j \Big(\boldsymbol{N}_j(\omega) + \boldsymbol{E}_j(\omega)\Big) \tag{6.34}$$

The electronic scattering length $\boldsymbol{E}(\omega)$ is relevant only for the promptly electronically scattered radiation. Therefore, only the nuclear resonant contribution $\boldsymbol{N}(\omega)$ will be considered here. Let $\boldsymbol{m}$ be the unit vector of the magnetic quantization axis given by the internal magnetic hyperfine field. Further, let $\boldsymbol{\sigma}$, $\boldsymbol{\pi}$ be the polarization basis vectors of the incident radiation (as for synchrotron radiation). Then the matrix elements of the nuclear resonant contribution $\boldsymbol{N}(\omega)$ to the scattering length $\boldsymbol{M}(\omega)$ are

$$
\begin{aligned}
N_{\sigma\sigma} &= \frac{3}{16\pi}\left[F_{+1} + F_{-1} + (\boldsymbol{\pi}\cdot\boldsymbol{m})^2(2F_0 - F_{+1} - F_{-1})\right] \\
N_{\sigma\pi} &= \frac{3}{16\pi}\left[-\mathrm{i}(\boldsymbol{k}_0\cdot\boldsymbol{m})(F_{+1} - F_{-1}) - (\boldsymbol{\sigma}\cdot\boldsymbol{m})(\boldsymbol{\pi}\cdot\boldsymbol{m})(2F_0 - F_{+1} - F_{-1})\right] \\
N_{\pi\sigma} &= \frac{3}{16\pi}\left[\mathrm{i}(\boldsymbol{k}_0\cdot\boldsymbol{m})(F_{+1} - F_{-1}) - (\boldsymbol{\sigma}\cdot\boldsymbol{m})(\boldsymbol{\pi}\cdot\boldsymbol{m})(2F_0 - F_{+1} - F_{-1})\right] \\
N_{\pi\pi} &= \frac{3}{16\pi}\left[F_{+1} + F_{-1} + (\boldsymbol{\sigma}\cdot\boldsymbol{m})^2(2F_0 - F_{+1} - F_{-1})\right]
\end{aligned}
\tag{6.35}
$$

The nuclear resonant scattering strengths F_M express the contributions of individual transitions to the nuclear resonant scattering length $\boldsymbol{N}(\omega)$, depending on the respective magnetic quantum number change $M = m_e - m_g$ for a given nuclear transition. Summing over all ground state magnetic quantum numbers m_g, the resonant scattering strength $F_M(\omega)$ of transitions with the magnetic quantum number change M is

$$
F_M(\omega) \propto \sum_{m_g} \frac{C^2(I_g 1 I_e; m_g M)}{\hbar(\omega - \omega_{m_g M}) + \mathrm{i}\Gamma_0/2} \tag{6.36}
$$

where $C^2(I_g 1 I_{e;m_g M})$ are the Clebsch-Gordan coefficients in the notation by Rose [77, 127]. The absolute squares of the resonant scattering strengths for ^{57}Fe with a magnetic hyperfine field strength of $B_{hf} = 33.3$T are shown in Fig. 6.17.

Note the crucial role of the magnetic quantization axis in Eqn. (6.35): Its orientation $\boldsymbol{m}$ with respect to the directions of the incident wave, $\boldsymbol{k}_0$, and of the polarization axes, $\boldsymbol{\sigma}$ and $\boldsymbol{\pi}$, controls which transitions contribute to the resonant scattering process. In turn, the frequencies of the re-emitted photons and thereby the pattern of quantum beats are determined on the contributing transitions. The shape imposed on the time spectrum by the quantum beats depends so sensitively on the excited transitions, that it can be used as a “magnetic fingerprint” of the magnetic state of the sample. Fig. 6.18 shows how quantum beats modulate the time spectra for different exemplary orientations $\boldsymbol{m}$ of the magnetic quantization axis.

The speed-up and so-called dynamical beats – an effect of the frequency-dependence of the group-velocity (see appendix A.1.2) – occur in addition to quantum beats. The graph for case A in Fig. 6.18 shows a natural decay

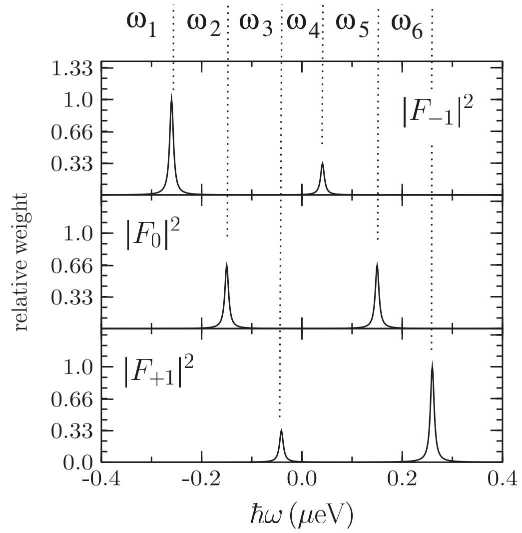

Figure 6.17: The absolute squares of the nuclear resonant scattering strengths $|F_M(\omega)|^2$ for ^{57}Fe with a magnetic hyperfine field strength of $B_{hf} = 33.3$T. ω_j denote the respective resonance frequencies.

	Geometry	Nuclear Scattering Length $\mathbf{N}(\omega)$	Time spectrum $\sigma \to$ unpolarized
A	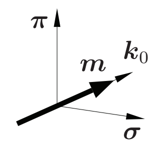	$\frac{3}{16\pi}\begin{pmatrix} F_{+1}+F_{-1} & -\mathrm{i}(F_{+1}-F_{-1}) \\ \mathrm{i}(F_{+1}-F_{-1}) & F_{+1}+F_{-1} \end{pmatrix}$	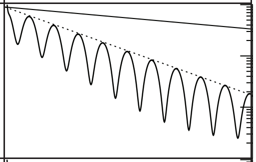
B	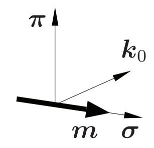	$\frac{3}{16\pi}\begin{pmatrix} F_{+1}+F_{-1} & 0 \\ 0 & 2F_0 \end{pmatrix}$	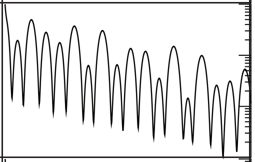
C	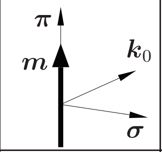	$\frac{3}{16\pi}\begin{pmatrix} 2F_0 & 0 \\ 0 & F_{+1}+F_{-1} \end{pmatrix}$	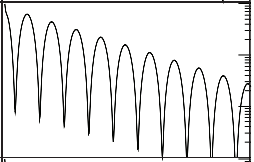
D	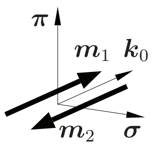	$\frac{3}{16\pi}\begin{pmatrix} F_{+1}+F_{-1} & 0 \\ 0 & F_{+1}+F_{-1} \end{pmatrix}$	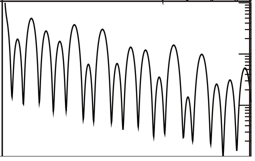

Figure 6.18: Quantum beats: Time spectra in case of magnetic hyperfine splitting, calculated for different orientations $\boldsymbol{m}$ of the magnetic quantization axis with respect to the direction $\boldsymbol{k}_0$ of the incident wave. The sample is a ferromagnetic α-^{57}Fe film of 2 nm thickness on a W substrate. The incident radiation is fully polarized along the $\boldsymbol{\sigma}$-direction and the detection is polarization-insensitive. Adapted from [77].

without speed-up or beating pattern (indicated by straight solid line), a decay with speed-up but without beating pattern (straight dashed line), and a decay with speed-up and quantum beats (solid curve). Simultaneously occurring quantum beats and dynamical beats are shown in Fig. 6.19 in exemplary calculated time spectra for α-^{57}Fe foils.

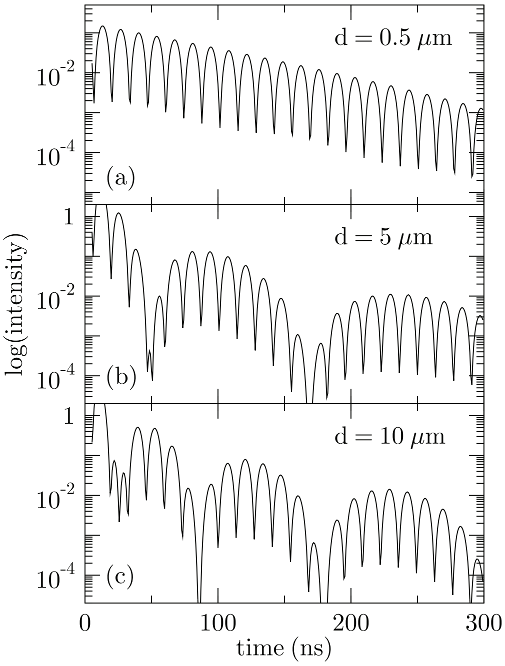

Figure 6.19: Dynamical beats and quantum beats: Time spectra calculated for α-^{57}Fe foils of different thicknesses with $\boldsymbol{m} \parallel \boldsymbol{k}_0$. With increasing sample thickness from top to bottom the apparent period of dynamical beats decreases. From [77].

The theory of nuclear resonant scattering has been fully implemented in the CONUSS software [128], which is employed for fitting calculated nuclear resonant scattering data to experimental data and thereby retrieve the relevant parameters describing the composition and magnetic state of the sample (see appendix A.1.3).

6.3.4 Practical realization of nuclear resonant scattering of synchrotron radiation

Apart from their higher brilliance, synchrotron radiation sources differ from other sources of x-rays in two important aspects: They provide polarization and a pulsed time structure of the emitted radiation (see chapter 4). A well defined polarization is necessary for investigating the orientation of magnetic hyperfine fields, i.e. magnetic quantization axes: The nuclear scattering strength depends sensitively on the relative orientations of the magnetic quantization axis, the incident wave vector $\boldsymbol{k}_i$, and its polarization vectors $\boldsymbol{\sigma}$ and $\boldsymbol{\pi}$ (in the case of synchrotron radiation), resulting in the characteristic shapes of time spectra shown in Fig. 6.18. Only a pulsed time structure of emitted radiation allows for the recording of time spectra at all: After each radiation pulse, which excites the nuclear resonant scatterers in the sample, there is a time window with no incident photon. Within this time window, only photons re-emitted upon the decay of the excited states (so-called delayed photons) are detected. With the next radiation pulse, the nuclear resonant scatterers are excited again. A time spectrum is accumulated over many of these excitation-decay cycles, until a sufficient statistical significance of the data is achieved. Obviously, the time separation of radiation pulses must be larger than the lifetime of the excited states of the material under investigation. This means to fill a storage ring with less bunches than there are available buckets, which requires a well-thought-out filling scheme. So-called spurious bunches in between the intended bunches can occur if this filling scheme is not met exactly. These spurious bunches critically disturb time-resolved NRS experiments by causing additional radiation pulses arriving in the time window assigned to recording delayed photons only.

Not only the shape, but also the integrated intensity of a time spectrum is characteristic of the magnetic state of a sample. Instead of recording a series of time spectra, the change in integrated intensity can be monitored while varying a parameter such as the strength or orientation of an external magnetic field. Fig. 6.20 shows, how the integrated intensity and the shape of time spectra change, when the orientation of the sample magnetization with respect to the incident wave vector is rotated in-plane.

One significant advantage of NRS is the fact that the scattering process is not only element- but isotope-selective. This can be exploited by placing Mössbauer isotopes at the sites of interest within the sample system, e.g. single ^{57}Fe probe layers in different depths in a Fe/Cr multilayer system. Furthermore, the isotope-selectivity results in background-free measurements,

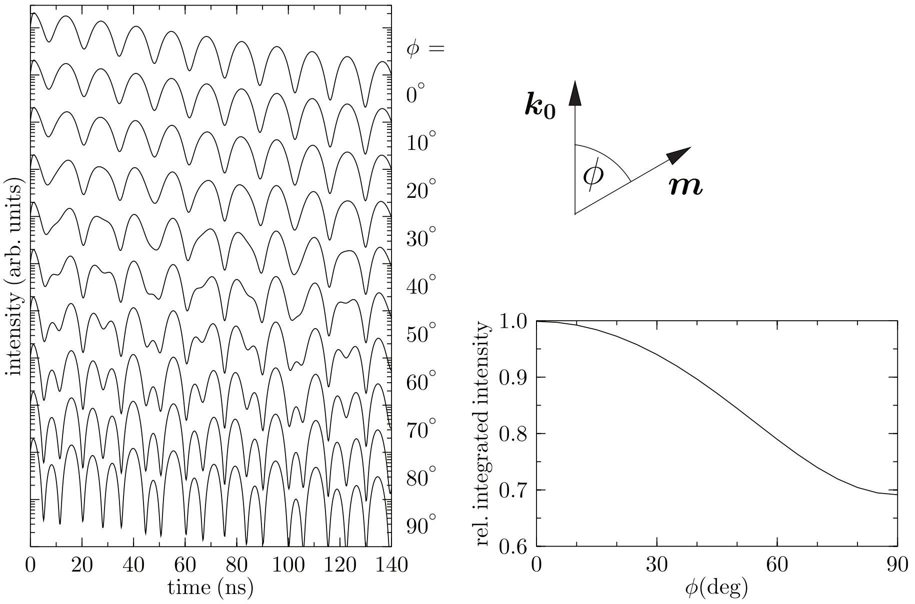

Figure 6.20: Calculated time spectra (left) and integrated intensities (right) for a magnetic film with the in-plane magnetization being rotated from $\boldsymbol{m} \parallel \boldsymbol{k}_0$ to $\boldsymbol{m} \perp \boldsymbol{k}_0$. From [77].

since exclusively the Mössbauer isotopes contribute to the nuclear resonant scattering.

NRS experiments pose some specific requirements concerning the components of a beamline. Detectors capable of counting single photons with sub-ns time resolution are necessary, since the lifetimes of most excited states in nuclear resonant materials are in the range of $\tau_0 = 10^0 \ldots\ 10^2$ ns. Avalanche photodiodes (APDs) have proved to be very well suited as detectors in nuclear resonant scattering experiments using synchrotron radiation (see for example the review article by Baron [129]). For these specialized detectors and electronics to work reliably, the non-resonant intensity has to be strongly reduced, which requires sophisticated monochromator setups with sub-meV energy resolution. Reviews on such devices were given for example by Toellner [130] and Shvyd'ko [131].

Fig. 6.21 shows the main elements of a beamline dedicated to nuclear resonant scattering at a third-generation synchrotron radiation source: The monochromator setup consisting of a high heat load monochromator and a high resolution monochromator reduces the energetic bandwidth of the radiation in two steps. The high-resolution monochromator has a low angular acceptance. Therefore, collimating lenses are placed in front of this

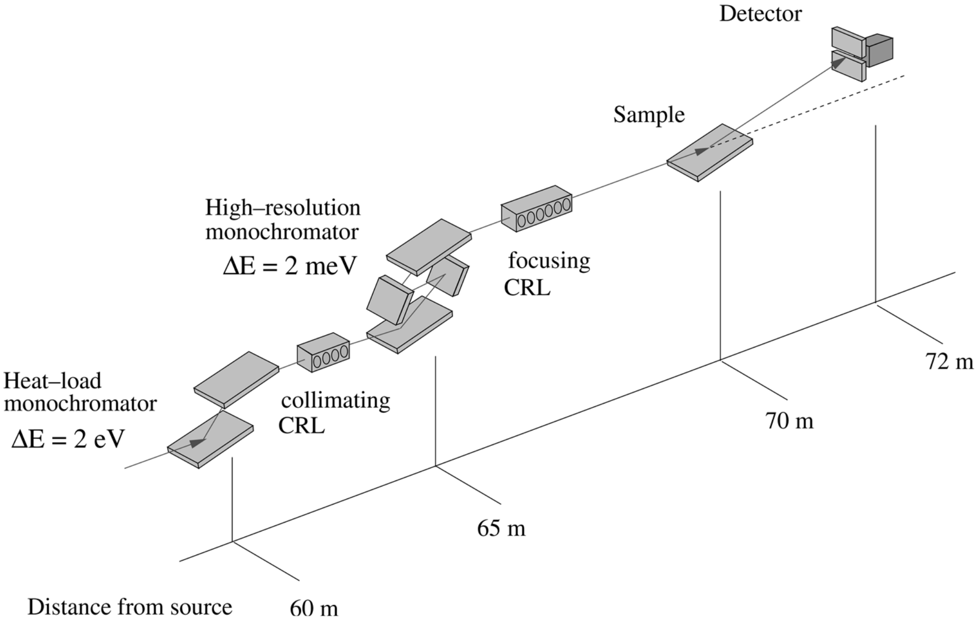

Figure 6.21: Scheme of a beamline dedicated to nuclear resonant scattering. From [77].

monochromator in order to increase the flux transmitted by it. Focusing optical elements such as lenses or Kirkpatrick-Baez mirrors are used to adjust the beam cross-section at the sample position.

Part III

Results

7 Nanofaceted α-Al_2O_3

Substrates of nanofaceted α-Al_2O_3 are at the basis of most of the samples investigated in this work. They serve directly and indirectly for the preparation of highly ordered metallic nanostructures: On the one hand, metals can be sputter deposited onto faceted α-Al_2O_3 under acute angles with respect to the macroscopic substrate surface, so that either parallel metal nanostripes will form due to shadowing by the facets or continuous metal films of periodically varying thickness are prepared (see chapter 8). On the other hand, the surface topography of faceted α-Al_2O_3 substrates provides a preferential direction for the self-assembly of diblock copolymer films (see section 9.2), which in turn are used as chemically highly-ordered templates for metal deposition (see chapter 10). The spontaneous faceting of M-plane α-Al_2O_3 is a self-assembly process, which is enabled by thermal annealing at high temperatures in air. Through a sequence of structural transformations (see section 1.2.3), the initially flat M-plane surface reconstructs into facets of $\{1\bar{1}02\}$ R-plane and $\{10\bar{1}1\}$ S-plane surfaces. These are of sufficiently similar orientation as the M-plane, but of significantly lower surface energy density than the M-plane: While the surface free energy density of the M-plane is $f_M^s = 6.87$ J/m^2, the R-plane and S-plane have free surface energy densities of $f_R^s = 2.57$ J/m^2 and $f_S^s = 3.27$ J/m^2, respectively [132]. The average orientation of the faceted surface remains the orientation of the initial M-plane surface (see section 1.2.1). The facet edges are all parallel to the $[11\bar{2}0]$ direction in the substrate crystal. The R- and S-plane enclose angles of $\phi_R = 32.4°$ and $\phi_S = 17.6°$, respectively, with the M-plane [23, 24].

In this chapter, investigations of the facet formation on α-Al_2O_3 M-plane surfaces by ex-situ AFM and in-situ GISAXS are described. The surface-topographical properties of α-Al_2O_3 substrates annealed at varied temperatures and for different durations are presented.

7.1 Facet formation

Spontaneous surface reconstruction and faceting is observed in a material-specific interval of temperatures: At temperatures below this interval, the respective surface remains metastable. A certain temperature has to be reached in order to overcome diffusion and nucleation barriers. Within the temperature interval, faceting occurs and the facet size increases to reduce the contributions of facet edges to the total free energy of the crystal. At temperatures above, the anisotropy of surface free energy densities is reduced by temperature-dependent contributions and a planar surface is formed [16]. Heffelfinger and Carter proposed that a flat M-plane surface of α-Al_2O_3 reconstructs into a faceted low-energy surface via five stages (see section 1.2.3) [28]:

- Surface smoothing
- Formation and growth of individual facets
- Formation of facet groups
- Coalescence of facet groups
- Facet coarsening

The faceting begins via heterogeneous nucleation, i.e. isolated facets form a specific sites and coexist with planar surface regions [16, 28].

7.1.1 Ex-situ AFM

Atomic force microscopy (NT-MDT Solver Next SPM with HA_NC Etalon probes) was used routinely to image the surface topography of α-Al_2O_3 substrates after annealing in a chamber furnace (Borel MO-1800) and thus assess their suitability for the fabrication of laterally ordered diblock copolymer templates and metal nanostructures. Topographies were found corresponding to all five stages of surface reconstruction identified by Heffelfinger and Carter [28]. After short annealing at 1400 °C for 2 hours one sample exhibited the first four stages of reconstruction in different surface regions. For comparison, the surface topography of an α-Al_2O_3 substrate was measured before annealing. Few scratches probably caused by the polishing process were spotted; the rms roughness was 0.11 nm.

The annealed sample features one region in which the surface is planar with a rms roughness of 0.14 nm (stage 1 – surface smoothing). In comparing the rms roughnesses of a substrate before and a substrate after annealing no surface smoothing is observed. However, the initial roughness of these M-plane α-Al_2O_3 substrates achieved by polishing is already one order of magnitude lower than the initial roughness of the substrates investigated by Heffelfinger and Carter [28].

In another region, the same annealed substrate exhibits individual facets on an otherwise planar surface, separated by distances of several μm (stage 2 – formation and growth of individual facets, see Fig. 7.1). The profile scan through the center of one facet shows the pronounced surface distortions next to the facet (compare to Fig. 1.5 [28]). These distortions serve as preferred nucleation sites for successional facets, some of which can be discerned in Fig. 7.1(a), center and bottom left. Since successional facets are likely to nucleate in the wake of existing facets, groups of parallel facets form (stage 3 – formation of facet groups, see Fig. 7.2(a)). These groups extend by facet nucleation and by growth in length, until they hit on other facets or facet groups (stage 4 – coalescence of facet groups, see Fig. 7.2(b)). Facet junctions are formed, because the facet edges of two different facet groups are in general not aligned with each other.

Upon extended annealing or at higher temperatures, facets are expected to grow in height and width at the expense of other facets (stage 5 – facet coarsening). This can be accomplished by motion and merging of facet junctions - which would also reduce the number of facet junctions [28]. Among the samples prepared for this work, the number of facet junctions was in general, but not always, found to decrease significantly with increasing annealing duration: Four α-Al_2O_3 substrates annealed at 1400°C are compared in Fig. 7.3; two of them were annealed simultaneously for 2 h, two were annealed simultaneously for 48 h. The number of facet junctions differs strongly in the two samples annealed for 2 h; it is very low in one, and very high in the other. In the samples annealed for 48 h it is intermediate or low, respectively. Properties of the initial M-plane surface which influence the facet nucleation, such as stress or defects, may strongly influence the number of facet junctions observed after a given annealing duration. It is apparent however, that the facets have increased in size after longer annealing: After 2 h of annealing, the facets are of average height $h \approx 6$ nm and $h \approx 10$ nm, respectively, and of period $L \approx 125$ nm and $L \approx 100$ nm, respectively. After 48 h of annealing these values are $h \approx 30$ nm and $h \approx 35$ nm, respectively, and $L \approx 170$ nm and $L \approx 210$ nm, respectively. The aspect ratio L/h of the facets has thus decreased by a factor of 2 to 3.5 upon extended annealing.

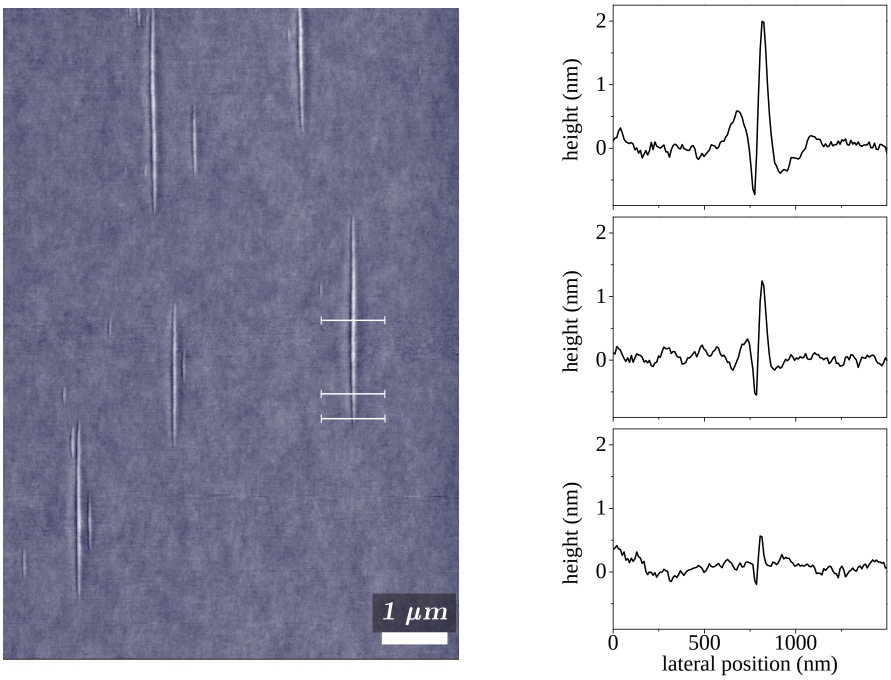

Figure 7.1: Individual facets on a α-Al_2O_3 surface in stage 2 of reconstruction. Profile sections through a facet as indicated by white lines.

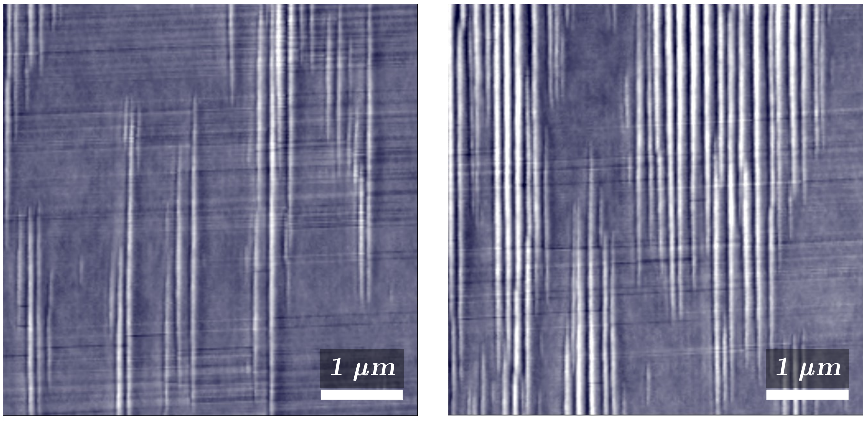

(a)

(b)

Figure 7.2: (a) Groups of facets on a α-Al_2O_3 surface in stage 3 of reconstruction. (b) Coalescence of facet groups on a α-Al_2O_3 surface in stage 4 of reconstruction. Horizontal lines are artifacts of the measurement.

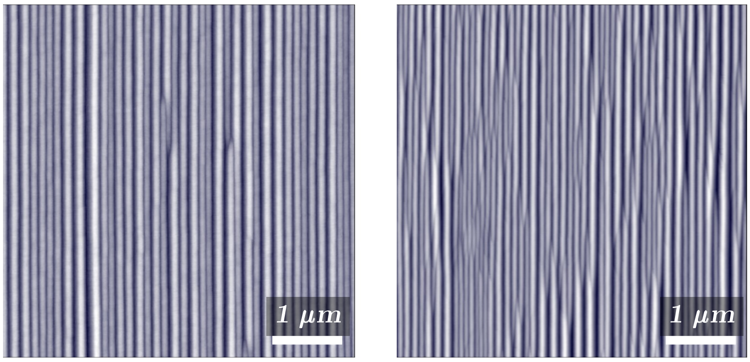

(a) 2 h at 1400 °C (b) 2 h at 1400 °C

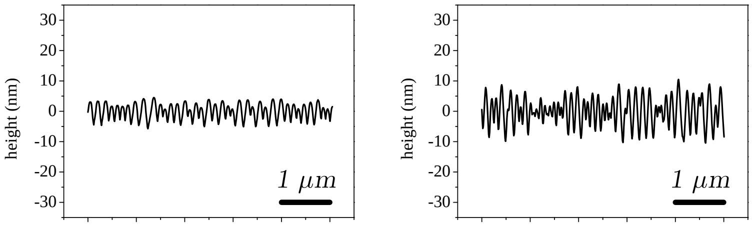

(c) section through (a) (d) section through (b)

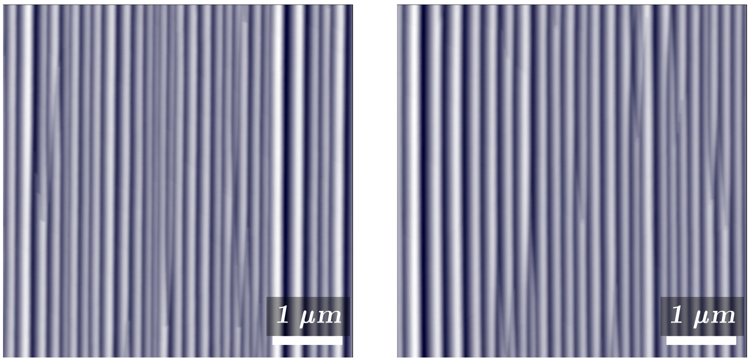

(e) 48 h at 1400 °C (f) 48 h at 1400 °C

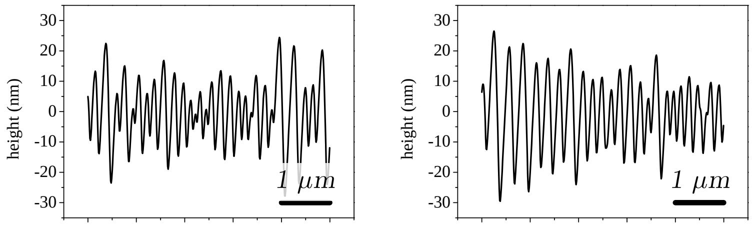

(g) section through (e) (h) section through (f)

Figure 7.3: Comparison of facet sizes for α-Al_2O_3 substrates in stage 5 of reconstruction, annealed at 1400 °C for 2 h and for 48 h, respectively.

7.1.2 In-situ GISAXS during annealing

While real-space information on the local surface structure is obtained by AFM, GISAXS yields averaged structural information about the entire sample illuminated by the incident X-ray beam. And while AFM is restricted to ex-situ measurements of the topographies resulting from high temperature annealing, GISAXS allows for in-situ observation of the facet formation.

An in-situ GISAXS experiment during high-temperature annealing of α-Al_2O_3 was set up at the beam-line BW4 at the DORIS III synchrotron radiation source in the following way (see also Fig. 7.4): The end caps were removed from the working tube of a horizontal tube furnace (Carbolite STF 16/180). This furnace was mounted on a tilt stage at the beam-line such that the x-ray beam passes through its working tube and the scattering pattern can be recorded with an area detector. Evacuated flight tubes with capton entrance and exit windows were employed to reduce background intensity from scattering at air molecules. The capton windows of the flight tubes were protected against the heat at the furnace tube openings by Mylar foils covered with aluminum tape. A custom-made alumina sample holder was used to position the sample in the center of the working tube and align the sample edges with respect to the azimuthal direction of the incident beam.

A polished M-plane α-Al_2O_3 wafer of 12 mm × 12 mm was placed on the sample holder and oriented so that the facet edges would be formed parallel to the incoming x-ray beam. The sample was aligned in the cold furnace, then it was heated at a rate of 420 K/h up to a temperature of 1325 °C and annealed at this temperature for 12 h. The sample was realigned frequently – especially during heating – to compensate for changes in the sample position or orientation due to thermal expansion of sample holder and working tube. The x-ray wavelength was $\lambda = 0.138$ nm, the distance between sample and detector (MAR SX-165 at 80 μm pixel size) was 1840 mm, and the incidence angle was $\alpha_i \approx (0.5 \pm 0.025)$ ° (variation due to thermal expansion of sample holder and working tube and limited time for realignment between two measurements). These parameters were chosen so as to cover a large angular range and provide high angular resolution. GISAXS patterns were taken approximately every 5 min during heating and approximately every 30 min during annealing at constant temperature. Fig. 7.5 points out the relevant features of these GISAXS patterns. A sequence of selected GISAXS patterns from this experiment is shown in Figs. 7.6 and 7.7 – the captions state the time elapsed since heating was started and the current tempera-

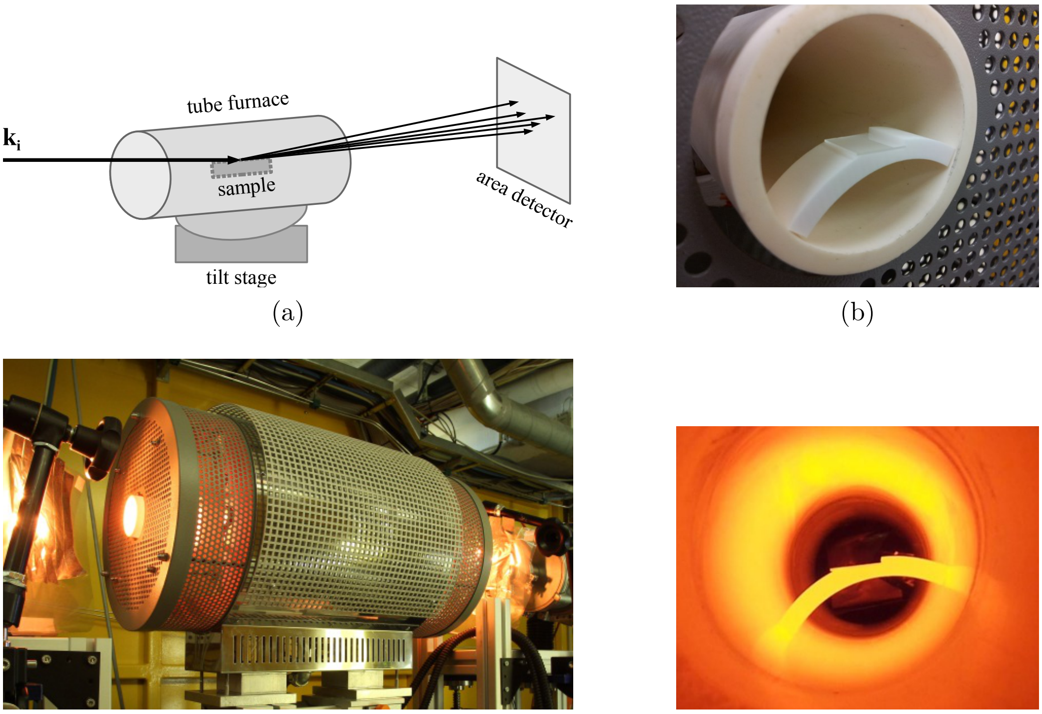

(a) (b) (c) (d)

Figure 7.4: (a, c) Sketch of the in-situ GISAXS setup at beam-line BW4 (DORIS III) and photograph of the mounted furnace with incident beam coming from the left. (b, d) Custom-made sample holder with sample at the working tube entrance, and view into the furnace during annealing; sample holder with sample in the center.

ture. The annealing temperature of 1325°C is reached after 195 min. The intense specular reflection is blocked out in some patterns in order to protect the detector. While the surface faceting process progresses, the specular reflection decreases in intensity as more and more of the incident radiation is scattered into the off-specular scattering rods. The beam-stop can therefore be removed in later stages of the faceting process.

The sequence of recorded patterns Figs. 7.6, 7.7 shows two kinds of off-specular scattering rods: vertical and tilted ones. The vertical scattering rods run parallel to the specular scattering rod and result from a laterally periodic surface structure of the sample (see Fig. 7.5(a)). They are most prominent in the early stage of the experiment, during heating and in the first hour of annealing. Additional tilted off-specular scattering rods (see Fig. 7.5(b)) then become more and more dominant. These result from the tilted facet surfaces into which the initial planar sample surface reconstructs at high temperatures - they are in fact specular scattering rods for the respective tilted facet surfaces [133].

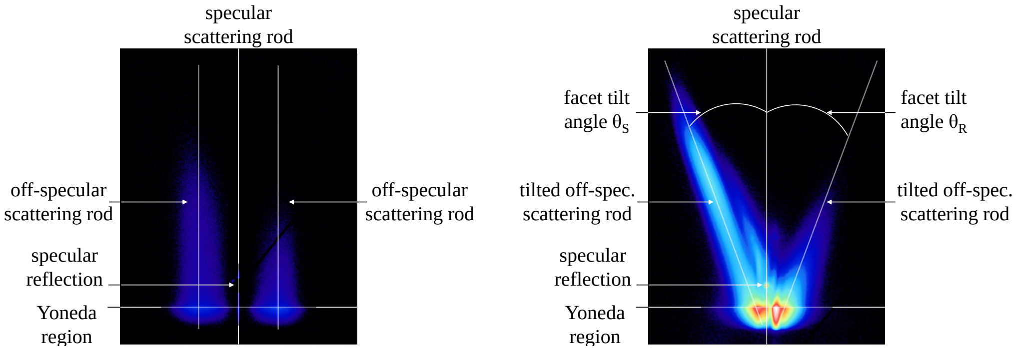

(a) (b)

Figure 7.5: Exemplary GISAXS patterns of α-Al$_2$O$_3$ during facet formation, featuring prominent (a) vertical off-specular scattering rods and (b) tilted off-specular scattering rods. In (a), the specular reflection is blocked out by a beamstop.

The GISAXS patterns are discussed with respect to characteristic aspects of these two kinds of off-specular scattering rods:
1) The angular positions of vertical off-specular scattering rods are identified by intensity maxima in horizontal line sections through the Yoneda region ($\alpha_f = \alpha_c$). Fig. 7.9 shows these sections from GISAXS patterns in Fig. 7.6. The value $2\pi/q_y$ derived from the angular positions of the intensity maxima in Fig. 7.9 according to Eq. (6.5) corresponds to a lateral periodicity in the surface structure of the sample.
2) The angles which the tilted off-specular scattering rods enclose with the specular scattering plane ($q_y = 0$) correspond to the angles which the surface normals of the facet faces enclose with the initial surface normal of the sample. The development of these angles during annealing is depicted in Fig. 7.10. The horizontal dashed lines indicate the equilibrium facet tilt angles $\phi_R = 32.4°$ and $\phi_S = 17.6°$, respectively.

As can be seen in Fig. 7.6 and 7.9, first broad vertical off-specular scattering rods at $|q_y| \approx 0.4$ nm^{-1} are observed after 160 min, at a temperature of 1070 °C[1]. They become more intense and shift toward lower $|q_y|$-values. After 185 min, at 1235 °C, the vertical off-specular scattering rods have become asymmetric, with a maximum at $|q_y| \approx 0.16$ nm^{-1} and a shoulder at $|q_y| \approx 0.32$ nm^{-1} each. Then the peaks become dominant and the shoulders vanish within about 10 minutes. The vertical off-specular scattering

---

[1] Three of these in-situ annealing experiments were conducted. Surface restructuring began at $T \approx 800$ °C, $T \approx 1000$ °C, and $T \approx 1070$ °C, respectively. This variation is attributed to unavoidable variations in the initial properties of the surfaces of the α-Al$_2$O$_3$ crystal wafers, resulting e.g. from growth, cutting, polishing, etc. A maximum miscut of 0.5° is specified by the manufacturer.

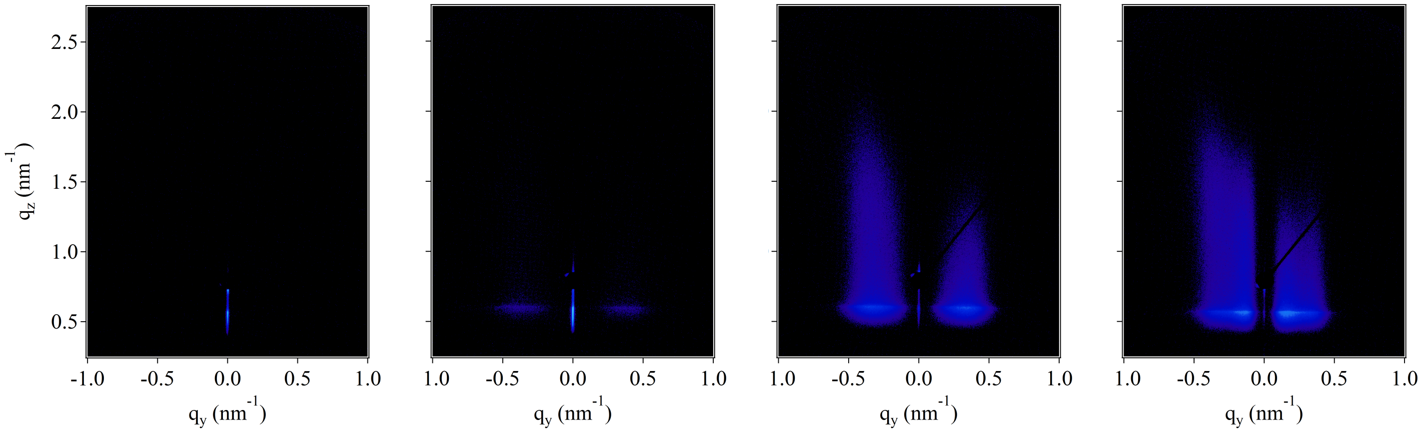

(a) 0 min, RT

(b) 160 min, 1070 °C

(c) 170 min, 1135 °C

(d) 185 min, 1235 °C

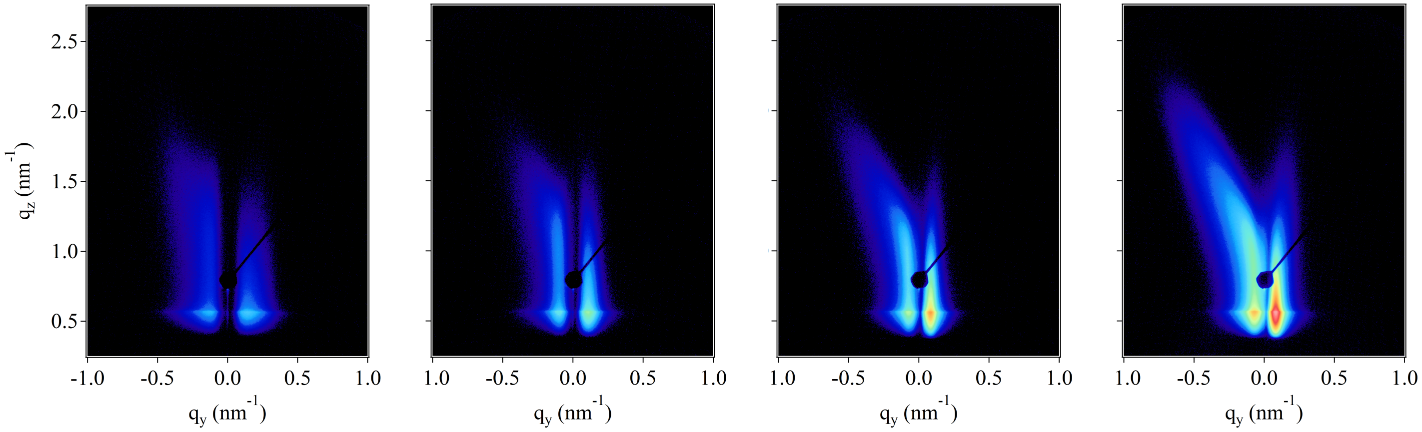

(e) 190 min, 1290 °C

(f) 200 min, 1325 °C

(g) 250 min, 1325 °C

(h) 290 min, 1325 °C

Figure 7.6: Sequence of GISAXS patterns recorded in-situ during heating and annealing an α-Al_2O_3 wafer; beam-line BW4 (DORIS III).

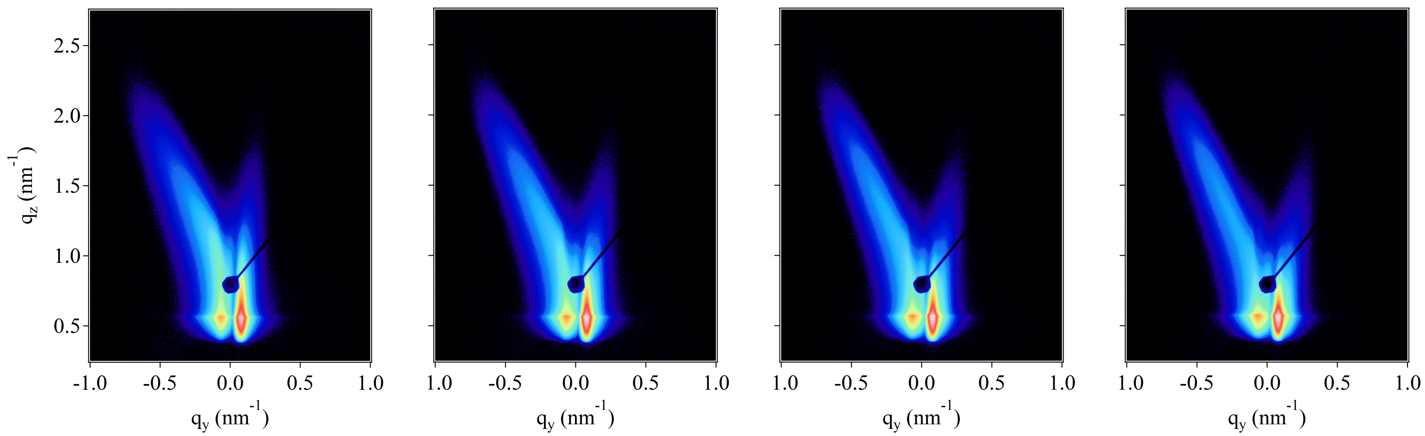

(a) 330 min, 1325 °C (b) 380 min, 1325 °C (c) 440 min, 1325 °C (d) 490 min, 1325 °C

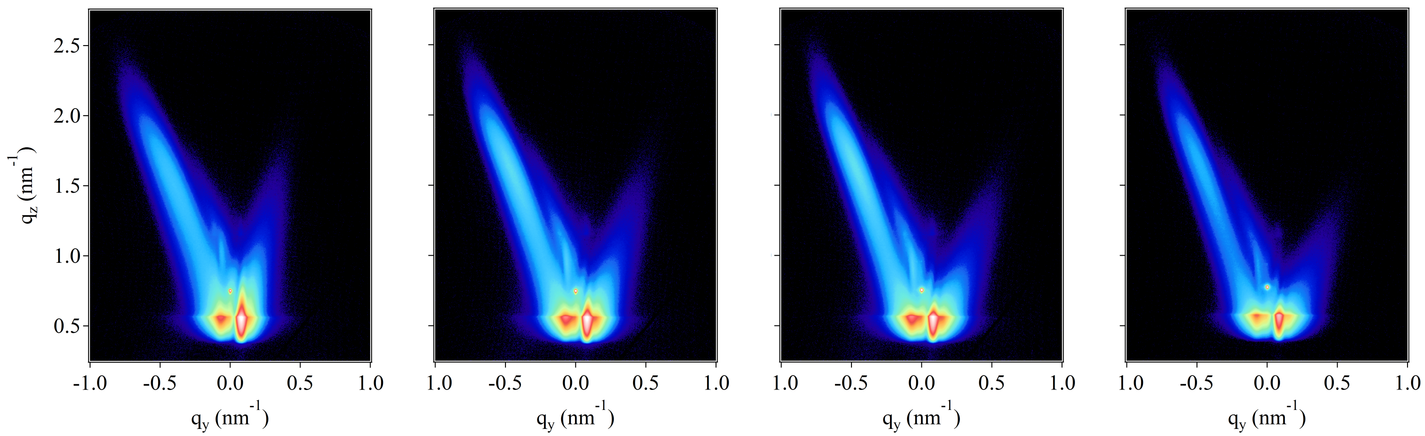

(e) 655 min, 1325 °C (f) 805 min, 1325 °C (g) 925 min, 1325 °C (h) 965 min, 810 °C

Figure 7.7: Sequence of GISAXS patterns recorded in-situ during annealing an α-Al_2O_3 wafer; beam-line BW4 (DORIS III).

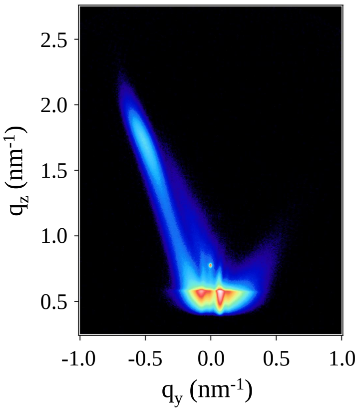

Figure 7.8: GISAXS pattern of a faceted α-Al_2O_3 surface with equilibrium facet angles, after 23 h of annealing at 1420 °C; beam-line BW4 (DORIS III).

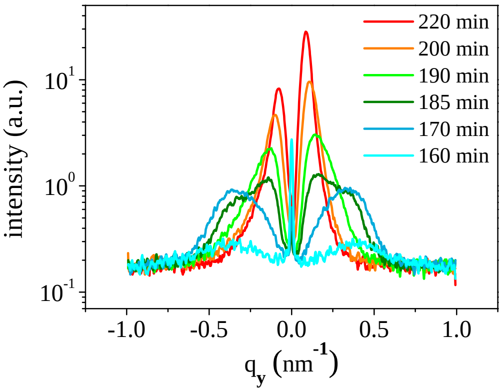

Figure 7.9: Horizontal sections through Yoneda regions in GISAXS patterns recorded during heating and annealing. Labels state the time elapsed since heating was started. The annealing temperature of 1325°C is reached after 195 min.

rods shift further toward lower $|q_y|$-values until the annealing temperature of 1325°C is reached, then remain at a constant value of $|q_y| \approx 0.095$ during annealing. Via $d = 2\pi/q$, this development corresponds to a laterally periodic surface structure becoming observable at a period of ≈ 20 nm and then increasing to a period of ≈ 80 nm (see Fig. 7.10(top)).

When interpreting the positions of the vertical off-specular scattering rods as being directly correlated to the facet period by $2\pi/q_y = L$, the observed increase in lateral period is understood as the coarsening, i.e. widening, of surface facets during annealing as proposed by Heffelfinger [28]. Indeed, an AFM surface topography measurement on the annealed sample after the in-situ GISAXS experiment showed the average facet period (i.e. width) to be $L \approx (80 \pm 10)$ nm (see Fig. 7.12), which agrees very well with the lateral period derived from the positions of the vertical off-specular scattering rods at the end of the annealing procedure.

Moreover, GISAXS provides a direct measure of the angles which the facet

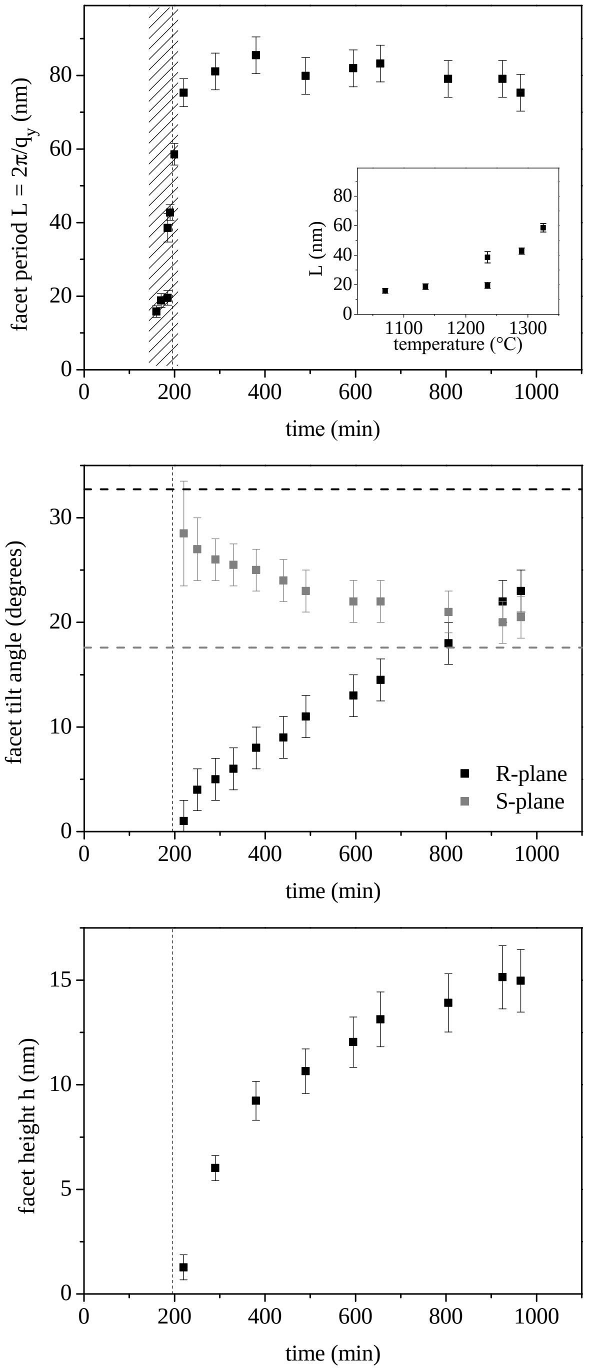

Figure 7.10: (top) Development of the facet period $L = 2\pi/q_y$ derived from the positions of the off-specular maxima in Fig. 7.9. The inset shows the values within the shaded region (heating phase) in dependence of the momentary temperature. (middle) The development of facet tilt angles ϕ_R and ϕ_S – extracted from GISAXS patterns in Figs. 7.6 and 7.7 – for the S-plane and the R-plane facet faces during annealing at 1325 °C. Horizontal dashed lines indicate the equilibrium values for ϕ_R and ϕ_S. (bottom) The development of the facet height h during annealing at 1325 °C, calculated from the facet period L and the facet tilt angles ϕ_R, ϕ_S. The vertical dashed lines indicate, when the annealing temperature is reached.

surfaces enclose with the initial M-plane substrate surface. As explained in section 6.2.1, these angles are immediately given by the angles enclosed between the corresponding tilted off-specular scattering rods and the vertical specular scattering plane ($q_y = 0$). In this experiment, the R-plane facet surfaces develop on the right side, the S-plane face surfaces on the left side (as “seen” by the incoming x-ray beam). Thus, in the GISAXS patterns the tilt angle of the right-hand off-specular scattering rod corresponds to the tilt angle of the R-plane facet surfaces, and the tilt angle of the left-hand off-specular scattering rod corresponds to the tilt angle of the S-plane facet surfaces. A clearly tilted left-hand off-specular scattering rod (≈ 27 °) can be discerned already very early in the annealing process, while the right-hand off-specular scattering rod yet shows only a very small tilting of approximately 4° (see Fig. 7.6(g)).

In the course of the annealing procedure, the tilt angle of the left-hand off-specular scattering rod decreases continuously, while that of the right-hand off-specular scattering rod is increasing at roughly twice the rate (see Fig. 7.10(middle)). After approximately 850 min the two tilt angles are equal, then continue to approach their respective equilibrium value. The GISAXS pattern of a sample annealed at 1420 °C for 23 h (see Fig. 7.8) shows off-specular scattering rods tilted at the equilibrium angles. Thus, in the beginning of facet formation, the facet profile is clearly asymmetric with the S-plane facet tilt angle being significantly larger than the R-plane facet tilt angle. The facet profile then becomes symmetric with equal tilt angles for both facet surfaces, before it finally assumes its asymmetric shape with the R-plane tilt angle $\phi_R = 32.4°$ and the S-plane tilt angle $\phi_S = 17.6°$.

In the annealing phase the facet period L has already reached its final value, the facet tilt angles are approaching the respective equilibrium value – thus the facets grow in height. The facet height h can be calculated from the facet period L and the facet tilt angles ϕ_R and ϕ_S via the trigonometric relation

$$h = L\frac{\sin(\phi_R)\sin(\phi_S)}{\sin(\phi_L)} \tag{7.1}$$

where $\phi_L = 180 - \phi_R - \phi_S$. The development of the facet height during annealing at 1325 °C is plotted in Fig. 7.10(bottom). The derived value of $h \approx 15$ nm for the facet height reached at the end of the experiment is in good agreement with the average facet height of $h \approx 12$ nm measured by AFM after the in-situ experiment. The development of the average structural dimensions of the facets as inferred from the in-situ GISAXS data is schematically sketched in Fig. 7.11 (dimensions are not to scale).

By in-situ GISAXS it was possible to observe the reconstruction of a planar M-plane α-Al_2O_3 surface into a faceted R-plane / S-plane surface during high temperature annealing. In-situ GISAXS proved to be especially useful in the early phase of facet formation: Surface facets with approximately 80 nm width but less than 1 nm height would not be readily detected by AFM. Moreover, since in-situ GISAXS provides averaged information over a much larger surface area than the usual scan range of an AFM, it is advantageous when studying sparsely distributed surface structures such as the individual facets or small facet groups in the first stages of surface reconstruction.

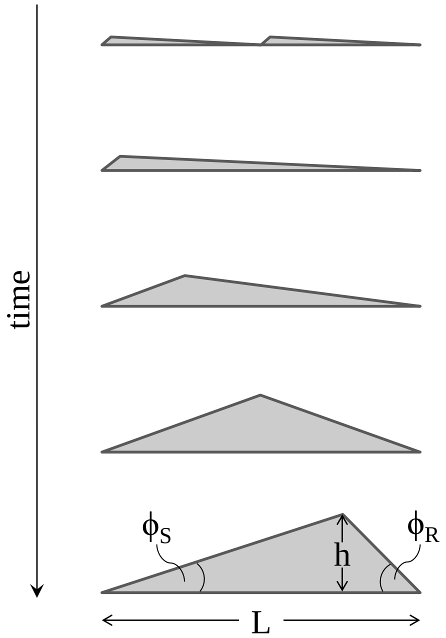

Figure 7.11

A few characteristic features of the scattering pattern, i.e. the q_y-positions of vertical off-specular scattering rods, combined with the angles enclosed by tilted off-specular scattering rods and the specular scattering rod, are sufficient to derive the relevant average structural dimensions of the facets, i.e. facet period, facet tilt angles, and facet height.

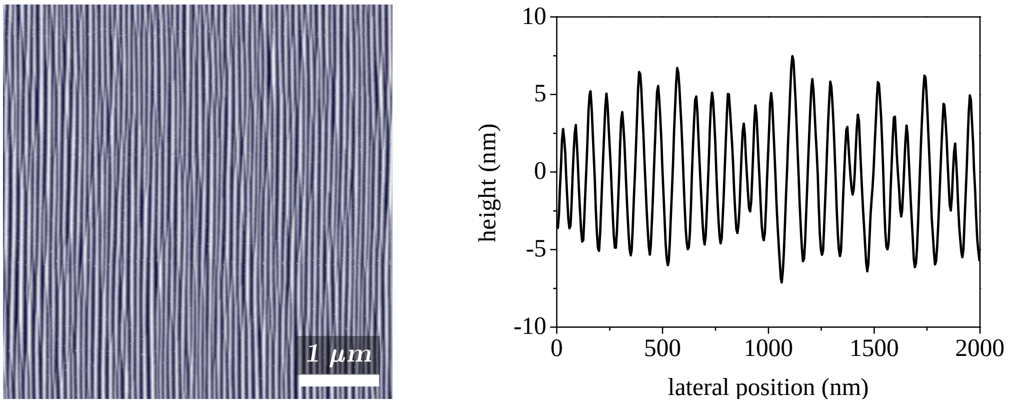

(a) (b)

Figure 7.12: AFM micrographs of the faceted sample surface after annealing: (a) area scan (b) section through (a) perpendicular to the facet edges.

7.2 Surface topographies of annealed α-Al_2O_3

Faceted α-Al_2O_3 substrates are intended for further use in the fabrication of metal nanostructure patterns. To make the entire fabrication procedure as effective as possible, it is desirable to know the correlations between the annealing conditions for α-Al_2O_3 substrates and the resulting geometric properties (height, width, tilt angles) of the surface facets. As opposed to the in-situ study on the process of α-Al_2O_3 facet formation during annealing described above, it is not feasible to conduct systematic studies on the influence of specific annealing conditions using in-situ GISAXS at a synchrotron radiation source. A large number of samples is required for such a study to find the relevant process parameters and their respective relevant ranges and to the able to identify actual correlations and outliers. Therefore, the influence of annealing parameters on the resulting topographical properties of nanofaceted α-Al_2O_3 was studied by ex-situ AFM on samples annealed in a chamber furnace in air.

A series of α-Al_2O_3 substrates (series 1) was annealed at four different temperatures from 1350 °C to 1600 °C for five different durations from 4 h to 48 h. Another series of α-Al_2O_3 substrates (series 2) was annealed at eight different temperatures from 1325 °C to 1600 °C for 8 h to 10 h. The resulting surface topographies were imaged by AFM and the extracted geometrical properties are shown in dependence of the annealing conditions in Figs. 7.13 (series 1) and 7.14 (series 2). Symbols mark the average values, error bars indicate the respective standard deviations. Horizontal dashed lines indicate the equilibrium values for the facet tilt angles. For clarity, a few obvious outliers have been omitted in Fig. 7.13(a, b).

In series 1, the correlations between the facet tilt angles ϕ_S, ϕ_R and the annealing conditions (see Fig. 7.13(a, b)) are in agreement with the findings from in-situ GISAXS: For samples annealed at 1350 °C and 1400 °C, the decrease in ϕ_S and the increase in ϕ_R toward the respective equilibrium values are observed. The equilibrium value of $\phi_S = 17.6°$ is reached first. For samples annealed at 1500 °C and 1600 °C, the higher temperatures accelerate the mass transport significantly. Thus, the equilibrium values have already been reached within less than 4 h and the facet tilt angles remain constant throughout the investigated interval of annealing durations.

The equilibrium facet tilt angles are determined by the crystal structure of α-Al_2O_3: they are given by the angles enclosed between the M$\{10\bar{1}0\}$-plane and the R$\{1\bar{1}02\}$-plane and S$\{10\bar{1}1\}$-plane, respectively. The development of

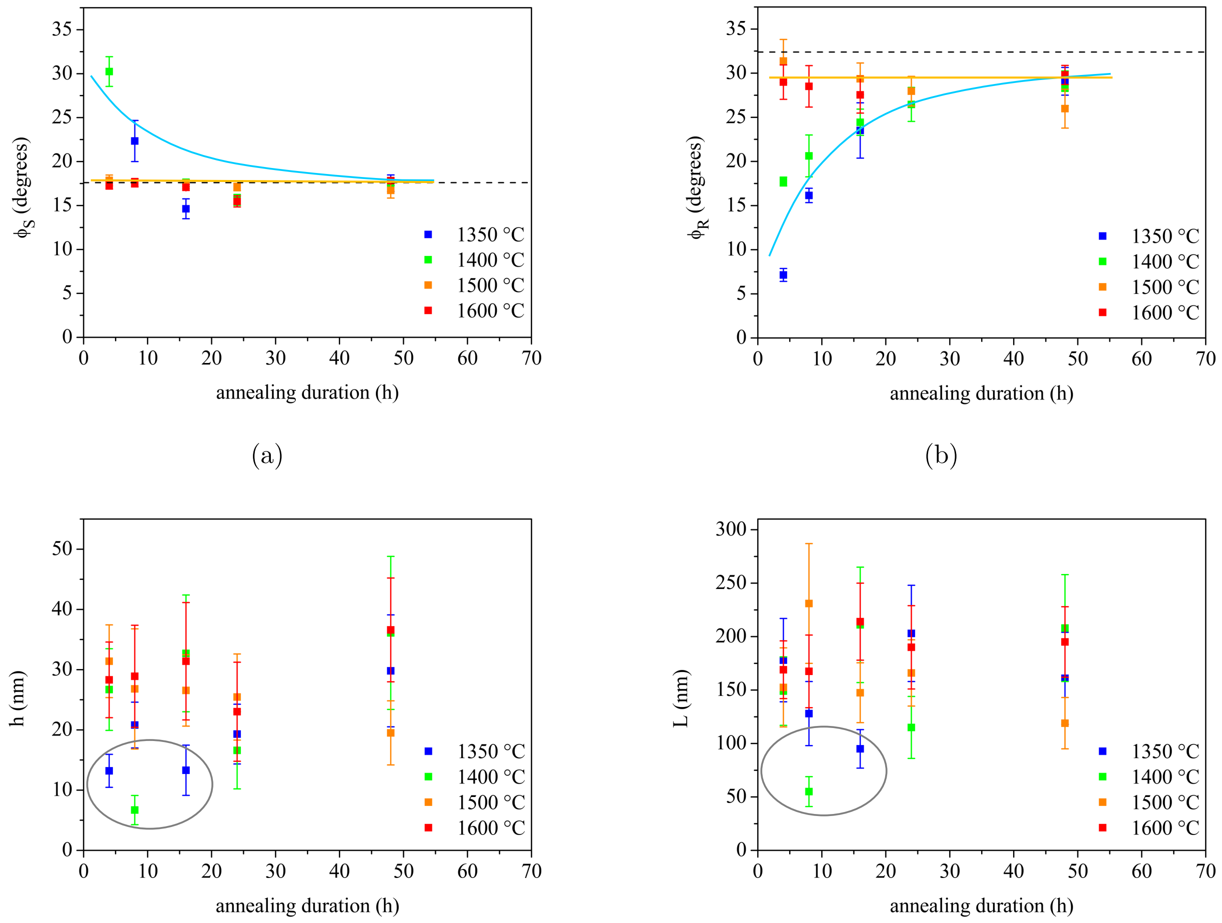

(a) (b)

(c) (d)

Figure 7.13: Geometric properties (a) facet tilt angle ϕ_S, (b) facet tilt angle ϕ_R, (c) facet height h, and (d) facet period L of α-Al_2O_3 surface facets in dependence of annealing temperature and duration. Symbols mark the average values, error bars indicate the respective standard deviations. Horizontal dashed lines indicate the equilibrium values for the facet tilt angles. Solid lines are guides to the eye. Circled values are suitable geometric properties of α-Al_2O_3 facets for preparing diblock copolymer templates.

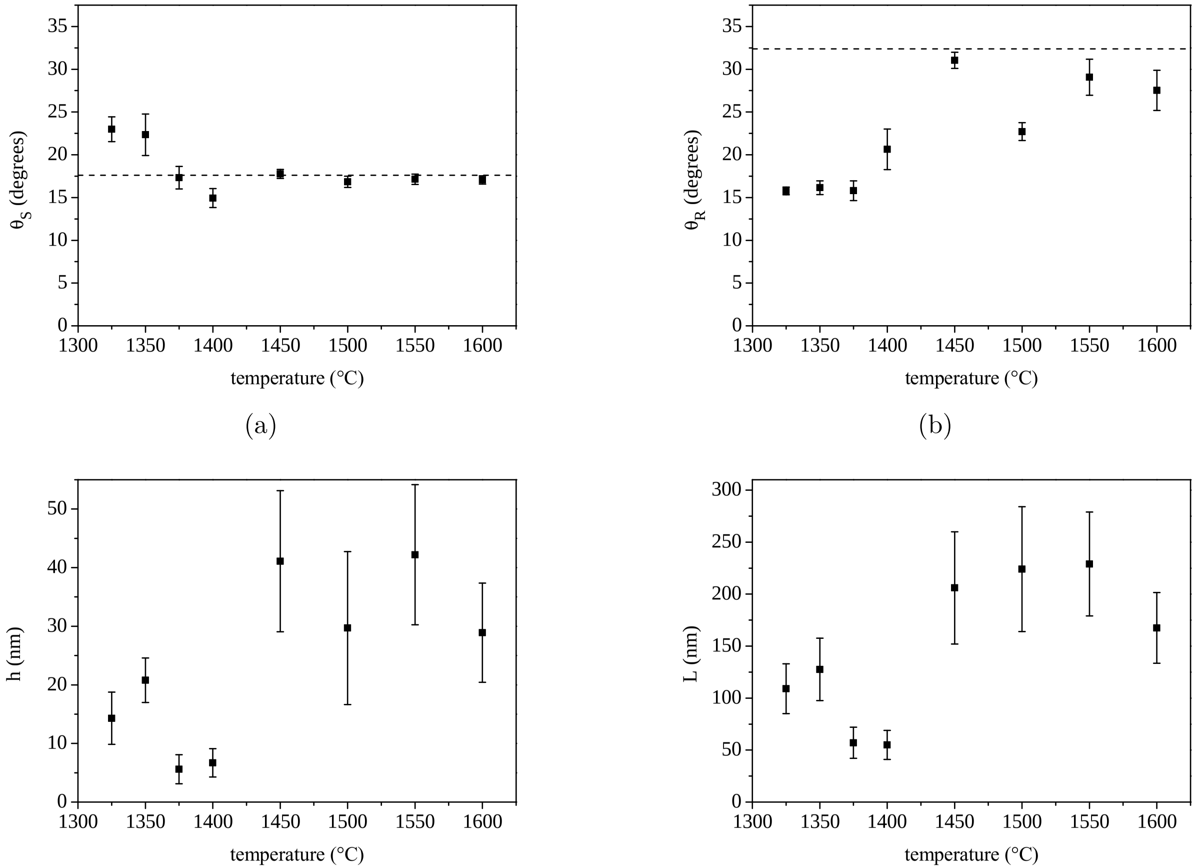

(a)

(b)

(c)

(d)

Figure 7.14: Geometric properties (a) facet tilt angle ϕ_S, (b) facet tilt angle ϕ_R, (c) facet height h, and (d) facet period L of α-Al_2O_3 surface facets in dependence of annealing temperature for an annealing duration of 8 h to 10 h. Symbols mark the average values, error bars indicate the respective standard deviations. Horizontal dashed lines indicate the equilibrium values for the facet tilt angles.

the facet tilt angles during annealing and their equilibrium values can therefore be expected to be robustly reproducible. The facet tilt angles relate the facet height to the facet period. The equilibrium facet period, however, depends sensitively on factors such as elastic properties and surface stress (see Eqns. (1.5) and (1.6)). It is beyond the scope of this study to clarify, which kinds and amounts of adhesives, impurities, surface inhomogeneities, or strains resulting from growing, cutting, polishing, and handling the α-Al_2O_3 substrates are present and to which extent they influence the outcome of the surface faceting process. Therefore, an unambiguous systematic dependence of facet period and height on the annealing conditions is hard to make out in this series.

Huth and coworkers found the average facet period to be $L \approx 350 \ldots 420$ nm and the aspect ratio of height and width to be $h/L \approx 1/8$ [24]. However, they did not specify the annealing conditions for their samples. The facet periods L in series 1 are considerably smaller, spanning a range of ≈ 50 nm to ≈ 225 nm. The aspect ratio h/L was found to range from 1/10 to 1/5, which is in agreement with the findings of Huth and coworkers. Gabai and coworkers annealed M-plane α-Al_2O_3 at 1500 °C for 20 h to 48 h [23]. They present a faceted surface with facet period $L \approx 40$ nm and height $h \approx 8$ nm, and state that they found facet periods of up to $L \approx 400$ nm for higher annealing temperatures. They claim that the facet period and height depend on the annealing conditions, but do also not describe these correlations further.

For preparing diblock copolymer templates on faceted α-Al_2O_3 (see section 9.2) facets with height $h \approx 5 \ldots 15$ nm and period $L \approx 40 \ldots 80$ nm are required to match the diblock copolymer film thickness d and equilibrium domain period D_0. In this series, such facet dimensions were only obtained for annealing durations from 4 h to 16 h at temperatures of 1350 °C or 1400 °C (see Fig. 7.13(c, d)).

In series 2, all samples were annealed for approximately the same duration (8 to 10 h), but in those annealed at higher temperatures the faceting process has progressed further during this time. Again, the decrease in ϕ_S and the increase in ϕ_R toward the respective equilibrium facet tilt angles are observed, in this case as a function of increasing annealing temperature (see Fig. 7.14(a, b)). There is a clear distinction between samples annealed at temperatures below 1425 °C and samples annealed at temperatures above. Samples annealed at lower temperatures exhibit facet tilt angles comparatively farther away from the respective equilibrium value and have smaller facets in both height and period. Samples annealed at temperatures above 1425 °C have facet tilt angles at the equilibrium value $\phi_S = 17.4°$ and close to the equilibrium value $\phi_R = 32.4°$. Their facets are on average about three times higher and wider than those of samples annealed below 1425 °C (see Fig. 7.14(c, d)). Independently of the annealing conditions, the average standard deviation in facet height is $\sigma_h \approx 0.3h$, and the average standard deviation in facet period is $\sigma_L \approx 0.25L$. Thus the correlation length ζ according to Eq.(1.7) normalized to the facet period L shows no correlation to the annealing conditions. Larger facet dimensions appear to coincide with equilibrium facet tilt angles. This agrees with the finding from series 1, where facets with height $h \approx 5 \ldots 10$ nm and period $L \approx 40 \ldots 80$ nm were only observed in samples annealed at lower temperatures for short durations, i.e. which had not reached the equilibrium facet tilt angles. In most cases, the facets with larger height and period are also longer – and thus have a lower density of facet junctions – than the smaller facets. For larger facets, maximum facet lengths of approximately 20 μm were observed, while smaller facets had a length up to approximately 5 μm.

In summary: The facet tilt angles are rather precisely adjustable via annealing temperature and / or duration. The facet period (and thus the facet height), however, appears to be only roughly determinable by choosing non-equilibrated surfaces (which have not yet reached the equilibrium orientation with $\phi_R = 32.4°$ and $\phi_S = 17.4°$) for smaller facets and equilibrated surfaces for larger facets.

8 Metal Nanostructures on Nanofaceted α-Al_2O_3 Substrates

8.1 Self-assembled metal nanostructures on faceted surfaces

One major focus of this work is the in-situ characterization of nanostructures during growth, which is made possible by employing self-assembly processes for nanostructure fabrication. Thus, all nanostructured samples discussed in this chapter were prepared in a transportable UHV sputter deposition chamber specifically designed for in-situ characterization (see section 5.5) so that their properties could be studied in dependence of their stage of growth by synchrotron-based x-ray scattering techniques.

8.1.1 Preparation by deposition under non-normal incidence

The periodically faceted α-Al_2O_3 surfaces described in chapter 7 are versatile substrates for nanopatterning and fabricating ordered nanostructures by metal deposition under non-normal incidence [24, 68, 134]. The microstructure of stripes or films grown with this method is described in section 3.4.1.

The orientation of the sputtering source is defined by one azimuthal (in-plane) angle and one polar (out-of-plane) angle. There are different variants of this preparation approach, but for all of them the in-plane angle is perpendicular to the orientation of the substrate facets. Thus, one surface of every facet is facing the sputtering source, the other one is avert from it. Depending on the polar angle ω, one of two mechanisms can be exploited:

- shadowing effects: self-shadowing and partial shadowing by adjacent facets
- different deposition rates on facet surfaces facing the sputtering source or being avert from it.

If the polar angle ω is shallow, the facet surface avert from the sputtering source is completely shadowed (self-shadowing). Also a portion of the facet surface facing the source is shadowed by the adjacent facet, with the width of this portion depending on the angle ω (partial shadowing by adjacent facets). This results in separated stripes of the sputtered material with adjustable width (see Fig. 8.1(a)). Stripe patterns consisting of two different materials can be prepared by sputtering from two opposite sides.

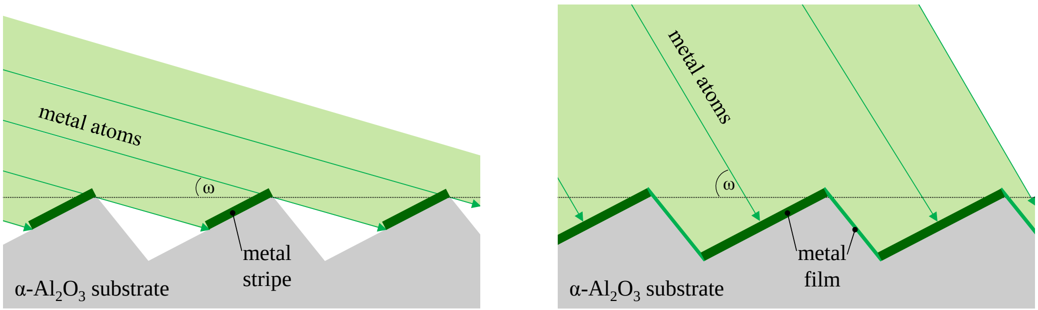

(a) Separated stripes – side view

(b) Nanopatterned film – side view

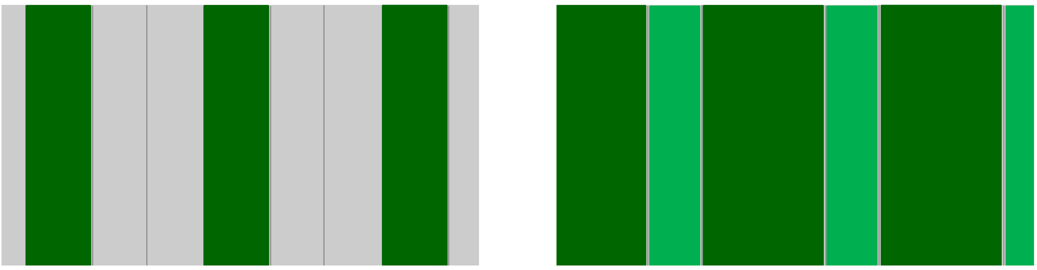

(c) Separated stripes – top view

(d) Nanopatterned film – top view

Figure 8.1: Fabrication of metal nanostructures on faceted α-Al_2O_3 substrates by sputter deposition under non-normal incidence. The directional distribution of the sputtered metal atoms is reduced by means of a slit mask, as indicated in (a).

The width of the deposited stripes can be determined geometrically. In Fig. 8.2, ω is the deposition angle, ϕ is the tilt angle of the facet surface facing the sputtering source, L is the facet period, and b is the width of the deposited stripe.

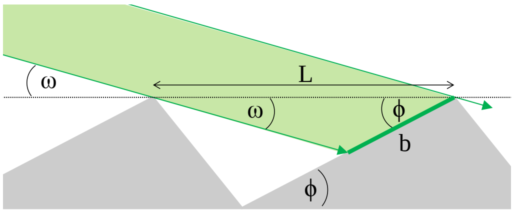

Figure 8.2

According to the law of sines

$$b = L\frac{\sin(\omega)}{\sin(180^\circ - \omega - \phi)} \quad (8.1)$$

A horizontal slit mask positioned between sputtering source and substrate has a collimating effect: only sputtered atoms on trajectories with directions within approximately about ±9 degrees around the nominal sputtering direction given by the polar angle ω can pass the mask and reach the substrate[1]. For the typical working gas pressure in the range of $p_{Ar} \sim 10^{-3}$ mbar the mean free path length is several cm (see section 5.4.2). Since the distance between the mask and the substrate in the employed deposition chamber is of the same order of magnitude as the mean free path length, an increase of the directional distribution by collisions between sputtered atoms and working gas atoms can be neglected.

Increasing the angle ω to exceed the tilt angle of the facet surfaces avert from the sputtering source leads to deposition on both surfaces of the facets, but with different deposition rates (see Fig. 8.1(b)). The result is a continuous film consisting of alternating stripe-like regions of different thickness. The thickness of the deposited material on both surfaces of the facets can be inferred from GISAXS patterns via simulations.

Isolated nanostripes have been prepared from Au and Cu. While the Cu nanostripes were heat treated to produce Cu nanospheres, the Au nanostripes may be interesting for applications making use of surface plasmon resonances [135]. These samples are presented in appendix A.2.1.

A continuous film of ^{57}Fe on faceted α-Al_2O_3 has been utilized as a sample to demonstrate the feasibility of Grazing Incidence Nuclear Small Angle X-ray Scattering (GINSAXS). This experiment is discussed in section 8.2. Results of some earlier studies on the growth mechanism, the evolution of the magnetic state during growth, and the magnetic anisotropy of Fe thin films were reviewed in section 3.4. This brief review is mainly restricted to the case of Fe film growth on oxide substrates at room temperature, as these were the conditions in the GINSAXS experiment, too.

---

[1] The value for the directional distribution of sputtered atoms, which reach the substrate through the mask, is geometrically determined: While the sputter target has a diameter of 25.4 mm, the slit mask has a vertical aperture of 5 mm and is positioned in a distance of 45 mm from the sputtering source.

8.2 Growth and magnetism of a ^{57}Fe thin film on faceted α-Al$_2$O$_3$: Merging GISAXS and NRS

The possibility of preparing a uniaxially corrugated iron film by a simple deposition routine has been demonstrated before (see e.g. [68]). The experiment described here utilizes such a sample with periodically varying film thickness to introduce in-situ Grazing Incidence *Nuclear* Small Angle X-ray Scattering (GINSAXS). This method combines the spatial resolution in the nm range provided by GISAXS with the sensitivity of NRS to the magnetic properties of a sample.

8.2.1 The GINSAXS principle

In a nuclear resonant sample exposed to a photon pulse both electronic and nuclear scattering of photons take place. Generally, the same form factor and structure factor determining the $\boldsymbol{q}$-space distribution of non-resonantly, electronically scattered intensity in grazing incidence geometry (see section 6.2.2) are also determining the $\boldsymbol{q}$-space distribution of the resonantly scattered intensity. Thus, scattering of photons from a nuclear resonant sample in grazing incidence geometry produces a scattering pattern with two contributions: The electronic part reflecting the structural properties of the sample and the nuclear resonant part additionally containing information on the magnetic state of the sample with spatial resolution. This is exploited in Grazing Incidence Nuclear Small Angle X-ray Scattering (GINSAXS): Due to the sample structure, the nuclear resonant signals from different structural units of the sample are scattered to different positions in $\boldsymbol{q}$-space. This allows the nuclear resonant signals containing information on the magnetic properties of these different structural units to be recorded independently. Information on the sample structure itself is more readily obtained from the more intense electronic scattering signal, which can be recorded using an area detector. Thus magnetic properties and dynamics inferred from the NRS time spectra can be related to the sample structure. This is possible also during in-situ experiments, e.g. for different stages of sample growth.

For a ^{57}Fe film on a faceted α-Al$_2$O$_3$ substrate, the scattering pattern features characteristic tilted scattering rods (as observed in the in-situ GISAXS investigation of α-Al$_2$O$_3$ surface facet formation; see section 7.1.2): If the facet edges are aligned parallel to the incoming x-ray beam, the faceted surface leads to x-rays impinging on the left (right) facet surfaces to be scattered to a tilted scattering rod in the left (right) half of the scattering pattern at $q_y < 0$ ($q_y > 0$). This holds not only for photons scattered by electrons, but also for photons scattered resonantly by the nuclei in the ^{57}Fe layer deposited on the faceted substrate. Thus, the nuclear resonant signal detected in the left (right) tilted scattering rod is related to the magnetic state of the ^{57}Fe film regions on the left (right) facet surfaces. For the ^{57}Fe film on faceted sapphire, the different thicknesses of the ^{57}Fe film on the left and right facet surfaces lead to intensity modulations on the tilted scattering rods with different periods – corresponding to the respective thickness. Thus, in an in-situ experiment it is not only possible to relate the nuclear resonant signals to scatterers on either surface of the facets, but also to connect them with the respective material thickness during film growth.

8.2.2 Experimental setup and procedure

The experiment was realized in the following way: The in-situ sputter deposition chamber (see section 5.5) was set up at the beamline ID18 at the synchrotron radiation source ESRF. The x-ray wavelength was 0.0861 nm, the sample-to-detector distance was 3010 mm (restricted by the length of the experimental hutch), and an evacuated flight tube was employed to reduce scattering in air. A MAR345 image plate (pixel size: 0.1 mm × 0.1 mm) and an APD point detector were mounted on a horizontal linear stage, so that either one of the detectors could be moved into the beam path to detect the scattered photons. Additionally, the APD detector could be scanned across the area covered by the image plate by means of a small y-z translational state mounted on the linear stage. The image plate was used to record the $\boldsymbol{q}$-space distribution of the scattered intensity without distinction between the resonant and the non-resonant part. The APD detector provided sub-ns time resolution and could thus distinguish between electronically and nuclear resonantly scattered photons. It was used to record nuclear resonant time spectra at specific positions within the $\boldsymbol{q}$-space distribution of the scattered intensity.

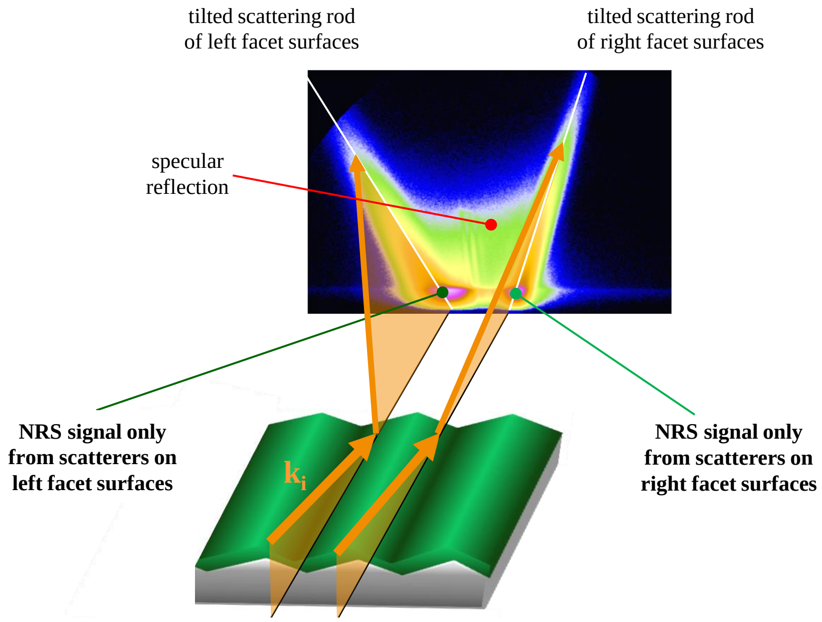

Figure 8.3: The principle of Grazing Incidence Nuclear Small Angle X-ray Scattering (GINSAXS) from a sample with faceted surface. Due to the topographical structure of the sample, all photons impinging on the film regions on the left (right) facet surfaces are – electronically or nuclear resonantly – scattered to the left (right) half of the scattering pattern. Thus, the nuclear resonant signals from film regions on the left or right facet surfaces are separated, and the NRS time spectra containing information on the magnetic properties of these different regions can be recorded independently.

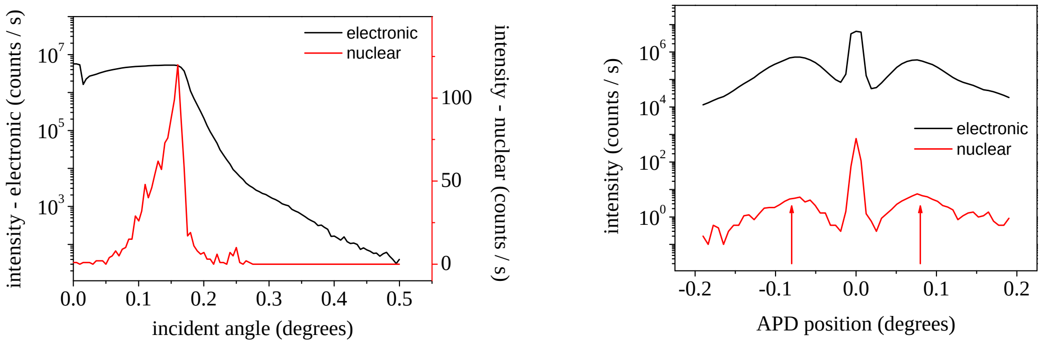

(a) (b)

Figure 8.4: (a) Nuclear and electronic reflectivity curves of ^{57}Fe on nanofaceted α-Al$_2$O$_3$ and (b) electronic and time-integrated nuclear signal during a horizontal APD scan across the GISAXS pattern at $\alpha_f = \alpha_i = \alpha_c$, recorded after 60 s of ^{57}Fe deposition. Time spectra (see Fig. 8.8) are recorded at the positions indicated by the arrows, at $\alpha_i = \alpha_c$.

The nanofaceted α-Al_2O_3 substrate was aligned with the facet edges parallel to the incoming beam. Viewing the sample along the direction of the incoming x-ray beam, the R-plane facet surfaces are on the left and the S-plane facet surfaces are on the right. Thus the scattering rod belonging to the R-plane (S-plane) facet surfaces is detected at $q_y < 0$ ($q_y > 0$). The nanofaceted α-Al_2O_3 substrate used for this experiment had facet tilt angles of $\phi_R = 30°$ and $\phi_S = 17°$, as can be readily determined by measuring the angle which the tilted scattering rods enclose with the vertical (see also section 7.1.2). The ^{57}Fe sputtering source was positioned at a polar angle of $\omega = 45°$ with respect to the macroscopic substrate surface and at an azimuthal angle of 90° with respect to the facet edges. Thus, a continuous ^{57}Fe film with alternating stripe-like regions of different thickness was prepared (see Fig. 8.1 (b)). The left facet surfaces were facing the sputtering source, so that the thicker film regions formed on the R-plane facet surfaces, the thinner film regions on the S-plane facet surfaces. The facet period is $L = (80 \pm 5)$ nm, as measured by AFM and corroborated by simulated GISAXS patterns. Via the law of sines, the widths of the R-plane and S-plane facet surfaces, $b_R \approx 32$ nm and $b_S \approx 55$ nm, are obtained. These correspond to the widths of the thick and thin ^{57}Fe regions, respectively.

The residual gas pressure in the deposition chamber was $p_0 = 2.8 \times 10^{-7}$ mbar. ^{57}Fe was deposited stepwise with the substrate at room temperature and at a power of the sputtering source of $P = 6$ W. After each deposition step, a GISAXS pattern and the nuclear resonant signals were recorded. GISAXS patterns were taken at an incident angle of $\alpha_i = 0.6°$ (exposure of $t \approx 300$ s), where the reflectivity is low enough not to damage the image plate detector. The nuclear resonant signals, however, were recorded at an incident angle of $\alpha_i = \alpha_c = 0.16°$, i.e. at the position of highest intensity in the nuclear resonant reflectivity curve (see Fig. 8.4(a)). The nuclear resonant signals comprise:

- The time-integrated nuclear resonant signal recorded during a horizontal scan of the APD across the GISAXS pattern at $\alpha_f = \alpha_i$
- A time spectrum at the specular reflection
- Time spectra at the intersections of the left and tilted scattering rod with the line of the horizontal scan

8.2.3 In-situ GINSAXS: Film growth and evolution of magnetic states observed with lateral resolution

The film thicknesses on the R-plane and S-plane facet surfaces were determined by simulating the GISAXS patterns with the program FitGISAXS [120] using the core-shell ripple form factor; more details can be found in appendix A.2.2. For the simulations, only the shell thickness of the core-shell ripple form factor (representing the respective ^{57}Fe film thickness) was varied. It is not possible to simulate a sample with independent ^{57}Fe film thicknesses on the R-plane and S-plane facet surfaces. Therefore, GISAXS patterns for $q_y < 0$ and $q_y > 0$ were simulated separately. Furthermore, the input parameter $\mathrm{t_{shell}}$ means the shell thickness measured perpendicular to the macroscopic sample surface. In order to obtain the actual film thicknesses measured normal to the tilted facet surfaces, $\mathrm{t_{shell}}$ has to be multiplied by a factor of $\cos(\phi)$, where ϕ is the respective tilt angle of the R-plane or S-plane facet surfaces with respect to the macroscopic sample surface. Fig. 8.5 shows the film thicknesses derived from simulations in dependence of the sputtering duration. It is apparent that the deposition rates on the R-plane and S-plane facet surfaces are not constant, but increase for later deposition stages. This is due to the following circumstances: No external magnetic field was applied before 120 s of deposition. Afterward, an external magnetic field was applied on several occasions to test the response of the magnetization orientation of the sample. The field strength applicable in the deposition chamber was too small to induce significant changes in the magnetization orientation. However, residual magnetization of the electromagnet pole shoes drastically influenced the plasma during deposition, causing the deposition rates to vary.

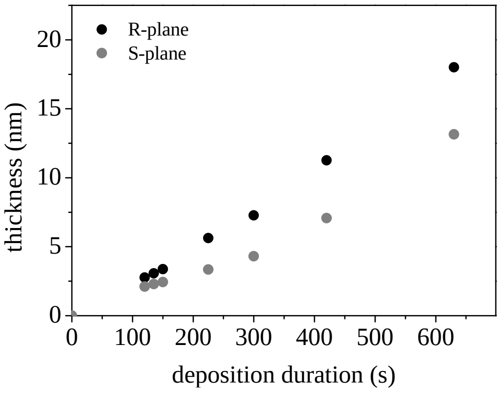

Figure 8.5: The thicknesses of the ^{57}Fe film on the R-plane and S-plane facet surfaces, respectively, in dependence of the sputtering duration. The deposition rates are not constant due to the conditions during the experiment (see main text).

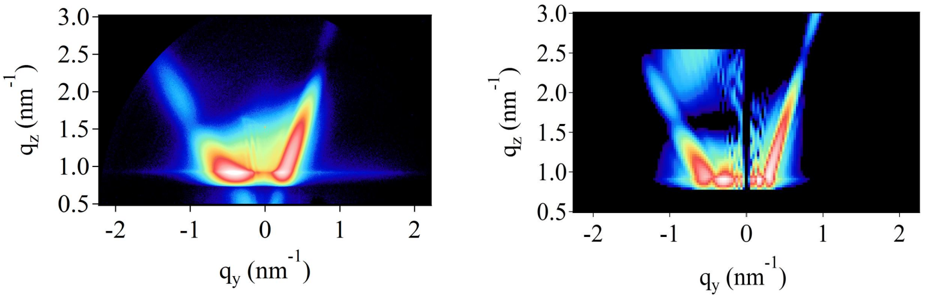

(a) GISAXS after 150 s of deposition (b) simulation

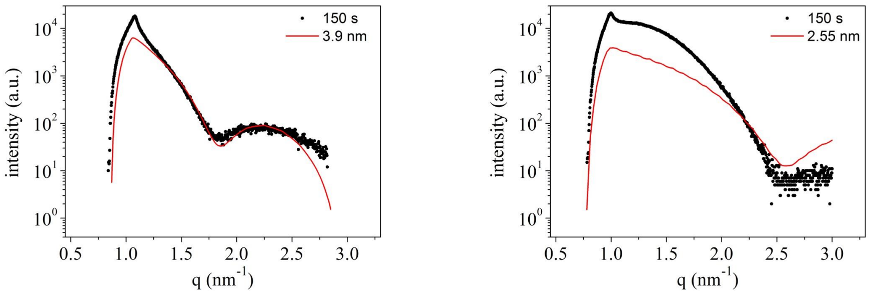

(c) at R-plane scattering rod (d) at S-plane scattering rod

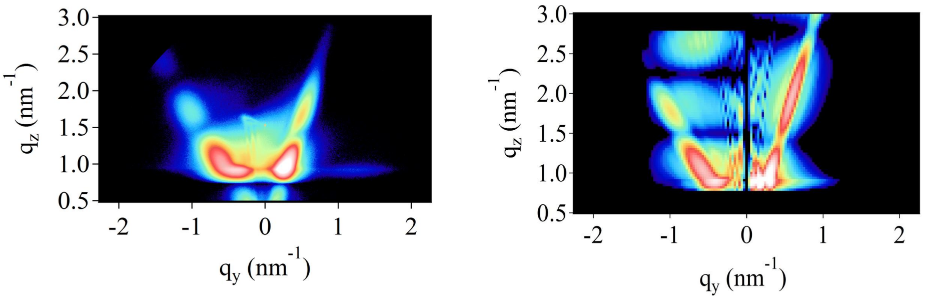

(e) GISAXS after 300 s of deposition (f) simulation

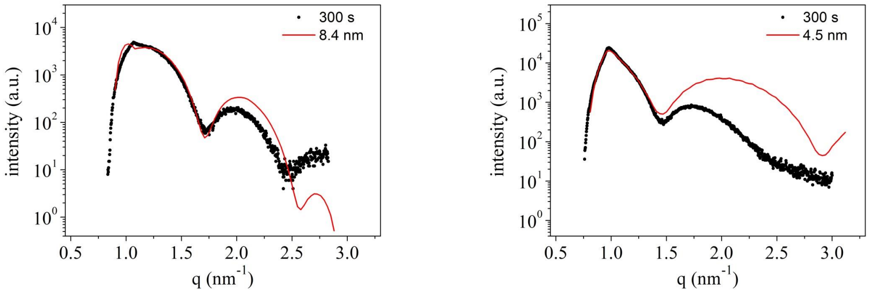

(g) at R-plane scattering rod (h) at S-plane scattering rod

Figure 8.6: Exemplary GISAXS patterns taken during deposition of the ^{57}Fe thin film on a nanofacetedα-Al_2O_3 substrate, corresponding 2D simulations performed with the program FitGISAXS [120] to determine the respective thicknesses of the ^{57}Fe film, and line cuts along the two scattering rods after 150 s of deposition (a - d) and 300 s of deposition (e - h).

Fig. 8.6 exemplarily compares measured and simulated GISAXS patterns (simulations of all measured GISAXS patterns can be found in appendix A.2.2). Regarding especially the sharpness of the intensity maxima along the two tilted scattering rods, it becomes apparent that the ^{57}Fe film thickness is less homogeneous on the S-plane facet surfaces (thin film regions) than on the R-plane facet surfaces (thick film regions). However, FitGISAXS does not offer the possibility to assume a distribution of the shell thickness, a wedge-shaped shell, a roughness at the core-shell or shell-vacuum interface, or the like in the simulation.

The limited accessible q_y- and q_z-range determined the number of detectable thickness oscillations. Therefore, film thicknesses for deposition durations less than 120 s could not be determined by simulations, but had to be extrapolated.

The ^{57}Fe growth on α-Al$_2$O$_3$ results in a polycrystalline film (see also section 3.4.1). Fig. 8.7 shows a GISAXS pattern recorded with the sample rotated by 90 degrees around the macroscopic surface normal as compared to the orientation for the GISAXS patterns plotted in Fig. 8.6, i.e. with the edges of the substrate facets being perpendicular to the direction of the incident x-ray beam. The positions of the broad off-specular intensity maxima evidence a lateral correlation length in the sample of approximately 5 nm – corresponding to the crystallite size of the ^{57}Fe film.

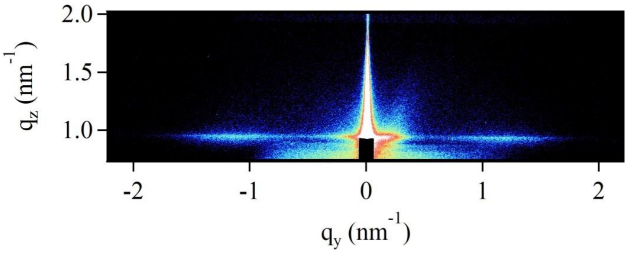

Figure 8.7: GISAXS pattern of the polycrystalline heterogeneous ^{57}Fe film on nanofaceted α-Al$_2$O$_3$ recorded with the substrate facet edges oriented parallel to direction of the incoming beam. The off-specular intensity maxima at $q_y = \pm 1.2$ nm^{-1} evidence a crystallite size of approx. 5 nm.

NRS time spectra were recorded at the specular scattering rod and at the R-plane and S-plane scattering rods after each deposition step. Simulation of these time spectra yields information on the evolution of the magnetic states of the thick and thin regions of the ^{57}Fe film, especially on the strength and orientation of the magnetic hyperfine field $\boldsymbol{B_{hf}}$. The magnetic hyperfine field is – to a very good approximation – proportional to the magnetization.

Thus, the development of the magnetization in both thin and thick film regions during film growth can be observed via the evolution of the magnetic hyperfine field extracted from the respective NRS time spectra.

The simulations of the NRS time spectra were performed with the program CONUSS [128]. As this program was designed for analyzing planar samples, the faceted morphology of the ^{57}Fe film on the α-Al$_2$O$_3$ substrate has to be accounted for when simulating the time spectra. In CONUSS, the scattering plane serves as a reference plane for the polarization vectors of the incident radiation and for the orientation of the magnetic hyperfine field. In the described experiment, there are two scattering planes, each tilted by a different angle with respect to the surface normal of the macroscopic sample surface, while the electric field vector of the incident synchrotron radiation is perpendicular to this macroscopic surface normal. Thus, the time spectra recorded at the R-plane and the S-plane scattering rod must be simulated separately, compensating for the different facet tilt angles $\phi_R = 30°$ and $\phi_S = 17°$ by adjusting the orientation of the electric field vector in the simulation appropriately (the sample orientation is fixed with respect to an external frame of reference). Two sublattices (SL1, SL2) of ^{57}Fe atoms were assumed for the simulations: The minority sublattice SL1 is identified with ^{57}Fe atoms at film and / or grain interfaces, while the majority sublattice is associated with ^{57}Fe atoms in a bulk-like atomic configuration.

The time spectra recorded at the specular scattering rod and at the R-plane and S-plane scattering rods after each deposition step are depicted in Fig. 8.8, together with CONUSS simulations (red curves). The spectra in each row show the state of the sample in the same deposition stage. From one deposition stage to the next, the magnetic hyperfine field strengths B_{hf} and their respective distribution, as well as the weights of the two sublattices were varied in the simulations: Fig. 8.9(a - b) shows the evolution of the magnetic hyperfine field strengths B_{hf} of the different regions of the ^{57}Fe film as functions of the increasing film thickness during deposition as derived from the simulations. The relative weights of sublattices SL1 and SL2 in dependence of the respective film thickness are plotted Fig. 8.9(c - d). In the first two deposition stages, finite values of isomer shift and quadrupole splitting were assumed for the atoms in the thinner film; these values are then decreased to zero in the third deposition stage.

For both the thicker and the thinner ^{57}Fe film regions the simulations resulted in the atoms of SL1 (interface component) having a magnetic hyperfine field strength B_{hf} which is by approximately 10% lower than that of the SL2 (bulk component) atoms, and having a full width at half maximum of the distribution of B_{hf} which is by a factor of about 2 larger than that of the SL2 atoms.

According to the simulations of the GISAXS patterns, during the experiment the thickness of the film regions on the R-plane facet surfaces increases from 1.0 nm to 3.1 nm, the thickness of the film regions on the S-plane facet surfaces increases from 0.8 nm to 2.3 nm. In each deposition stage, distinctly different time spectra shapes, i.e. different temporal beat patterns, are observed at the three scattering rods. The time spectrum recorded at the specular scattering rod appears as an intermediate between the spectra taken at the R-plane and S-plane scattering rod, as the nuclear resonant signals of both the thick and thin ^{57}Fe film regions are superposed here.

Stable ferromagnetic ordering in thin films is obtained when the film thickness exceeds a critical value d_c. The critical film thickness for Fe has been found to depend on growth conditions, on temperature and on the substrate and to range from a few monolayers to $d_c = 3$ nm [136–138]. In Fe thin films with uniaxially corrugated shape, comparable to the film discussed here, the magnetization stabilization process from the superparamagnetic to the ferromagnetic phase takes place at film thicknesses 1 nm $< d <$ 3 nm (see section 3.4.2 and references therein). The results of this experiment agree well with those findings: First evidence of the influence of a magnetic hyperfine field on the nuclear energy levels is given by the appearance of quantum beats in the time spectra for film thicknesses larger than 1 nm. Comparing time spectra of the different film regions for similar respective film thicknesses, however, one finds that the time spectra of the film regions on the R-plane and S-plane facet surfaces are of very similar shape, indicating a similar magnetic state. However, the time spectrum recorded at the S-plane scattering rod at a film thickness of 2.3 nm is dissimilar to the time spectrum recorded at the R-plane scattering rod at 2.4 nm film thickness, but rather comparable to that recorded at the R-plane scattering rod at 2.8 nm film thickness: Both show a pronounced quantum beating pattern, clearly evidencing a higher degree of stable ferromagnetic ordering than the time spectrum recorded at the R-plane scattering rod at 2.4 nm film thickness. This development of the time spectra shape corresponds to the evolution of the magnetic hyperfine field strength. The establishment of ferromagnetic behavior is indicated by a rapid decrease of the full width at half maximum of the magnetic hyperfine field strength distribution: The full width at half maximum of the magnetic hyperfine field strength distribution in both the thick and the thin film regions decreases by a factor of 5 for the SL2 atoms (bulk), while it remains decreases by only a factor of about 1.5 for the SL1 atoms (interface). Ferromagnetic behavior is established at a film thickness of 2.8 nm for the ^{57}Fe film regions

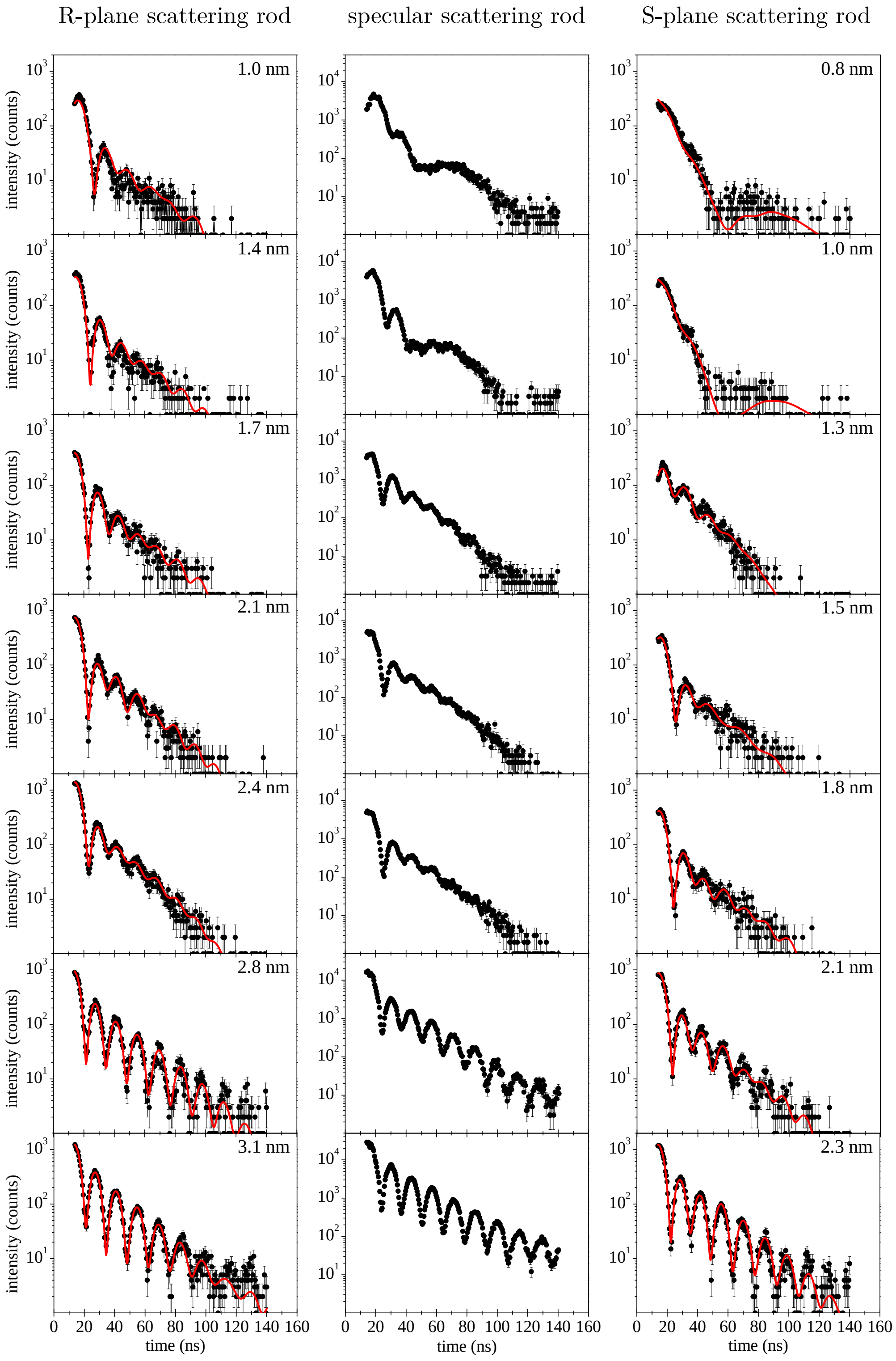

Figure 8.8: Time spectra recorded at the positions indicated in Figs. 8.3 and 8.4 (b) with simulations (red curves). Graphs in each row show the state of the sample in the same deposition stage. Labels state the respective thicknesses of the ^{57}Fe film. From one deposition stage to the next, the magnetic hyperfine field strengths B_{hf} and their respective distribution, as well as the weights of the two sublattices were varied in the simulations.

on the R-plane facet surfaces. In the thinner film regions on the S-plane facet surfaces ferromagnetic behavior is established at a film thickness of 2.3 nm already, evidenced by a rapid decrease of the full width at half maximum of the magnetic hyperfine field strength distribution.

It is peculiar, that the strength of the magnetic hyperfine fields does not increase monotonously with increasing film thickness for both the thicker film regions on the R-plane facet surfaces and the thinner film regions on the S-plane facet surfaces. Simulations assuming values for the magnetic hyperfine fields which conform to a monotonous increase do not yield adequate fits to the experimental data. This non-monotonous evolution of the magnetic hyperfine fields may be due to dependencies of the magnetic properties on several factors: (i) the growth mechanism of ^{57}Fe on α-Al$_2$O$_3$ for the given incidence angles of sputtered atoms on the R-plane and S-plane facet surfaces, (ii) the resulting microstructure of the film, (iii) the corrugated film shape with alternating stripe-like regions of different thickness. Due to the long duration of the experiment, an influence of oxidation effects can be considered, too. Further investigations of the structure of the ^{57}Fe film and its chemical composition would be required to gain more insight into the reasons why the magnetic hyperfine fields evolve in this way.

At 3.1 nm thickness, the film regions on the R-plane facet surfaces have a magnetic hyperfine field strength of $B_{hf} = 33.2$ T (in SL2), very close to the α-Fe bulk value of $B_{hf} = 33.3$ T. At this deposition stage, the film regions on the S-plane facet surfaces have reached a thickness of 2.3 nm and a magnetic hyperfine field strength of $B_{hf} = 32.4$ T (in SL2). Both the thin and thick film regions now show time spectra shapes which are characteristic of ferromagnetically ordered ^{57}Fe with the magnetic quantization axis oriented parallel to the direction of the incoming beam (compare with Fig. 6.18 A): Due to the magnetic anisotropy induced by the uniaxially corrugated shape of the ^{57}Fe film on the faceted substrate (see section 3.4.2), the magnetic hyperfine field is oriented along the facet edges.

After this in-situ experiment, ^{57}Fe deposition was continued until a final film thickness of 18 nm on the R-plane facet surfaces and of 13 nm on the S-plane facet surfaces was reached. The sample was then capped with 3 nm of Cr to prevent oxidation before removing it from the UHV chamber.

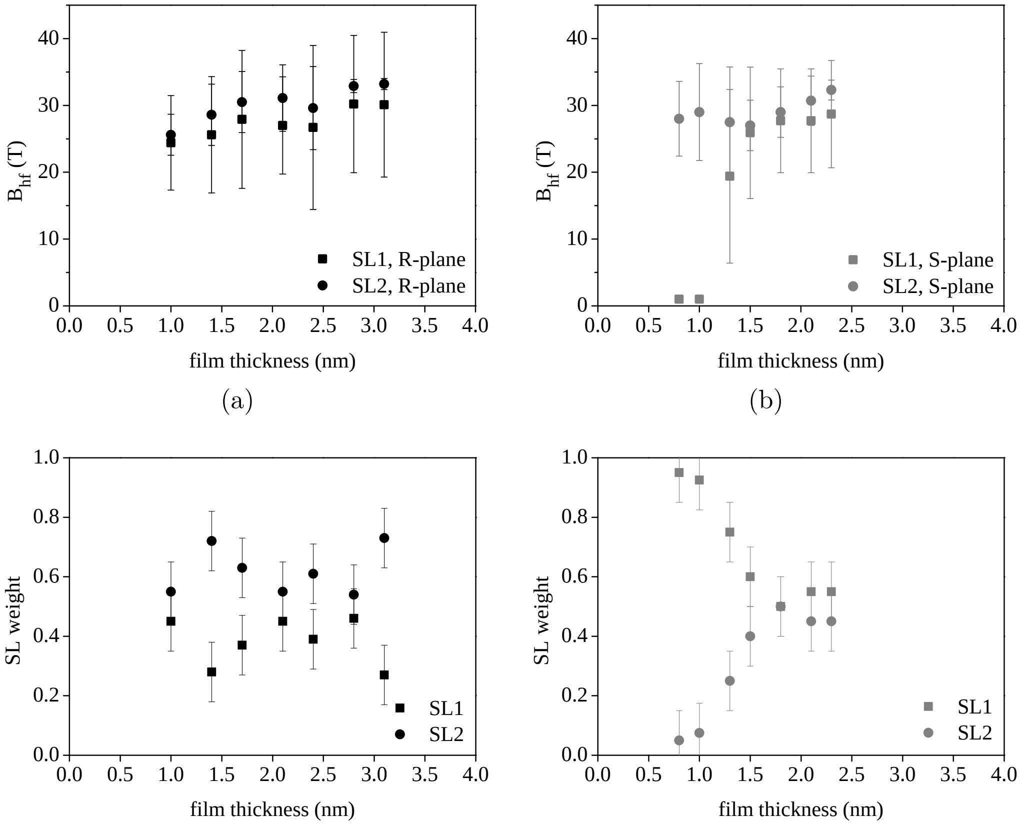

(a) (b)

(c) (d)

Figure 8.9: The evolution of the magnetic hyperfine field strengths B_{hf} of the ^{57}Fe film regions on the R-plane and S-plane facet surfaces during film growth. Bars indicate the full width at half maximum of the distribution of B_{hf}. The ^{57}Fe film is assumed to be composed of two sublattices (SL1, SL2) of ^{57}Fe atoms. The fraction of SL1 atoms decreases as the volume fraction of interface atoms decreases with proceeding deposition, as sketched in (c).

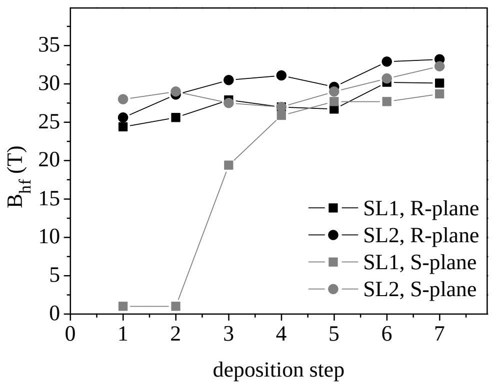

Figure 8.10: Direct comparison of the evolution of the magnetic hyperfine field strengths for the film regions growing on the R-plane and the S-plane facet surfaces. Distributions of the magnetic hyperfine fields as shown in Fig. 8.9 were omitted for clarity.

8.2.4 Ex-situ GINSAXS: Response to external magnetic fields

The in-situ experiment described above focused on investigating the evolution of the magnetic hyperfine field strength as an indication of the degree of ferromagnetic order in the different regions of the ^{57}Fe film. The orientation of the magnetic hyperfine field was given by the uniaxial magnetic anisotropy of the sample. In another experiment an external magnetic field was applied and the response of the sample in terms of the orientation of the magnetic hyperfine field vector was studied by evaluation of NRS time spectra recorded separately for the thick and thin ^{57}Fe film regions. Since the magnetic hyperfine field is – in close approximation – proportional to the magnetization, these measurements provide spatially resolved information on the dependence of the field-dependence of the magnetization in the thick and thin film regions, respectively.

This ex-situ experiment was conducted at the beamline P01 (PETRA III) at an x-ray energy of 14.4 keV with the sample at room temperature. The sample was mounted on a goniometer, with the facet edges aligned parallel to the direction of the incident beam. By means of an electromagnet, external magnetic fields of up to $B_{ext} = 300$ mT could be applied within the macroscopic sample plane, perpendicular to the incident beam direction. Nuclear resonant time spectra at the scattering rods belonging to the R-plane and S-plane facet surfaces were recorded with an APD detector for different applied external magnetic fields. First, the sample was rotated around its macroscopic surface normal by 90 degrees, so that the facet edges were parallel to the orientation of the external magnetic field, and then exposed to the maximum applicable external magnetic field of $B_{ext} = 300$ mT. With no external magnetic field applied, the sample was then rotated back into its original orientation, so that its magnetization was parallel to the direction of the incident beam. Then, the following sequence of external magnetic fields was applied to the sample: +100 mT, +200 mT, +300 mT, +100 mT, 0 mT, -50 mT, -300 mT, 0 mT. After each change of the applied external magnetic field, NRS time spectra were recorded at the specular scattering rod and at the R-plane and S-plane scattering rods, respectively.

The time spectra were simulated using the program CONUSS [128]. It was assumed that the orientation of the magnetic hyperfine fields is the same in both sublattices of ^{57}Fe atoms (representing atoms at interfaces and in bulk-like configurations, respectively), but that it varies for the thick and thin regions and for different applied external magnetic fields. Again, the specific morphology of the faceted sample has to be taken into account: The orientation of the magnetic hyperfine fields of the ^{57}Fe film on the R-plane and S-plane facet surfaces can be described by the polar angles $\theta_{R,S}$ and the azimuthal angles $\psi_{R,S}$. Within the simulation program, the reference plane for these angles is the respective scattering plane, which is tilted by $\phi_R = 30°$ in case of R-plane facet surface and by $\phi_S = 17°$ in case of the S-plane facet surface. For the ^{57}Fe film region on the R-plane and S-plane facet surfaces the angles θ_R, ψ_R and θ_S, ψ_S are defined such that

θ_R	ψ_R	orientation of the magnetic hyperfine field
90°	0°	in the film plane, parallel to the facet edges
60°	+90°	parallel to the external field for $B_{ext} > 0$ mT
120°	−90°	parallel to the external field for $B_{ext} < 0$ mT

θ_S	ψ_S	orientation of the magnetic hyperfine field
90°	0°	in the film plane, parallel to the facet edges
107°	+90°	parallel to the external field for $B_{ext} > 0$ mT
73°	−90°	parallel to the external field for $B_{ext} < 0$ mT

The recorded NRS time spectra are plotted in Figs. 8.11 and 8.12; the red curves show the simulated time spectra for the ^{57}Fe film regions on the R-plane and S-plane facet surfaces, respectively. By comparing the time spectra for the film regions on the R-plane and S-plane facet surfaces, it becomes apparent, that the magnetizations of the thick and thin ^{57}Fe film regions respond to the applied external magnetic field with different reorientations (compare these spectra to the calculated spectra in Fig. 6.18 for different orientations of the magnetic quantization axis). The different deviations of the spectra for the film regions on the R-plane and S-plane facet surfaces from the spectra recorded at the specular reflection are very well reproduced by the simulations. Thus the differences in the dependence of the magnetization orientations of the thick and thin ^{57}Fe film regions on the applied external magnetic field can be quantified.

Quantitative values for the polar and azimuthal angles of the magnetic hyperfine field (i.e. magnetization) orientations can be extracted from the simulated time spectra. $\theta_{R,S}$ and $\psi_{R,S}$ are plotted as functions of the applied external magnetic field in Fig. 8.13. The plots show virgin curves for the first increase of the applied external magnetic field strength, followed by minor loop curves of the magnetic hyperfine field orientation as functions of the varied external magnetic field strength.

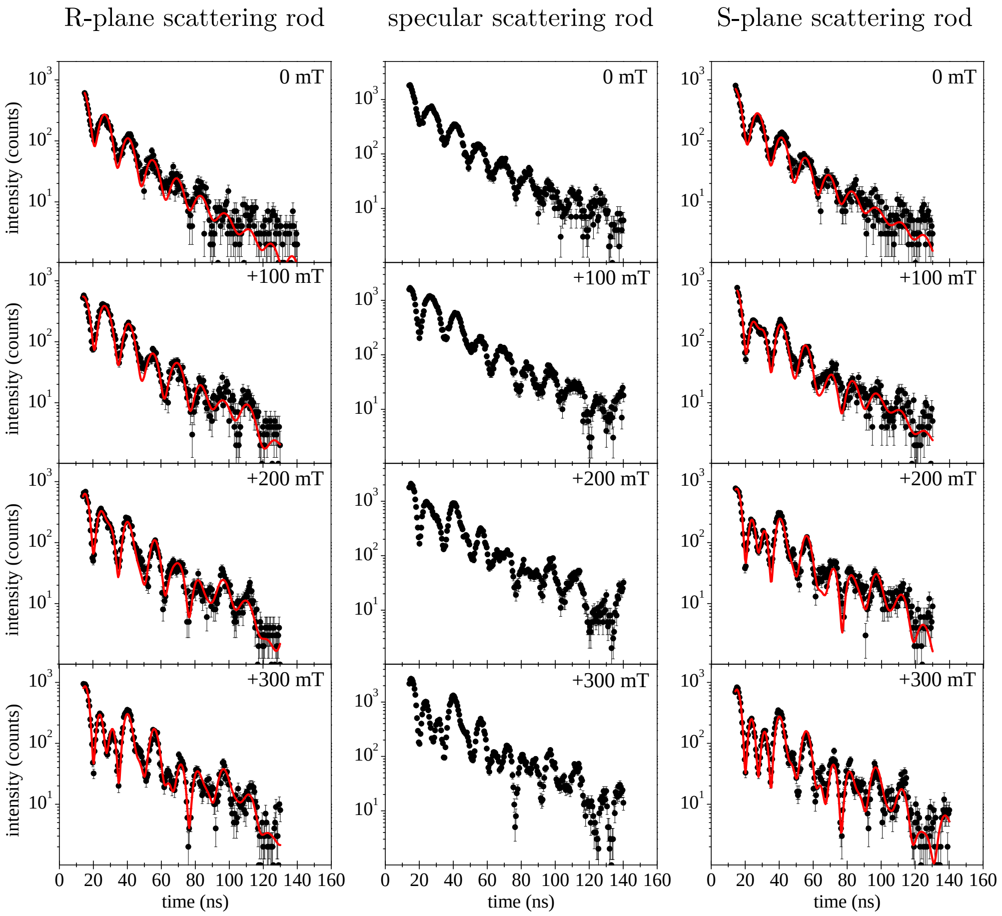

Figure 8.11: Time spectra recorded at the specular, R-plane, and S-plane scattering rods, as indicated in Fig. 8.3, for a sequence of applied external magnetic fields from saturation to $B_{ext} = +300$ mT. Graphs in each row show the state of the sample for the same applied external magnetic field as labeled. In the simulations (red curves), varied polar and azimuthal angles of the magnetic hyperfine field orientation were assumed for thick and thin regions and for different applied external magnetic fields.

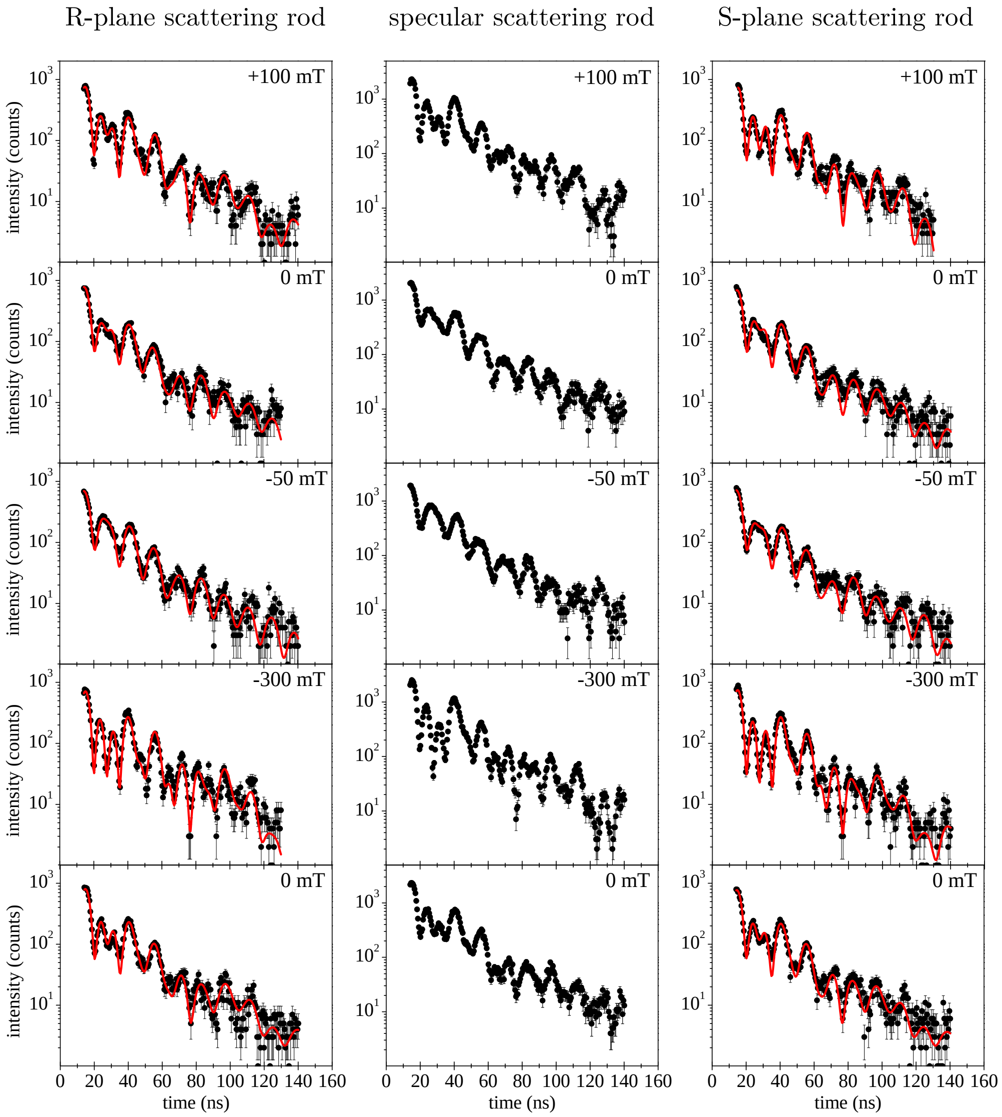

Figure 8.12: Time spectra recorded at the specular, R-plane, and S-plane scattering rods, as indicated in Fig. 8.3, for a sequence of applied external magnetic fields from $B_{ext} = +100$ mT to $B_{ext} = -300$ mT to $B_{ext} = 0$ mT. Graphs in each row show the state of the sample for the same applied external magnetic field as labeled. In the simulations (red curves), varied polar and azimuthal angles of the magnetic hyperfine field orientation were assumed for thick and thin regions and for different applied external magnetic fields.

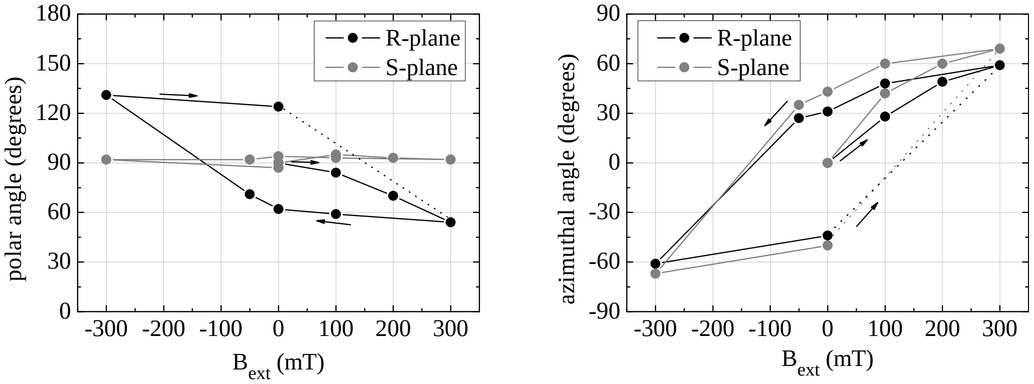

Figure 8.13: The polar angles $\theta_{R,S}$ (left) and the azimuthal angles $\psi_{R,S}$ (right) defining the orientation of the magnetic hyperfine fields in the thick and thin ^{57}Fe film regions as functions of the applied external magnetic field. Arrows indicate the sequence in which the applied external magnetic field was varied.

The monotonous change of the magnetic hyperfine field orientation in dependence of the applied external magnetic field strength indicates a coherent rotation of the magnetic moments in order to align with the external magnetic field. One exception is the polar angle of the magnetic hyperfine field orientation in the thinner ^{57}Fe film regions on the S-plane facet surfaces: It remains almost constant at $\theta_S = 90°$, i.e. the magnetization of these regions remains within the film plane even at highest applied external magnetic field strength. The magnetic hyperfine field in the thicker regions, however, reorients from being parallel to the R-plane facet surface at $\theta_R = 90°$ to being parallel to the macroscopic sample surface at $\theta_R = 60°$ and $\theta_R = 120°$, i.e. reorients out of the ^{57}Fe film plane and into the plane of the applied external magnetic field. The dependence of the azimuthal angles of the magnetic hyperfine field orientation is more similar for the thinner and thicker regions of the ^{57}Fe film, but not identical: Neither in the thinner nor in the thicker regions does the azimuthal orientation of the magnetization align with the orientation of the applied external magnetic field (parallel azimuthal alignment would be given at $\psi_{R,S} = \pm 90°$). This may be accounted for by the expected pronounced uniaxial in-plane magnetic anisotropy of the film, with the easy axis of magnetization parallel to the facet edges, due to the uniaxially corrugated film shape (see section 3.4.2). However, in the thinner film regions the magnetization orientation rotates further from the easy axis along the facet edges.

Several reasons can be considered for the different dependence of the magnetization orientation on the external applied field in the thick and thin film regions, respectively. In contrast to the uniaxially corrugated Fe thin films discussed in section 3.4.2, which were prepared on substrates with symmetric facet profiles, the film regions on the R-plane and S-plane facet surfaces in the present sample are not identical: The incident angle of the sputtered atoms with respect to the facet surface normals is significantly different on the R-plane and S-plane facet surfaces: On the R-plane facet surfaces with a tilt angle of $\phi_R = 30°$ and facing the sputtering source the incident angle is about 15°, i.e. only slightly deviating from normal incidence. On the S-plane facet surfaces with a tilt angle of $\phi_S = 17°$ and avert from the sputtering source the incident angle is about 62°. Resulting different film structures may account for the observed differences in the external field dependence of the magnetization orientation [139–141].

Moreover, the film regions on the S-plane facet surfaces are both thinner and wider than those on the R-plane facet surfaces. The higher width-thickness aspect ratio of the thinner film may result in more pronounced shape anisotropy in the regions on the S-plane facet surfaces, favoring an in-plane orientation of the magnetization more strongly than in the film regions on the R-plane facet surfaces. Thus, in the film regions on the R-plane facet surfaces, the shape anisotropy energy may be overcome more easily by the dipolar energy related to alignment of the magnetization with the external magnetic field, than in the film regions on the S-plane facet surfaces. Such an effect may account for the observation, that the magnetization of the thicker regions reorients out of the film plane and the magnetization of the thinner film regions does not.

Furthermore, the external magnetic field is applied parallel to the macroscopic sample surface and does therefore not enclose the same angle with the R-plane and S-plane facet surfaces. Consequently, as sketched in Fig.8.14, the magnitude of the applied external magnetic field component perpendicular to the film plane is by approximately 70% larger for the film regions on the R-plane facet surfaces for the film regions on the S-plane facet surfaces. This fact, too, may contribute to explaining why the magnetization of the thicker regions reorients out of the film plane to align with the external magnetic field, while the magnetization of the thinner regions remains within the film plane.

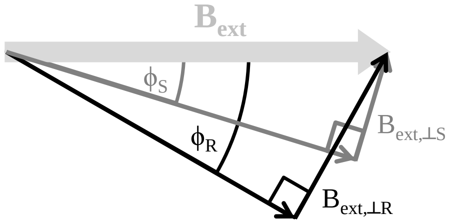

Figure 8.14: Components of the applied external magnetic field. $\phi_R = 30°$ and $\phi_S = 17°$ denote the facet tilt angles with respect to the macroscopic sample surface and the orientation of the external magnetic field.

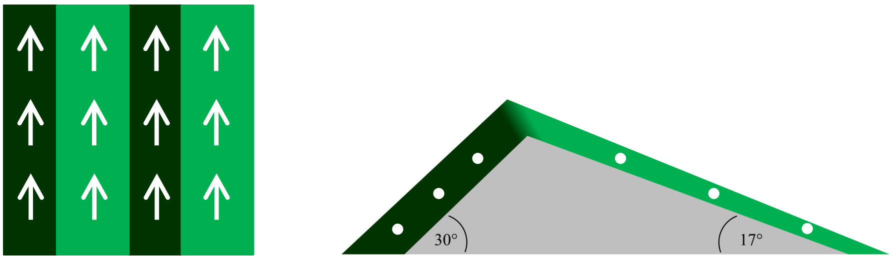

(a) $B_{ext} = +0$ mT

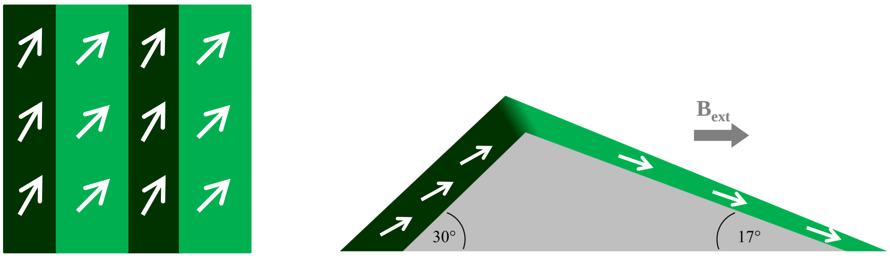

(b) $B_{ext} = +200$ mT

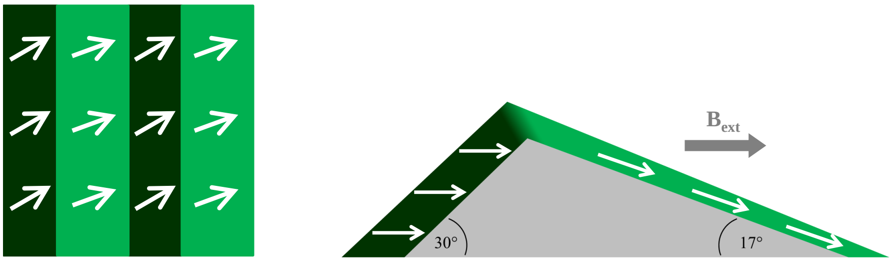

(c) $B_{ext} = +300$ mT

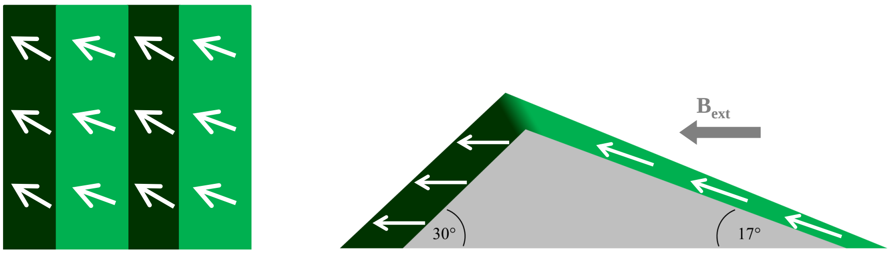

(d) $B_{ext} = -300$ mT

Figure 8.15: Top view and side view sketches of the ^{57}Fe film of periodically varying thickness on nanofaceted α-Al$_2$O$_3$. White arrows indicate the orientation of magnetic moments for different applied external magnetic fields. The polar and azimuthal angles of the individual magnetization orientations for thick and thin film regions were extracted from simulations of the respective time spectra (see Figs. 8.11 and 8.12).

If only time spectra at the specular reflection were accessible, an interpretation of the NRS signal in terms of the individual contributions would be far from trivial – one complication, e.g., is the fact that the specular signal is expected to include contributions from parts of the film on the facet edges and in the facet grooves, i.e. where thick and thin regions meet. Moreover, the orientation of the electric field vector of the incident radiation with respect to the scattering plane and the film magnetization is different for the film regions on the R-plane and S-plane facet surfaces, respectively, due to the different facet tilt angles. Simulating the time spectra recorded separately at the R-plane and S-plane scattering rods is straightforward, as the individual spectra in principle correspond to time spectra recorded of thin films in standard reflection geometry (see section 6.3.2). Thus, simulations with very good agreement with the experimental data were obtained and allowed to draw consistent conclusions on the magnetic properties of the different film regions.

Both the in-situ and ex-situ experiment demonstrate, that GINSAXS is a feasible method to obtain NRS time spectra from specific parts of a sample, in which heterogeneous structural and magnetic properties are correlated. GINSAXS can exploit the sample structure in order to separate nuclear resonant signals from different structural units of a sample and thus to disentangle their different contributions to the overall magnetic properties of the sample.

This method is not limited to samples with faceted surfaces, however. Samples with a periodically structured morphology and a corresponding spin structure can be investigated too. The spin configurations in a nanostripe pattern during magnetic reversal have recently been studied by GINSAXS (Schlage, Dzemiantsova, et al.; publication in preparation). Also, a nuclear resonant variant of Small Angle X-ray Scattering is conceivable: if the sample has a bimodal size or distance distribution, nuclear resonant time spectra recorded at the corresponding $\boldsymbol{q}$-space positions could reveal the individual magnetic properties of different particle species.

9 Nanopatterned Diblock Copolymer Templates

Block copolymers have already found several applications in nanotechnology. For example, they can be used as masks in nanolithography [142], as templates for arranging nanoparticles [143], or in the production of nanoporous films [144]. Prerequisites for technological applications and highly-desired properties for scientific purposes are:

- uniformity in size, shape, and orientation of nanodomains
- long-range regularity in lateral placement of nanodomains
- defect density approaching zero

In general, nanopattern formation in block copolymers occurs due to equilibration of energetic and entropic factors (see section 2.3). After deposition onto a substrate, a block copolymer at ambient conditions is usually kinetically trapped in a non-equilibrium state. The equilibration process is enabled by either thermal annealing or solvent vapor annealing, both promoting microphase separation into chemically distinct domains on the scale of the specific equilibrium period D_0 (see section 5.3). Solvent vapor annealing was chosen here because of its advantage of being considerably faster than thermal annealing. Section 9.1 describes how the resulting chemical domain morphology of the diblock copolymer film surface depends on both intrinsic parameters of the diblock copolymer and externally controllable parameters of the solvent vapor annealing procedure.

The chemical domain morphologies presented in section 9.1 feature nanodomains which are uniform in size, shape, and orientation. However, they do not exhibit long-range regularity in the lateral placement of nanodomains. There are three main approaches to optimize the formation of regular patterns of these chemical domains: By applying electric, magnetic or other external fields, by control of the interactions at the interfaces of the diblock copolymer film, e.g. by a chemically pre-patterned substrate, or by applying controllable constraints such as film thickness and/or substrate topography [145]. The latter approach was followed in the present work by depositing the diblock copolymer films onto faceted α-Al_2O_3 substrates and by controlling the film thickness via the polymer solution concentration and the angular velocity during spin coating. In section 9.2 the resulting highly ordered chemical domain morphologies are presented and the influences of substrate topography and diblock copolymer molecular mass are discussed.

The data reviewed here are obtained from AFM topography measurements in non-contact constant force mode (see section 6.1.3) using a NT-MDT Solver Next SPM with HA_NC Etalon probes. Brighter (higher) areas correspond to the PS block, while darker (lower) regions represent the PMMA block, with typical height differences between PS and PMMA domains of ≤ 5 nm for the specific types of PS-b-PMMA used in this work. The measured height information can therefore be interpreted as information about the local chemical composition: The measured topographical surface patterns correspond directly to chemical surface patterns.

9.1 PS-b-PMMA templates on planar SiO_x substrates

This section describes thin films of symmetric and asymmetric PS-b-PMMA diblock copolymers on polished SiO_x substrates. A regular chemical patterning of these films by microphase separation is brought about by solvent vapor annealing. The influence of different intrinsic parameters and process parameters (see sections 2.3.2 and 5.3.1) on the resulting chemical domain morphology of these films is discussed. A method for removing the PMMA block from the patterned film, leaving a pattern of isolated PS structures on the substrate, is presented.

The general preparation routine for the samples shown here is described in section 5.5. If not stated otherwise, all samples discussed in this section were deposited on SiO_x substrates by spin coating at an angular velocity of 3000 rpm, were dried for 2.5 hours at 50 °C, and underwent solvent vapor annealing in saturated acetone vapor for 3h at room temperature immediately afterward.

9.1.1 Dependence of film morphology on solvent vapor annealing

For all samples presented in this section, all preparation steps prior to solvent vapor annealing were identical: A solution of the cylinder-forming PS-b-PMMA(63/142) in toluene with concentration c = 10 mg/ml was prepared and spin coated onto cleaned SiO_x substrates. The samples were then dried for 2.5 hours at 50 °C. Immediately afterward they were subject to solvent vapor annealing in saturated acetone vapor at room temperature.

Performing solvent vapor annealing is mandatory for the samples to develop a regular chemical patterning, which can serve as a template for the fabrication of metal nanostructures. Fig. 9.1 shows AFM topography micrographs of three thin film samples of the asymmetric diblock copolymer PS-b-PMMA(63/142): in the as-cast state, after three hours, and after six hours of solvent vapor annealing, respectively. The left and right row of micrographs shows sample surface areas of 5 μm × 5 μm and 2 μm × 2 μm, respectively.

The as-cast sample is not smooth but exhibits an irregular surface structure with individual features on a length scale expected for the chemical domains of phase separated PS-b-PMMA(63/142) with a calcuated equilibrium period of $D_0 = 66$ nm. This may indicate, that a microphase separation has taken place to a certain degree during preparation of the film. However, a regular chemical patterning of the film is only achieved by solvent vapor annealing: After three hours of solvent vapor annealing the sample surface displays circular domains of PS surrounded by a continuous PMMA matrix. This chemical surface structure is consistent with an interior film structure of surface-perpendicular PS cylinders in a PMMA matrix ($C^{\perp}$ morphology, see section 2.3.2). In this sample, the PS domains are hexagonally packed within grains of several square microns. The grain orientation is isotropic but can be clearly determined for each grain. After six hours of solvent annealing, this regularity is impaired: The PS domains have lost their uniform circular shape. The arrangement of PS domains is not evenly hexagonal anymore but appears distorted. As seen for the PS-b-PMMA restructuring process during solvent vapor annealing investigated by Xuan and coworkers [94] (see 5.3.1), this is most likely due to the equilibrium morphology at the given film thickness being the s-$L^{\parallel}$ phase for symmetric wetting conditions (refer to the phase diagram in Fig. 2.8). Upon extended solvent vapor annealing in acetone, PMMA therefore continues to migrate toward the free surface and the $C^{\perp}$ morphology will be replaced by the s-$L^{\parallel}$ morphology, in which PMMA dominates both the free surface and the substrate surface of the film.

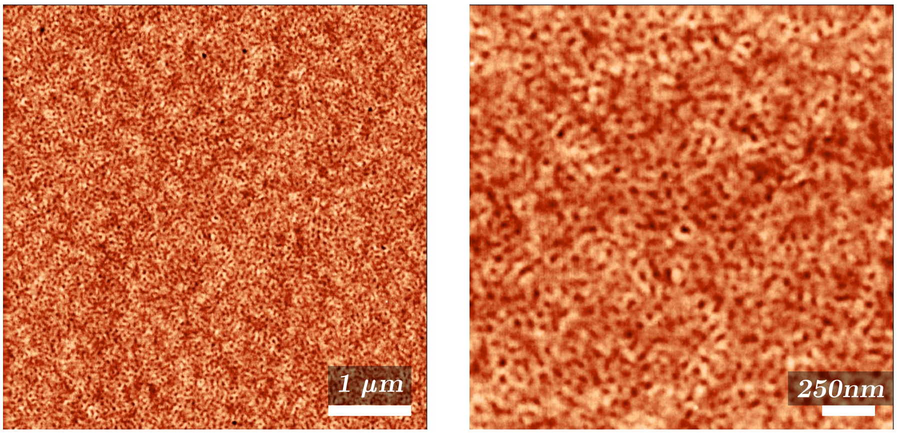

(a) as cast (b) as cast

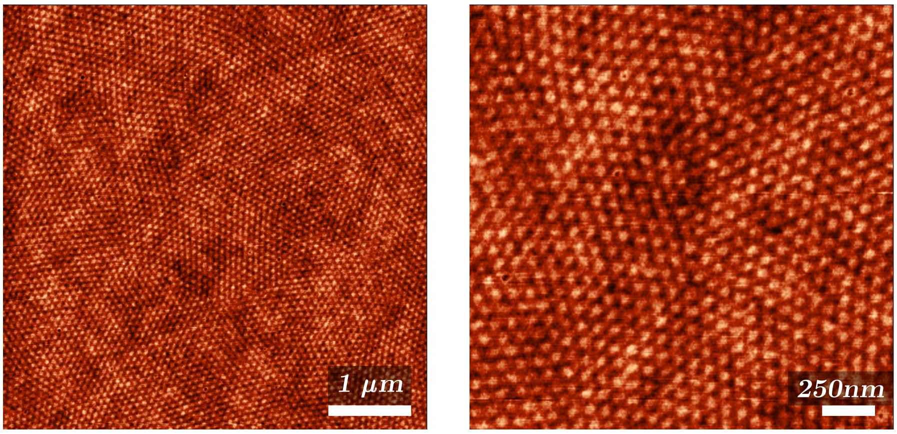

(c) after 3 h (d) after 3 h

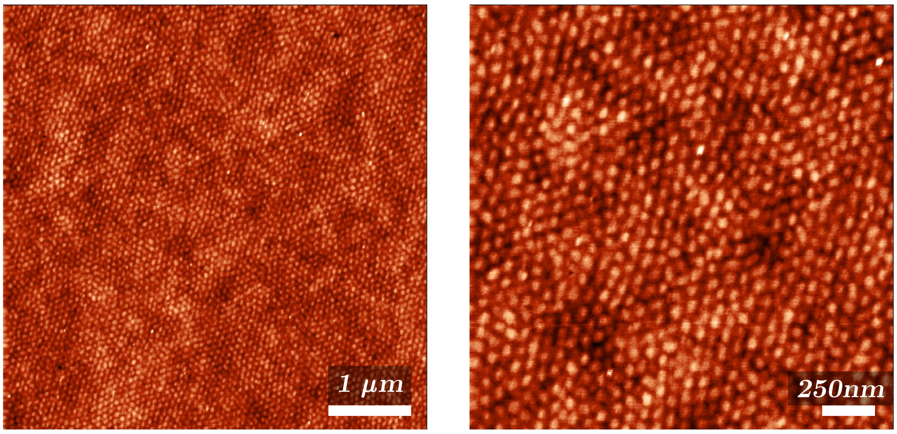

(e) after 6 h (f) after 6 h

Figure 9.1: Cylinder-forming PS-b-PMMA(63/142) thin films on SiO_x substrates, as cast and after solvent vapor annealing for different durations. Micrographs in each row show different areas of the same sample.

9.1.2 Dependence of film morphology on PS-b-PMMA composition and molecular mass

The chemical phase morphology of a microphase separated diblock copolymer is determined by its composition f, i.e. the volume fractions of the two blocks, and by the total molecular mass, i.e. degree of polymerization N (see section 2.3.1, Fig. 2.5): A compositionally symmetric diblock copolymer assumes a morphology with equal domain volumes of the two blocks, such as the lamellar L morphology. A compositionally asymmetric diblock copolymer adopts a morphology with unequal domain volumes of the majority and the minority block, such as the cylindrical C morphology. The molecular mass of the diblock copolymer determines the domain size via the equilibrium period D_0. To illustrate this, the chemical surface patterns of three PS-b-PMMA thin films on $\mathrm{SiO_x}$ are compared in Fig. 9.2. All samples shown in Fig. 9.2 were prepared on $\mathrm{SiO_x}$ substrates from solutions of concentration $c = 10$ mg/ml.

PS-b-PMMA(203/203) and PS-b-PMMA(47/53) are compositionally symmetric with $f_{PS} = 0.5$ and $f_{PS} = 0.47$, respectively; PS-b-PMMA(63/142) is asymmetric with $f_{PS} = 0.31$ (see section 5.5). Therefore, in the microphase separated state symmetric PS-b-PMMA(203/203) and PS-b-PMMA(47/53) are expected to assume a L-type morphology of alternating, equally wide lamellar domains of PS and PMMA. The asymmetric PS-b-PMMA(63/142) should express a C-type morphology of cylindrical PS (minority component) domains in a PMMA (majority component) matrix. . If the diblock copolymer film thickness d is smaller than the equilibrium period D_0, surface-perpendicular domain orientations can occur (see section 2.3.2). This is observed in the samples shown here: The surface domain morphology of PS-b-PMMA(63/142) in Fig: 9.2a, b is consistent with an interior film structure of surface-perpendicular PS cylinders in a PMMA matrix ($\mathrm{C}^{\perp}$ morphology), while the surface domain morphologies of PS-b-PMMA(203/203) and PS-b-PMMA(47/53) in Fig: 9.2c, d and Fig: 9.2e, f, respectively, conform to surface perpendicular lamellae of PS and PMMA (s-H or $\mathrm{S\text{-}L}^{\perp}$ morphology), see section 2.3.2). Moreover, PS-b-PMMA(203/203) has a bulk equilibrium period of $D_0 = 103$ nm, PS-b-PMMA(47/53) of $D_0 = 41$ nm (see section 5.5). The AFM micrographs show domain spacings of $D = (103 \pm 10)$ nm for PS-b-PMMA(203/203) and $D = (48 \pm 10)$ nm for PS-b-PMMA(47/53), which is in very good agreement with the calculated values. It is thus possible to control the morphology and the characteristic length scales of chemically nanopatterned diblock copolymer surfaces by appropriate choice of the diblock copolymer composition and molecular mass.

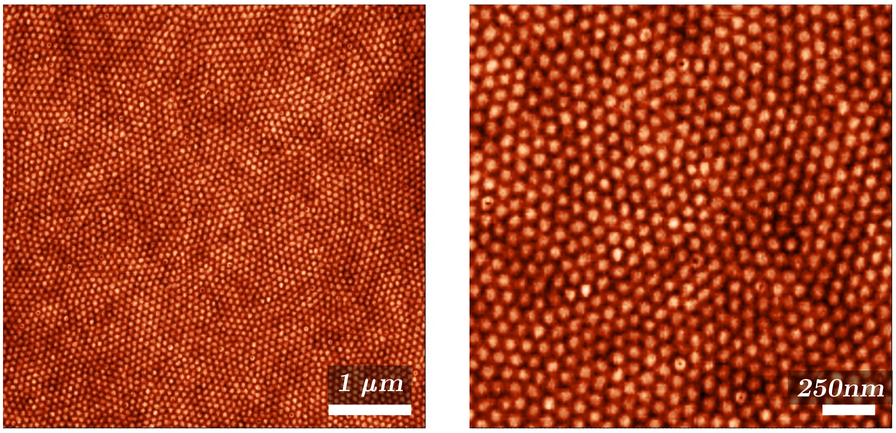

(a) PS-b-PMMA(63/142), C$^{\perp}$ (b) PS-b-PMMA(63/142), C$^{\perp}$

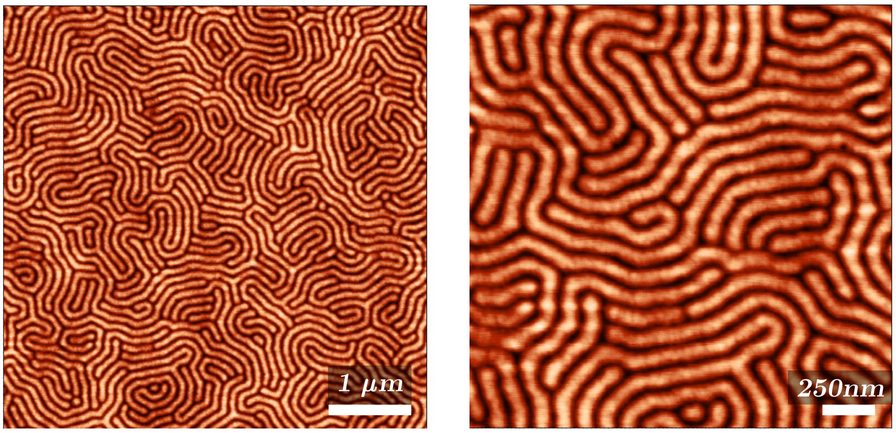

(c) PS-b-PMMA(203/203), s-L$^{\perp}$ (d) PS-b-PMMA(203/203), s-L$^{\perp}$

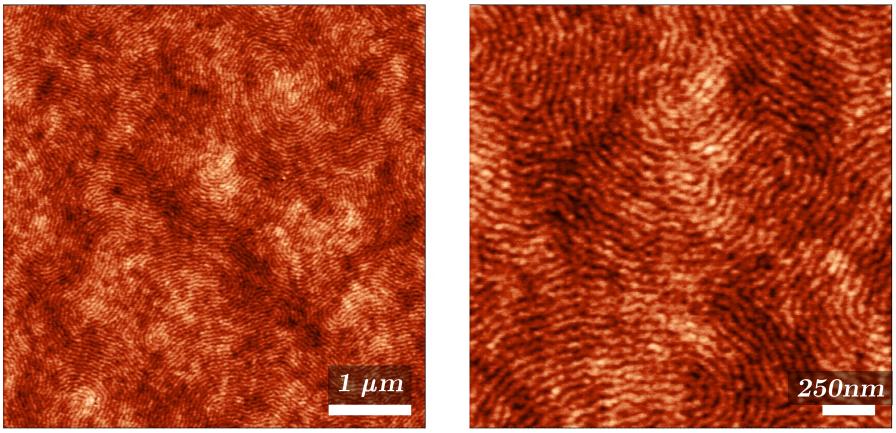

(e) PS-b-PMMA(47/53), s-L$^{\perp}$ (f) PS-b-PMMA(47/53), s-L$^{\perp}$

Figure 9.2: PS-b-PMMA thin film surface patterns for i) different compositional asymmetries: $f = 0.3$ (a, b) and $f = 0.5$ (c, d) and ii) different molecular masses: $M = 406$ (c, d) and $M = 100$ (e, f). Micrographs in each row show different areas of the same sample.

9.1.3 Dependence of film morphology on PS-b-PMMA film thickness

The wetting conditions during solvent vapor annealing of PS-b-PMMA on $\mathrm{SiO_x}$ in acetone are symmetric. Thus, morphologies on the right half of the thin film morphology phase diagram Fig. 2.8 can be obtained and fixed by rapid solvent removal. The aim in preparing diblock copolymer thin films as templates for nanostructure fabrication is to produce a regular chemical surface pattern, which requires the diblock copolymer nanodomains to be oriented perpendicular to the film surfaces. This is achieved with a $\mathrm{C}^{\perp}$ morphology of hexagonally packed, upright PS cylinders in a PMMA matrix for compositionally asymmetric PS-b-PMMA, or with a s-H or s-$\mathrm{L}^{\perp}$ morphology of upright lamellar domains for symmetric PS-b-PMMA. Here, the formation of the hybrid s-H morphology appears favorable due to the strongly preferred expression of PMMA at the interface with the oxidic substrate [54, 146]. However, the result of removing the PMMA block from the phase separated film (see appendix A.3.2) suggests rather that the s-$\mathrm{L}^{\perp}$ morphology has formed. In any case, a surface-perpendicular domain orientation requires PS-b-PMMA film of sufficiently low thickness of $d \lesssim 0.5D_0$.

Asymmetric PS-b-PMMA

Thin films of the cylinder-forming PS-b-PMMA(63/142) were cast from solutions with concentrations ranging from $c = 8$ mg/ml to $c = 15$ mg/ml – resulting in film thicknesses from $d_8 = 37.5$ nm to $d_{15} = 69$ nm (see appendix A.3.1) – and subject to solvent vapor annealing for 3 h. For all film thicknesses the chemical surface pattern consists of circular PS domains in a PMMA matrix (see Fig. 9.3), consistent with an interior film structure of surface-perpendicular PS cylinders in a PMMA matrix. The domain spacing is $D = (80 \pm 10)$ nm, which can also be taken as an estimate for the equilibirum domain period D_0. The value for the equilibrium period calculated from Eq.(2.23) would be 66 nm; however, this equation was derived for symmetric diblock copolymers. The PS domains are hexagonally packed within grains of random orientation. All prepared samples – eight with $c = 8$ mg/ml, fifteen with $c = 10$ mg/ml, and one with $c = 15$ mg/ml – exhibit the same surface domain morphology. Thus, for all chosen film thicknesses from $d_8 = 37.5$ nm $\approx 0.47D_0$ to $d_{15} = 69$ nm $\approx 0.86D_0$ a surface-perpendicular domain orientation of the PS cylinders is preferred. Such chemical surface patterning is therefore highly reproducible and insensitive to variations of

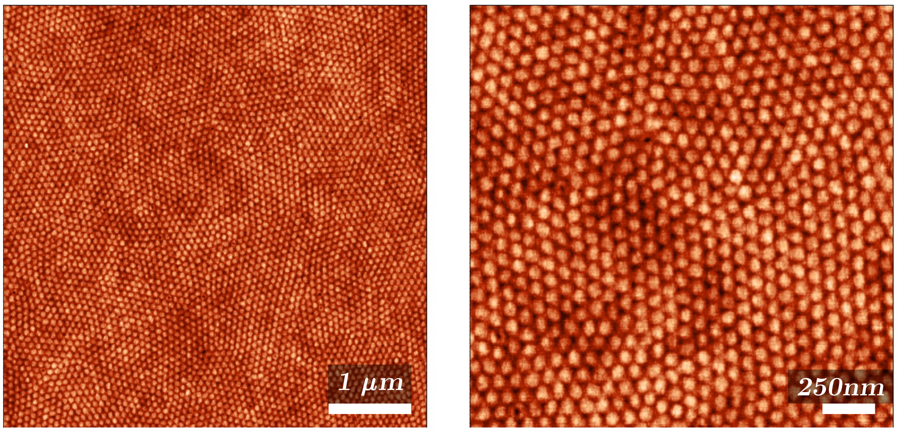

(a) $d_8 = 37.5$ nm (b) $d_8 = 37.5$ nm

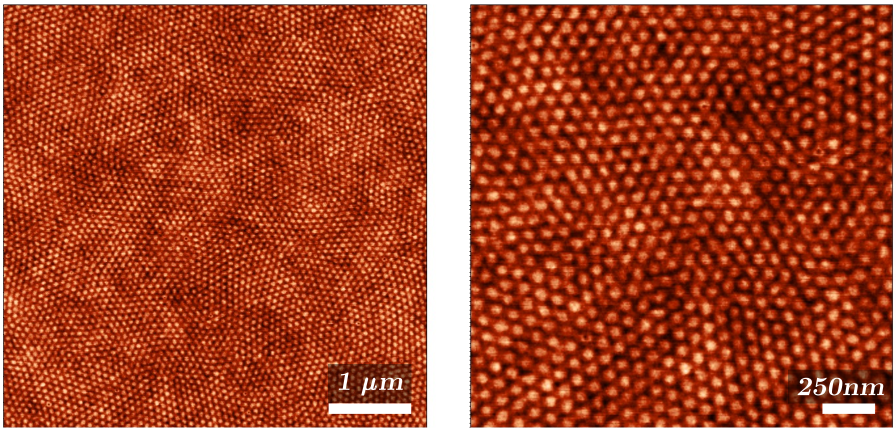

(c) $d_{10} = 44$ nm (d) $d_{10} = 44$ nm

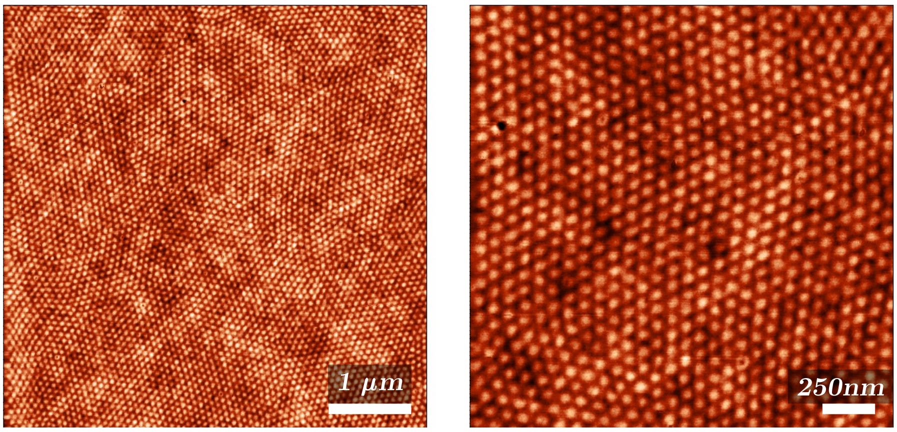

(e) $d_{15} = 69$ nm (f) $d_{15} = 69$ nm

Figure 9.3: PS-b-PMMA(63/142) thin films on $\mathrm{SiO_x}$ substrates, cast from solutions of increasing concentration c, therefore of increasing thickness $d_8 < d_{10} < d_{15} < D_0$ (top to bottom). Micrographs in each row show different areas of the same sample.

the film thickness in the range given by the varied solution concentration or to inhomogeneities of the film thickness resulting from the casting process.

Symmetric PS-b-PMMA

Thin films of lamellae-forming PS-b-PMMA(203/203) were cast from solutions with concentrations ranging from $c = 6$ mg/ml to $c = 15$ mg/ml, resulting in film thicknesses from $d_6 = 30$ nm $\approx 0.3D_0$ to $d_{15} = 85$ nm $\approx 0.8D_0$ (see appendix A.3.1). The film surface morphologies after microphase separation are shown in the AFM topography micrographs in Figs. 9.4 and A.15. For all film thicknesses a patterned surface morphology develops which is characterized by alternating stripe-like domains of PS and PMMA with isotropic, random orientation (Fig. 9.4(a), (c), (e), and Fig. A.15(a), (c), (e), (f)). This surface structure is consistent with a s-$L^{\perp}$ morphology in the interior of the films (see section 2.3.2 and appendix A.3.2). For all samples up to a thickness of $d_{12} = 65$ nm the domain spacings D range from (103 ± 10) nm to (111 ± 10) nm. These values are in very good agreement with the calculated bulk equilibrium period for PS-b-PMMA(203/203) of $D_0 = 103$ nm (see section 5.5). The samples of thickness $d_{15} = 85$ nm have a domain spacing of $D = (122 \pm 10)$ nm. For the films of $d_{12} = 65$ nm $\approx 0.6D_0$, the height difference between the PS and the PMMA domains – as an indication of the quality of microphase separation – is about 3 nm as compared to 5 nm for the other samples. For these films, branching and looping of domains occurs more often than for the other films and the domains are of more irregular width. The regular s-$L^{\perp}$ morphology as shown in Fig. 9.4 is expressed in about half of all investigated samples, while various alternative morphologies occur in the other cases - these are discussed in appendix A.3.3.

As indicated by the domain morphology phase diagram in Fig. 2.8, a surface-parallel domain orientation is preferred for film thicknesses $d > 0.5D_0$ under symmetric wetting conditions. The experimentally observed surface morphologies confirm, that film thicknesses $d_6 = 30$ nm to $d_{10} = 51$ nm, i.e. film thicknesses lesser than half the equilibrium domain period D_0, are best suited for preparing diblock copolymer thin films with perpendicular domain orientation. This perpendicular domain orientation results in a uniform chemical patterning of the film surface, which can then serve as a template for metal nanostructure fabrication (see section 10).

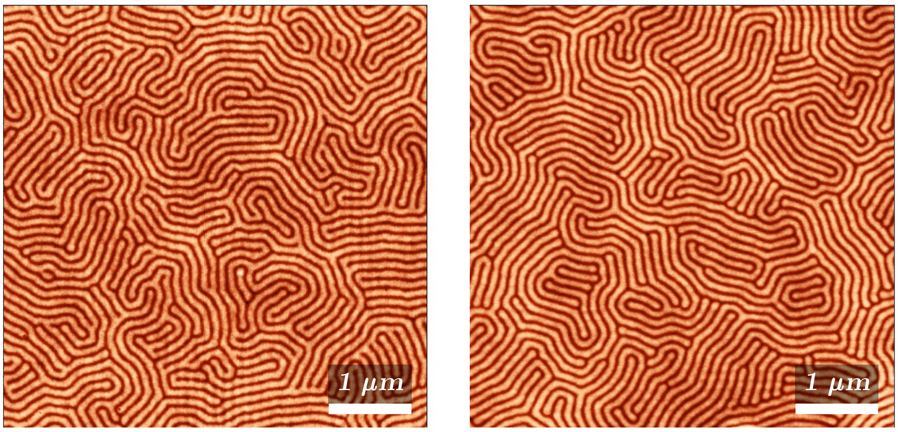

(a) $d_6 = 30$ nm (b) $d_8 = 41$ nm

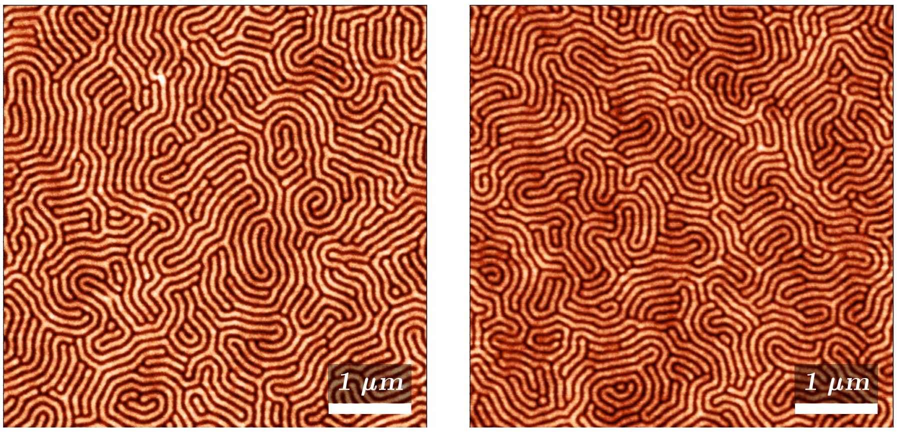

(c) $d_9 = 46$ nm (d) $d_{10} = 51$ nm

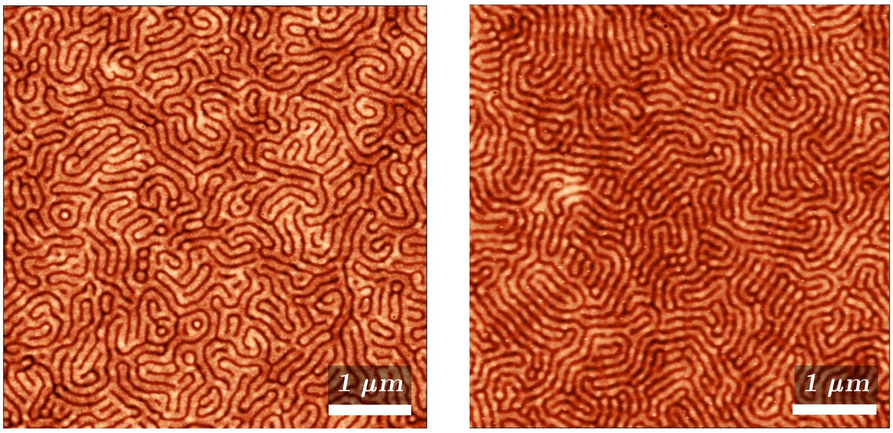

(e) $d_{12} = 65$ nm (f) $d_{15} = 85$ nm

Figure 9.4: Lamellae-forming PS-b-PMMA(203/203) thin films of increasing thicknesses $d_6 = 30$ nm to $d_{15} = 85$ nm on $\mathrm{SiO_x}$ substrates; $d_{10} = 51\mathrm{nm} \approx 0.5D_0$. The films exhibit the surface-perpendicular s-$\mathrm{L}^{\perp}$ morphology.

9.1.4 Removal of the PMMA block by acetic acid

The different behavior of the two blocks in PS-b-PMMA upon irradiation with UV light can be exploited to remove the PMMA block from a microphase separated PS-b-PMMA thin film [147–149][1]. When exposed to UV radiation, PS forms crosslinks - stable bonds between two different PS chains or PS chain segments - which enhances its resistance against chemicals and heat [150]. PMMA on the other hand can degrade upon UV irradiation [151], and can be removed using acetic acid. In order not to destabilize the entire PS-b-PMMA film, the sample must be dried for a sufficient duration after exposure to UV radiation and the acetic acid concentration must not be too high.

Following the optimized procedure for PMMA removal, a thin film of PS-b-PMMA(63/142) was prepared via the standard routine (see Fig. 9.5(a), (b)), then irradiated with UV light of $\lambda = 254$ nm wavelength for 6 h at room temperature (neoLab UVAC-60, power of lamp: 6 W distance to sample: 12.5 cm) and dried afterwards for 48 h at 50 °C. The sample was then placed onto a spin coater, acetic acid (70 %) was applied to the sample so that its surface was entirely covered with one large drop of acetic acid, and the sample was spun at 3000 rpm for 10 s. Spinning was repeated under excess distilled water. The sample with removed PMMA block is shown in Fig. 9.5(c), (d). The treatment with UV radiation and acetic acid leaves isolated PS cylinders on the SiO_x substrate. Note the increased height range as compared to the untreated film shown in Fig. 9.5(a), (b) – keeping in mind the size of the AFM probe (curvature radius approx. 10 nm). No PMMA residues can be found and the PS cylinders are evenly spaced.

In this way, isolated PS nanostructures supported on flat substrates can be prepared from microphase separated PS-b-PMMA thin films. A possible application of such structures is patterned etching of a substrate [152].

---

[1] See also references therein.

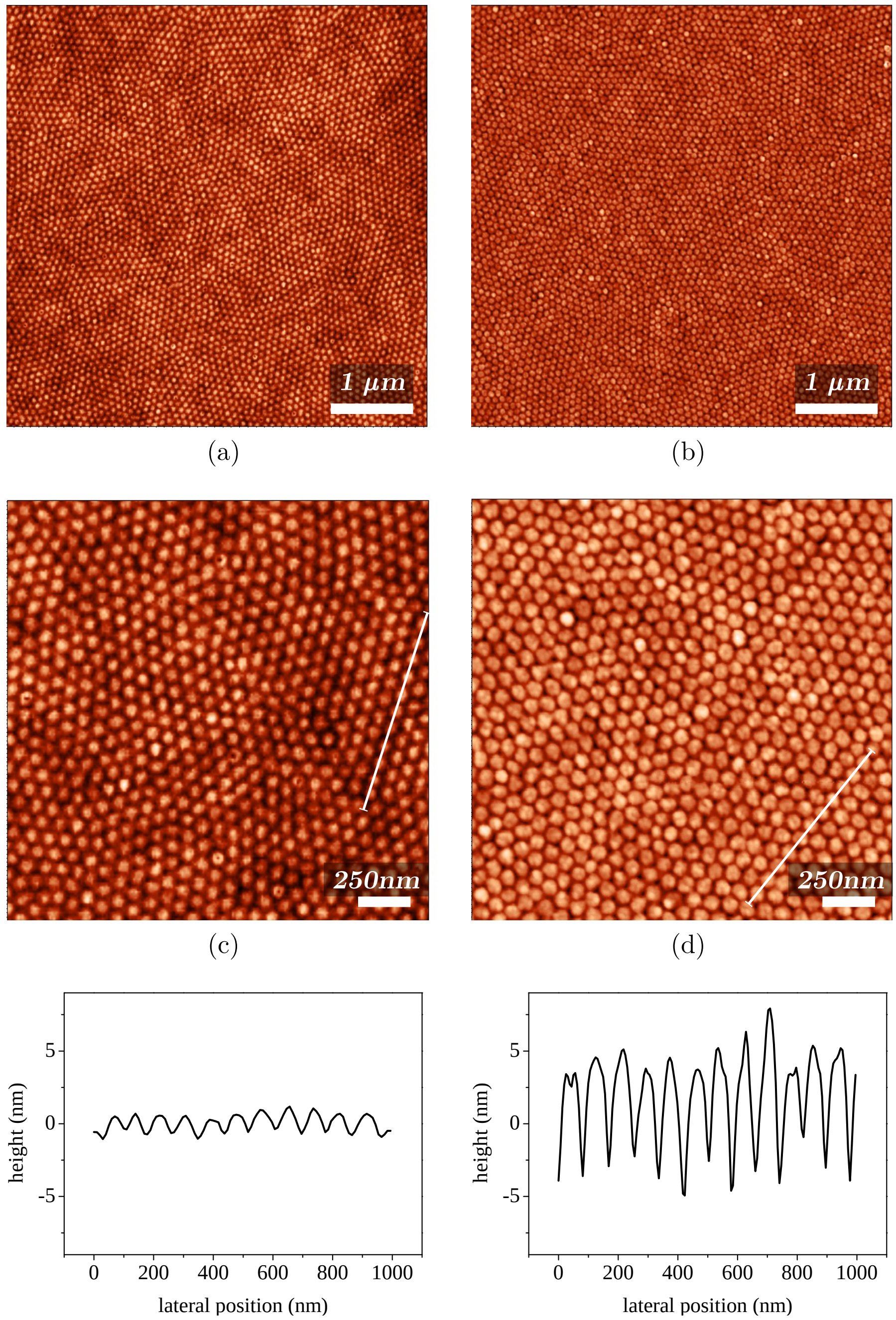

(a) (b)

(c) (d)

(e) section through (c) (f) section through (d)

Figure 9.5: Thin films of cylinder-forming PS-b-PMMA(63/142) on SiO_x substrates before (left column) and after UV irradiation and removal of the PMMA block by acetic acid (right column). Micrographs in each column show different areas of the same sample.

9.2 PS-b-PMMA on nanofaceted α-Al_2O_3 substrates

The PS-b-PMMA thin films on SiO_x discussed in section 9.1 exhibit uniformity in nanodomain size, shape, spacing, and orientation with respect to the surface. They lack, however, a long-range regularity in the lateral arrangement of nanodomains. There are essentially three different approaches followed to induce long-range positional order in diblock copolymers, mostly applied to thin films:

- Application of external fields
- Facilitation of self-assembly
- Control of surface interactions

A review on these approaches was published by Lazzari and co-editors [145]. Promising results have been achieved following the second approach by using substrates with chemically or topographically structured surfaces - mainly structured by lithographical methods [153–159]. Patterning a substrate with lithographical techniques, however, has severe drawbacks: As an example, e-beam lithography is serial and therefore slow; as compared to nanopatterning by self-assembly, only small areas can be patterned with justifiable effort. Nanoimprint lithography is parallel thus fast, but requires a defect-free master pattern to copy. In any case, lithographical patterning requires an additional extensive step in sample preparation, but yields highly controllable substrate surface patterns. On the other hand, a substrate patterned by a self-assembly process can be considerably easier to prepare, but the patterning will generally be less determinable and have a higher defect density. However, this need not impair the quality of long-range lateral ordering of the supported block copolymer [67].

In this work, nanofaceted α-Al_2O_3 substrates (see sections 1.2.3 and 7) were employed to guide the self-assembly of microphase separating diblock copolymer thin films. It has been established that the facets forming during annealing on the surface of initial M-plane α-Al_2O_3 have their edges all parallel to the $[11\bar{2}0]$ direction and are sufficiently uniform in spacing and peak-to-valley height over the entire substrate surface [23, 24, 28, 160]. These substrates are therefore very well-suited to induce long-range lateral order in diblock copolymer nanodomain placement over large sample areas[2].

---

[2] The substrate facets run vertically in all respective AFM topography micrographs shown here.

For fabricating nanofaceted α-Al_2O_3 substrates, M-plane α-Al_2O_3 wafers were annealed at 1325 °C to 1400 °C for 8 h to 12 h in air (see chapter 7). This resulted in facets of $L \approx 50$ nm to $L \approx 100$ nm and heights $h \approx 4$ nm to $h \approx 12$ nm (see also [23, 24, 28, 160]). PS-b-PMMA thin films on these substrates were prepared as described in sections 5.5 and 9.1.

9.2.1 Long-range lateral order

Even on a faceted substrate, the shape and equilibrium period D_0 determine the placement of diblock copolymer nanodomains. The substrate is expected to have little to no influence on the relative lateral placement of the diblock copolymer nanodomains, as long as the diblock copolymer thin film is not disrupted by the substrate facets. The relative nanodomain placement is therefore tolerant to structural defects in the substrate topography [67]. However, the substrate topography induces the preferential orientation of the lattice planes of the diblock copolymer domain pattern. The long axes of lamellar domains in symmetric diblock copolymers and the $\{10\}$ planes of the hexagonal domain pattern of asymmetric diblock copolymers align parallel to the facet edges [67, 161]. This avoids facet edges crossing domain boundaries, thus minimizes perturbations of the domain packing and reduces deformations of chains at the substrate interface [67].

Fig. 9.6 and 9.7 compare thin films of the symmetric, lamellae-forming diblock copolymer PS-b-PMMA(47/53) and the asymmetric, cylinder-forming PS-b-PMMA(63/142), respectively, on planar substrates and on nanofaceted α-Al_2O_3 substrates. AFM topography micrographs are shown along with corresponding Fourier transforms of the topographical information. The measured domain period D on both planar and nanofaceted substrates is compared to the calculated equilibrium domain period D_0 in order to confirm that the domain placement is not disturbed by the surface topography of nanofaceted substrates.

The presence of a faceted substrate has a significant impact on the long-range lateral ordering of PS-b-PMMA nanodomains: On SiO_x, the lamellar domains of the symmetric PS-b-PMMA(47/53) are isotropically oriented – the FFT shows a single ring with radius $r = \frac{q}{2\pi} = 21.0\ \mu m^{-1}$, which corresponds to a lateral period of $D = 47.6$ nm and thus (given the lateral instrumental resolution of 10 nm) to the calculated equilibrium domain period $D_0 = 41$ nm. The seeming orientational anisotropy indicated by the inhomogeneity of the ring is a local property of the selected AFM scan area. On faceted α-Al_2O_3 the lamellar domains align parallel with the facet edges –

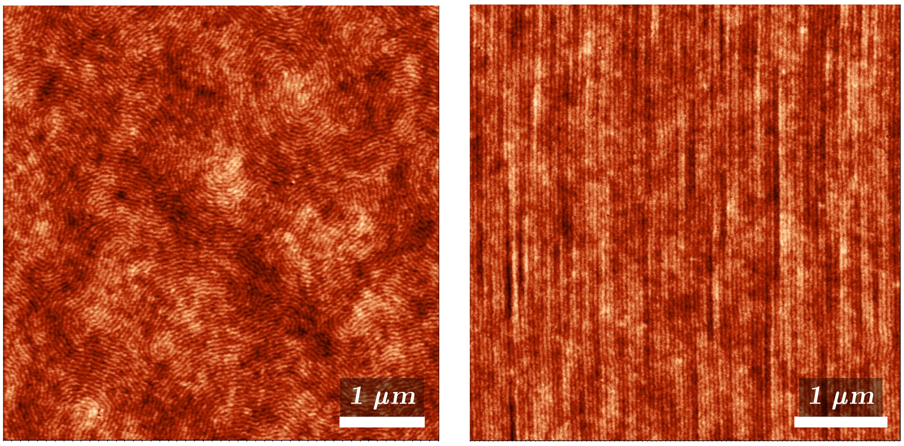

(a) on $\mathrm{SiO_x}$ (b) on faceted α-$\mathrm{Al_2O_3}$

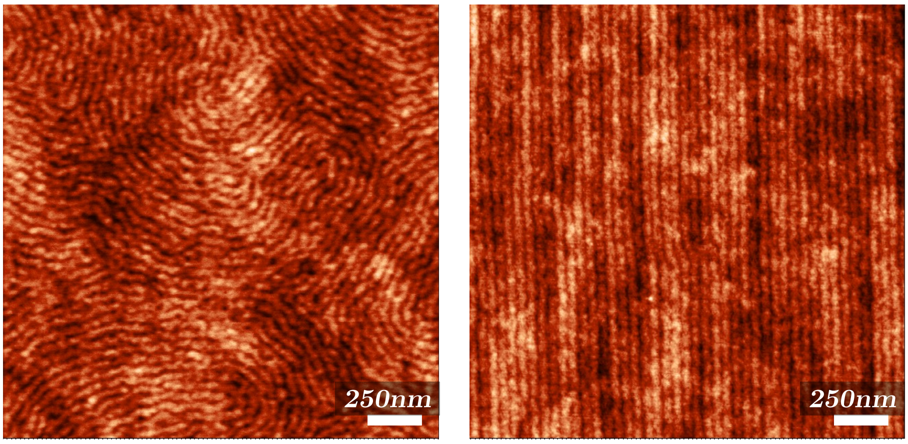

(c) on $\mathrm{SiO_x}$ (d) on faceted α-$\mathrm{Al_2O_3}$

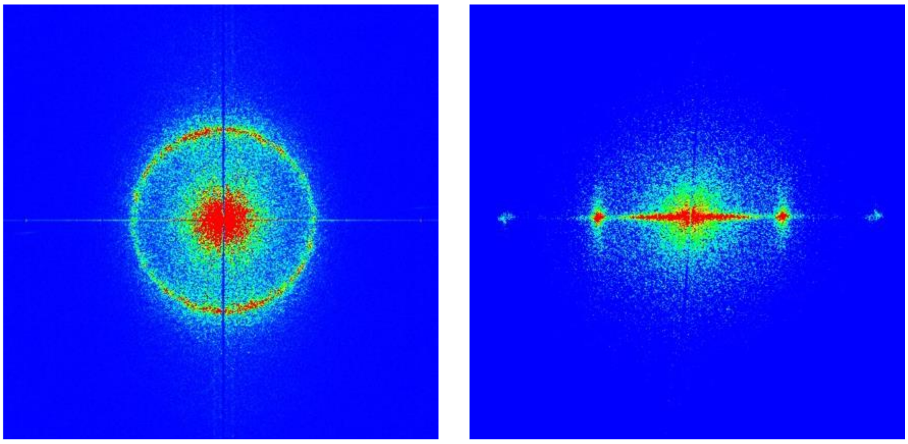

(e) FFT of (a) (f) FFT of (b)

Figure 9.6: Comparison of lateral domain ordering in thin films of symmetric, lamellae-forming PS-b-PMMA(47/53) on $\mathrm{SiO_x}$ (left) and on faceted α-$\mathrm{Al_2O_3}$ substrates (right). Each column shows data from the same sample.

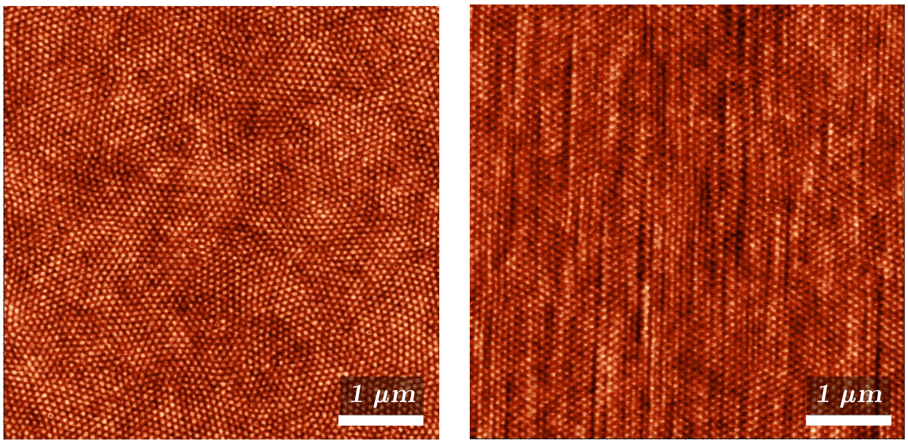

(a) on SiO_x (b) on faceted α-Al_2O_3

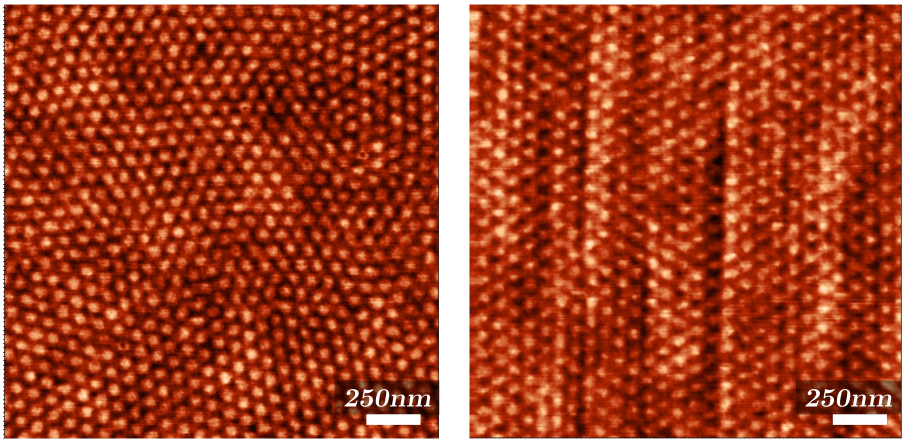

(c) on SiO_x (d) on faceted α-Al_2O_3

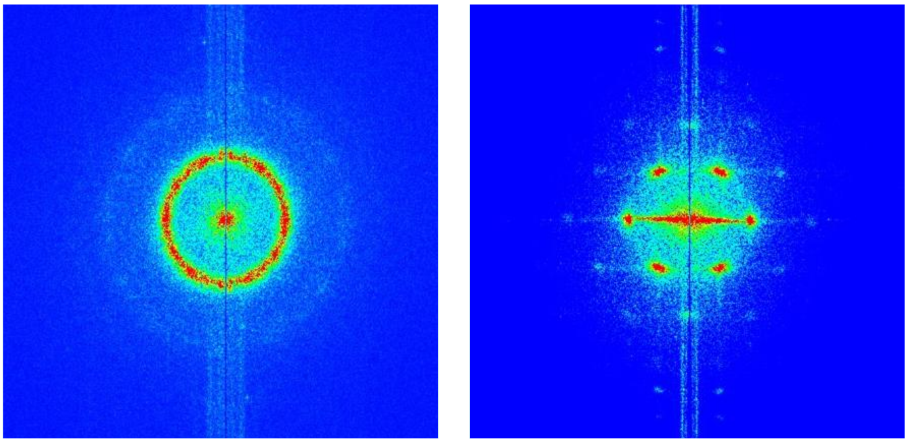

(e) FFT of (a) (f) FFT of (b)

Figure 9.7: Comparison of lateral domain ordering in thin films of asymmetric, cylinder-forming PS-b-PMMA(63/142) on SiO_x (left) and on faceted α-Al_2O_3 substrates (right). Each column shows data from the same sample.

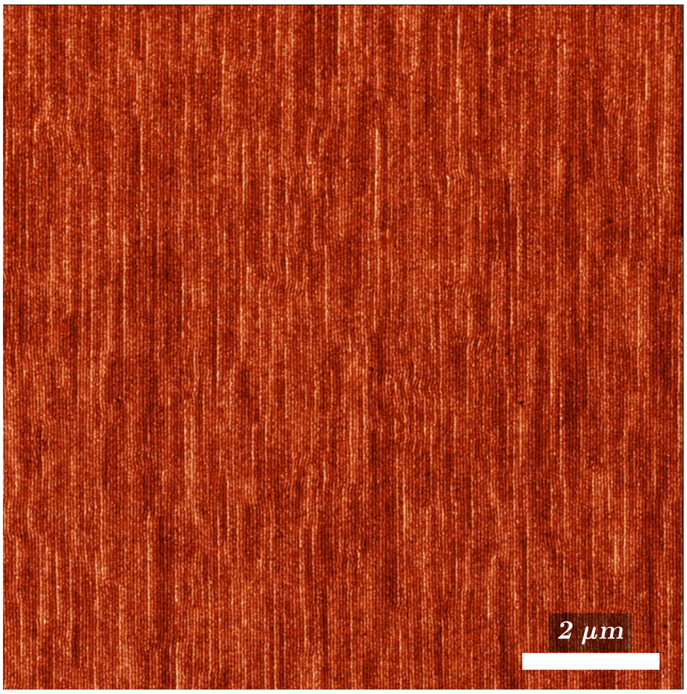

(a) Lamellae-forming PS-b-PMMA(47/53)

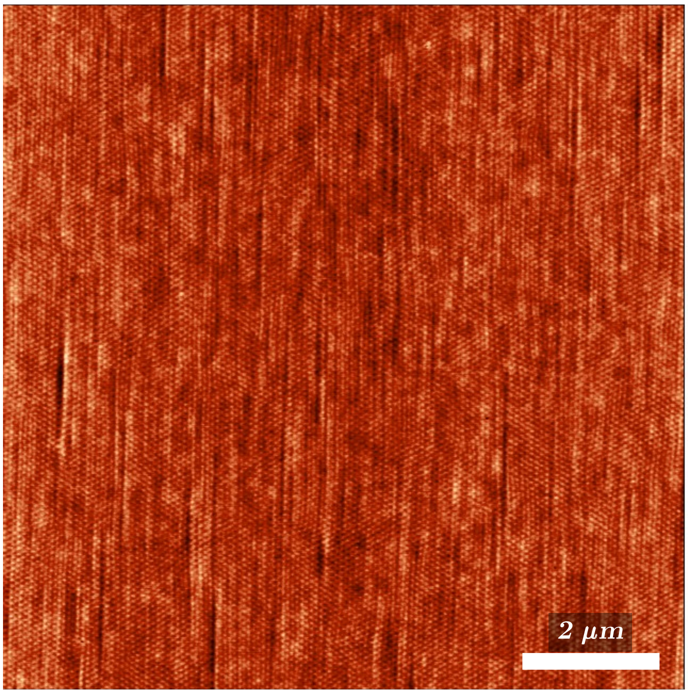

(b) Cylinder-forming PS-b-PMMA(63/142)

Figure 9.8: Thin films of (a) symmetric, lamellae-forming PS-b-PMMA(47/53) and (b) asymmetric, cylinder-forming PS-b-PMMA(63/142) on faceted α-Al_2O_3 substrates (right).

the FFT has distinct maxima of two orders in a two-fold symmetry reflecting the high degree of translational order. The distances of the maxima from the origin are $r_1 = \frac{q}{2\pi} = 21.5\ \mu\text{m}^{-1}$ and $r_2 = \frac{q}{2\pi} = 43.0\ \mu\text{m}^{-1}$, corresponding to a lateral period of $D = 46.5$ nm and $D/2 = 23.3$ nm, respectively. These values are again in good agreement with the calculated equilibrium domain period $D_0 = 41$ for PS-b-PMMA(47/53): The spacing of the lamellar domains is not considerably stretched or compressed by the periodically faceted substrate. The cylindrical PS nanodomains of the asymmetric PS-b-PMMA(63/142) (see Fig. 9.7) on SiO_x are laterally ordered on a short range: They adopt hexagonal packing within grains of a few μm^2 which are themselves isotropically oriented – the FFT exhibits one pronounced ring ($r = \frac{q}{2\pi} = 13.7\ \mu\text{m}^{-1}$, which corresponds to a lateral period of $D = 73.0$ nm) and one weak higher order ring, indicative of high uniformity in the lateral characteristic length given by D_0; but also evidencing the lack of orientational ordering of the grains. On α-Al_2O_3 almost all grains are aligned with their (10) directions parallel to the edges of the substrate facets – the FFT has distinct maxima of two orders in a six-fold symmetry reflecting the long-range hexagonal packing of the PS nanodomains. The distances of the maxima from the origin are $r_1 = \frac{q}{2\pi} = 13.5\ \mu\text{m}^{-1}$ and $r_2 = \frac{q}{2\pi} = 27.0\ \mu\text{m}^{-1}$, corresponding to a lateral period of $D = 74.1$ nm and $D/2 = 37.0$ nm, respectively. As observed for the lamellae-forming PS-b-PMMA(47/53), the faceted substrate does not influence the domain spacing in the cylinder-forming PS-b-PMMA(63/142). AFM topography micrographs, extending over larger scan areas of 10 μm × 10 μm to emphasize the long range of nanodomain ordering in PS-b-PMMA (47/53) and PS-b-PMMA(63/142) on faceted α-Al_2O_3, can be seen in Fig. 9.8[3].

9.2.2 Dependence of film morphology on PS-b-PMMA film thickness and substrate facet dimensions

The diblock copolymer film must be adapted to the substrate facet peak-to-valley height. In case the copolymer film is too thin, the facets may protrude through the film and distort shape and spacing of the diblock copolymer domains. If the film is too thick, the guiding effect of the facets on the domain pattern orientation is lost.

---

[3] Fig. 9.8(b) shows a template after deposition of ^{57}Fe (see section 10). This increases the height differences on the sample surface, thus emphasizing the surface topography corresponding to the chemical domain patterning.

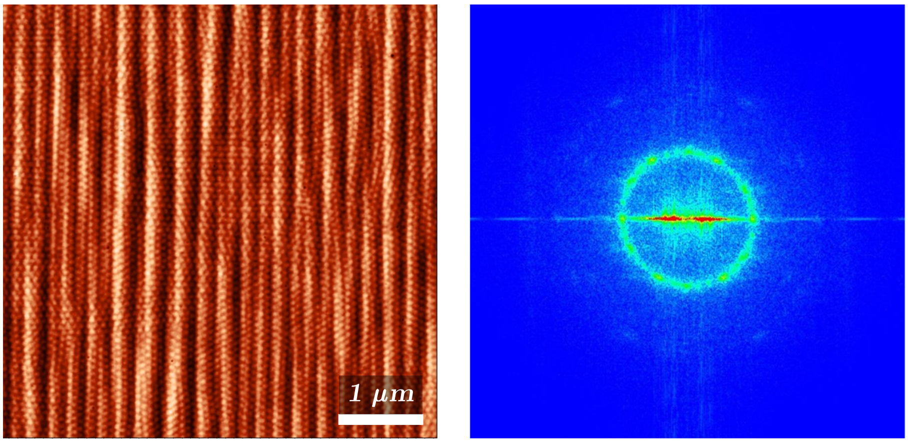

(a) d_8 = 37.5 nm (b) FFT of (a)

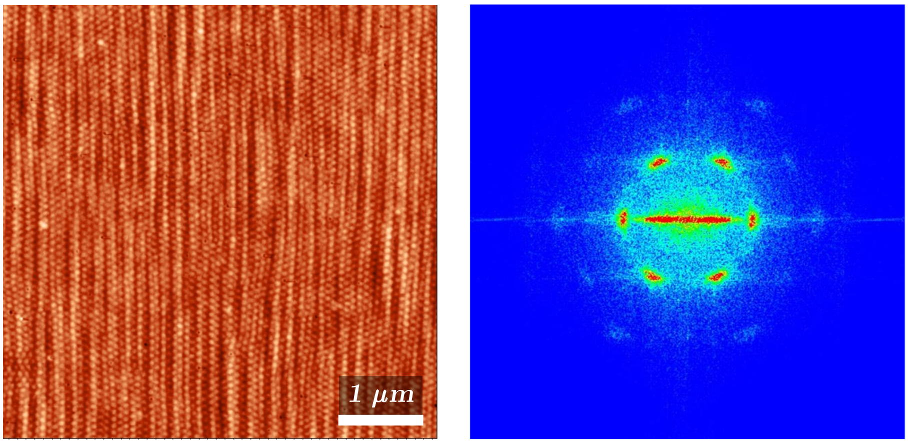

(c) d_{10} = 44 nm (d) FFT of (c)

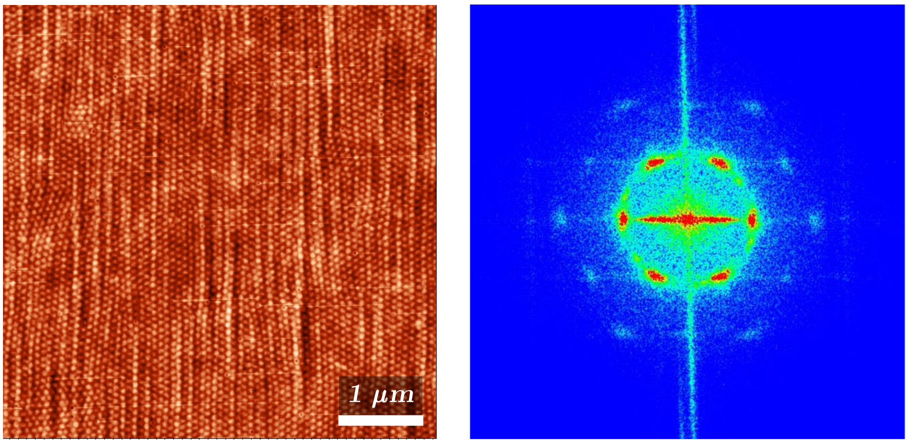

(e) d_{12} = 54.5 nm (f) FFT of (e)

Figure 9.9: AFM topography micrographs and corresponding Fourier transforms for thin films of cylinder-forming PS-b-PMMA(63/142) of different thicknesses $d_8 < d_{10} < d_{12} < D_0$ on faceted α-Al_2O_3 substrates ($L \approx 190$ nm, $h \approx 15$ nm).

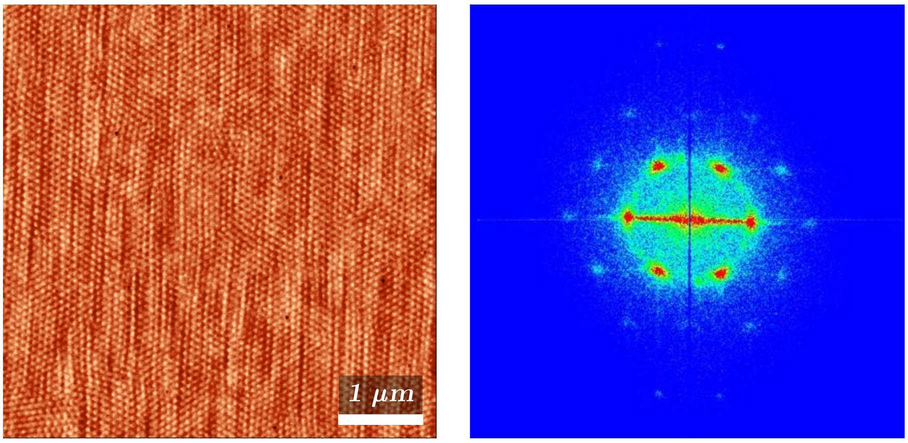

(a) $d_8 = 37.5$ nm (b) FFT of (a)

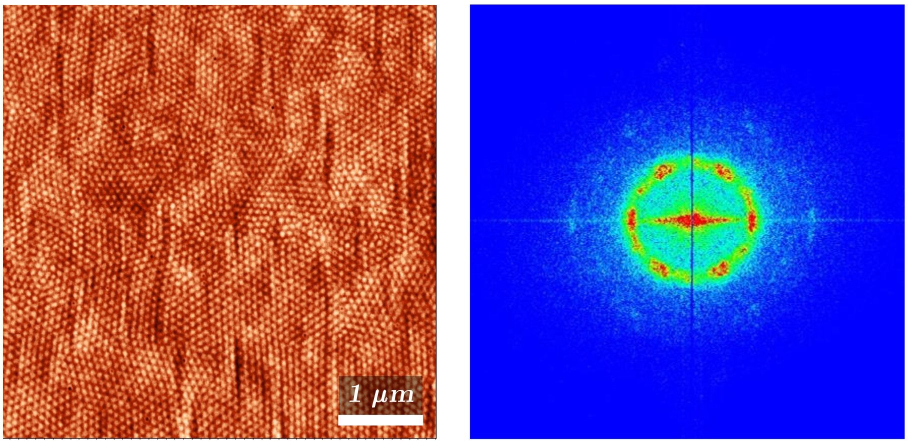

(c) $d_{10} = 44$ nm (d) FFT of (c)

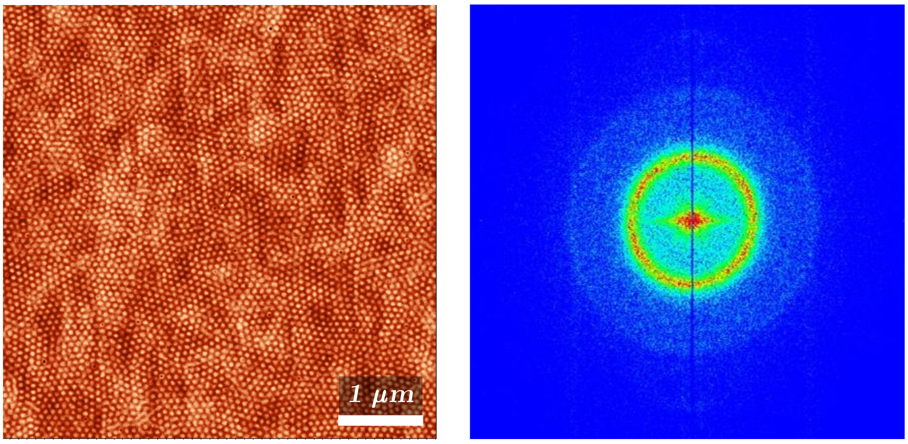

(e) $d_{12} = 54.5$ nm (f) FFT of (e)

Figure 9.10: AFM topography micrographs and corresponding Fourier transforms for thin films of cylinder-forming PS-b-PMMA(63/142) of different thicknesses $d_8 < d_{10} < d_{12} < D_0$ on faceted α-Al_2O_3 substrates ($L \approx 65$ nm, $h \approx 5$ nm).

The series of PS-b-PMMA(63/142) thin films on faceted α-Al_2O_3 substrates shown in Fig. 9.9 was cast from solutions of increasing concentrations, resulting in increasing film thicknesses. All samples were prepared on pieces of the same substrate, thus the topographical features of the substrates can be assumed to be identical for all samples. It is apparent that a flatter film surface is achieved for thicker films. The substrate facets modulate the film surface and hinder long-range ordering of the PS nanodomains, as is especially evident for the thinnest film of thickness $d_8 = 37.5$ nm ($c = 8$ mg/ml). Best film flatness and highest degree of lateral nanodomain ordering are achieved for the thickest film of thickness $d_{12} = 54.5$ nm ($c = 12$ mg/ml).

The substrate supporting the PS-b-PMMA(63/142) thin films in Fig. 9.9 had large facets ($L \approx 190$ nm, $h \approx 15$ nm) as compared to the faceted α-Al_2O_3 substrates used for most of the other samples. Therefore, Fig. 9.10 illustrates the effect of increasing the film thickness on a substrate with considerably smaller facets ($L \approx 65$ nm, $h \approx 5$ nm). The sample topographies are shown along with corresponding Fourier transforms of the topographical information. Thus, the loss of long-range hexagonal order with increasing film thickness becomes evident: The long-range hexagonal order of the nanodomains of the thinnest film of thickness $d_8 = 37.5$ nm ($c = 8$ mg/ml) is reflected in the six-fold symmetry of the maxima in the corresponding Fourier transform. The grains in the intermediate film still tend to align with the facet edges, but the decrease in the degree of orientational order of the grains as compared to the thinnest film is apparent in the Fourier transform of the topographic information. In the thickest film of thickness $d_{12} = 54.5$ nm ($c =$ 12 mg/ml), all influence of the faceted substrate on the nanodomain ordering is lost; the PS nanodomains are isotropically arranged and the corresponding Fourier transform shows no anisotropy.

Park and coworkers [67] studied asymmetric diblock copolymers on faceted α-Al_2O_3 substrates. They found best nanodomain ordering for a ratio of diblock copolymer film thickness d and substrate peak-to-valley height h of $d/h \approx 8$. With a film thickness of $d = 37.5$ nm, a very similar ratio of d/h $= 7.5$ is found here for the asymmetric PS-b-PMMA(63/142).

9.2.3 Commensurability of nanodomain period and substrate periodicity

Attention must be paid to the relation of the diblock copolymer equilibrium period and the facet period of the substrate. Park and coworkers [67] concluded from their studies, that the optimum ratio of substrate facet spacing

L and diblock copolymer equilibrium period D_0 is $L/D_0 \leq 3$. Rockford and coworkers [161] investigated symmetric diblock copolymers on Si(113) substrates, which were faceted by annealing and additionally chemically patterned by metal evaporation. The ratio of diblock copolymer film thickness d and substrate peak-to-valley height h in their samples was $d/h \approx 3$. By varying the diblock copolymer molecular mass, i.e. the equilibrium domain period D_0 (see Eq.(2.23)), they found that optimum control over the diblock copolymer domain ordering was gained, if the mismatch $\Delta = 1 - D_0/L$ between the diblock copolymer equilibrium period D_0 and substrate facet period L was less than $\Delta = \pm 0.25$. Defects in the ordering of the diblock copolymer domains – such as dislocations, merging of domains, or grain reorientations – are attributed to the mismatch and to structural imperfections of the substrate [161]. For all diblock copolymers investigated here, samples exhibited best lateral ordering of nanodomains, if the ratio of substrate facet spacing L and diblock copolymer equilibrium period D_0 was close to one. This is in agreement with the findings of Rockford and coworkers, who used diblock copolymers of molecular masses comparable to those of PS-b-PMMA(47/53), PS-b-PMMA(63/142), and PS-b-PMMA(203/203) [161]. For PS-b-PMMA(26/68), a high degree of lateral ordering was also found for facet spacings L being considerably larger than the equilibrium period D_0 (up to $L/D_0 \approx 2.3$, samples with larger facet spacing L were not prepared). This is rather in agreement with the results of Park and coworkers, who studied diblock copolymers of very low molecular mass [67]. It may be due to the fact, that achieving a high degree of lateral nanodomain ordering is in general more facile for diblock copolymers with lower molecular mass. Commensurability between the substrate period and the diblock copolymer period may be of lesser importance then.

9.2.4 PS-b-PMMA molecular mass

The translational ordering of nanodomains and orientational ordering of grains in a diblock copolymer domain pattern improves with decreasing equilibrium period D_0, i.e. with decreasing degree of polymerization N or total molecular mass M (see Eq.(2.23)), i.e. in fact with the increasing chain mobility for lower molecular mass [67, 162]. This is already indicated in the morphologies of thin films of the high molecular mass PS-b-PMMA(203/203) and the low molecular mass PS-b-PMMA(47/53) on flat substrates - compare Figs. 9.2 (d) and (f). While for PS-b-PMMA(203/203) the run of one domain has little influence on the run of the adjacent domain, in PS-b-PMMA(47/53) groups of several domains are observed to run in parallel. This stronger

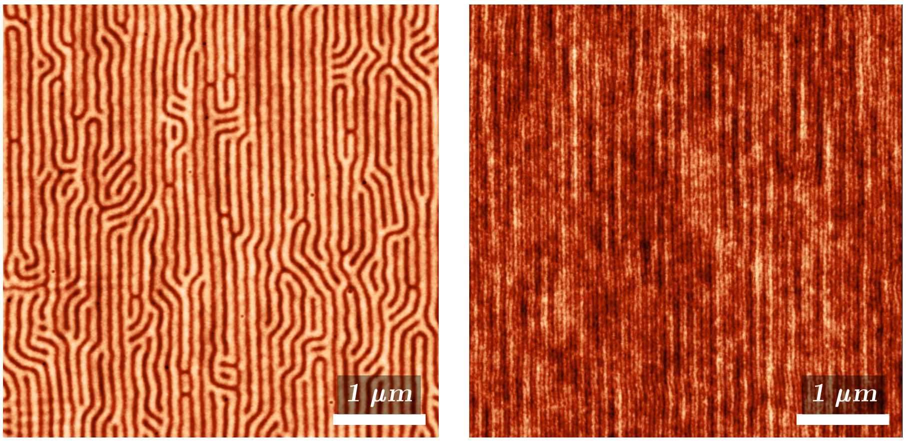

(a) $M = 406$ kg/mol (b) $M = 100$ kg/mol

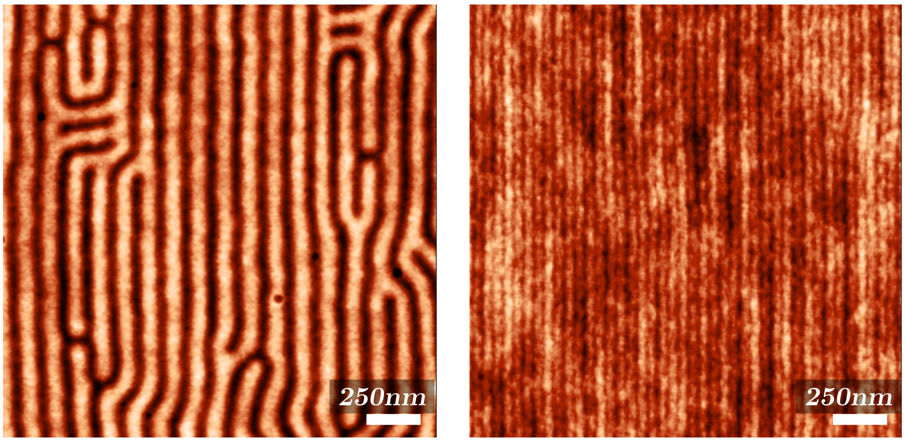

(c) $M = 406$ kg/mol (d) $M = 100$ kg/mol

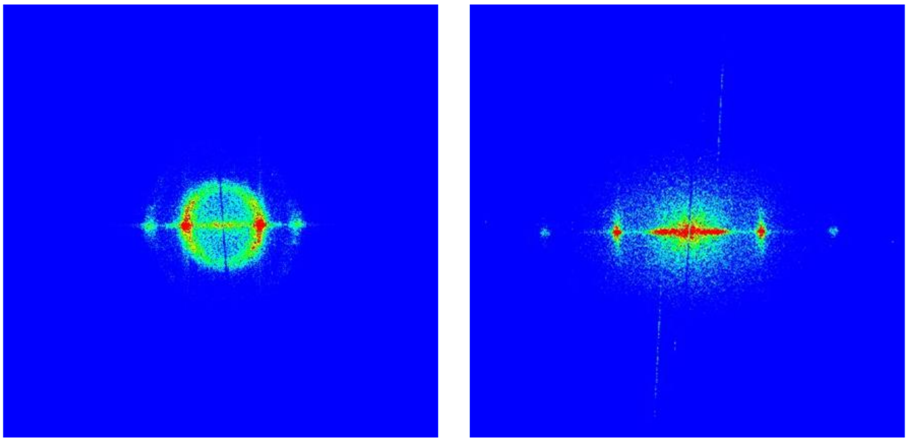

(e) FFT of (a) (f) FFT of (b)

Figure 9.11: Thin films of lamellae-forming PS-b-PMMA of high and low molecular mass on faceted α-Al_2O_3 substrates, showing the higher degree of lateral domain ordering in the low molecular mass diblock copolymer. Each column shows data from the same sample.

tendency for lateral domain ordering is amplified by a structured substrate surface. It becomes thus clearly evident when contrasting the two symmetric diblock copolymers PS-b-PMMA(203/203) and PS-b-PMMA(47/53) on nanofaceted α-Al_2O_3 substrates, see Fig. 9.11. For the high molecular mass diblock copolymer PS-b-PMMA(203/203), the Fourier transform of the AFM topography micrograph features a ring and broadened maxima, reflecting the lateral disorder of the nanodomains. For the low molecular mass diblock copolymer PS-b-PMMA(47/53), the Fourier transform exhibits only slightly broadened maxima in a distinct two-fold symmetry, evidencing the high degree of lateral order in this type of sample.

9.2.5 Removal of the PMMA block by acetic acid

The PMMA block can also be removed from PS-b-PMMA thin films on faceted α-Al_2O_3 substrates, using the same routine as described in section 9.1.4. Removing the PMMA block from the diblock copolymer film significantly increases the height contrast in the AFM topography micrograph, see Fig. 9.12. This in turn increases the number of higher order maxima in the corresponding Fourier transforms and thus allows to better appreciate the high degree of uniformity and lateral ordering in the PS domains.

Regular nanopatterns of various materials can be fabricated from such templates, e.g. by depositing nanoparticles onto the template and then removing the PS domains together with excess nanoparticles, leaving nanoparticles in the volume previously occupied by PMMA [163]. This routine may especially be interesting for materials which exhibit no strong selectivity for one of the two blocks of the diblock copolymer.

This work, however, will focus on highly ordered nanopatterns prepared on intact PS-b-PMMA templates. Nanopatterning is accomplished by making use not of the topographical but of the chemical surface structure of the microphase separated diblock copolymer films and of the selectivity of the deposited materials for the PS block.

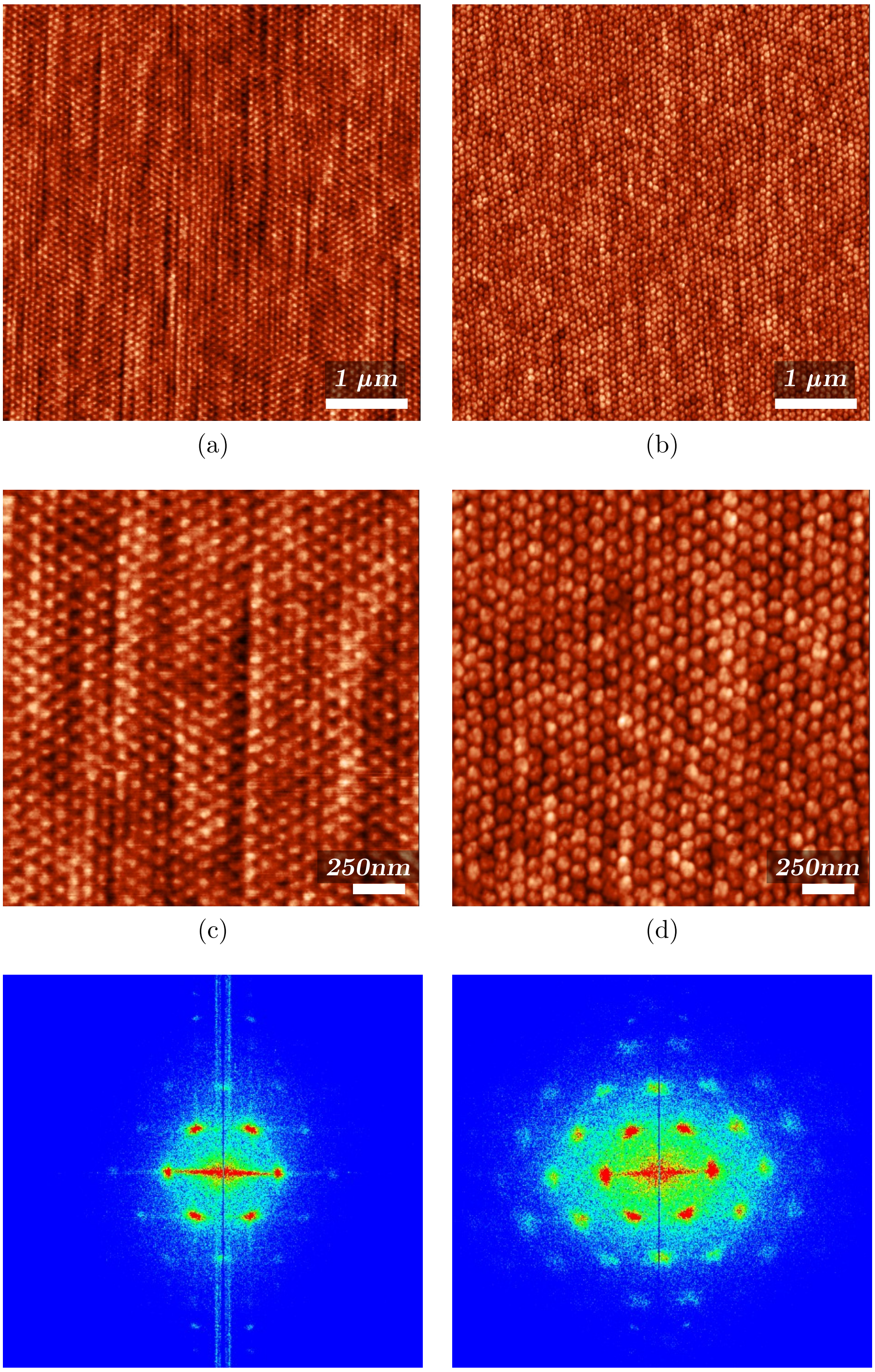

(a) (b) (c) (d)

(e) FFT of (a) (f) FFT of (b)

Figure 9.12: Thin films of cylinder-forming PS-b-PMMA(63/142) on faceted α-Al_2O_3 substrates before (a, b) and after UV irradiation and removal of the PMMA block by acetic acid (c, d). Each column shows data from the same sample.

10 Metal Nanostructures On Diblock Copolymer Templates

An intriguing way of preparing large, ordered arrays of uniform metallic nanostructures via self-assembly is by sputter deposition onto microphase-separated diblock copolymer templates. Although – in contrast to sputter deposition onto faceted α-Al_2O_3 substrates under shallow polar angles (see section 8.1.1) – the entire template surface is exposed to the sputtered atoms, well-defined nanostructures form reproducing the template pattern of chemical surface domains. On microphase-separated diblock copolymer templates, the mechanism of metallic nanostructure formation is not of geometrical but of chemical nature.

The microphase-separated diblock copolymer template films with surface perpendicular domain orientation present chemically patterned surfaces to the sputtered atoms, with distinct conditions for adhesion or surface diffusion within the different chemical surface domains. Given suitable kinetic conditions, this results in the metal atoms agglomerating on one type of chemical surface domain and clearing the other.

The possible morphologies and the long-range regularity of these templates were described in chapter 9. This chapter presents the morphological and magnetic properties of metallic nanostructures grown on microphase-separated diblock copolymers.

10.1 Energetic and kinetic considerations

For understanding the self-assembly of metals into nanostructures on diblock copolymer templates, it is important to clarify some energetic and kinetic properties of these systems. Having fabricated diblock copolymer templates with highly-ordered chemical surface patterning (see section 9.2), ideally one would now want to deposit metal atoms on the template surface and see them replicate any chemical surface pattern of the template, guided by the differing interactions between the metal and the chemically distinct copolymer blocks of the template[1]. However, from an energetic point of view, it is not apparent why the metal atoms should do so. Kinetic aspects must be taken into account. It turns out that metal nanostructures deviating from a spherical, minimum-surface shape are non-equilibrium states, even on a chemically patterned polymeric surface. Nevertheless, they can be prepared under certain conditions and preserved for periods of time exceeding many months [165, 166].

Ag and Au on microphase separated PS-b-PMMA templates have been studied as model systems to investigate the disparate self-assembly behavior of different metals on polymer templates [164–167]. On a template of PS-b-PMMA with surface-perpendicular lamellar domains (see e.g. Fig. 9.11) Au never formed elongated nanostructures to accommodate with the chemical surface patterning under the given deposition conditions. Ag, however, self-assembled under certain preparation conditions into continuous nanowires decorating the PS domains [165, 166] (see Fig. 10.1).

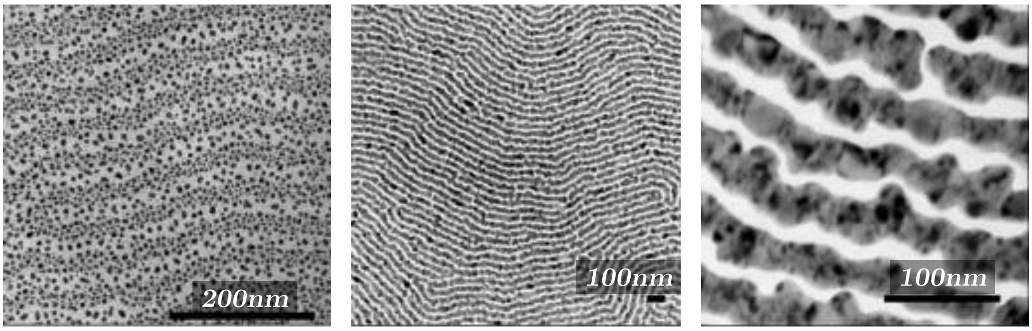

(a) (b) (c)

Figure 10.1: As-deposited nanostructures of (a) Au and (b, c) Ag on microphase-separated diblock copolymer templates with lamellar chemical surface patterning. Both Au and Ag prefer to adsorb to the PS block, but only Ag forms elongated nanowires following the template pattern. From [165].

---

[1] The height profile of the diblock copolymer template (which allows to infer their chemical surface structure from AFM topography measurements, see chapter 9) appears to have no influence on the positioning of metal atoms or clusters: They are not found at the chemical domain boundaries, where height steps occur, but centered on their preferred domains (see [164] and references therein).

This finding raises the question, whether or not nanowires can be an equilibrium morphology for a self-assembling metal on a diblock copolymer template. The question is answered by comparing the total free energies $F^{sp,el}$ of a spherical (sp) and an elongated (el) metal nanoparticle of identical volume on the same chemically patterned PS-b-PMMA surface (see Fig. 10.2) [167]:

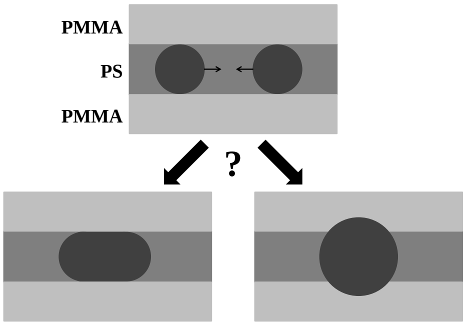

Figure 10.2: From [167], modified.

$$F^{sp,el} = \gamma_{m,vac} A^{sp,el}_{m,vac} + \gamma_{m,PS} A^{sp,el}_{m,PS} + \gamma_{m,PMMA} A^{sp,el}_{m,PMMA} \tag{10.1}$$

where $\gamma_{i,j}$ are the free energy densities of the metal / vacuum and metal / polymer block interfaces and $A^{sp,el}_{i,j}$ denote the respective contact areas for a spherical or an elongated nanoparticle. It is assumed that the spherical particle is centered on but not restricted to the PS domain, while the elongated particle is strictly confined to the PS domain. $\gamma_{m,PS}$ and $\gamma_{m,PMMA}$ differ noticeably, but $\gamma_{m,vac}$ is larger than both by an order of magnitude. Therefore, the surface tension of the metal is expected to determine the equilibrium shape of a metal nanoparticle on a polymeric template surface, leading to spherical nanoparticles irrespective of the chemical patterning of the template. Indeed, by inserting the corresponding values into Eq.(10.1) a difference of $F^{el} - F^{sp} \approx 10^4 k_B T$ is obtained for T being room temperature. Thus, elongated structures such as the continuous nanowires formed by Ag are not equilibrium shapes for a metal on a polymeric template.

The fact that they are observed and can even be preserved for considerable periods of time can only be explained by considering the kinetic aspects of the metal / polymer system. There are three relevant time scales in these systems: The equilibration time t_{eq}, which it takes a nanoparticle to reach its equilibrium shape, the finding time t_f, which it takes two atoms or clusters to impinge on each other while each is diffusing on the template surface, and the deposition time t_d, which it takes to deposit all atoms required for the desired structure onto the template surface [167]. Given typical values for diffusion constants of clusters and their distances on a surface, the finding time is on the order of $t_f \approx 1$ s (see also references in [167]). Typical deposition times t_d range from minutes to few hours. For estimating the equilibration time t_{eq}, the nanoscopic size of the metallic structures is crucial: The widely accepted and employed theory of Herring, Nichols, and Mullins [19,168,169], stating that the equilibration time scales with the number of atoms N in the particle as $t_{eq} \propto N^{4/3}$, does not hold for nanoscale objects at temperatures well below their roughening or melting temperatures. Instead, t_{eq} scales with N with a significantly larger exponent, up to $t_{eq} \propto N^7$, depending on the temperature [170]. At room temperature, equilibration times can be as long as many months, i.e. $t_{eq} \gg t_f, t_d$ [167]. This allows for the formation of elongated nanostructures following the chemical patterning of the template[2]. However, even under the same deposition conditions, only some metals do reproduce the template pattern [165, 166]. Apart from the metal being kinetically allowed to form elongated nanostructures, the metal also has to exhibit an adequate selectivity towards the two components of the diblock copolymer template. Investigations of diblock copolymer films deposited on metal coated substrates indicate that metal atoms and copolymer molecules interact via contact interaction (see [164] and references therein), depending on the specific combinations of metal and polymer species. This results in different metal diffusion constants, i.e. mobilities of metal atoms and clusters, on the different template surface domains. Since the diffusion constants depend on the metal / polymer combination, different metals favor different domains on the same template. For example, on a PS-b-PMMA template, Ag and Au preferably adsorb to the PS domains, while In, Pb, Sn, and Bi prefer to adsorb to the PMMA domain. On the one hand, the difference in metal diffusion constants $D_i < D_j$ must be large enough, i.e. the mobility ratio $m \approx D_i/D_j$ must be sufficiently near to zero. On the other hand, the sticking coefficient $S = 1 - \exp\left(-E_b/k_B T\right)$ (with the metal-metal bond energy E_b) must be of a value which avoids that large, immobile clusters form sooner than the metal can migrate to the preferred domain. Only then will the metal behave effectively selective toward the chemical components of the template, i.e. clear one domain and aggregate on the other. There is no theoretical elaboration on this effect, but it has been demonstrated by Monte Carlo simulations [165, 166].

In summary: Depending on the deposition conditions, either energetics or kinetics can govern the metal self-assembly and prohibit or permit the formation of elongated nanostructures. Sufficient selectivity of the metal for one of the blocks in the copolymer template is required for elongated nanostructures to actually form. If the metal atom mobility allowing for selective wetting of one of the copolymer blocks is to be augmented by increasing the temperature, the simultaneous reduction of the equilibration time must be kept in mind.

---

[2] The metal deposition rate does not qualitatively influence the nanostructure morphology [165], because $t_{eq} \gg t_d$.

10.2 Morphologies of self-assembled metal nanostructures

Au, Ag, Ni, Pt, and Fe were deposited onto diblock copolymer templates of asymmetric, cylinder-forming PS-b-PMMA and symmetric, lamellae-forming PS-b-PMMA (see chapter 9) by sputter deposition. The aim was to prepare smooth nanostructures reproducing the chemical domain pattern of the template surface, as is schematically sketched in Fig. 5.10. With the given resources regarding time and manpower, this was not achieved for all metals. However, the morphologies shown in this section may give an impression of the diverse behavior of different metals on PS-b-PMMA templates, but also of the potential of the proposed nanostructure preparation routine.

The samples depicted in the AFM micrographs were prepared in the in-situ UHV deposition chamber (see section 5.5). The metals were deposited stepwise, in deposition steps of a few minutes each with intermissions of a few minutes. The metal deposition rates vary, but are not expected to have any qualitative influence on the resulting metal nanostructure morphology [166].

In the deposition chamber a magnetic field with a strength of up to $H_{ext} = 750$ Oe can be applied in the sample plane. The presence of this external field during metal deposition was not found to influence the resulting morphology qualitatively, but it changes the deposition rate via its effect on the Ar plasma in the chamber.

The depicted samples were prepared at template temperatures ranging from 140 °C to 175 °C . The metal diffusion constant is proportional to temperature and inversely proportional to the metal cluster size. Thus, in order to mobilize larger clusters and allow for selective nanostructure formation on the template, it can be required to raise the sample temperature during deposition [166, 171]. However, the equilibration time t_{eq} is reduced by increasing the temperature [170]. These two effects have to be appropriately balanced to allow for the formation of nanostructures reproducing the template pattern. If the equilibration time at this increased temperature is longer than the deposition time, non-equilibrium structures can still form. They can be preserved by quenching the sample after deposition, thus increasing the equilibration time again to the order of many months.

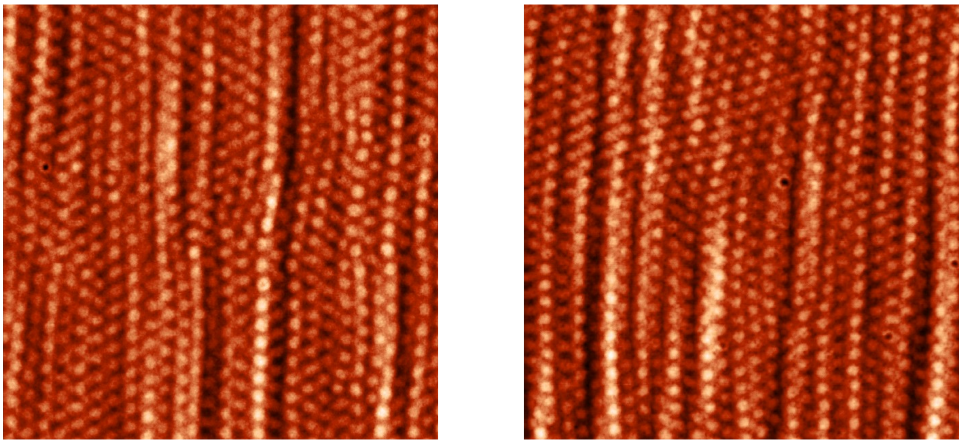

(a) as-prepared template

(b) template after heating

Figure 10.3: AFM micrographs (scan area: 2 μm × 2 μm) of a PS-b-PMMA film on faceted α-Al_2O_3 before and after heating for 2 h at 200 °C. The morphology does not change, as long as the order-disorder transition temperature of $T \approx 300$ °C is not exceeded.

The domain morphology of the diblock copolymer template is stable under heating as long as the order-disorder temperature is not exceeded [52, 165]. For PS-b-PMMA the respective temperature range is 105 °C $\lesssim T \lesssim$ 300 °C. The template stability was confirmed by imaging the morphology of a template with surface-perpendicular PS domains in a PMMA matrix before and after heating at 200 °C for 2h (see Fig. 10.3).

Among the number of samples prepared, smooth nanostructures reproducing the chemical domain pattern of the template surface were achieved readily for Ni, Pt, and Fe, rarely for Ag, and not for Au. Au forms small clusters of about 10 nm to 20 nm in diameter (see Fig. 10.4 (c, d)). A slight preference for decorating the minority PS domains of the template surface was observed for deposition at 200 °C template temperature, hinting at the increased cluster mobility at higher temperatures. Au is not known to exhibit qualitatively different behavior for other deposition conditions [164–166], especially not to form elongated nanostructures. For the other elements, small metal clusters left on the unpreferred PMMA domain can be present to different extents.

For most deposition conditions, Ag growth resulted in a morphology dominated by small clusters alike Au, but with the effective selectivity for the PS domains more strongly evidenced by the higher number density of Ag clusters on these domains (see Fig. 10.1 and [165, 166]). However, different behavior was observed for low Ag coverage (nominal thickness ≈ 0.4 nm) deposited at 140 °C: Ag formed nanodots on the surface domains of the minority component PS and can also be seen to form elongated nanostructures where the template provides for this due to imperfect PS domain orientation.

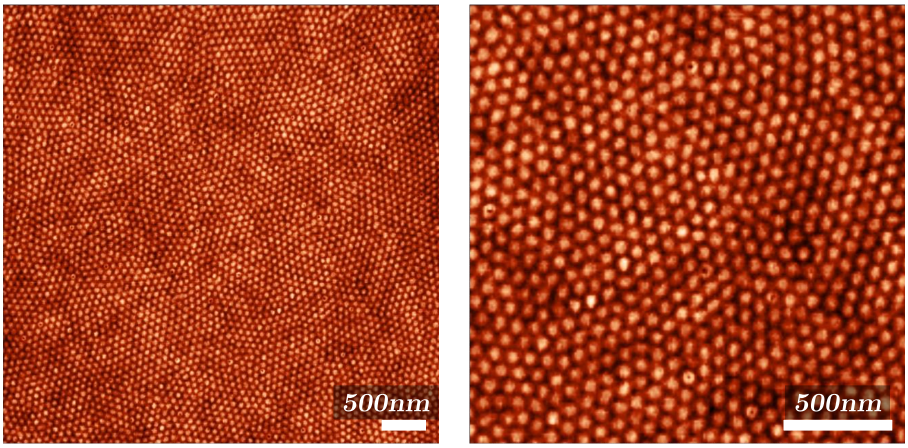

(a) template type (b) template type

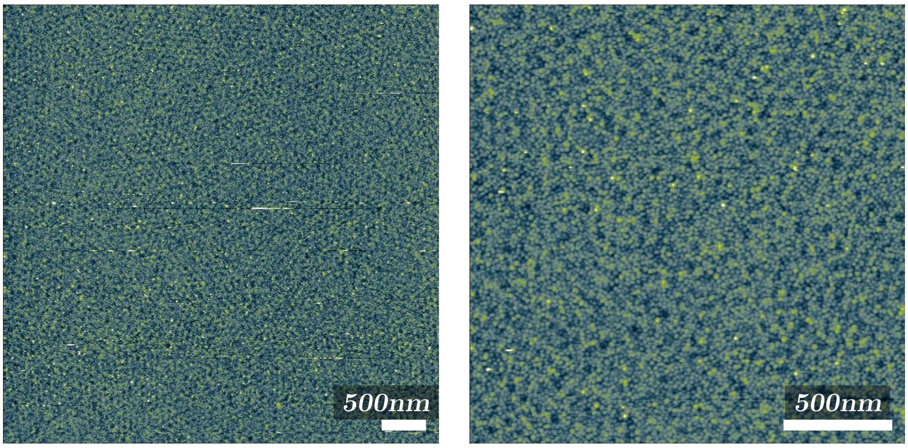

(c) Au (d) Au

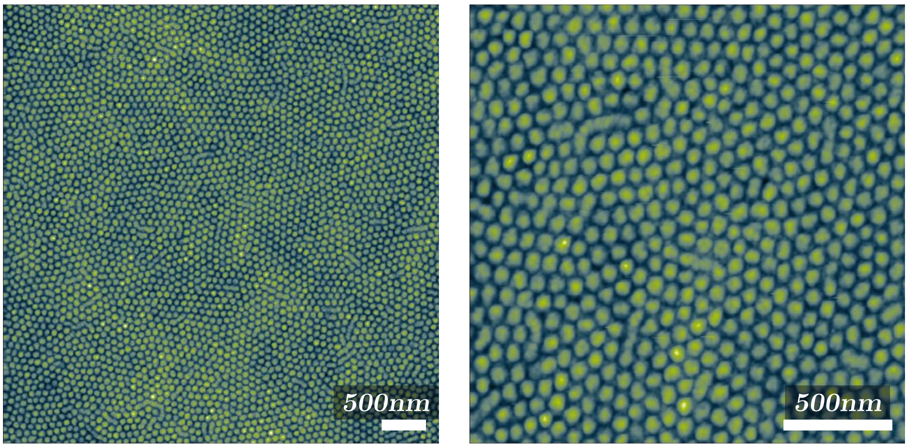

(e) Ag (f) Ag

Figure 10.4: (a) - (b) Diblock copolymer template of asymmetric PS-b-PMMA(63/142) before metal deposition. (c) - (f) Au and Ag sputter deposited on the templates at 140 °C. Micrographs in each row show areas on the same sample.

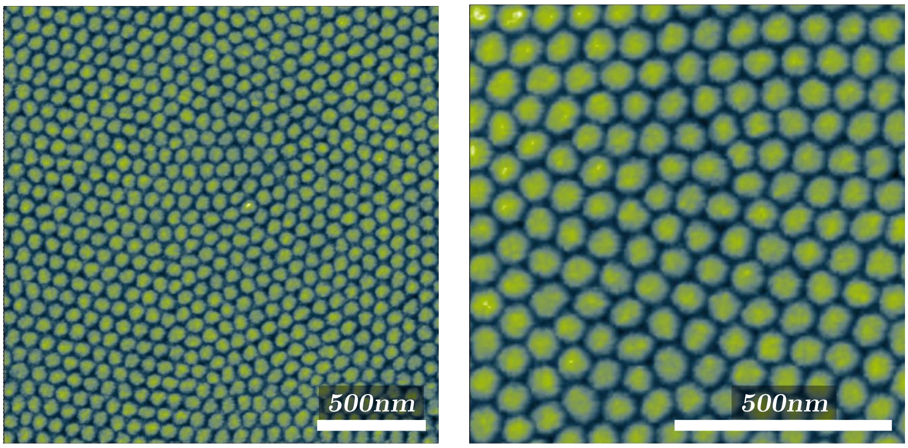

(a) Ni (b) Ni

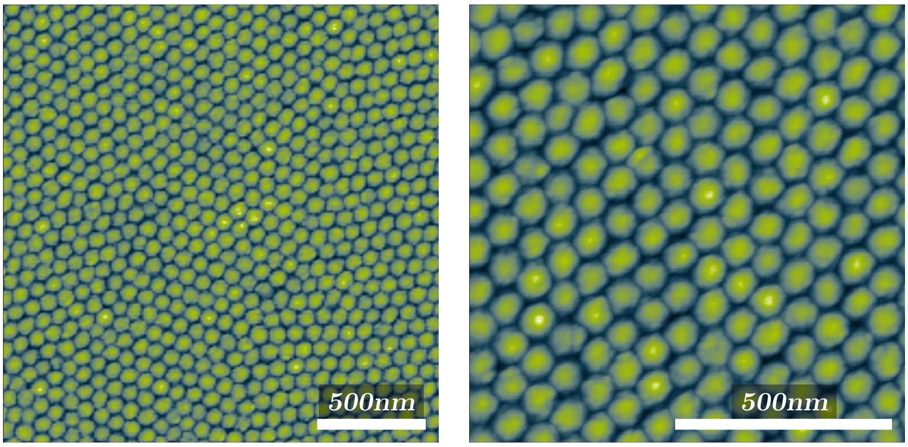

(c) Pt (d) Pt

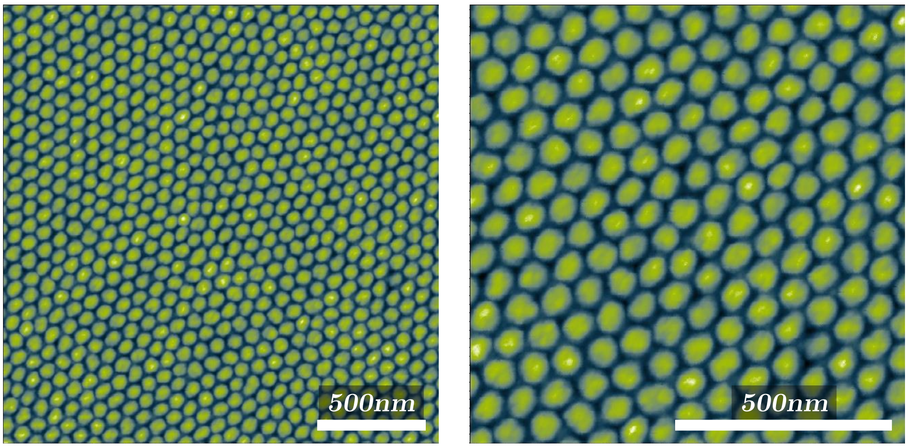

(e) Fe (f) Fe

Figure 10.5: Ni, Pt, and Fe sputter deposited on a diblock copolymer template of asymmetric PS-b-PMMA(63/142). All metals show pronounced effective selectivity for the minority PS block. Micrographs in each row show areas on the same sample.

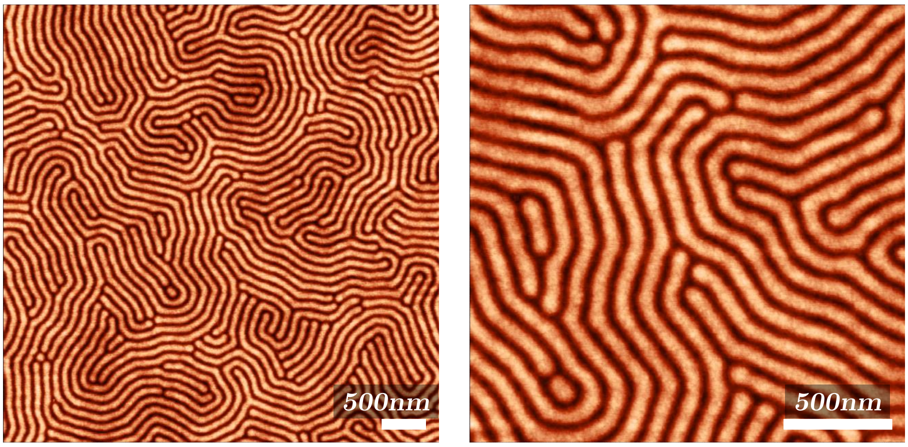

(a) template type (b) template type

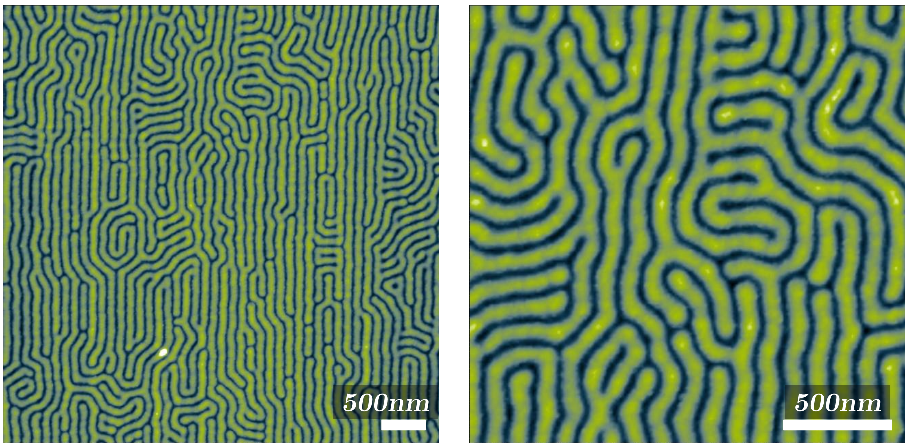

(c) Pt (d) Pt

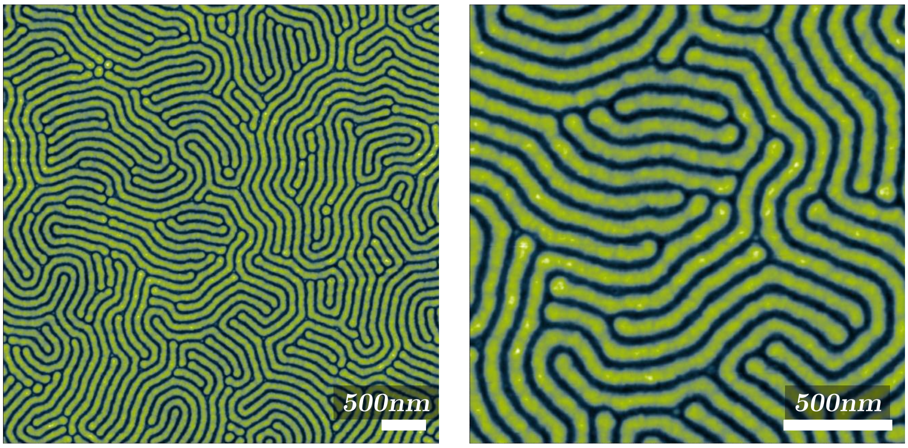

(e) Fe (f) Fe

Figure 10.6: Pt and Fe sputter deposited on a diblock copolymer template of symmetric PS-b-PMMA(203/203) with lamellar chemical domains, forming smooth and continuous nanowires which follow the template pattern. Micrographs in each row show areas on the same sample.

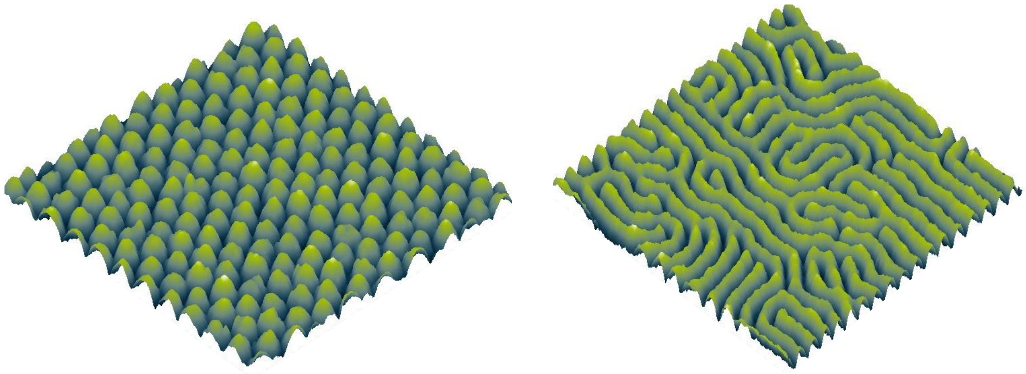

(a) Pt

(b) Pt

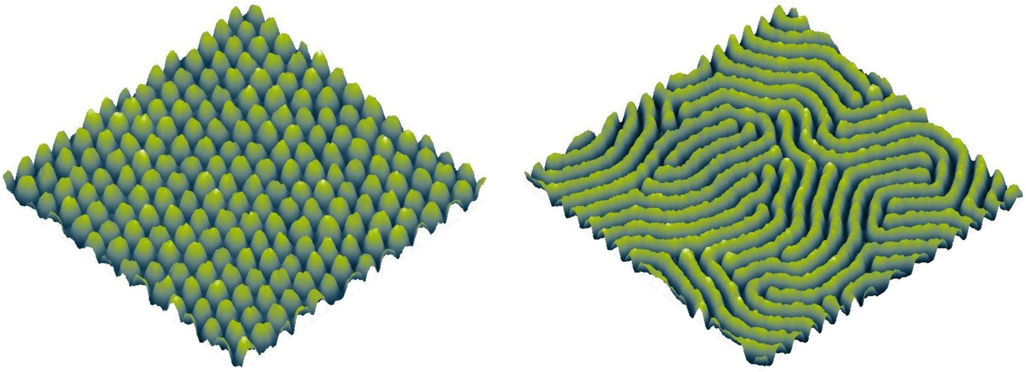

(c) Fe

(d) Fe

Figure 10.7: 3D views of the Fe and Pt nanostructures shown in Figs. 10.5 to 10.6. The depicted areas are 1 μm × 1 μm for the nanodot samples on the left and 2 μm × 2 μm for the nanowire samples on the right. The height range is about 10 nm.

On the other hand, Ni, Pt, and Fe show pronounced effective selectivity on the PS-b-PMMA templates for a wide range of deposition conditions[3]. These metals form smooth and well-separated dot-shaped nanostructures on the PS domains and reproduce the template pattern very well (see Fig. 10.5). Metals with pronounced effective selectivity toward PS-b-PMMA, such as Ni, Pt, and Fe, are also suited to grow smooth and continuous nanowires, i.e. elongated, non-equilibrium structures, on PS-b-PMMA(203/203) templates with lamellar morphology, as shown in Fig. 10.6.

A dependence of nanostructure formation on the template temperatures could not be made out unambiguously by means of AFM topography imaging within the investigated temperature range (from room temperature to 200 °C). However, an enhancement of the effective selectivity of Fe on PS-b-PMMA at increased template temperature was indicated by results of in-situ GISAXS experiments. These will be discussed in section 10.3.1.

Continuous metal films only grow when an element-specific limiting nominal thickness of deposited material is exceeded [166]. Below this limit, a remarkable morphological transition with increasing amount of deposited material was observed for nanostructure samples grown on templates of asymmetric, cylinder-forming PS-b-PMMA(63/142). Fig. 10.9) depicts this transition for the example of Fe, but individual stages of this transition were also observed for Pt and Ag.

The morphological transition was observed to proceed as follows: First, well-separated metal nanodots form. Then the dots begin to merge: deposited metal bridges the PMMA domains in between the nanodots on the PS domains (see left half of Fig. 10.8). Finally, an antidot pattern, i.e. a continuous metal film with holes, is produced. Even a secondary layer of nanodots can grow in between the holes of the antidot pattern (see Fig. 10.9(d)).

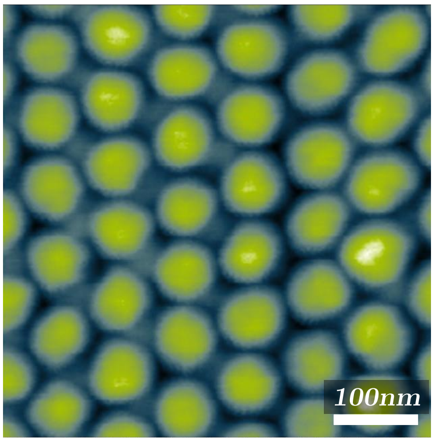

Figure 10.8: Merging nanodots.

---

[3] In the AFM topographies this is evidenced by the height range increasing from approx. 1.25 nm difference between PS and PMMA domains on the plain template surface to approx. 5 nm to 10 nm after deposition (depending on the amount of deposited metal).

Thus, the chemical surface pattern of a diblock copolymer film can not only be used as a template for exact reproduction by the deposited metal – it can also serve as scaffold for other, related metal nanostructure morphologies.

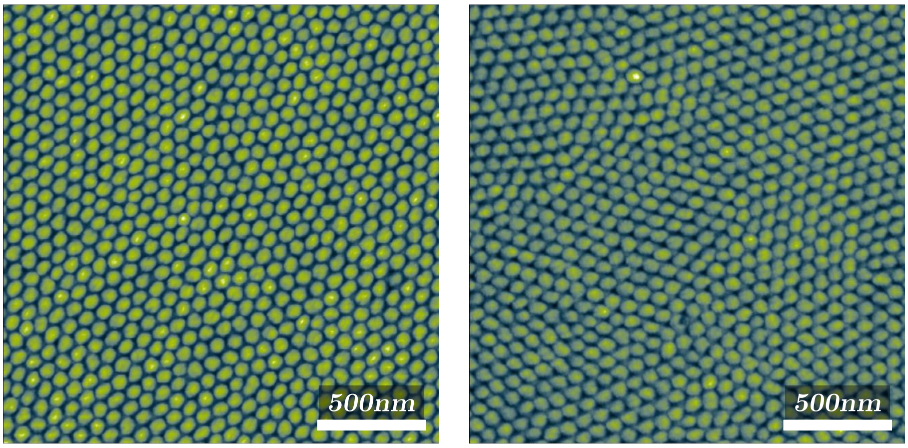

(a) 8 ML (b) 16 ML

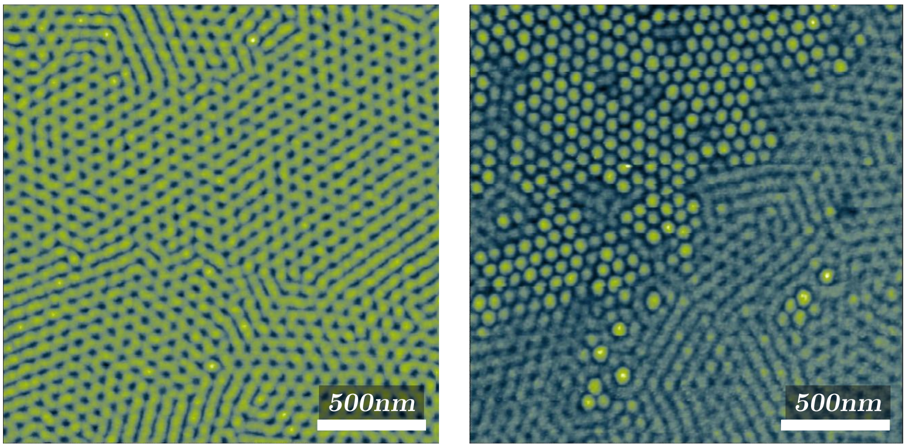

(c) 26.5 ML (d) 48 ML

Figure 10.9: Morphology of Fe nanostructures for increasing amounts of deposited metal on PS-b-PMMA(63/142) templates with surface-perpendicular cylindrical PS domains. The labels state the nominal thickness of deposited Fe in monolayers (ML).

Given that a metal such as Ni, Pt, or Fe reproduces the template pattern well, control over shape, size, and lateral arrangement of the metal nanostructures is obtained via control over the morphology of the diblock copolymer template: Metal nanostructures with a high degree of regularity in lateral positioning can be prepared on diblock copolymer templates with nanofaceted α-Al_2O_3 substrates, as shown in Fig. 10.10. During solvent vapor annealing the chemical domains of the template arrange following the preferential direction given by the orientation of the substrate facets (see section 9.2). Deposited metal adatoms agglomerate on one of the template surface domains due to their effective selectivity for one of the copolymer blocks. Thus, the chemical surface patterning of the diblock copolymer template is transferred into a highly regular pattern of three-dimensional metallic nanostructures. Moreover, the metal nanostructures can be scaled in size and distance by providing templates with corresponding sizes of the copolymer domains, as determined by the composition and molecular mass of the diblock copolymer (see section 9.1.2). Fig. 10.10 (b - d) shows Fe nanostructures on templates prepared from PS-b-PMMA with total molecular masses of $M = M_{PS} + M_{PMMA} = 205$ kg/mol, 94 kg/mol, and 100 kg/mol, respectively.

Numerous publications deal with alternative nanopatterning routines, in which diblock copolymer films fulfill the function of masks (see e.g. [163, 172–174]), which requires removal of one copolymer block or subsequent removal of both blocks. Others demonstrate how selectivity toward the blocks of a copolymer template can be used to assemble pre-synthesized nanoparticles (see e.g. [175, 176]).

Only few efforts are made to develop nanopatterning procedures based on the insights in metal self-assembly on diblock copolymer via effective selectivity. A nanoporous Fe film (i.e. an antidot pattern) was prepared by deposition onto an asymmetric diblock copolymer template with PS as the majority component [177]. Also the selective decoration of a diblock copolymer film with lamellar surface domain morphology by Co has been studied [178]. However, both sample systems lack long-range order in lateral positioning of the nanostructures.

In the routine proposed here, effective selectivity is utilized, and the diblock copolymer template acts not as a mask, but as a scaffold. On this scaffold the metal adatoms self-assemble into smooth compact nanostructures of different shapes: dots, wires, or antidots. Long-range positional ordering of the self-assembled metallic nanostructures is achieved by the use of nanofaceted α-Al_2O_3 substrates for the diblock copolymer templates. By means of controlling few parameters of the self-assembly processes (such as diblock copolymer mass and composition, conditions of annealing, conditions of metal deposition), highly-ordered patterns of nanostructures in a variety of sizes and shapes can be fabricated with this routine.

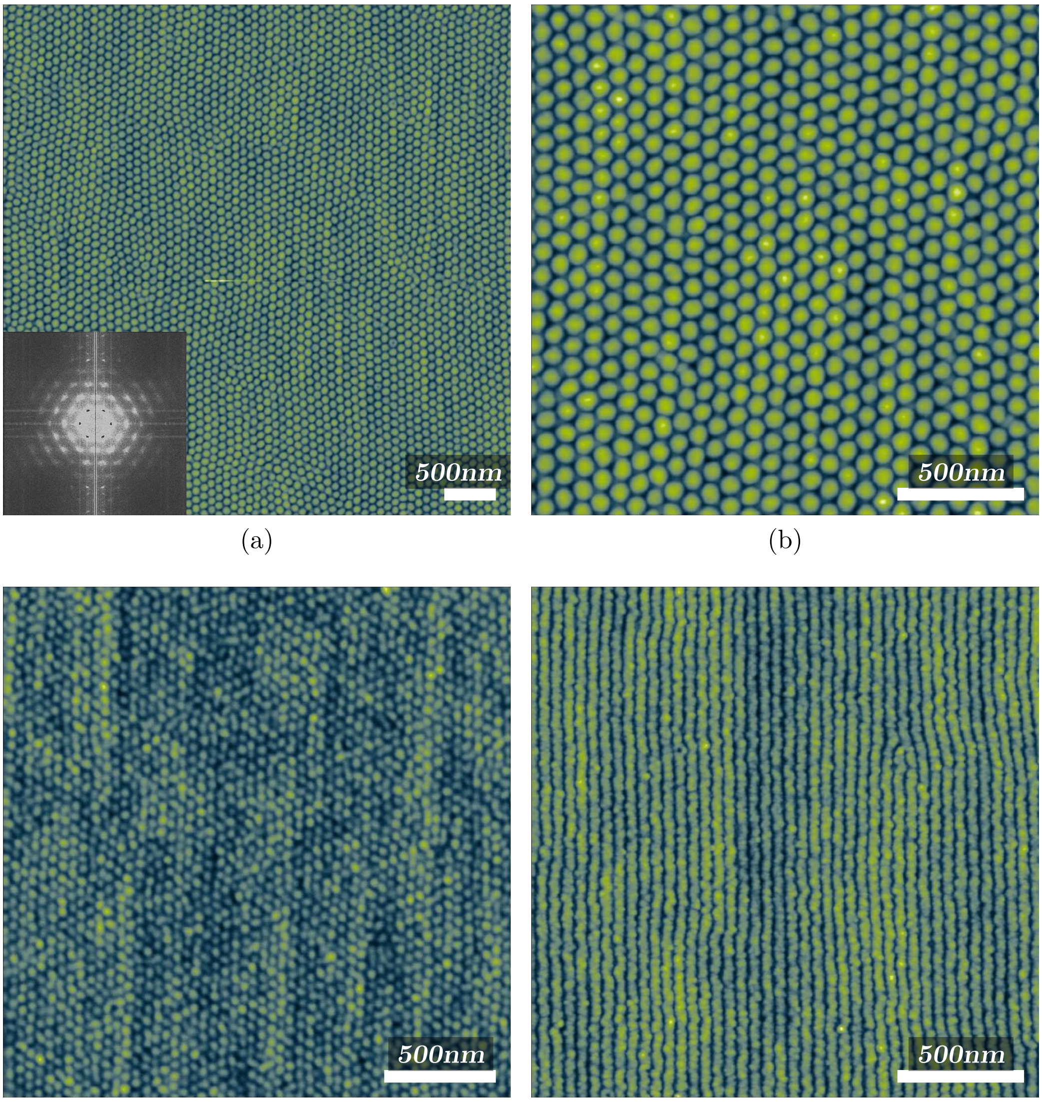

(a) (b)

(c) (d)

Figure 10.10: Fe nanodots and nanowires grown on PS-b-PMMA templates on nanofaceted α-Al_2O_3 substrate. The substrate facets provide a preferential direction for the self-assembly of the diblock copolymer domains, and thus for the positioning of the Fe nanodots. The inset in (b) shows a FFT of the height information. Comparison of (b) and (c) demonstrates, how the nanostructure sizes can be scaled by choosing diblock copolymers with low molecular masses as templates. (a, b): $M = 205$ kg/mol, (c): $M = 94$ kg/mol, (d): $M = 100$ kg/mol. Micrographs in (a) and (b) show areas on the same sample.

10.3 Growing ^{57}Fe nanostructures on diblock copolymer templates: In-situ studies with GISAXS and NRS

The possibility of conducting in-situ experiments during preparation on growing nanostructures is one key advantage of nanofabrication methods based on self-assembly. Even several different probing methods can be applied simultaneously, thus allowing to study correlations between different nanostructure properties during self-assembly. This section describes the in-situ investigation of hexagonal arrays of ^{57}Fe nanodots growing on PS-b-PMMA templates by GISAXS and NRS. GISAXS yields information on the lateral arrangement of the nanodots and especially on how their average shape changes during growth and in dependence of the template temperature. In-situ NRS provides insights into the magnetism of the ^{57}Fe nanodot array, on the evolution of the magnetic state and the dynamics of magnetic moments.

For this in-situ experiment, the portable UHV deposition chamber was mounted at the beamline P01 at the synchrotron radiation source PETRA III. The x-ray energy was set to 14.4 keV. A MAR 345 image plate detector and a time-resolving APD detector were used to record the GISAXS patterns and the NRS time spectra, respectively, at an angle of incidence of $\alpha_i = 0.3°$. The distance between sample and detector was bridged with an evacuated flight tube to reduce scattering in air. Hexagonal arrays of ^{57}Fe nanodots were prepared by sputter deposition onto templates of cylinder-forming PS-b-PMMA(63/142) on nanofaceted α-Al_2O_3 substrates. After a base pressure of $p_0 < 4 \times 10^{-7}$ mbar had been reached, ^{57}Fe was deposited onto the template in steps of 1 min at an Ar pressure of $p_{Ar} = 1.5 \times 10^{-2}$ mbar. GISAXS patterns and NRS time spectra were recorded in between two subsequent steps. ^{57}Fe nanodot array samples were prepared at room temperature and at a template temperature of 200 °C.

10.3.1 The influence of template temperature on the shape of ^{57}Fe nanodots observed via in-situ GISAXS

Considering the temperature dependence of the equilibration time and the diffusion constants of metals on polymer surfaces, an influence of the template temperature on the growth of metal nanostructures can be expected.

However, for Fe on PS-b-PMMA templates within a temperature range from room temperature to 200 °C, a dependence was not observed unambiguously by ex-situ AFM topography imaging. In-situ GISAXS on growing nanostructures allows for more insight.

The GISAXS patterns of the growing ^{57}Fe nanostructures were simulated using the program IsGISAXS [117]. Simulations were performed for horizontal and vertical line cuts through the GISAXS patterns[4] at the positions indicated by dashed lines in Fig. 10.12 (a, b). The figure shows simulations of these line cuts for the final stage of nanodot growth after five deposition steps of 60 s each. Simulations of all recorded GISAXS patterns from earlier growth stages can be found in appendix A.4.1. The nanostructure array was described by a lattice with the following adjustable parameters: lattice constants L(1) and L(2), lattice angle γ, and orientation with respect to the incoming beam direction (see Fig. 10.11 (b)). The nanostructure shape was described by a cone with the following adjustable geometric parameters: base radius R, height H, base angle α (see Fig. 10.11 (a)). Note, that this is merely an approximation to the average nanodot shape, which the form factors implemented in the program allow for; this is not the exact actual shape of the nanodots. However, this approximation yields information on the shape proportions of nanodots growing at different template temperatures. No distribution of any simulation parameter had to be assumed, evidencing a high degree of regularity and uniformity in both the arrangement and shape of the nanostructures in the respective samples. The nanodot arrangement was simulated by a regular two-dimensional lattice with lattice parameters L(1) = L(2) = 83 nm and an angle of 60° between the lattice vectors for both samples. This value of the lattice parameters agrees with the domain spacing in cylinder-forming PS-b-PMMA(63/142) found by AFM topography measurements (see section 9.2.1) within the lateral measurement accuracy of the AFM. The lattice was oriented with the (10) direction parallel to the projection of the direction of the incoming beam onto the sample plane.

The simulation yielded values of 26 nm and 36 nm for the thicknesses of the diblock copolymer template layers in the two samples. Actually, a thickness of about 44 nm is expected for a thin film of PS-b-PMMA(63/143) cast from a solution of concentration $c = 10$ mg/ml (see section 9.1.3 or appendix A.3.1). This thinning may be attributed to a degradation of the diblock copolymer template due to irradiation with x-rays during the experiment. However, judging by the GISAXS data, the lateral domain ordering is not affected.

---

[4] In the horizontal direction, ten adjacent cuts were added up to improve the signal-to-noise ratio.

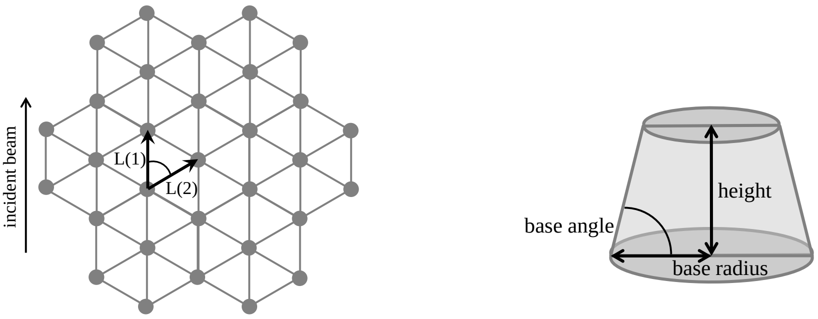

(a) (b)

Figure 10.11: Simulation parameters for (a) the nanostructure arrangement and (b) the nanostructure shape used in the program IsGISAXS [117]. Grey circles in (a) denote positions of nanodots on the lattice.

The results of the simulation regarding the nanostructure shape are summarized in Fig. 10.13. When plotting the nanodot volume as a function of the deposition duration (Fig. 10.13 (a)), it becomes apparent that the deposition rate is different for the two samples. This not due to the different template temperatures, but rather caused by the following: Other experiments during this beamtime, conducted in between the experiments on the two presented samples, required to apply an external magnetic field in the deposition chamber. Residual magnetization of the electromagnet pole shoes affects the plasma in the deposition chamber and can thereby cause the deposition rate to change. The deviation from a linear volume increase in the first stages of deposition is probably caused by oxidation of the ^{57}Fe nanodots due to contact with the diblock copolymer template [177].

The deposition rate is not expected to qualitatively influence the nanostructure growth [166], as long as finding time t_f, deposition time t_d, and equilibration time t_{eq} are related as $t_f < t_d \ll t_{eq}$ (see section 10.1). Indeed, for both samples the geometrical parameters of the nanodots evolve qualitatively similar with deposition duration. Remarkably, at any given deposition stage, the nanodots growing at 200 °C reach about 80% of the height of those growing at room temperature, even though these nanodots have a much larger volume due to the higher deposition rate. Consequently, the base radius of these nanodots is accordingly larger, resulting in an aspect ratio of height to base radius of about 0.33. In contrast, the nanodots growing at 200 °C have a height / base radius aspect ratio of about 0.62 (Fig. 10.13 (a - c)). The respective height / base radius ratio remains con-

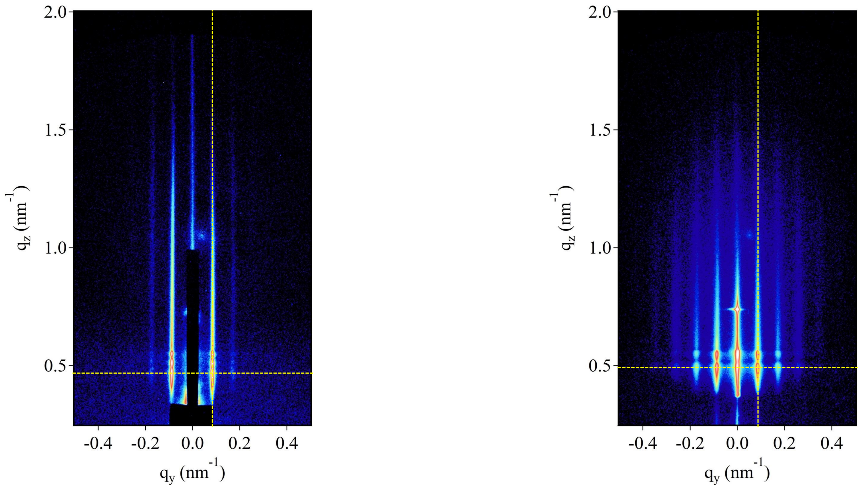

(a) prepared at RT (b) prepared at 200 °C

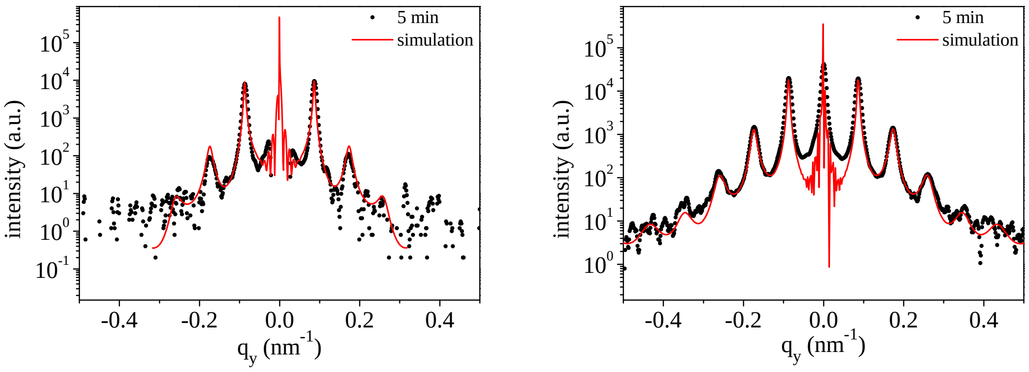

(c) horizontal cut (d) horizontal cut

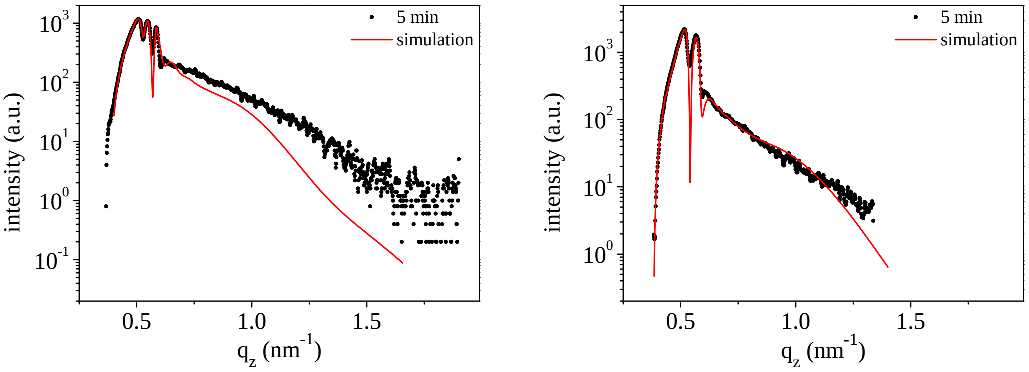

(e) vertical cut (f) vertical cut

Figure 10.12: GISAXS patterns (a, b) and exemplary simulations of corresponding line cuts (c - f) of hexagonal arrays of nanodots growing on cylinder-forming diblock copolymer thin films, at room temperature (left column) and at 200 °C (right column).

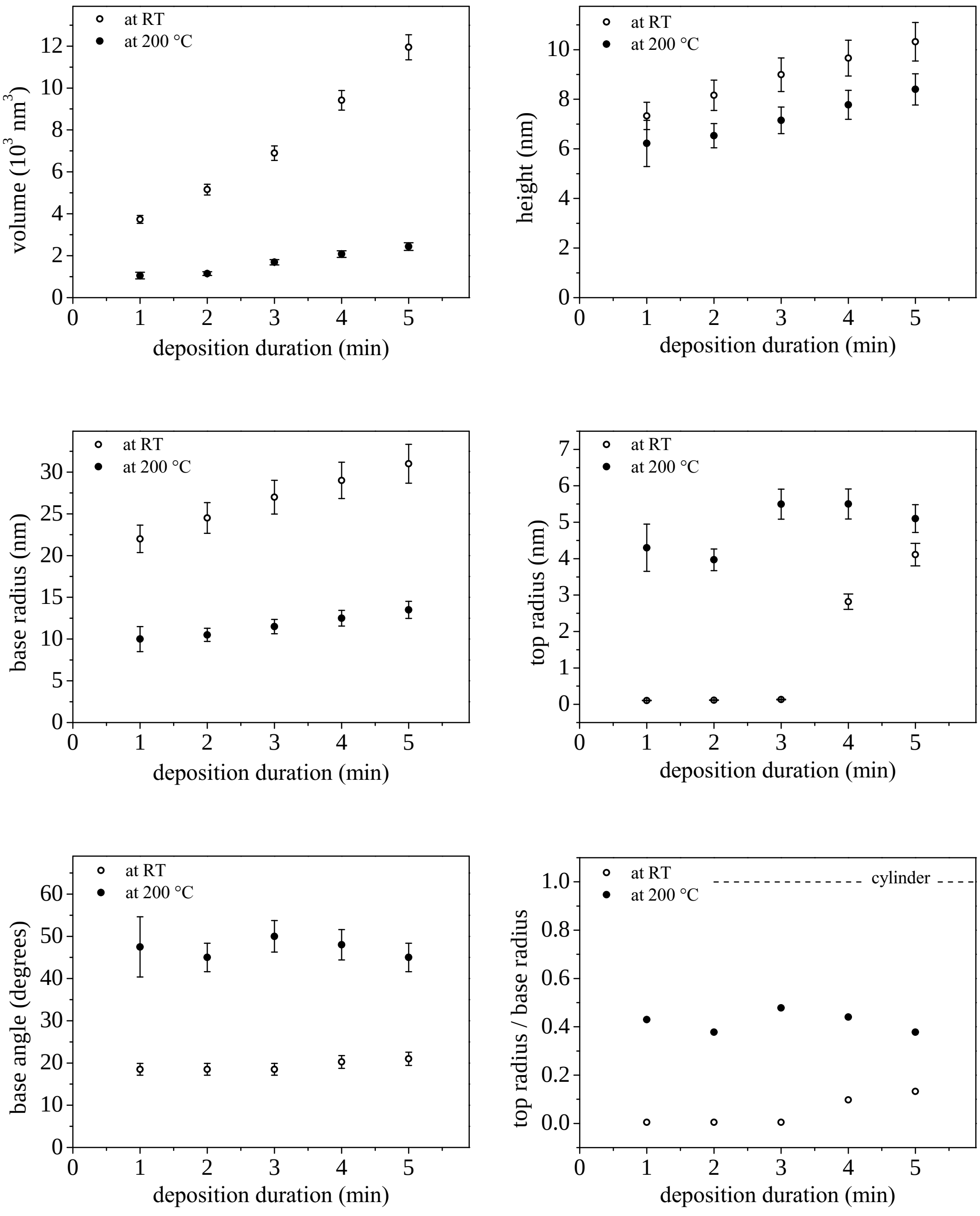

Figure 10.13: Evolution of the geometrical parameters describing the shapes of nanodots growing at room temperature and at 200 °C, respectively, as derived from simulations of horizontal and vertical line cuts through the GISAXS patterns. The nanodots grown at 200 °C are closer to the optimum cylindrical shape.

stant during the process. For both samples also the base angle of the nanodots is constant throughout the growth process; it is about 19° for the nanodots growing at room temperature, and more than twice as large, about 47°, for the nanodots growing at 200 °C . In order to compare the actual shape of the nanostructures to the optimum cylindrical shape, the ratio of top and base radius is plotted in Fig. 10.13 (f). This ratio is 1 for a cylinder; the nanodots grown at room temperature reach a value of about 0.15 at best, while those grown at 200 °C reach a value of about 0.4. Assuming as a rough approximation that the PS area fraction in the template surface is the same as the PS volume fraction in the bulk of the PS-b-PMMA film, i.e. 0.3, the radius of the PS domains can be estimated to be about 20 nm. The nanodots growing at room temperature exceed this radius rather than growing in height to accommodate their increasing volume. At room temperature, the mobility contrast of ^{57}Fe on PS and PMMA appears to be low and the equilibration time is in the range of months [167,170]. As a consequence, the growing nanostructures are only weakly influenced by the chemical pattern of the template, and nanostructure shapes far from the equilibrium shape are stable. Therefore, growth at room temperature results in wide, flat nanostructures. At higher template temperatures the mobility contrast of ^{57}Fe on PS and PMMA is enhanced and the equilibration time is reduced. For the sample prepared at 200 °C these two effects appear to be well-balanced. If the equilibration time was too short at 200 °C, small clusters would form all over the template. However, here ^{57}Fe grows only on PS domains, forming compact nanodots which approach a spherical shape. Fig. 10.14 compares the simulated shapes of nanodots grown at room temperature and at 200 °C.

These shapes are the best approximation to the average nanodot shape, which is possible using the form factors implemented in the simulation program. Given the high degree of uniformity of the nanodots (no distributions in particle dimensions had to be assumed), it is valid to consider this average particle shape to correspond well to the shape of an individual nanodot.

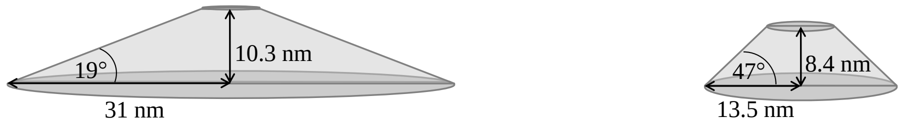

(a) grown at RT

(b) grown at 200 °C

Figure 10.14: Shapes of nanodots grown at room temperature and at 200 °C after 5 minutes of ^{57}Fe deposition as deduced from simulations of GISAXS patterns (see Fig. 10.12).

The evolution of the magnetic state of these samples during growth of the nanodot array was monitored via in-situ NRS. However, in order to achieve a reliable interpretation of the data, it is first necessary to consider a complementary ex-situ NRS experiment.

10.3.2 Magnetization stabilization in ^{57}Fe Nanodots

The temperature dependence of the magnetic state of a hexagonal ^{57}Fe nanodot arrays was studied by ex-situ NRS. The ^{57}Fe nanodot sample had been prepared ex-situ at elevated template temperature and capped with Al to prevent oxidation. It was positioned in a cryostat at the beamline P01, and NRS time spectra were recorded at room temperature and at 10 K (see Fig. 10.15). Simulations performed by K. Schlage, using the program CONUSS [128], approximate the measured time spectra by assuming a number of different discrete states between which the orientation of the sample magnetization fluctuates with a certain frequency. Details of analogous simulations for the in-situ NRS study will be discussed in section 10.3.3. These simulations show that at room temperature the magnetization orientation fluctuates isotropically - the sample is in a superparamagnetic state. At 10 K however, the magnetization os restricted to the surface of a cone with an opening angle of approximately 20° around the surface normal of the sample. In both conditions, the assumed states of the magnetization orientation are occupied with the same frequency: Each state is occupied approximately once during one lifetime of $\tau_0 = 141$ ns. This information is highly relevant for the simulations of the time spectra recorded during growth of the ^{57}Fe nanodot array, as will be discussed below.

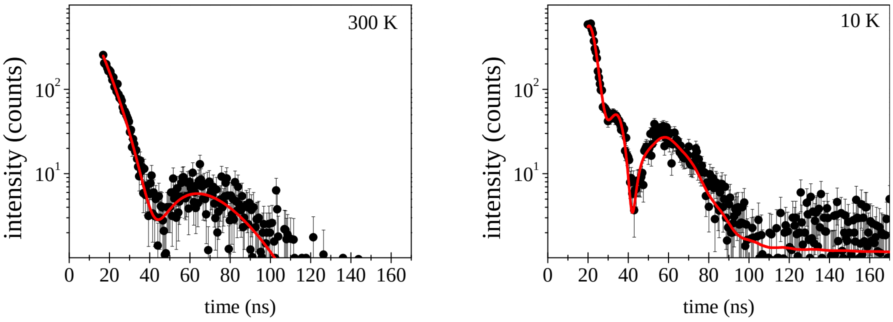

Figure 10.15: NRS time spectra of a hexagonal ^{57}Fe nanodot array at room temperature and at 10 K. Simulations (red curves, by K. Schlage) evidence a magnetization stabilization process from superparamagnetic fluctuations of the magnetic moments at room temperature to their collective precession around the surface normal of the sample at 10 K.

10.3.3 The magnetic evolution of ^{57}Fe nanostructures observed via in-situ NRS

Nuclear resonant scattering of synchrotron radiation is a powerful tool to elucidate the evolution of the magnetic state of a nanostructure sample in-situ during self-assembly. In combination with in-situ GISAXS, comprehensive information on the relations between shape, size, arrangement and magnetic properties of the nanostructures can be obtained.

Ideally, GISAXS and NRS data from the same sample would be correlated. Unfortunately, here it was only possible to combine data from two samples prepared with the same deposition parameters: The NRS data of the nanodot array discussed in section 10.3.1 (grown at 200 °C) were of low quality, most probably because the nanodots oxidized considerably during a longer interruption of the deposition process. This lead to much less pronounced features in the NRS time spectra as compared to those of a second sample, where ^{57}Fe was deposited without interruptions longer than necessary for data acquisition. However, due to its orientation with the substrate facet edges parallel to the incident beam, the GISAXS patterns of this second sample contain a significant contribution of scattered intensity from the substrate. Complete simulations of these GISAXS patterns were not feasible. However, both the overall shape of the time spectra and the GISAXS patterns for q-space regions without contribution by the substrate agree very well for both samples, i.e. their structural and magnetic evolution is sufficiently similar. It is therefore considered valid to combine GISAXS and NRS data from these two samples.

NRS time spectra were recorded in between the deposition steps at 200 °C and simulations were performed with the program CONUSS [128]. The simulations yield strength and orientation dynamics of the magnetic hyperfine field, which is – to a very good approximation – proportional to the magnetization. With volumes smaller than that of a sphere of 25 nm in diameter, the nanodots are assumed to be single-domain nanoparticles (see section 3.1).

The nanodot shape cannot be input into the simulations - it had to be approximated by assuming a continuous ^{57}Fe film consisting of four layers with decreasing density from bottom to top. The total height of the film is consistent with the nanodot height derived from simulations of the GISAXS patterns (see section 10.3.1, sample grown at 200 °C).

Two species of ^{57}Fe atoms (so-called sublattices SL1 and SL2) were assumed, each with six possible states between which the orientation of the magnetic hyperfine field can fluctuate as defined by a transition matrix. The two atomic species differed in their fraction of the total number of ^{57}Fe atoms, in the strength of the magnetic hyperfine field, the quadrupole splitting and the isomer shift for these atoms. For both atomic species, identical polar and azimuthal angles of the possible magnetization orientation states and the same transition matrix defined the dynamics of the magnetic hyperfine field orientation.

Time spectra for five different stages of growth of the ^{57}Fe nanodot array were simulated (see Fig. 10.16). It turned out that the magnetic hyperfine field strength and distribution as well as the frequency of fluctuation between the possible magnetization orientation states influence the shape of the time spectra in a similar way: During nanodot growth, the time spectra are affected by the changing magnetic hyperfine field strength and distribution as well as by its dynamics. Only with additional data, the simulation can be entirely unambiguous. This complementary information is provided by the temperature-dependent measurements of NRS time spectra presented in section 10.3.2. In these ex-situ measurements, magnitude and distribution of the magnetic hyperfine field does not change, as there is no volume increase of the nanodots. The difference in the two time spectra at room temperature and at 10 K can therefore be attributed to changes of the magnetic hyperfine field dynamics alone. It was concluded that upon cooling the dynamics of the magnetic hyperfine field, changed from isotropic fluctuations of the magnetization orientation to fluctuations restricted to the surface of a cone around the surface normal of the sample. During this stabilization, the frequency with which each state would be occupied remained the same: Each state was occupied approximately once during a period of $\tau_0 = 141$ ns, the lifetime of an excited nuclear state in ^{57}Fe .

These insights were transferred to the simulations of the time spectra recorded during nanodot growth. The occupation frequency for the different magnetization orientation states was kept constant: Each state was occupied once during approximately six lifetimes of $\tau_0 = 141$ ns; the slower motion of magnetic moments as compared to the nanodot sample described in section 10.3.2 is attributed to the larger nanodot volume in the sample discussed here [179]. The magnetic hyperfine field strength, distribution, and orientation were adjusted to fit the simulation to the experimental data.

Having clarified the ambiguity outlined above, more reliable information on the evolution of the magnetic hyperfine field during nanodot growth could be obtained: In between the first and the second time spectrum, recorded after 6 and 8 minutes of deposition, respectively, a stabilization of the magnetiza-

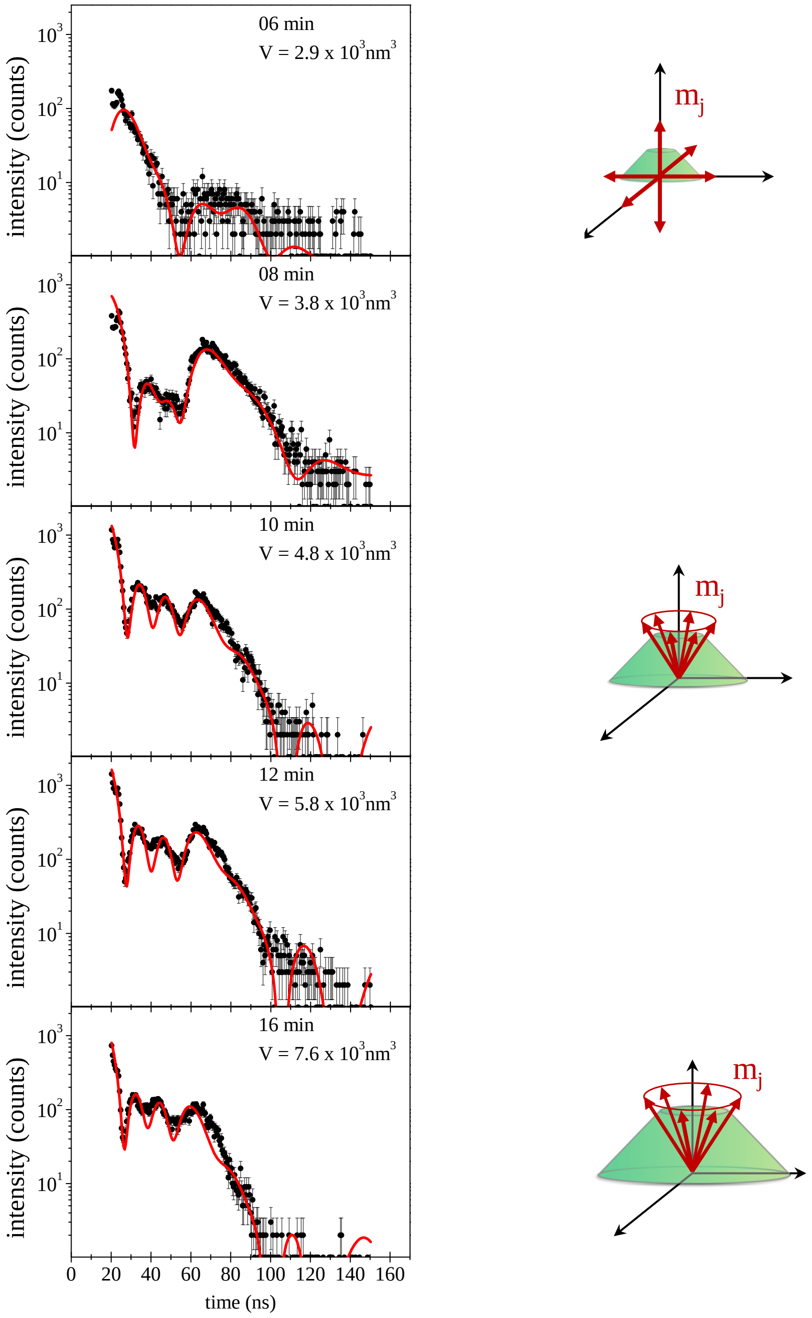

Figure 10.16: NRS time spectra of a hexagonal arrays of ^{57}Fe nanodots during growth. Experimental data are given as black symbols, corresponding simulations as solid red lines. The labels state the respective duration of ^{57}Fe deposition and approximate nanodot volume. Sketches on the left depict the evolution of the magnetic state of the sample. As the nanodots volume increases, a stabilization process of the nanodot magnetization is observed, from isotropic superparamagnetic fluctuations of the magnetization to fluctuations restricted to the surface of a cone.

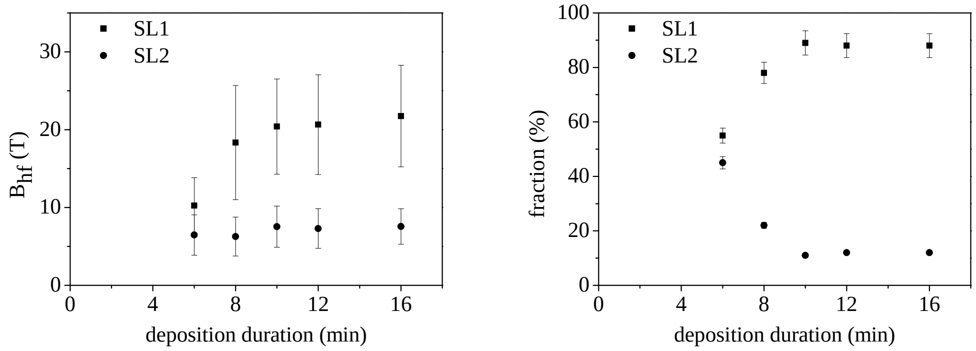

Figure 10.17: The evolution of the magnetic hyperfine field strength for two species of resonant atoms in a ^{57}Fe nanodot array during the growth and magnetization stabilization process. The error bars in the right graph indicate the distribution of the magnetic hyperfine field strength.

tion from isotropic superparamagnetic fluctuations to fluctuations restricted to the surface of a cone around the surface normal of the sample is observed. The opening angle of the cone is about 32°, and remains constant during further nanodot growth. The evolution of the fractions of the two atomic species and of the magnetic hyperfine field strengths B_{hf} for the two species in dependence of the elapsed deposition time is shown in Fig. 10.17. After 6 minutes of deposition, each of the atomic species (SL1 and SL2) constitutes approximately half of the ^{57}Fe atoms and their magnetic hyperfine field is similar. This changes noticeably during the magnetization stabilization process: The fraction of species SL1 rises to 90%. The magnetic hyperfine field strength of this majority atomic species increases from $B_{hf} = 10$ T to $B_{hf} = 18$ T during the stabilization process. Upon further nanodot growth, it saturates at a value of approximately $B_{hf} = 21.5$ T. The magnetic hyperfine field of the minority species SL2 only increases slightly from $B_{hf} = 6.5$ T to $B_{hf} = 7.5$ T during the observed process. The distribution of the magnetic hyperfine field strength decreases slightly for both atomic species.

A uniform precession of the magnetization orientation was presumed for the presented simulations and very good agreement with the experimental data was obtained. It should be noted, however, that the time spectra cannot provide any information on the sequence in which the assumed magnetization orientation states are occupied; random fluctuations between states are conceivable, too, and may lead to equally adequate fits. Further experiments, e.g. by photon polarization precession spectroscopy [180], would be required to elucidate the magnetization dynamics in more detail.

Nevertheless, the fluctuation frequency and the fact that the magnetization is restricted to the surface of a cone, can be reliably concluded: Simulations assuming magnetization orientation states not only on the surface of the cone (i.e. with the same polar angle $\theta = 32°$ of the magnetization direction) but also within the cone (i.e. with different polar angles $0° \leq \theta \leq 32°$) did not yield adequate fits.

The magnetic hyperfine field strength in the nanodots is strongly reduced as compared to the bulk value of 33.3 T at room temperature. A reduction of the magnetic hyperfine field is expected with increasing temperature – the experiment discussed here was conducted at a sample temperature of 200 °C. Moreover, as nanostructures are considered here, surface effects or intrinsic size effects can play a role [181]: It has been suggested that the magnetic hyperfine field strength at surface nuclei is lower than that at nuclei in the interior. The average magnetic hyperfine field strength will be lowered by this surface effect [182]. Another proposition claims that collective magnetic excitations, i.e. fluctuations of the magnetization on timescales which are short compared to the timescale of Mössbauer spectroscopy, can account for the observed reduced magnetic hyperfine field strength. The magnitude of this intrinsic size effect depends strongly on which magnetic anisotropy and magnetic interactions are dominant in the sample [183]. Further characterization of self-assembled ^{57}Fe nanodot arrays may clarify which mechanism causes the reduction of the magnetic hyperfine field strength in these systems. In nanostructures, stable ferromagnetic behavior at a given temperature is reached at a critical size. At this point, dipolar interactions outweigh thermal excitations of the magnetic moments. For spherical iron nanoparticles the critical diameter has been calculated to be about 15 nm at room temperature, assuming single-domain particles with the magnetic anisotropy properties of bulk bcc iron [177]. Extrapolating from the results of the corresponding GISAXS measurements, the volume of the nanoparticles at the beginning of the magnetization stabilization process equals that of a spherical particle with a diameter of approximately 18 nm. The elevated sample temperature of 200 °C may account for the difference in the critical radius as compared to the calculated value (see section 3.3).

This study has shown that is it feasible to analyze NRS time spectra of nanostructure arrays by means of simulations employing a relaxation model. Future investigations may explore which insights can be gained from NRS time spectra recorded, e.g., during systematic variation of sample temperature or external magnetic field. Moreover, the integrated nuclear resonant intensity as a function of temperature and external magnetic field could be evaluated in analogy to conventional $M(T)$ and $M(H)$ magnetization curves.

The presented observations by means of an x-ray scattering technique, which inherently averages information from the entire illuminated sample volume, were possible only due to the high degree of regularity of the self-assembling nanostructure array. As a consequence of the uniform shape and highly-ordered arrangement of the nanodots, all individual nanodots show practically identical magnetic behavior, resulting in an average signal which can be evaluated to yield meaningful information on the magnetic evolution of the system.

11 Conclusions

In this work, different self-assembly processes have been employed for the fabrication of various highly-ordered nanostructure systems: periodically nanofaceted α-Al_2O_3 surfaces, metallic thin films of periodically varying thickness, diblock copolymer thin films with highly regular chemical surface patterning, metallic nanowire and nanodot arrays. The proposed routines rely exclusively on self-assembly processes. They require no lithography-based preparation steps, no treatment of the α-Al_2O_3 substrates other than thermal annealing, and no treatment of the copolymer templates other than solvent vapor annealing. Apart from their relative simplicity, the routines have further significant advantages: The sample areas can be arbitrarily large, because self-assembly processes are parallel processes, occurring simultaneously over the entire sample. It is feasible to observe sample properties of interest in-situ during the self-assembly processes of the three steps, because these preparation steps are performed in environments which can be made accessible to contact-less probes, such as x-rays.

Nanofaceted α-Al_2O_3 surfaces serve as substrates for growing separated parallel metal nanowires or continuous metal films of periodically varying thickness (and related properties) by sputter deposition under non-normal incidence. Morphological features such as the aspect ratio of nanowires or the thicknesses in continuous films can readily be adjusted by choice of the deposition angle and duration.
Arrays of uniform metal nanostructures – dots, antidots, wires – with a high degree of long-range order in lateral positioning and adjustable nanostructure size and shape can be fabricated via a three-step routine: 1) faceting of α-Al_2O_3 substrate by high-temperature annealing, 2) regular chemical patterning of a template surface by deposition and solvent vapor annealing of a diblock copolymer film on the substrate, 3) growth of metal nanostructures reproducing the template pattern by sputter deposition. This routine brings two approaches in nanostructure fabrication together: The directed microphase separation of diblock copolymer films on corrugated sub-

strate surfaces was combined with the effective selectivity of sputtered atoms on microphase-separated diblock copolymer templates. Thus, large area arrays of uniform metallic nanostructures with long-range positional order were produced.

This work has exploited one substantial advantage of nanostructure preparation via self-assembly over lithographical nanostructure fabrication: The nanostructures were studied in-situ during formation. Multiple probes can be applied simultaneously or in alternation.

The in-situ GISAXS experiment on α-Al_2O_3 has revealed details on the formation of surface facets upon high-temperature annealing and thus complemented the ex-situ AFM studies of this process. Knowledge of the faceting process in dependence of the annealing conditions helps to purposefully prepare substrates with facet dimensions adapted to specific requirements. Such substrates can serve as topographical guides for the self-assembly of diblock copolymers, lipid films or similar systems, or for preparing nanowires (conductive, magnetic, thermoelectric, etc.) by geometrical shading.

The study of a uniaxially corrugated ^{57}Fe film on a nanofaceted α-Al_2O_3 substrate has shown how GISAXS and NRS are merged into a method yielding laterally resolved magnetic information from a sample with heterogeneous magnetic properties. This method was applied in-situ to observe the magnetic evolution in the distinct structural units of the sample during film growth, and ex-situ to examine the different responses of the structural units to external magnetic fields. It may be appealing to conduct an analogous experiment not with a compositionally homogeneous film, but with a system combining two different materials, e.g. ferromagnet and antiferromagnet, or ferromagnet and superconductor. Moreover, the method is applicable to further systems with periodic morphological and magnetic structure and can be extended to merging SAXS and NRS.

The investigation of hexagonal ^{57}Fe nanodot arrays has demonstrated that combining GISAXS and NRS yields comprehensive information on both the structural and magnetic evolution of nanostructured samples during their self-assembly. The dependence of the nanostructure shape on the temperature during growth was shown by in-situ GISAXS. Careful analysis of NRS time spectra revealed a magnetization stabilization process, upon which the superparamagnetic fluctuation of magnetic moments changes to a fluctuation restricted to the surface of a cone, in two cases: ex-situ upon cooling a sample with constant nanodot volume and in-situ during nanodot growth. Nanodot arrays of the demonstrated uniformity and regularity may be well-suited as seed patterns for crystallization of macromolecules, and ferromagnetic nanodot arrays could be employed to pin magnetic flux vortices in adjacent superconductors. Moreover, it may be intriguing to study inter-particle interactions or coherent behavior (e.g. coherent spin dynamics) in such nanodot arrays.

The nanostructured systems – homogeneous or hybrid, in two or even three dimensions – which can be manufactured by means of self-assembly processes are plentiful. X-ray scattering techniques make it feasible and fruitful to study the evolution of their properties in-situ during self-assembly.

A Appendix

A.1 Nuclear Resonant Scattering

Some more details on the so-called dynamical beats and speed-up shall be given. These effects are of different origins than the Quantum beats, but still shape NRS time spectra in characteristic ways. Moreover, the determination of the magnetic structure of a thin layer from the time spectrum of resonantly reflected intensity will be outlined briefly.

For determining the time-dependence of the resonantly scattered intensity, the amplitude of incident radiation is assumed to be equal for all frequencies: $\boldsymbol{A}_i(\omega) = \boldsymbol{A}_i$ [124]. Moreover, for a pulsed synchrotron radiation source, the time-dependence of the incident amplitude is well approximated by $\boldsymbol{A}_i(t) = \delta(t)\boldsymbol{A}_i$ [77]. Then the Fourier transformation of the amplitude $\boldsymbol{A}(x,\omega)$ from the energy domain into the time domain yields

$$\boldsymbol{A}(x,t) = \Big(\delta(t) - \boldsymbol{G}(x,t)\Big)\boldsymbol{A}_i \tag{A.1}$$

Here, $\delta(t)$ represents the instantaneous non-resonant transmission and $\boldsymbol{G}(x,t)$ is the resonantly scattered, delayed part of the amplitude $\boldsymbol{A}(x,t)$ [77,124,125]. As an example, for a sample with thickness d and one allowed transition (no hyperfine splitting) the transmitted amplitude in the time domain is given by

$$\boldsymbol{A}(t) = \left(\delta(t) - \frac{\chi}{\tau_0}\exp\left(-\frac{t}{2\tau_0}\right)\frac{J_1\left(2\sqrt{\chi t/\tau_0}\right)}{\sqrt{\chi t/\tau_0}}\right)\boldsymbol{A}_i \tag{A.2}$$

with

$$\chi = \frac{1}{4}\beta_0 d = \frac{1}{4}\sigma_0 f_{LM}\rho_n d \tag{A.3}$$

where $\beta_0 = \sigma_0 f_{LM}\rho_n$ is the absorption coefficient at resonance, with the nuclear photon absorption cross-section σ_0 at resonance, the Lamb-Mössbauer factor f_{LM}, and the number density of resonant nuclei ρ_n. χ is often referred to as the "effective" thickness of the sample [77, 126]. An amplitude of the form of Eqn. (A.2) results in a time-dependent intensity as plotted in the time spectrum shown in Fig. A.1. $\exp(-\frac{t}{2\tau_0})$ describes the decay function for isolated resonant nuclei. J_1 is the Bessel function of the first kind and first order, which represents the so-called dynamical beats (see appendix A.1.2).

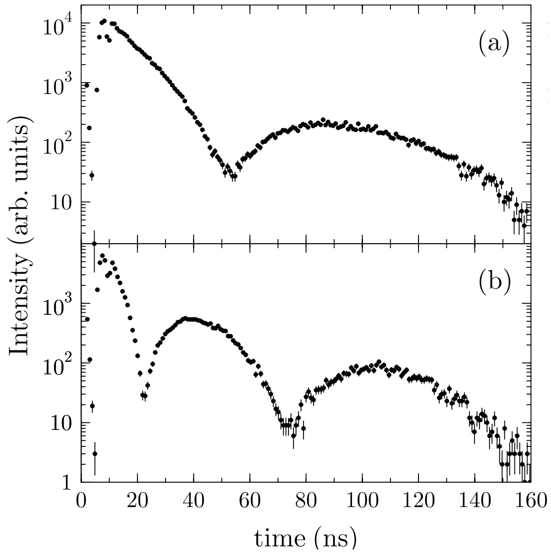

Figure A.1: Dynamical beats: Time spectra in case of a single-line resonance, measured for samples of a) 6 μm and b) 12 μm thickness. From [77].

A.1.1 Speed-up

Consider the amplitude $\boldsymbol{A}(t)$ for a single resonance as given by Eqn. (A.2). In approximation for $t/\tau_0 < 1/(1+\chi)$, i.e. for thin samples and early delay times, the envelope $I_{en}(t)$ of the corresponding intensity is

$$I_{en}(t) \approx \frac{\chi^2}{\tau_0^2} \exp\left(-(1+\chi)\frac{t}{\tau_0}\right) \tag{A.4}$$

This reveals the so-called speed up [77,124,126]: Coherent resonant scattering from an ensemble of nuclei results in an accelerated decay of the excited state as compared to incoherent resonant scattering by isolated nuclei. The time-dependence of the intensity $I(t)$ emitted by isolated nuclei is expressed by an exponential function:

$$I(t) \propto \exp\left(-\frac{\Gamma_0}{\hbar}t\right) = \exp\left(-\frac{t}{\tau_0}\right) \tag{A.5}$$

As can be seen from comparing Eqn. (A.4) and Eqn. (A.5), the increase in the decay constant is given by the effective thickness χ, i.e. the decay speeds up linearly with increasing sample thickness d [124]. This is evidenced in a time spectrum $I(t)$ by the slope of the envelope $I_{en}(t)$ increasing with sample thickness. The decay rate is significantly enhanced further in grazing incidence geometry, where the length of the beam path through the sample is much larger than the sample thickness in forward geometry [77].

A.1.2 Dynamical beats

For nuclear resonant scattering experiments with synchrotron radiation, the energetic bandwidth of the incident radiation is typically reduced to the low (or even sub-) meV range by means of monochromators. But still, the bandwidth of the incident radiation is about five orders of magnitude larger than the linewidth of the nuclear resonance. This fact leads to the occurrence of dynamical beats in the time spectrum $I(t)$ of resonantly scattered intensity. Dynamical beats are recognized by some characteristic properties [126]: The time spectrum shows an aperiodic intensity modulation (see Fig. A.1. The apparent period of this modulation increases with time. However, it decreases for an increased sample thickness. The increase of the apparent beat period with time is expressed by the $\sqrt{t}$-dependence of the Bessel function J_1 in Eqn. (A.2). The increase of the apparent beat period with decreasing sample thickness is given by the dependence of the Bessel function J_1 on the product of effective thickness χ and time t.

This behavior can be interpreted in terms of the spectral group velocities of the radiation pulse [126]: Since the synchrotron radiation pulse is so much broader in energy than the resonance width, no single group velocity can be assigned to it in a meaningful way. Instead, the radiation pulse is decomposed into individual frequency components, to which individual spectral group velocities can then be assigned. For frequencies ω near a resonance frequency ω_0 the real part of the dispersion relation

$$\omega = \frac{c}{n(\omega)} k_0 \tag{A.6}$$

is split into two branches, a high-frequency branch for $\omega > \omega_0$ and a low-frequency branch for $\omega < \omega_0$, as shown in Fig. A.2. The spectral group velocity $v_g(\omega_j)$ of pulse components with frequency ω_j is given by the slope of $\omega(k_0)$ at the corresponding value of the wave vector norm $k_0(\omega_j) = \omega_j/c = 2\pi/\lambda_j$, where c is the speed of light in vacuum:

$$v_g(\omega_j) = \frac{d\omega}{dk_0}(\omega_j) \tag{A.7}$$

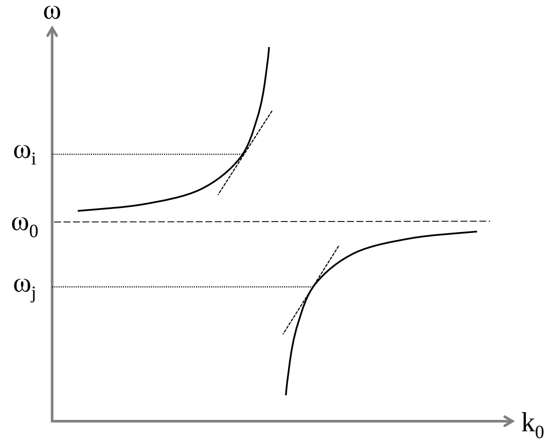

Figure A.2: The dispersion relation near a resonance. ω_i and ω_j indicate the frequencies of two pulse components with identical spectral group velocity $v_g = d\omega/dk$.

$$v_g(\omega_i) = v_g(\omega_j)$$

As can be seen from Fig. A.2, pulse components with frequencies far from the resonance frequency ω_0 have a high spectral group velocity v_g. Pulse components with frequencies close to the resonance frequency ω_0, however, have a low group velocity. For each pulse component with frequencies ω_i there is another component with frequency ω_j, which has the same group velocity v_g, as indicted in Fig. A.2. These two pulse components will therefore reach the detector at the same time and interfere. This results in a beating in the distribution of scattered intensity in time $I(t)$ with the difference frequency $\omega_i - \omega_j$. Pulse components with frequencies ω_i, ω_j far from the resonance frequency ω_0 have a high group velocity v_g and a large frequency difference $\omega_i - \omega_i$. They cause a fast beating at early times in $I(t)$. Pulse components with frequencies close to the resonance frequency have a low group velocity and a small frequency difference. They cause a slow beating at later times in $I(t)$. This different behavior of different pulse components results in the aperiodic beating described by the Bessel function J_1 in the amplitude $\boldsymbol{A}(t)$, Eqn. (A.2).

Also the dependence of the aperiodic beating on the sample thickness can be explained in this picture [126]: At a given time t those pulse components with the group velocity $v_g = d/t$ arrive at the detector. For a sample with larger thickness this means that pulse components arriving at the same time t must have traveled with a higher group velocity. As discussed above, a higher group velocity is related to a larger difference in the frequencies of the pulse components, and this in turn corresponds to a faster beating in $I(t)$. Thus, the apparent period of dynamical beats decreases with increasing sample thickness.

A.1.3 Determining the magnetic structure of a thin layer

Consider a sample consisting of a substrate supporting a thin layer of ^{57}Fe with a magnetic hyperfine field of strength $B_{hf} = 33.3$ T, causing hyperfine splitting of the nuclear levels as shown in Fig. (6.13), and with a given arrangement of different in-plane orientations $\boldsymbol{m}_j$ of the magnetic quantization axis, i.e. with a certain spin structure. Assume further, that the incident radiation is fully $\boldsymbol{\sigma}$-polarized and that the detection is insensitive to polarization, as for many experiments with synchrotron radiation. In this case, only nuclear transitions with quantum number change $M = \pm 1$ contribute to the resonantly scattered intensity. For each magnetic sublattice j with orientation $\boldsymbol{m}_j$ the nuclear scattering length matrix $\boldsymbol{N}(\omega)$ (see Eqn. (6.35)) is then reduced to

$$\begin{aligned} \boldsymbol{N}_j(\omega) &= \frac{3}{16\pi}\begin{pmatrix} N_{j,\sigma\sigma} & N_{j,\sigma\pi} \end{pmatrix} \\ &= \frac{3}{16\pi}\begin{pmatrix} F_{+1} + F_{-1} & -\mathrm{i}(\boldsymbol{k}_0 \cdot \boldsymbol{m}_j)(F_{+1} - F_{-1}) \end{pmatrix} \end{aligned} \tag{A.8}$$

The total nuclear scattering length matrix for all sublattices in the entire sample is given by

$$\begin{aligned} \boldsymbol{N}(\omega) &= \sum_j p_j \boldsymbol{N}_j(\omega) \\ &= \frac{3}{16\pi}\begin{pmatrix} F_{+1} + F_{-1} & -\mathrm{i}S(\phi)(F_{+1} - F_{-1}) \end{pmatrix} \end{aligned} \tag{A.9}$$

with

$$S(\phi) = \boldsymbol{k}_0 \cdot (\boldsymbol{D}(\phi)\boldsymbol{\mathcal{M}}) \qquad , \qquad \boldsymbol{D}(\phi) = \begin{pmatrix} \cos\phi & \sin\phi \\ -\sin\phi & \cos\phi \end{pmatrix} \tag{A.10}$$

The rotation matrix $\boldsymbol{D}(\phi)$ describes a rotation of the sample about its surface normal by an angle of ϕ. The magnetic structure function $\boldsymbol{\mathcal{M}}$ sums the orientations $\boldsymbol{m}_j$ of the magnetic quantization axes of all sublattices j. It describes the spin structure of the sample. The atom positions are taken into account by the phase factor $\exp(\mathrm{i}\boldsymbol{q}\boldsymbol{R}_j)$, where $\boldsymbol{q}$ is the wave vector transfer in the scattering process and $\boldsymbol{R}_j$ is the lattice vector (see Eqn. (6.18)) of the respective sublattice.

$$\boldsymbol{\mathcal{M}} = \sum_j p_j \boldsymbol{m}_j \exp(\mathrm{i}\boldsymbol{q}\boldsymbol{R}_j) \quad , \quad \sum_j p_j = 1 \tag{A.11}$$

To obtain the resonantly reflected intensity $I(t)$ (considering only nuclear resonant scattering processes and not the prompt electronic scattering), the Fourier transforms $\tilde{f}_{\sigma\sigma}(t)$ and $\tilde{f}_{\sigma\pi}(t)$ of the nuclear scattering amplitude matrix elements in Eqn. (6.31) are replaced by the Fourier transforms of the nuclear scattering length matrix elements $N_{\sigma\sigma}(\omega)$ and $N_{\sigma\pi}(\omega)$:

$$I(t) = \left(\left| \tilde{F}_{+1}(t) + \tilde{F}_{-1}(t) \right|^2 + S^2(\phi) \left| \tilde{F}_{+1}(t) - \tilde{F}_{-1}(t) \right|^2 \right) \frac{\chi'^2}{\tau_0^2} \exp\left(-\chi' \frac{t}{\tau_0} \right) \tag{A.12}$$

$\tilde{F}_{\pm1}(t)$ are the Fourier transforms of the nuclear scattering strengths $F_{\pm1}(\omega)$ (see Eqn. (6.36)) with:

$$\begin{aligned} \tilde{F}_{+1}(t) &= (a_1 \exp(\mathrm{i}\omega_1 t) + a_4 \exp(\mathrm{i}\omega_4 t)) \exp\left(-\frac{t}{2\tau_0} \right) \\ \tilde{F}_{-1}(t) &= (a_3 \exp(\mathrm{i}\omega_3 t) + a_6 \exp(\mathrm{i}\omega_6 t)) \exp\left(-\frac{t}{2\tau_0} \right) \end{aligned} \tag{A.13}$$

a_j are the relative weights of the different transitions with $a = a_1/a_4 = a_6/a_3 = 1/3$. Since $a_1 = a_6$ and $a_3 = a_4$, it is $|\tilde{F}_{+1}(t)|^2 = |\tilde{F}_{-1}(t)|^2$. Inserting Eqns. (A.13) into Eqn. (A.12) results in the occurence of frequency differences $\omega_i - \omega_j$:

$$\begin{aligned} \Omega_1 &= \omega_4 - \omega_1 = \frac{\Delta_e + \Delta_g}{\hbar} \\ \Omega_2 &= \omega_3 - \omega_1 = \frac{2\Delta_e}{\hbar} \end{aligned} \tag{A.14}$$

Defining the function

$$G(\nu_1, \nu_2, \nu_3) = \cos(\nu_1 t) + a^2 \cos(\nu_2 t) + 2a \cos(\nu_3 t) \tag{A.15}$$

the resonantly reflected intensity can be expressed as

$$\begin{aligned} I(t) =& \Big(G(0, 0, \Omega_1)(1 + S^2(\phi)) \\ &+ G(\Omega_1 + \Omega_2, \Omega 1 - \Omega_2, \Omega_2)(1 - S^2(\phi)) \Big) \cdot \frac{\chi^2}{\tau_0^2} \exp\left(-\chi \frac{t}{\tau_0} \right) \end{aligned} \tag{A.16}$$

The function $S(\phi)$ is obtained by fitting a calculated time spectrum to a measured reflected intensity $I(t)$ with a suitable program such as CONUSS [128]. In this way, the magnetic structure function $\boldsymbol{\mathcal{M}}$, i.e. the spin structure of the sample, is recovered.

A.2 Metal nanostructures on faceted α-Al_2O_3 substrates

A.2.1 Au and Cu nanostructures

A ^{57}Fe thin film with periodically varying thickness on a nanofaceted α-Al_2O_3 substrate has been discussed in section 8.2. This film was prepared by sputter deposition under a polar angle exceeding the tilt angle of the substrate facet surface facing the sputter source. If a polar angle smaller than the facet tilt angle is chosen, separated parallel metal nanostripes are grown on the nanofaceted substrate. While the width of the nanostripes can be adjusted via the polar angle of the sputter source and / or the facet dimensions (see Eq.(8.1)), the thickness of the nanostripes can be determined via the deposition duration. Thus, nanostripes with a variety of aspect ratios can be prepared by varying readily adjustable parameters. As an example, Au nanostripes were grown on α-Al_2O_3 substrates with different facet dimensions. The widths of the nanostripes were 100 nm and 25 nm, respectively. GISAXS pattern were taken during sputter deposition (see Fig. A.3): they exhibit intensity modulations on the scattering rod at $q_y < 0$, the period of which corresponds to the thickness of the Au nanostripes growing on the S-plane facet surfaces. The different aspect ratios of the Au nanostripe samples result in different wavelength dependencies of their UV/VIS reflectance (see Fig. A.4). This facile way of adjusting the nanostripe aspect ratio by sputter deposition onto a faceted substrate may be of interest for applications employing surface plasmon resonances [135].

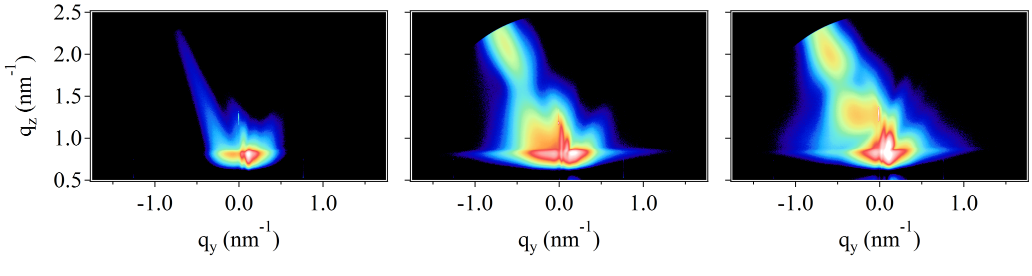

Figure A.3: GISAXS patterns recorded during sputter deposition of Au onto the S-plane facet surfaces of a nanofaceted α-Al_2O_3 substrate. Intensity scattered from the S-plane facet surfaces is recorded at $q_y < 0$. The increasing period of the intensity modulations on the scattering rod $q_y < 0$ corresponds to the increasing thickness of the Au nanostripes.

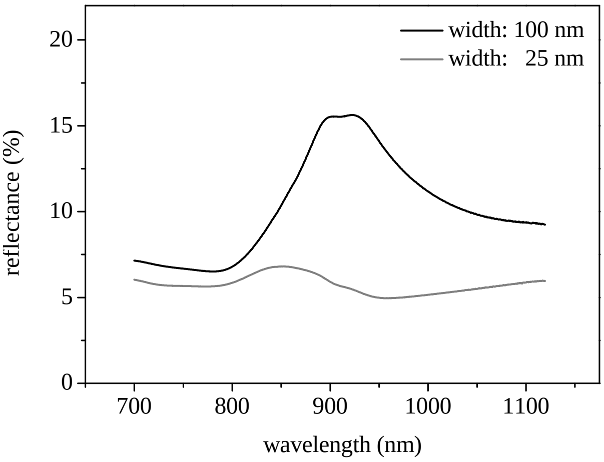

Figure A.4: UV/VIS reflectance spectra of Au nanostripe samples width 100 nm and 25 nm stripe width, respectively. The reflectance maximum of the wider nanostripes is of higher intensity and shifted toward longer wavelengths.

Cu nanostripes have been prepared in the same manner. Heating the sample to 1000 °C for 10 s resulted in the formation of spheres with a trimodal size distribution, as can be seen in Fig. A.5. Such a sample of nanospheres with three different sizes prepared from ^{57}Fe can be suitable for demonstrating the applicability of the GINSAXS principle (see section 8.2) to further sample systems. The dimensions and size distribution of the Cu nanpsheres could be adjusted by the dimensions of the initial Cu nanostripes and by the thermal treatment procedure.

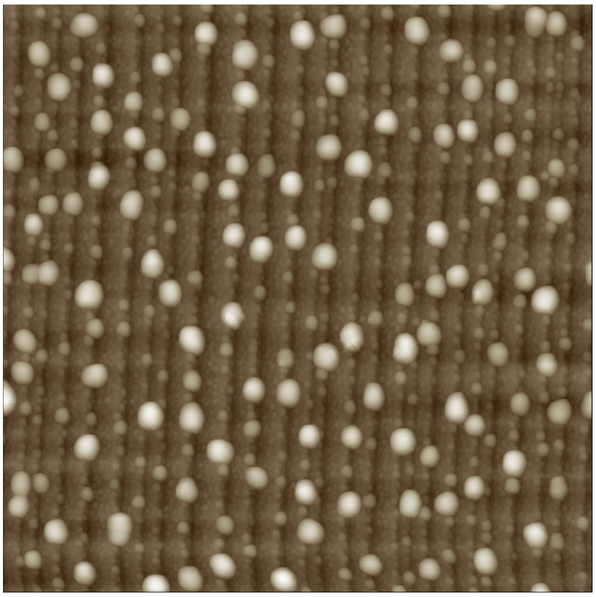

Figure A.5: AFM topograpy micrograph (5 μm × 5 μm scan area) of Cu nanospheres produces by heating Cu nanostripes on a nanofaceted α-Al_2O_3 substrate.

A.2.2 ^{57}Fe film with periodically varying thickness: Simulation of GISAXS patterns

GISAXS patterns of a continuous ^{57}Fe film with periodically varying thickness on faceted α-Al_2O_3 (see section 8.2) were simulated using the program FitGISAXS [120]. The reader is referred to the manual to the program for definitions of the individual input parameters. The parameter $\mathrm{t}_{\mathrm{shell}}$, meaning the thickness of the ^{57}Fe shell as measured perpendicular to the substrate surface (see Fig. A.6), is varied in the simulations.

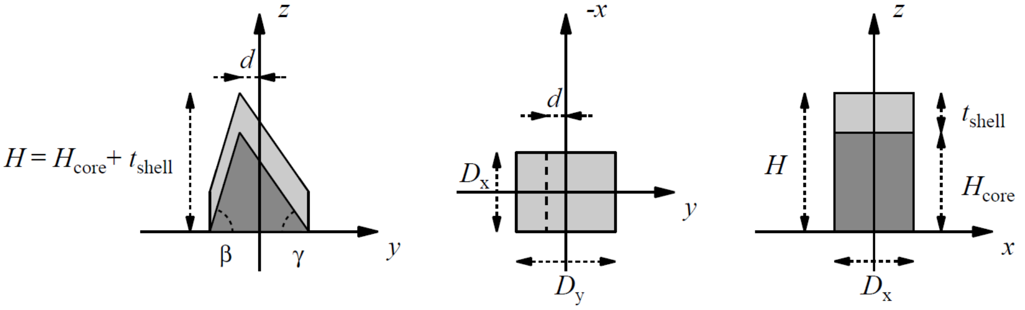

Figure A.6: The core-shell ripple form factor in FitGISAXS. From [120].

2D simulations and experimental data of the GISAXS intensity distribution $I(\boldsymbol{q_y}, \boldsymbol{q_z})$ recorded after subsequent sputter deposition steps are compared in Figs. A.7 to A.8. Note, that the left and right half of each pattern had to be simulated separately and were combined into one figure afterward: The core-shell ripple form factor in the employed simulation program is defined such that the shell thickness on the two faces of the facets (ripples) cannot be chosen independently. However, independent shell thicknesses on both facet surfaces are required to describe the sample system properly. Furthermore, as can be seen from Fig. A.6, the input parameter $\mathrm{t}_{\mathrm{shell}}$ means the shell thickness measured perpendicular to the macroscopic sample surface. In order to obtain the actual film thicknesses measured normal to the tilted facet surfaces, $\mathrm{t}_{\mathrm{shell}}$ has to be multiplied by a factor of $\cos(\phi)$, where ϕ is the respective tilt angle of the left or right facet faces. The appropriate values of $\mathrm{t}_{\mathrm{shell}}$ were identified by the best agreement of line cuts along the tilted scattering rods in corresponding experimental and simulated scattering patterns (see Figs. A.9 and A.10). The primary focus was on finding the thicknesses of the ^{57}Fe film on the different facet surfaces by means of these simulations. Apart from shape and lateral distribution of the facets, further parameters were not optimized in the simulations.

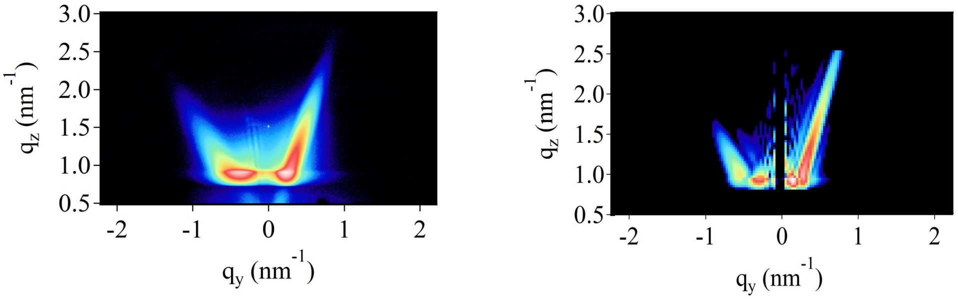

(a) bare substrate (b) bare substrate

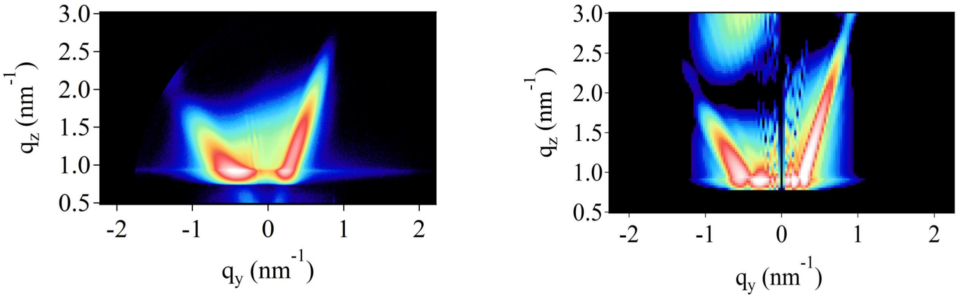

(c) 120 s deposition (d) 120 s deposition

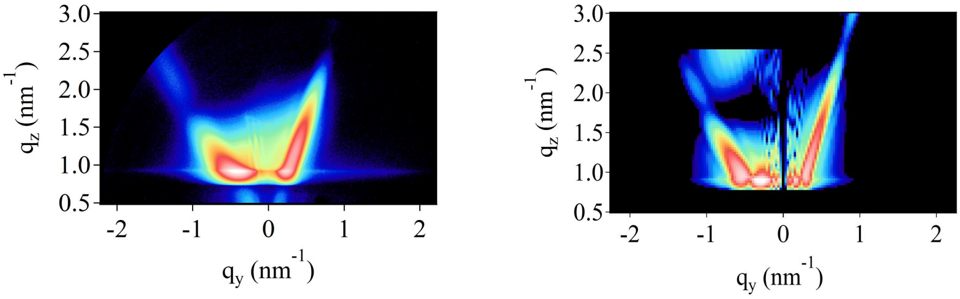

(e) 135 s deposition (f) 135 s deposition

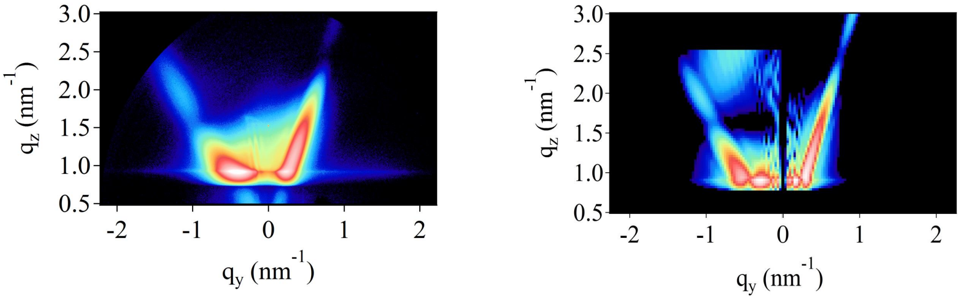

(g) 150 s deposition (h) 150 s deposition

Figure A.7: GISAXS patterns of a ^{57}Fe film on a nanofaceted α-Al_2O_3 substrate after subsequent steps of sputter deposition: Comparison of experimental data (left) and simulations (right).

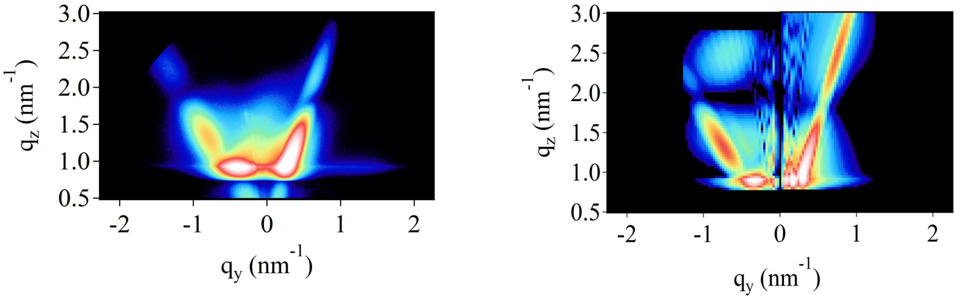

(a) 225 s deposition (b) 225 s deposition

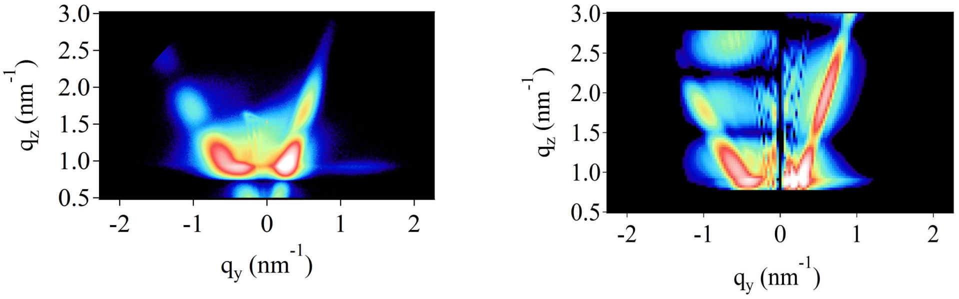

(c) 300 s deposition (d) 300 s deposition

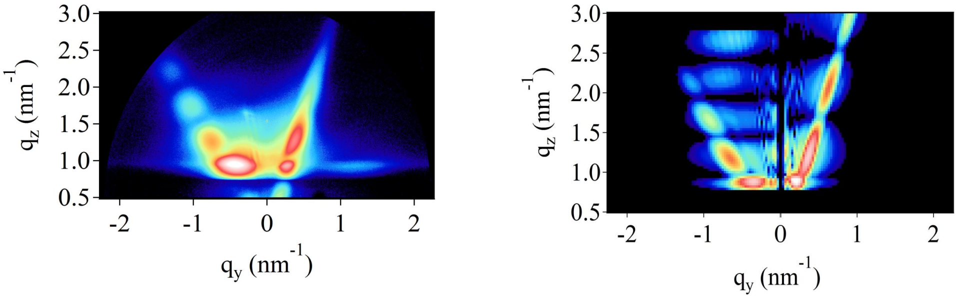

(e) 420 s deposition (f) 420 s deposition

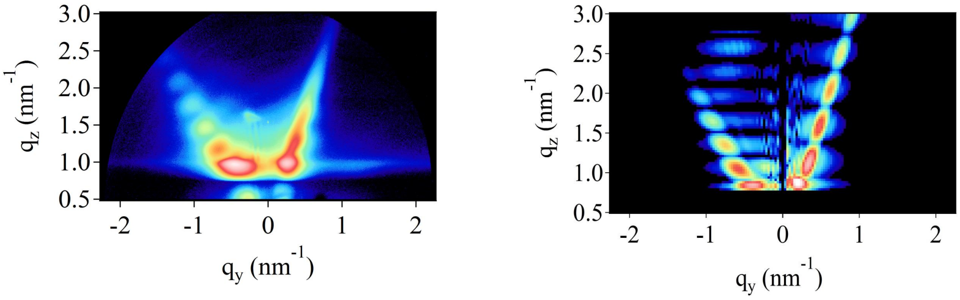

(g) 630 s deposition (h) 630 s deposition

Figure A.8: GISAXS patterns of a ^{57}Fe film on a nanofaceted α-Al_2O_3 substrate after subsequent steps of sputter deposition: Comparison of experimental data (left) and simulations (right).

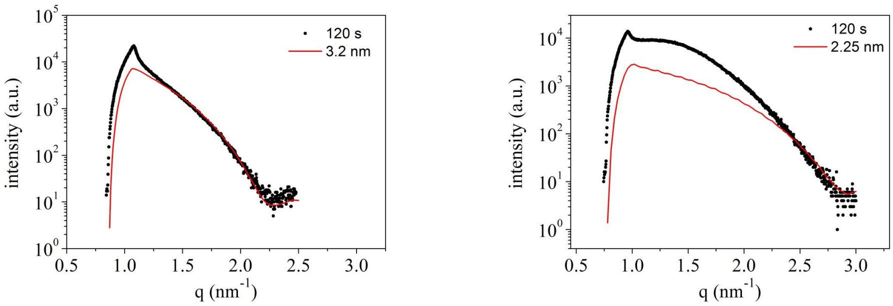

(c) 120 s deposition (d) 120 s deposition

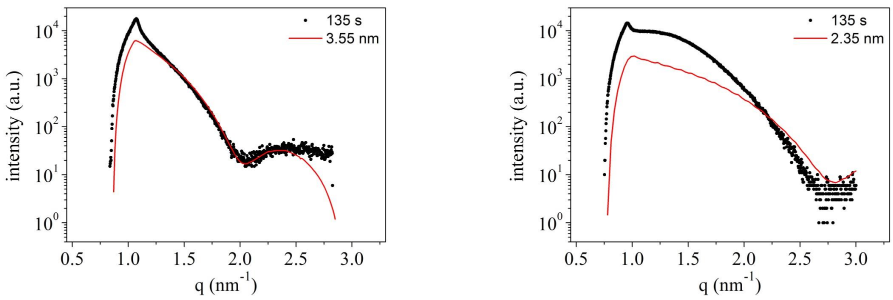

(e) 135 s deposition (f) 135 s deposition

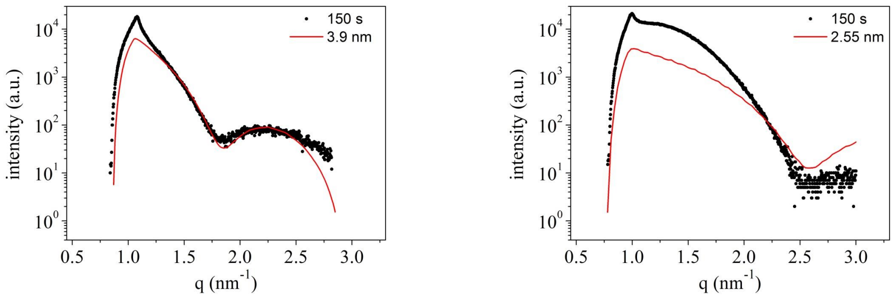

(g) 150 s deposition (h) 150 s deposition

Figure A.9: Cuts through the left and right tilted scattering rods in GISAXS patterns of a ^{57}Fe film on a nanofaceted α-Al_2O_3 substrate after subsequent steps of sputter deposition (see Figs. A.7 and A.8): Comparison of experimental data (black dots) and simulations (red lines). Labels state the value of the simulation parameter t_{shell}.

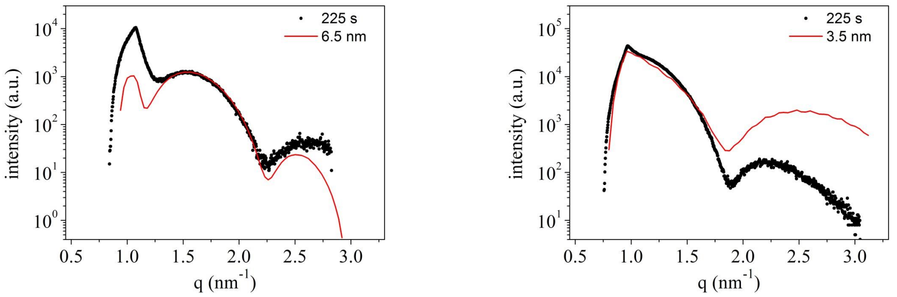

(a) 225 s deposition

(b) 225 s deposition

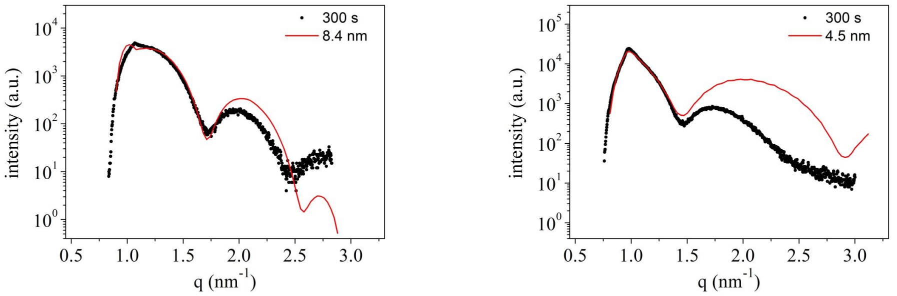

(c) 300 s deposition

(d) 300 s deposition

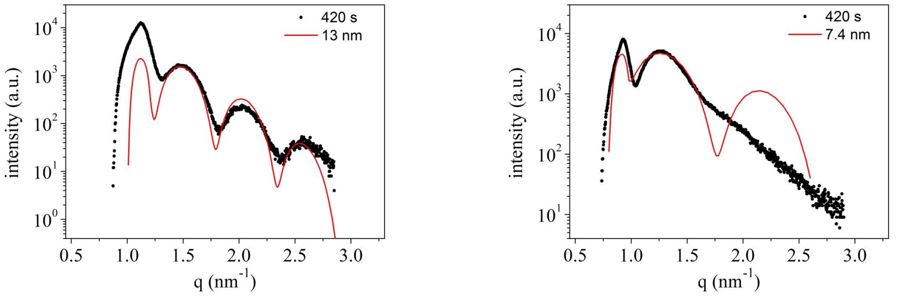

(e) 420 s deposition

(f) 420 s deposition

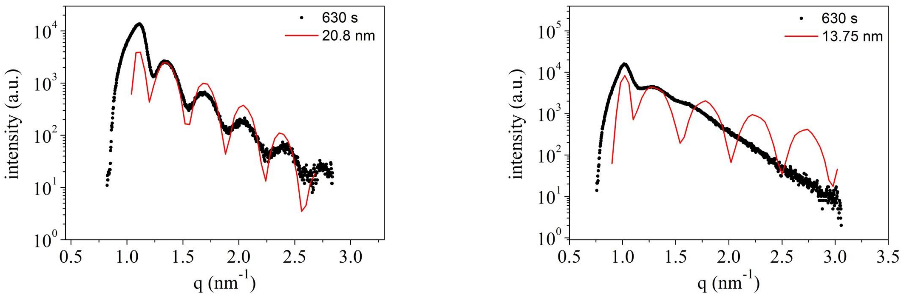

(g) 630 s deposition

(h) 630 s deposition

Figure A.10: Cuts through the left and right tilted scattering rods in GISAXS patterns of a ^{57}Fe film on a nanofaceted α-Al_2O_3 substrate after subsequent steps of sputter deposition (See Figs. A.7 and A.8): Comparison of experimental data (black dots) and simulations (red lines). Labels state the value of the simulation parameter t_{shell}.

A.3 Diblock copolymer templates

A.3.1 Determination of the thickness of diblock copolymer films by x-ray reflectivity

The thickness of diblock copolymer films in dependence of the solution concentration was determined from x-ray reflectivity curves. These were recorded on a laboratory x-ray diffraction system (Seifert XRD 3003 PTS). The system was run at a power of $P = U \cdot I = 40$ kV $\cdot$ 40 mA $= 1.6$ kW, the wavelength was $\lambda = 0.154$ nm, and the beamsize was approximately 15 mm in the sample plane and 0.2 mm perpendicular to the sample plane. All but two samples were 20 mm × 20 mm; one sample was 15 mm × 15 mm and one sample was 10 mm × 10 mm.

Fig. A.11 shows the reflectivity curves of thin films of the symmetric PS-b-PMMA(203/203) and the asymmetric PS-b-PMMA(63/142), respectively, prepared from solutions of different concentrations as indicated by the labels. The films were cast by spin coating at an angular velocity ω of 3000 rotations per minute, i.e. $\omega = 113076$ rad/s. The peak at $2\theta = 3.4$ ° is a feature of the instrument and does not originate from the samples.

According to Bragg's law, destructive interference is given for

$$\frac{2n+1}{2}\lambda = 2d\sin(\theta) \tag{A.17}$$

where $n = 0, 1, 2, \ldots$, λ is the wavelength of incident radiation, d is the layer thickness, and θ is the incident and exit angle. Thus, the angular values $\theta = 2\theta/2$ for destructive interference were read from the measurements as the positions of intensity minima in the reflectivity curves. The film thickness d for each sample was then determined as the slope of the line $y = mx$ with $y = (2n+1)\lambda/2$ and $x = 2\sin(\theta)$. Fig. A.12 shows the extracted film thicknesses as functions of the solution concentration. Within the investigated range of concentrations, the film thickness depends approximately linearly on the solution concentration with $d \approx 5.25c$ for PS-b-PMMA(203/203) and $d \approx 4.55c$ for PS-b-PMMA(63/142), where d is given in nm and c is given in mg/ml.

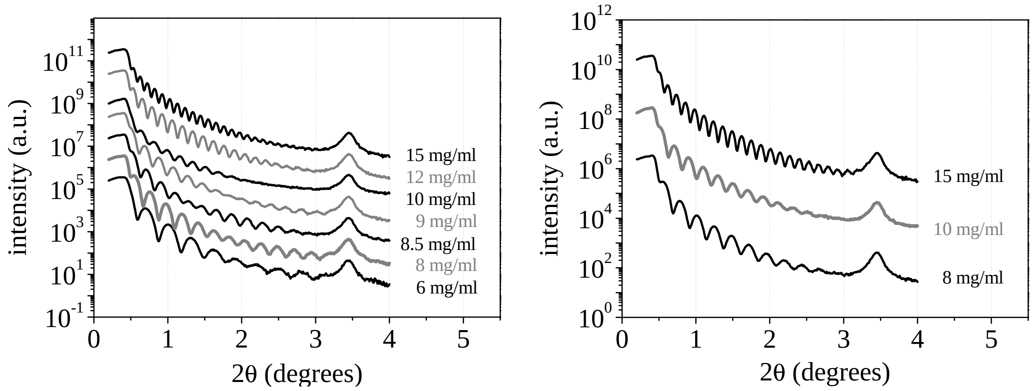

(a) Symmetric PS-b-PMMA(203/203) (b) Asymmetric PS-b-PMMA(63/142)

Figure A.11: X-ray reflectivity curves of diblock copolymer thin films on SiO_x substrates. Curves have been shifted along the intensity scale for clarity. Labels state the respective solution concentration. Laboratory x-ray source, $\lambda = 1.54$ nm.

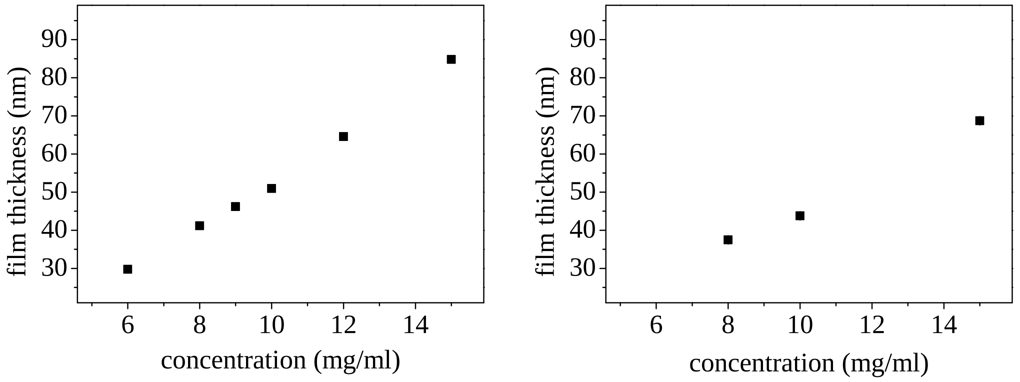

(a) Symmetric PS-b-PMMA(203/203) (b) Asymmetric PS-b-PMMA(63/142)

Figure A.12: The thicknesses of diblock copolymer films in dependence of the concentration of the solution they were prepared from. Error bars are too small to be displayed.

A.3.2 Removal of the PMMA block by acetic acid

Fig. A.14 shows the result of exposing a thin film of PS-b-PMMA(203/203) to UV radiation of $\lambda = 254$ nm wavelength for 6 h, drying it for 15 h at 50 °C, and then immersing it into undiluted acetic acid for 2 s. In the right half of the micrograph all of the initial PS-b-PMMA film is missing. Some PS lamellae at the edge are partly detached from the array of other PS lamellae. The distance between the PS lamellae is generally uneven. Residues of PMMA remain on top of the PS lamellae. This observation suggests, that the PS-b-PMMA film had assumed a s-L$^{\perp}$ morphology with surface-perpendicular PS domains reaching vertically down to the film / substrate interface (see Fig. A.13). If the film had assumed the symmetric hybrid s-H morphology with a continuous PMMA layer at the substrate interface, it would appear unlikely to find any PS domains left attached to the substrate after removal of the PMMA block.

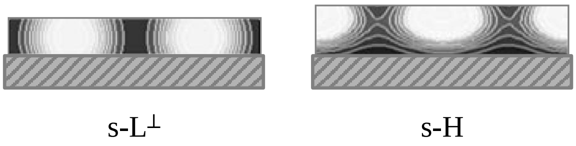

Figure A.13

A.3.3 Alternative morphologies in thin films of symmetric PS-b-PMMA

Different alternative morphologies to the s-L$^{\perp}$ morphology can occur in compositionally symmetric PS-b-PMMA thin film with thicknesses between $d_6 =$ 30 nm and $d_{12} =$ 65 nm, depending on the film thickness as shown in Fig. A.15. No alternative morphology was observed for the films of $d_{15} =$ 85 nm $\approx 0.8 D_0$ - however, the number of investigates samples was small in this case. Tab. A.1 lists the frequency with which the alternative morphologies occurred in the set of samples considered here. This set is surely too small to allow for statistically significant conclusions. Nevertheless, it may give a first impression of how reproducible the chemically nanopatterned surfaces prepared by the proposed routine are.

The alternative morphologies are characterized by the presence of cylindrical domains, which are not expected for the symmetric, lamellae-forming diblock copolymer PS-b-PMMA(203/203). The type of alternative morphology

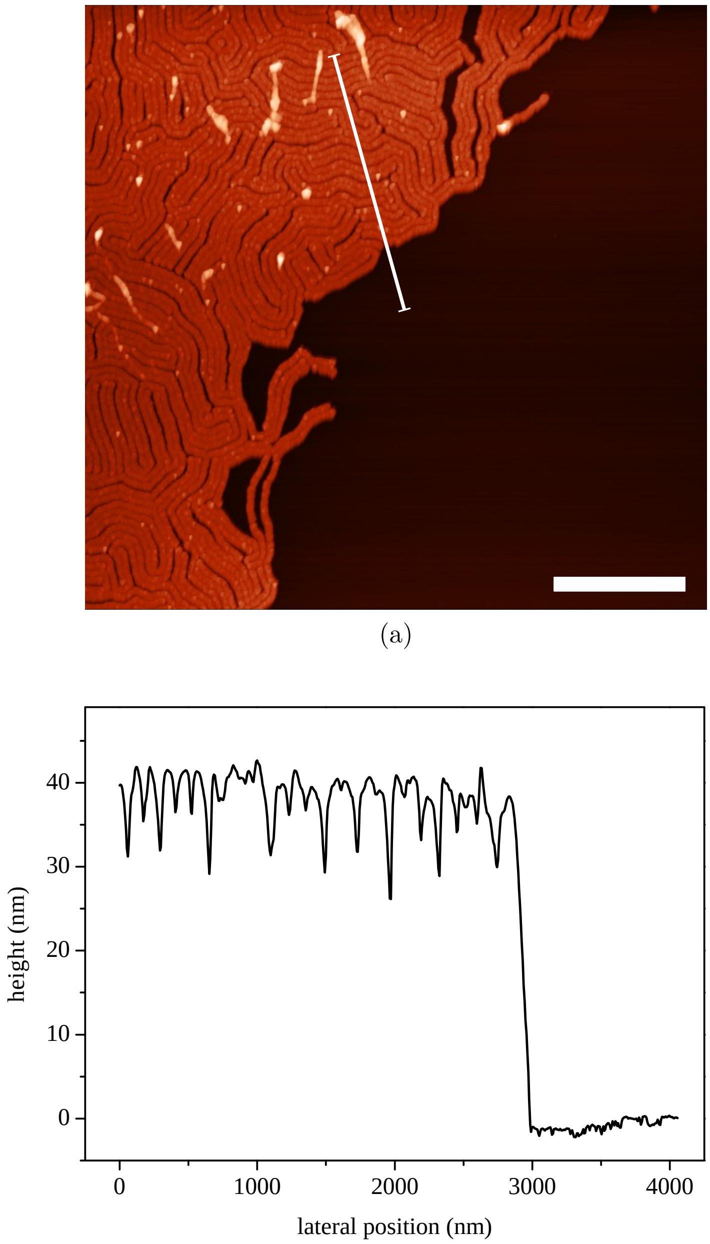

(a)

(b) section as indicated in (a)

Figure A.14: AFM topography micrograph of a thin film of lamellae-forming PS-b-PMMA(203/203) which underwent a non-optimized treatment of exposure to UV irradiation and cleaning with acetic acid. The scale bar is 2 μm long.

solution concentration	film thickness	total number of samples	s-H or s-$L^{\perp}$ morphology	alternative morphology
6 mg/ml	30 nm	3	2	1
8 mg/ml	41 nm	7	3	4
9 mg/ml	46 nm	3	1	2
10 mg/ml	51 nm	12	7	5
12 mg/ml	65 nm	3	2	1
15 mg/ml	85 nm	3	3	0

Table A.1

found in a sample depends on the film thickness: Samples of the same thickness exhibit the same alternative morphology. The alternative morphologies may vary quantitatively – e.g. in the ratio of areas covered by cylindrical and lamellar domains, respectively, for samples of thickness $d_8 = 41$ nm – but do not vary qualitatively for samples prepared from solutions with the same concentration and with homogeneous thickness. The alternative morphology for thickness $d_6 = 30$ nm contains lamellar and cylindrical PMMA domains, while the alternative morphology for thicknesses larger than $d_8 = 41$ nm show lamellar and cylindrical PS surface domains. Beginning at thickness $d_{8.5}$ ($c = 8.5$ mg/ml), poorly separated lamellar domains occur – resembling those observed in the regular morphology for thickness $d_{12} = 65$ nm. Their frequency increases with increasing film thickness, until almost all lamellar domains are poorly separated in films of thickness for $d_{10} = 51$ nm, while the cylindrical domains remain well-separated. The alternative morphology for film thickness $d_{12} = 65$ nm includes lamellar domains with varying quality of microphase separation – resembling those of the morphology of films with thickness $d_{15} = 85$ nm: Here, the height difference between PS and PMMA domains alternates regularly between high and low along the lamellae, but is the same for adjacent sections of neighboring lamellae.

The surface topography of a sample with undesired inhomogeneous film thickness is depicted in Fig. A.16. It corroborates the thickness dependence of the alternative morphologies. The film was prepared from a solution with $c = 8.5$ mg/ml. However, besides the corresponding alternative morphology with few poorly separated lamellar domains (region 2) it also exhibits the alternative morphology for film thickness $d_8 = 41$ nm with no poorly separated lamellar domains in thinner film regions (1) and the alternative morphology for film thickness $d_9 = 46$ nm with many poorly separated lamellar domains in thicker film regions (3). Analogous behavior was found for samples of

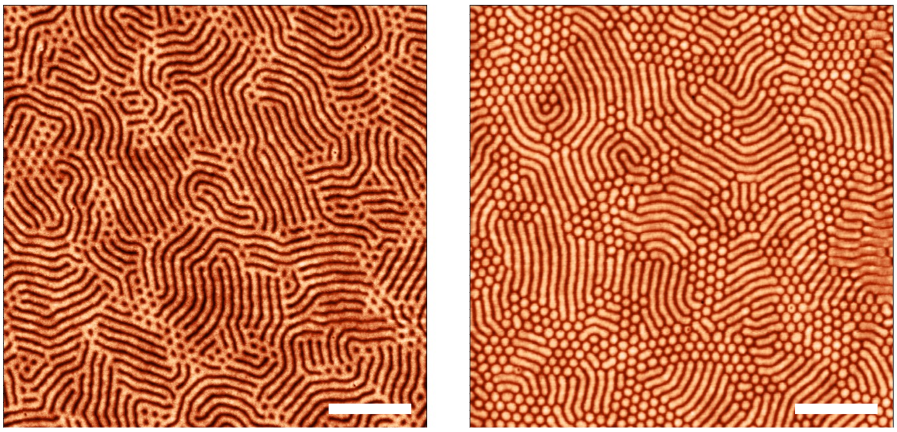

(a) $d_6 = 30$ nm (b) $d_8 = 41$ nm

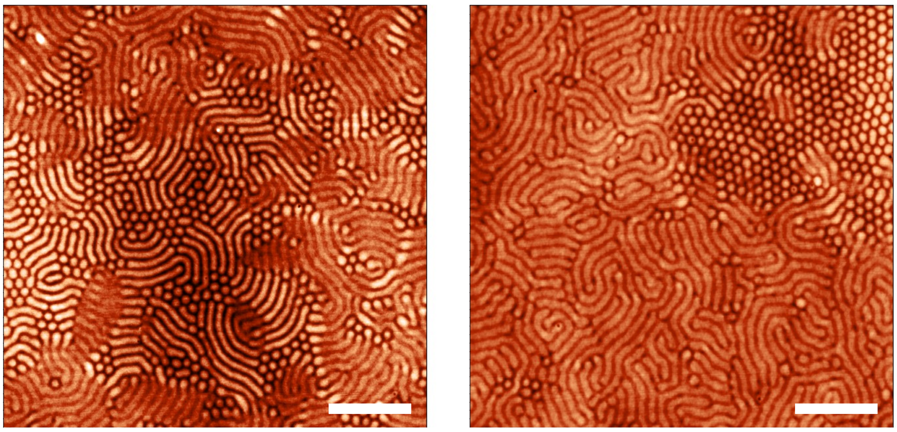

(c) $d_9 = 46$ nm (d) $d_{10} = 51$ nm

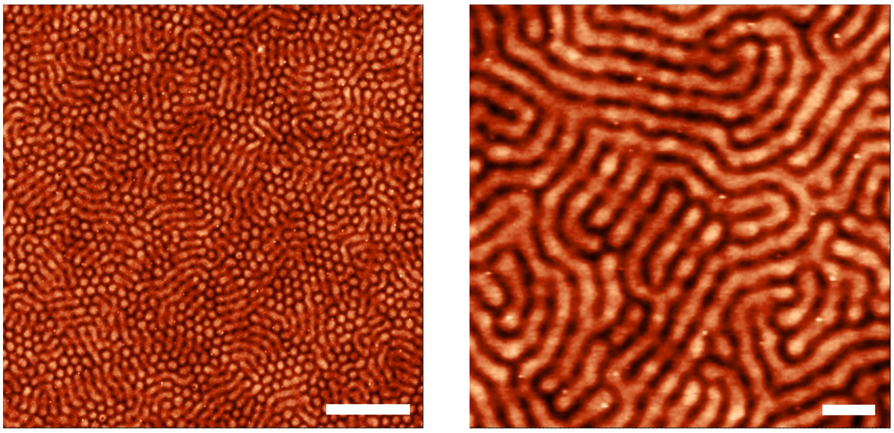

(e) $d_{12} = 65$ nm (f) $d_{15} = 85$ nm

Figure A.15: Lamellae-forming PS-b-PMMA(203/203) thin films of increasing film thickness $d_6 = 30$ nm to $d_{15} = 85$ nm on $\mathrm{SiO_x}$ substrates; $d_{10} = 51\mathrm{nm} \approx 0.5 D_0$. The films exhibit alternative surface-perpendicular morphologies deviating from the regular s-L^{perp} morphology. Scale bars are 1 μm long; scale bar in (f) is 250 nm long.

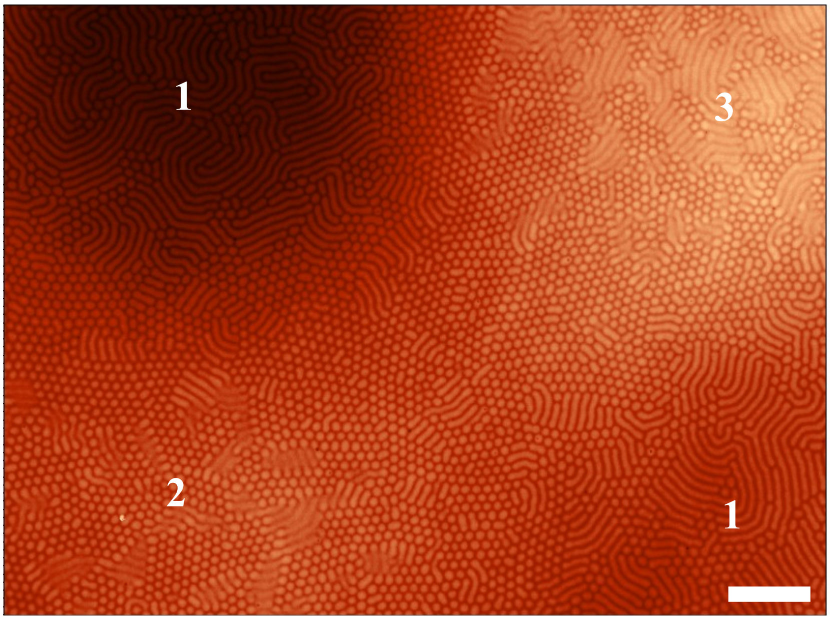

(a)

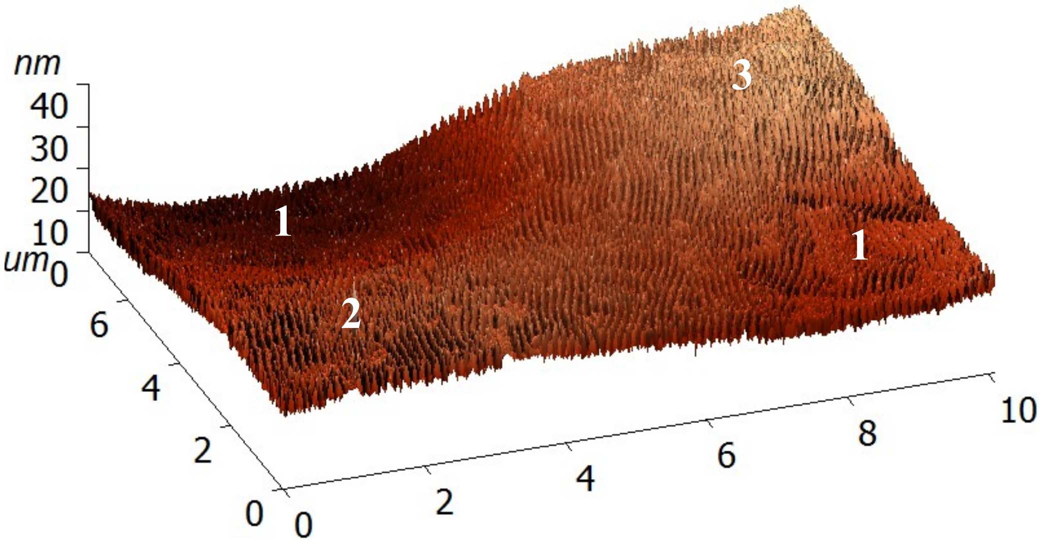

(b) perspective view of (a)

Figure A.16: Lamellae-forming PS-b-PMMA(203/203) thin film with inhomogeneous thickness, exhibiting different alternative morphologies corresponding to the local film thickness. The scale bar is 1 μm long.

inhomogeneous thickness prepared from solutions with c = 9 mg/ml and c = 10 mg/ml.

Chen and coworkers have also observed cylindrical PS domains in thin films of symmetric PS-b-PMMA and identified this as a non-equilibrium state [6]. Why here these alternative morphologies occur under the same conditions as the regular morphologies cannot be clarified by means of the available data. Several factors which may influence the outcome of the solvent vapor annealing were not subject to control in the setup and procedure as described in section 5.5: The substrate cleaning process may have left residues on the substrate surface which alter the interactions between substrate and PS-b-PMMA film. Minimal changes of the ambient temperature cannot be excluded, the exact solvent vapor pressure was neither monitored nor controllable, and the same holds especially for the rate of solvent removal.

A.3.4 Buffer layers

Using the standard procedure of spin coating, drying, and solvent vapor annealing, PS-b-PMMA thin film with chemically patterned surfaces can not only be produced on plain SiO_x substrates, but also on SiO_x substrates with different buffer layers. Fig. A.17 shows the surface morphologies of thin films of asymmetric PS-b-PMMA(63/142) (c = 8 mg/ml) and of symmetric PS-b-PMMA(47/53) (c = 10 mg/ml) on SiO_x substrates with Pt, Ti, and Fe buffer layers, respectively. The buffer layers were deposited by sputter deposition in a UHV system, but were in contact with air during preparation of the diblock copolymer thin films.

All samples exhibit well-separated chemical domains of the morphologies expected for the respective chemical composition of the diblock copolymers, i.e. surface-perpendicular cylindrical PS domains for the asymmetric PS-b-PMMA and surface-perpendicular lamellar domains for symmetric PS-b-PMMA. Fe and Pt have a high selectivity for the PS block, when deposited onto a microphase separated PS-b-PMMA film (see section 10.2). However, when Fe or Pt are used as a buffer layers, this selectivity does not alter the interactions between the PS-b-PMMA and its support in a way which would change the morphology of the film surface. The oxidized Fe surface may even be preferred by PMMA, generating asymmetric wetting conditions as on SiO_x.

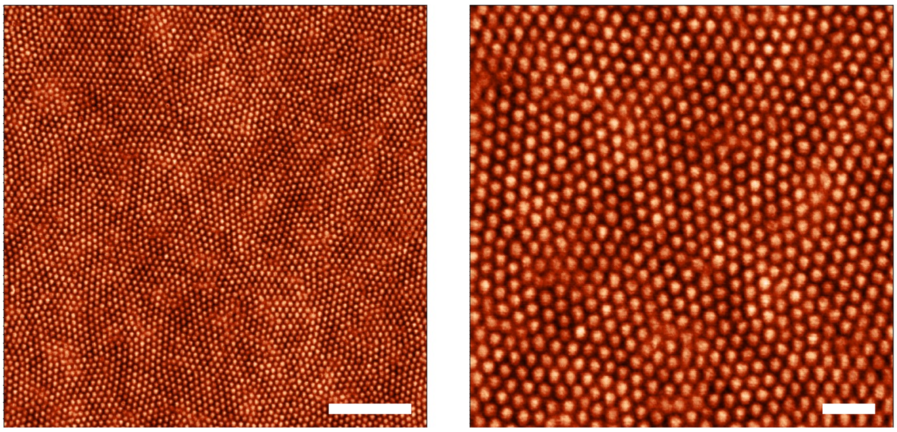

(a) PS-b-PMMA(63/142)/Pt/SiO_x (b) PS-b-PMMA(63/142)/Pt/SiO_x

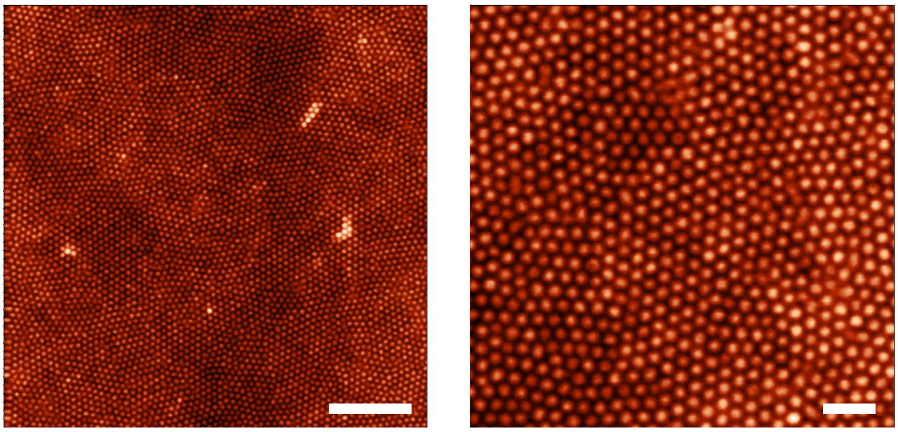

(c) PS-b-PMMA(63/142)/Ti/SiO_x (d) PS-b-PMMA(63/142)/Ti/SiO_x

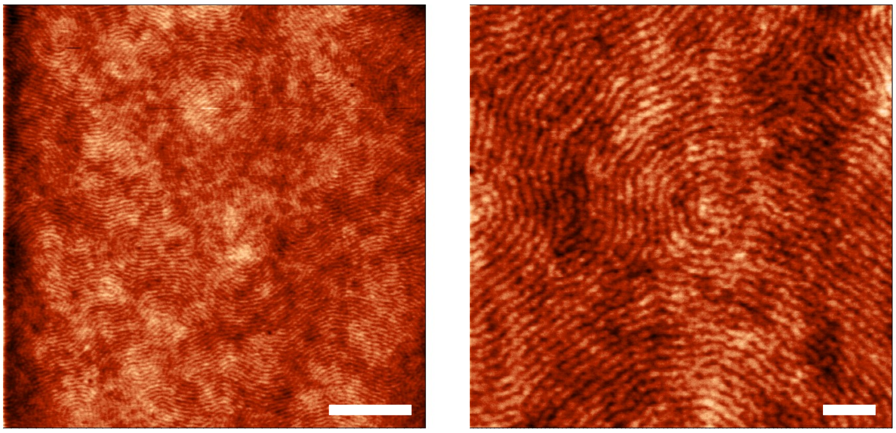

(e) PS-b-PMMA(47/53)/Fe/SiO_x (f) PS-b-PMMA(47/53)/Fe/SiO_x

Figure A.17: Thin films of cylinder-forming PS-b-PMMA(63/142) and lamellae-forming PS-b-PMMA(47/53) on SiO_x substrates with buffer layers, exhibiting regular microphase separation. Micrographs in each row show different areas of the same sample. Left / right column: Scale bars are 1 μm / 250 nm long.

A.4 ^{57}Fe nanodots on diblock copolymer templates

A.4.1 Simulation of GISAXS patterns

An in-situ GISAXS experiment on the temperature dependence of the shape of ^{57}Fe nanodots growing on a diblock copolymer template was discussed in section 10.3.1. The GISAXS patterns recorded during nanodot growth at room temperature and at 200 °C, respectively, were simulated using the program IsGISAXS [117], assuming cone-shaped nanodots. Figs. A.18 and A.19 show horizontal and vertical line cuts through the GISAXS patterns recorded during the first 240 s of ^{57}Fe sputter deposition together with the corresponding simulations.

The agreement between experiment and simulation is good for the sample grown at room temperature, except for high q_z values in the vertical line cuts. However, the measured scattered intensity in this q_z regime is two to four orders of magnitude lower than the maximum scattered intensity. Overall, the assumption of cone-shaped nanodots appears to fit the actual sample morphology well.

For the sample grown at 200 °C, the simulation is in excellent agreement with the experiment for later deposition stages (180 s to 300 s, see also Fig. 10.12 (d, f)). However, if the deduced growth behavior of the ^{57}Fe nanostructures in these late deposition stages is extrapolated to the earlier deposition stages (60 s and 120 s of ^{57}Fe deposition), the simulations fit the experimental data less well, especially in the horizontal line cuts for $q_z > 0.75$ nm^{-1}. This indicates a qualitative change of the nanodot shape between 120 s and 180 s of deposition - however, a better agreement between simulation and experiment was not achieved with the available form factors and in the given time for data evaluation.

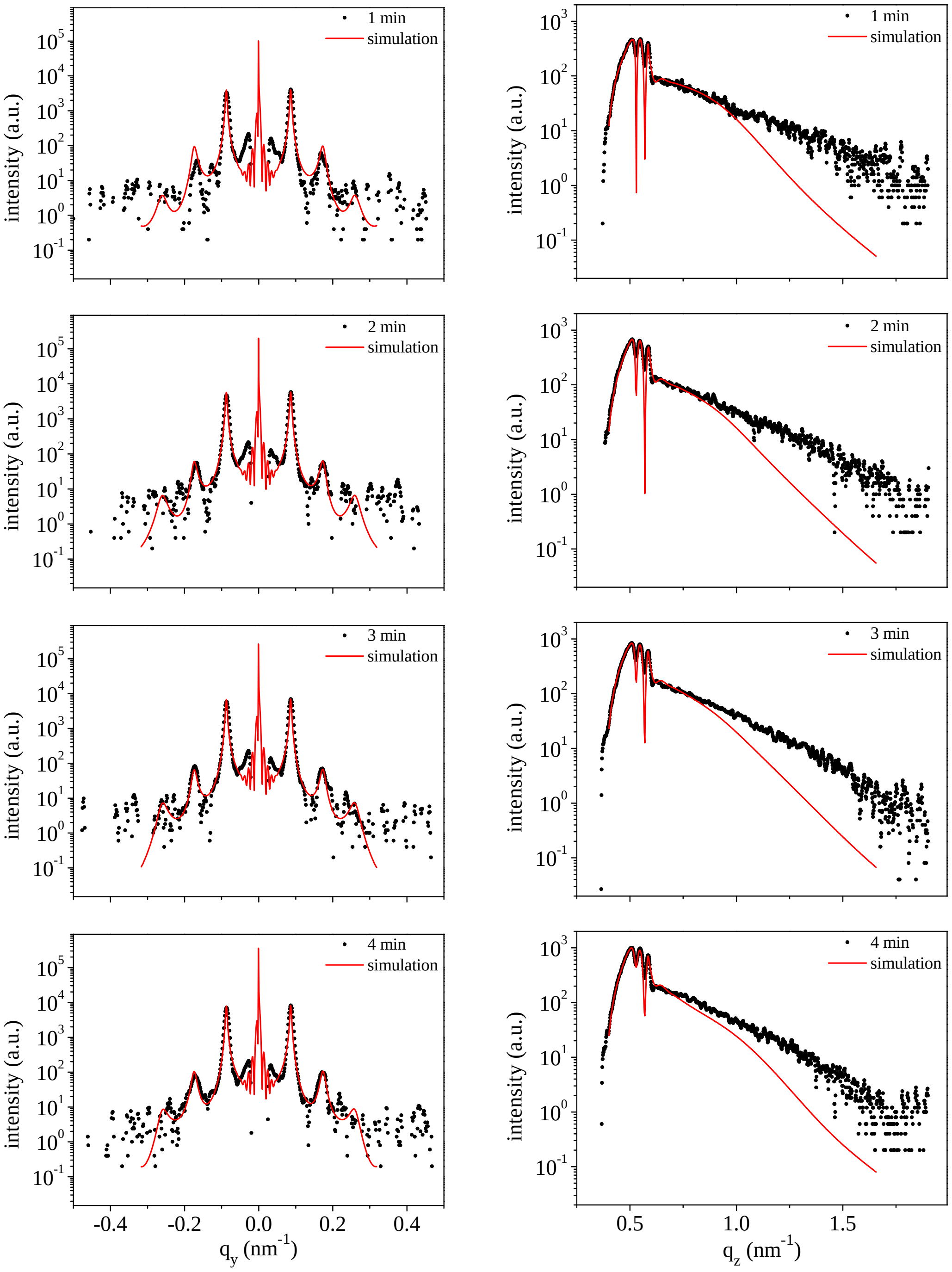

Figure A.18: Simulations of horizontal (left column) and vertical (right column) line cuts through GISAXS patterns of a hexagonal array of nanodots on a diblock copolymer template, recorded during nanodot growth at room temperature. Labels state the elapsed deposition time.

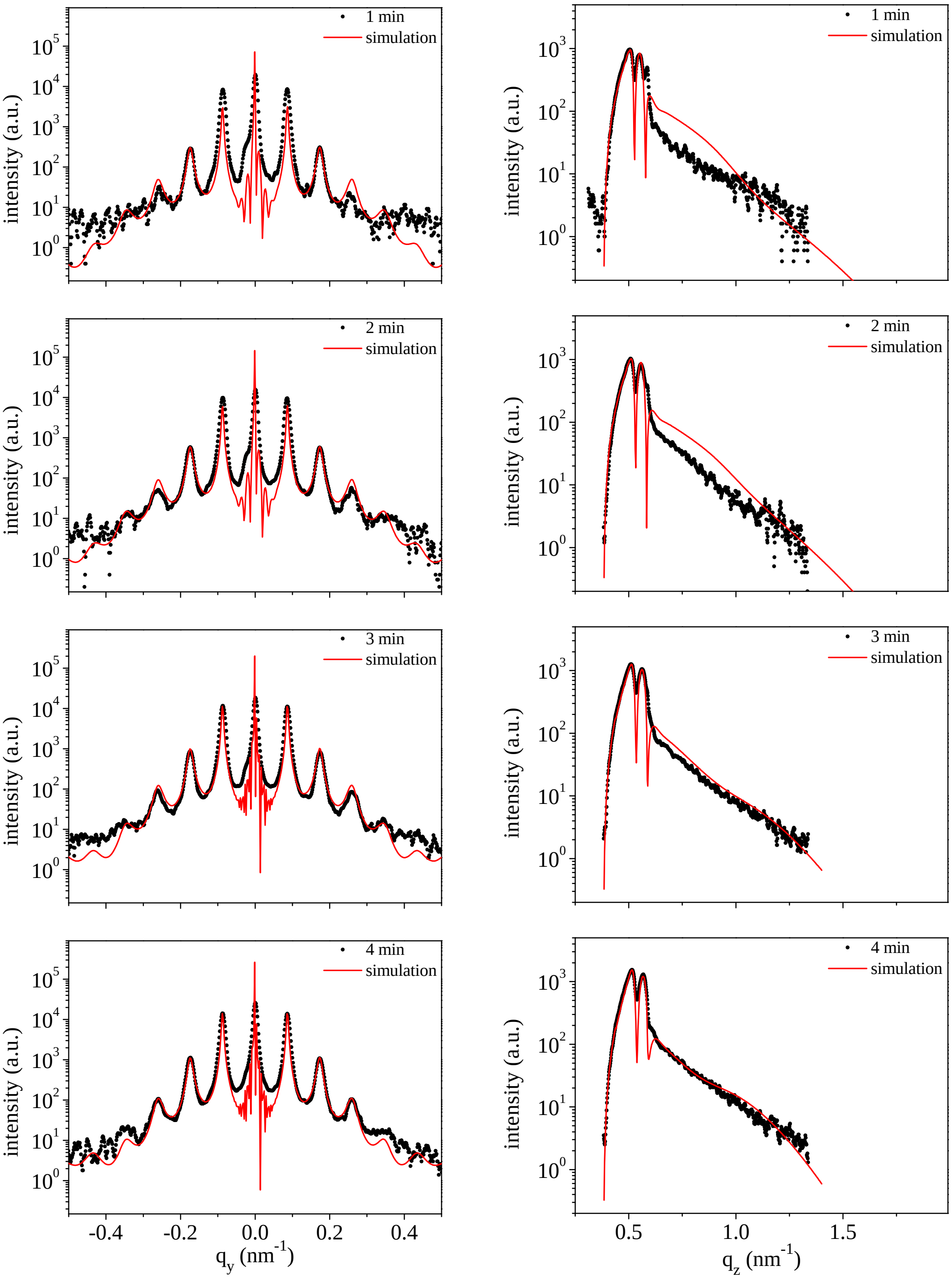

Figure A.19: Simulations of horizontal (left column) and vertical (right column) line cuts through GISAXS patterns of a hexagonal array of nanodots on a diblock copolymer template, recorded during nanodot growth at 200 °C. Labels state the elapsed deposition time.

Bibliography

[1] E. S. Putna, T. R. Younkin, M. Leeson, R. Caudillo, T. Bacuita, U. Shah, and M. Chandhok, EUV lithography for 22nm half pitch and beyond: exploring resolution, LWR, and sensitivity tradeoffs, *Proc. SPIE* **7969**, 79692K (2011).

[2] A. T. Tilke, F. C. Simmel, R. H. Blick, H. Lorenz, and J. P. Kotthaus, Coulomb blockade in silicon nanostructures, *Prog. Quantum Electron.* **25**, 97 (2001).

[3] F. Watt, A. A. Bettiol, J. A. van Kan, E. J. Teo, and M. B. H. Breese, Ion Beam Lithography and Nanofabrication: A Review, *Int.J.Nanosci.* **4**, 269 (2005).

[4] S. Y. Chou and P. R. Krauss, Imprint Lithography with Sub-10nm Feature Size and High Throughput, *Microelectronic Eng.* **35**, 237 (1997).

[5] A. Marcovich and T. Shinn, Instrument Research, Tools, and the Knowledge Enterprise 1999-2009: Birth and Development of Dip-Pen Nanolithography, *STHV* **36**, 864 (2011).

[6] Y. Chen, H. Huang, Z. Hu, and T. He, Lateral Nanopatterns in Thin Diblock Copolymer Thin Films Induced by Selective Solvents, *Langmuir* **20**, 3805 (2004).

[7] C. L. Haynes and R. P. Van Duyne, Nanosphere Lithography: A Versatile Tool for Studies of Size-Dependent Nanoparticle Optics, *J. Phys. Chem. B* **105**, 5599 (2001).

[8] H. Yan, S. H. Park, G. Finkelstein, J. H. Reif, and T. H. LaBean, DNA-Templated Self-Assembly of Protein Arrays and Highly Conductive Nanowires, *Science* **301**, 1882 (2003).

[9] J. D. Halley and D. A. Winkler, Consistent Concepts of Self-organisation and Self-assembly, *Complexity* **14**, 10 (2008).

[10] R. Waser, editor, *Nanoelectronics and Information Technology*, Wiley-VCH Weinheim, 2003.

[11] S. Y. Yang, I. Ryu, H. Y. Kim, J. K. Kim, S. K. Jang, and T. P. Russell, Nanoporous Membranes with Ultrahigh Selectivity and Flux for the Filtration of Viruses, *Adv. Mater.* **18**, 709 (2006).

[12] S. Y. Yang, J.-A. Yang, E.-S. Kim, G. Jeon, E. J. Oh, K. Y. Choi, S. K. Hahn, and J. K. Kim, Single-File Diffusion of Protein Drugs through Cylindrical Nanochannels, *ACS Nano* **4**, 3817 (2010).

[13] W. A. Phillip, B. O'Neill, M. Rodwogin, M. A. Hillmyer, and E. L. Cussler, Self-Assembled Block Copolymer Thin Films as Water Filtration Membranes, *ACS Appl. Mater. Interfaces* **2**, 847 (2010).

[14] E. A. Jackson and M. A. Hillmyer, Nanoporous Membranes Derived from Block Copolymers: From Drug Delivery to Water Filtration, *ACS Nano* **4**, 3548 (2010).

[15] T. Hashimoto, K. Tsutsumi, and Y. Funaki, Nanoprocessing Based on Bicontinuous Microdomains of Block Copolymers: Nanochannels coated with Metals, *Langmuir* **13**, 6869 (1997).

[16] T. E. Madey, W. Chen, H. Wang, P. Kaghazchi, and T. Jacob, Nanoscale surface chemistry over faceted substrates: structure, reactivity and nanotemplates, *Chem. Soc. Rev.* **37**, 2310 (2008).

[17] C. Rottman and M. Wortis, Statistical Mechanics of Equilibrium Crystal Shapes: Interfacial Phase Diagrams and Phase Transitions, *Phys. Rep.* **103**, 59 (1984).

[18] G. Wulff, On the question of speed of growth and dissolution of crystal surfaces, *Z. Kristallogr. Mineral.* **34**, 449 (1901).

[19] C. Herring, Some Theorems on the Free Energies of Crystal Surfaces, *Phys.Rev.* **82**, 87 (1951).

[20] V. A. Shchukin and D. Bimberg, Spontaneous ordering of nanostructures on crystal surfaces, *Rev. Mod. Phys.* **71**, 1125 (1999).

[21] V. I. Marchenko and A. Y. Parshin, Elastic properties of crystal surfaces, *Sov. Phys. JETP* **51**, 129 (1980).

[22] V. I. Marchenko, Theory of the equilibrium shape of crystals, *Sov. Phys. JETP* **54(3)**, 605 (1981).

[23] R. Gabai, A. Ismach, and E. Joselevich, Nanofacet Lithography: A Novel Bottom-Up Approach to Nanopatterning and Nanofabrication by Soft Replication of Spontaneously Faceted Crystal Surfaces, *Adv. Mater.* **19**, 1325 (2007).

[24] M. Huth, K. A. Ritley, J. Oster, H. Dosch, and H. Adrian, Highly Ordered Fe and Nb Stripe Arrays on Facetted α-Al_2O_3, *Adv. Funct. Mater.* **12(5)**, 333 (2002).

[25] J. H. Choi, D. Y. Kim, B. J. Hockey, S. M. Wiederhorn, C. A. Handwerker, J. E. Blendell, W. C. Carter, and A. R. Rosen, Equilibrium Shape of Internal Cavities in Sapphire, *J. Am. Ceram. Soc.* **80(1)**, 62 (1997).

[26] G. Paglia, Determination of the Structure of γ-Alumina using Empirical and First Principles Calculations Combined with Supporting Experiments, Master's thesis, Curtin University of Technology, Perth, 2004.

[27] E. R. D. dn L. A. Lytvynov and V. Pishchik, *Sapphire. Material, Manufacturing, Applications*, Springer Science+Business Media, New York, 2009.

[28] J. R. Heffelfinger and C. B. Carter, Mechanisms of surface faceting and coarsening, *Surface Science* **389**, 188 (1997).

[29] H. Staudinger, Über Polymerisation, *Ber. Deut. Chem. Ges.* **53**, 1078 (1920).

[30] P. Flory, *Principles of Polymer Chemistry*, Cornell University Press, 1953.

[31] P.-G. de Gennes, Exponents for the excluded volume problem as derived by the Wilson method, *Phys. Lett.* **38A**, 339 (1972).

[32] P.-G. de Gennes, *Scaling concepts in polymer physics*, Cornell University Press, 1979.

[33] H. Mark, Über die röntgenographische Ermittlung der Struktur organischer besonders hochmolekularer Substanzen, *Chemische Berichte* **59**, 2982 (1926).

[34] W. H. Carothers, An introduction to the general theory of condensation polymers, *J. Am. Chem. Soc.* **51**, 2548 (1929).

[35] W. H. Carothers, Polymerization, *Chem. Rev.* **8**, 353 (1931).

[36] C. K. Chiang, C. R. Fincher, Y. W. Park, A. J. Heeger, H. Shirakawa, E. J. Louis, S. C. Gau, and A. G. MacDiarmid, Electrical Conductivity in Doped Polyacetylene, *Phys. Rev. Lett.* **39**, 1098 (1977).

[37] A. D. McNaught and A. Wilkinson, editors, *IUPAC. Compendium of Chemical Terminology*, Blackwell Scientific Publications, Oxford, 2nd edition, 1997.

[38] J. W. Nicholson, *The Chemistry of Polymers*, The Royal Society of Chemistry, Cambridge, 1997.

[39] R. A. L. Jones, *Oxford Master Series in Condensed Matter Physics - Soft Condensed Matter*, Oxford University Press, 2002.

[40] J. H. Hildebrand, Solubility. XII. Regular Solutions, *J. Am. Chem. Soc.* **51**, 66 (1929).

[41] F. S. Bates and G. H. Fredrickson, Block Copolymer Thermodynamics: Theory and Experiment, *Annu. Rev. Phys. Chem.* **41**, 525 (1990).

[42] V. Abetz, R. Stadler, and L. Leibler, Order-disorder- and order-order-transitions in AB and ABC block copolymers: description by a simple model, *Polymer Bulletin* **37**, 135 (1996).

[43] M. W. Matsen and F. S. Bates, Origins of Complex Self-Assembly in Block Copolymers, *Macromolecules* **29**, 7641 (1996).

[44] M. W. Matsen and F. S. Bates, Unifying Weak- and Strong-Segregation Block Copolymer Theories, *Macromolecules* **29**, 1091 (1996).

[45] E. Helfand and Z. R. Wasserman, Microdomain Structure and the Interface in Block Copolymers, in *Developments in Block Copolymers 1*, pages 99 – 125, Applied Science Publishers Ltd., 1982.

[46] A. N. Semenov, Contribution to the theory of microphase layering in block-copolymer melts, *Sov. Phys. JETP* **61**, 733 (1985).

[47] T. Ohta and K. Kawasaki, Equilibrium Morphology of Block Copolymer Melts, *Macromolecules* **19**, 2621 (1986).

[48] K. Kawasaki, T. Ohta, and M. Kohrogui, Equilibrium Morphology of Block Copolymer Melts. 2, *Macromolecules* **21**, 2972 (1988).

[49] D. M. Anderson and E. L. Thomas, Microdomain Morphology of Star Copolymers in the Strong-Segregation Limit, *Macromolecules* **21**, 3221 (1988).

[50] S. P. Gido, D. W. Schwark, E. L. Thomas, and M. do Carmo Conçalves, Observation of a Non-Constant Mean Curvature Interface in an ABC Triblock Copolymer, *Macromolecules* **26**, 2636 (1993).

[51] M. J. Fasolka, P. Banerjee, A. M. Mayes, G. Picket, and A. C. Balazs, Morphology of Ultrathin Supported Diblock Copolymer Films: Theory and Experiment, *Macromolecules* **33**, 5702 (2000).

[52] M. J. Fasolka and A. M. Mayes, Block Copolymer Thin Films: Physics and Applications, *Annu. Rev. Mater. Res.* **31**, 323 (2001).

[53] D. G. Walton, G. J. Kellog, A. M. Mayes, P. Lambooy, and T. P. Russell, A Free Energy Model for Confined Diblock Copolymers, *Macromolecules* **27**, 6225 (1994).

[54] T. L. Morkved and H. M. Jaeger, Thickness-induced morphology changes in lamellar diblock copolymer ultrathin films, *Europhys. Lett.* **40**, 643 (1997).

[55] M. S. Turner, Equilibirum Properties of a Diblock Copolymer Lamellar Phase Confined between Flat Plates, *Phys. Rev. Lett.* **69**, 1788 (1992).

[56] P. Lambooy, T. P. Russell, G. J. Kellogg, A. M. Mayes, P. D. Gallagher, and S. K. Satija, Observed Frustration in Confined Block Copolymers, *Phys. Rev. Lett.* **72**, 2899 (1994).

[57] N. Koneripalli, N. Singh, R. Levicky, F. S. Bates, P. D. Gallagher, and S. K. Satija, Confined Block Copolymer Thin Films, *Macromolecules* **28**, 2897 (1995).

[58] H. P. Huinink, J. C. M. Brokken-Zijp, M. A. van Dijk, and G. J. A. Sevink, Asymmetric block copolymers confined in a thin film, *J. Chem. Phys.* **112**, 2452 (2000).

[59] C. Kittel, *Introduction to Solid State Physics*, John Wiley & Sons, Inc., 1996.

[60] J. Stöhr and H. C. Siegmann, *Magnetism*, Springer-Verlag, Berlin, 2006.

[61] S. Blundell, *Oxford Master Series in Condensed Matter Physics - Magnetism in Condensed Matter*, Oxford University Press, 2007.

[62] M. Getzlaff, *Fundamentals of Magnetism*, Springer-Verlag Berlin, 2008.

[63] A. Hubert and R. Schäfer, *Magnetic Domains. The Analysis of Magnetic Microstructures.*, Springer-Verlag Berlin, 2000.

[64] R. Schäfer, Magnetische Mikrostrukturen, in *30. Ferienkurs des Instituts für Festkörperforschung 1999: Magnetische Schichtsysteme*, edited by I. für Festkörperforschung der Forschungszentrum Jülich GmbH, page B6.1, Forschungszentrum Jülich GmbH, 1999.

[65] C. Kittel, Theory of the Structure of Ferromagnetic Domains in Films and Small Particles, *Phys. Rev.* **70**, 965 (1946).

[66] R. P. Cowburn, D. K. Koltsov, A. O. Adeyeye, M. E. Welland, and D. M. Tricker, Single-Domain Circular Nanomagnets, *Phys. Rev. Lett.* **83**, 1042 (1999).

[67] S. Park, D. H. Lee, J. Xu, B. Kim, S. W. Hong, U. Jeong, T. Xu, and T. P. Russell, Macroscopic 10-Terabit-per-Square-Inch Arrays from Block Copolymers with Lateral Order, *Science* **323**, 1030 (2009).

[68] A. Sugawara, G. G. Hembree, and M. R. Scheinfein, Self-organized mesoscopic magnetic structures, *J. Appl. Phys.* **82**, 5662 (1997).

[69] Y. Shiratsuchi, M. Yamamoto, Y. Endo, D. Li, and S. D. Bader, Superparamagnetic behavior of ultrathin Fe films grown on Al_2O_3(0001) substrates, *J. Appl. Phys.* **94**, 7675 (2003).

[70] Y. Shiratsuchi, Y. Endo, and M. Yamamoto, Thickness dependence of magnetic state of Fe thin films grown on Al_2O_3(0001) substrates with an inclined angle, *Sci. Tech. Adv. Mater.* **5**, 73 (2004).

[71] Y. Shiratsuchi, Y. Endo, and M. Yamamoto, Transition from superparamagnetic to ferromagnetic state of ultrathin Fe films grown on inclinded Al_2O_3(0001) substrates, *Thin Solid Films* **464-465**, 141 (2004).

[72] Y. Shiratsuchi, Y. Endo, M. Yamamoto, D. Li, and S. D. Bader, Magnetic phase transition and anisotropy of ultrathin Fe films grown on inclinded Al_2O_3(0001) substrates, *J. Appl. Phys.* **95**, 6897 (2004).

[73] Y. Shiratsuchi, Y. Endo, M. Yamamoto, and S. D. Bader, Effect of substrate inclination on the magnetic anisotropy of ultrathin Fe films grown on Al_2O_3(0001) substrates, *J. Appl. Phys.* **97**, 10J106 (2005).

[74] K. Fukunaga and A. Sugawara, Anisotropic cross-tie walls and their confinement in self-organized undulating Fe film, *J. Appl. Phys.* **103**, 053909 (2008).

[75] F. Cebbolada, A. Hernando-Mañeru, A. Hernando, C. Martínez-Boubeta, A. Cebollada, and J. M. González, Anisotropy, hysteresis,

and morphology of self-patterned epitaxial Fe/MgO/GaAs films, *Phys. Rev. B* **66**, 174410 (2002).

[76] A. Encinas-Oropesa and F. Nguyen Van Dau, Origin of magnetic anisotropy in thin films deposited on step-bunched substrates, *JMMM* **256**, 301 (2002).

[77] R. Röhlsberger, *Nuclear Condensed Matter Physics with Synchrotron Radiation*, Springer-Verlag, Berlin, 2004.

[78] M. Sands, The Physics Of Electron Storage Rings: An Introduction, *Conf. Proc. C* **6906161**, 257 (1969).

[79] H. Wiedemann, *Synchrotron Radiation*, Springer-Verlag, Berlin, 2003.

[80] http://doris.desy.de
http://photon-science.desy.de/facilities/doris_iii_archive/facility
_information/index_eng.html (April 02, 2014).

[81] http://photon-science.desy.de/facilities/petra_iii
http://photon-science.desy.de/facilities/petra_iii/beamlines/p01
_dynamics/index_eng.html (April 02, 2014).

[82] http://www.esrf.eu
http://www.esrf.eu/UsersAndScience/Experiments/DynExtrCond/ID18
(April 02, 2014).

[83] R. Gehrke, SAXS activities at DORIS III, seminar talk at Hasylab, DESY, on December 12, 2005.

[84] K. Norrman, A. Ghanbari-Siahkali, and N. B. Larsen, Studies of spin-coated polymer films, *Annu. Rep. Prog. Chem. Sect. C* **101**, 174 (2005).

[85] A. G. Emslie, F. T. Bonner, and L. G. Peck, Flow of a Viscous Liquid on a Rotating Disk, *J. Appl. Phys.* **29**, 858 (1958).

[86] C. J. Lawrence, The mechanisms of spin coating of polymer films, *Phys. Fluids* **31**, 2786 (1988).

[87] L. L. Spangler, J. M. Torkelson, and J. S. Royal, Influence of Solvent and Molecular Weight in Thickness and Surface Topography of Spin-Coated Polymer Films, *Polym. Eng. Sci.* **30**, 644 (1990).

[88] A. Weill and E. Decheneaux, The Spin-Coating Process Mechanism Related to Polymer Solution Properties, *Polym. Eng. Sci.* **28**, 945 (1988).

[89] R. J. Albalak, M. S. Capel, and E. L. Thomas, Solvent swelling of roll-cast triblock copolymer films, *Polymer* **39**, 1647 (1998).

[90] C.-Y. Hui and K.-C. Wu, Case-II diffusion in polymers. I. Transient swelling, *J. Appl. Phys.* **61**, 5129 (1987).

[91] T. P. Lodge, B. Pudil, and K. J. Hanley, The Full Phase Behavior for Block Copolymers in Solvents of Varying Selectivity, *Macromolecules* **35**, 4704 (2002).

[92] S. H. Anastasiadis, T. P. Russell, S. K. Satija, and C. F. Majkrzak, Neutron Reflectivity Studies of the Surface-Induced Ordering of Diblock Copolymer Films, *Phys. Rev. Lett.* **62**, 1852 (1989).

[93] P. F. Green, T. M. Christensen, and T. P. Russell, Ordering at Diblock Copolymer Surfaces, *Macromolecules* **24**, 252 (1991).

[94] Y. Xuan, J. Peng, L. Cui, H. Wang, B. Li, and Y. Han, Morphology Development of Ultrathin Symmetric Diblock Copolymer Film via Solvent Vapor Treatment, *Macromolecules* **37**, 7301 (2004).

[95] W. R. Grove, On the Electro-Chemical Polarity of Gases, *Phil. Trans. R. Soc. Lond.* **142**, 87 (1852).

[96] W. Schweika, Schichtpräparation mit Sputterverfahren, in *30. Ferienkurs des Instituts für Festkörperforschung 1999: Magnetische Schichtsysteme*, edited by I. für Festkörperforschung der Forschungszentrum Jülich GmbH, page A5.1, Forschungszentrum Jülich GmbH, 1999.

[97] M. Ohring, *The Materials Science of Thin Films*, Academic Press Ltd., London, 1992.

[98] J. A. Thornton, Influence of apparatus geometry and deposition conditions on the structure and topography of thick sputtered coatings, *J. Vac. Sci. Technol.* **11**, 666 (1974).

[99] W. Petry and W. Schmid, Verfahren zur Herstellung von Ausgangsmaterial für einen Technetium-Generator, PCT/EP2012/057494 (2012).

[100] S. H. Anastasiadis, T. P. Russell, S. K. Satija, and C. F. Majkrzak, The morphology of symmetric doblock copolymers as revealed by neutron reflectivity, *J. Chem. Phys.* **92**, 5677 (1990).

[101] T. P. Russell, Temperature Dependence of the Interaction Parameter of Polystyrene and Poly(methyl methacrylate, *Macromolecules* **23**, 890 (1990).

[102] Y. Zhao, E. Sivaniah, and T. Hashimoto, SAXS Analysis of the Order-Disorder Transition and the Interaction Parameter of Polystyrene-*block*-poly(methyl methacrylate), *Macromolecules* **41**, 9948 (2008).

[103] G. Binnig, C. F. Quate, and C. Gerber, Atomic Force Microscope, *Phys. Rev. Lett.* **56**, 930 (1986).

[104] F. J. Giessibl, Atomic resolution of the silicon(111)-(7x7) surface by atomic force microscopy, *Science* **267**, 68 (1995).

[105] D. Rugar and P. Hansma, Atomic Force Microscopy, *Physics Today* **43**, 23 (1990).

[106] F. J. Giessibl, Advances in atomic force microscopy, *Rev. Mod. Phys.* **75**, 949 (2003).

[107] G. Binnig, Force microscopy, *Ultramicroscopy* **42 - 44**, 7 (1992).

[108] G. Meyer and N. M. Amer, Novel optical approach to atomic force microscopy, *Appl. Phys. Lett.* **53**, 1045 (1988).

[109] S. Santos, V. Barcons, H. K. Christenson, J. Font, and N. H. Thomson, The Intrinsic Resolution Limit in the Atomic Force Microscope: Implications for Heights of Nano-Scale Features, *PLoS ONE* **6**, e23821 (2011).

[110] L. Tsarkova, G. J. A. Sevink, and G. Krausch, Nanopattern Evolution in Block Copolymer Films: Experiment, Simulations and Challenges, *Adv. Polym. Sci.* **227**, 33 (2010).

[111] R. Magerle, Nanotomography, *Phys. Rev. Lett.* **85**, 2749 (2000).

[112] J. R. Levine, J. B. Cohen, Y. W. Chung, and P. Georgopoulos, Grazing-Incidence Small-Angle X-ray Scattering: New Tool for Studying Thin Film Growth, *J. Appl. Cryst.* **22**, 528 (1989).

[113] G. Renaud, R. Lazzari, and F. Leroy, Probing surface and interface morphology with Grazing Incidence Small Angle X-Ray Scattering, *Surface Science Reports* **64**, 255 (2009).

[114] S. K. Sinha, E. B. Sirota, S. Garoff, and H. B. Stanley, X-ray and neutron scattering from rough surfaces, *Phys. Rev. B* **38**, 2297 (1988).

[115] J. Als-Nielsen and D. McMorrow, *Elements of modern x-ray physics*, John Wiley & Sons Ltd, 2001.

[116] V. Holý, U. Pietsch, and T. Baumbach, *High-Resolution X-Ray Scattering from Thin Films and Multilayers*, Springer, Berlin, 1999.

[117] R. Lazzari, IsGISAXS: a program for grazing-incidence small-angle X-ray scattering analysis of supported islands, *J. Appl. Cryst.* **35**, 406 (2002).

[118] M. Rauscher, R. Paniago, H. Metzger, Z. Kovats, J. Domke, J. Peisl, H.-D. Pfannes, J. Schulze, and I. Eisele, Grazing incidence small angle x-ray scattering from free-standing nanostructures, *J. Appl. Phys.* **86**, 6763 (1999).

[119] M. Rauscher, T. Salditt, and H. Spohn, Small-angle x-ray scattering under grazing incidence: The cross section in the distorted-wave Born approximation, *Phys. Rev. B* **52**, 16855 (1995).

[120] D. Babonneau, FitGISAXS: software package for modelling and analysis of GISAXS data using IGOR Pro, *J. Appl. Cryst.* **43**, 929 (2010).

[121] R. Röhlsberger, J. Bansmann, V. Senz, K. L. Jonas, A. Bettac, K. H. Meiwes-Broer, and O. Leupold, Nanoscale magnetism probed by nuclear resonant scattering of synchrotron radiation, *Phys. Rev. B* **67**, 245412 (2003).

[122] G. Schatz and A. Weidinger, *Nukleare Festkörperphysik*, B. G. Teubner, Stuttgart, 1997.

[123] R. Röhlsberger, Imaging the Magnetic Structure of Thin Films and Nanoparticles, *Hyperfine Interactions* **144/145**, 33 (2002).

[124] U. van Bürck, D. P. Siddons, J. B. Hastings, U. Bergmann, and R. Hollatz, Nuclear forward Scattering of synchrotron radiation, *Phys. Rev. B* **46**, 6207 (1992).

[125] Y. Kagan, A. M. Afanas'ev, and V. G. Kohn, On excitation of isomeric nuclear states in a crystal by synchrotron radiation, *J. Phys. C: Solid State Phys.* **12**, 615 (1979).

[126] U. van Bürck, Coherent pulse propagation through resonant media, *Hyperfine Interactions* **123/124**, 483 (1999).

[127] M. E. Rose, *Elementary Theory of Angular Momentum*, Wiley, New York, 1957.

[128] W. Sturhahn, CONUSS and PHOENIX: Evaluation of nuclear resonant scattering data, *Hyperfine Interactions* **125**, 149 (2000).

[129] A. Q. R. Baron, Detectors for nuclear resonant scattering experiments, *Hyperfine Interact.* **125**, 29 (2000).

[130] T. S. Toellner, Monochromatization of synchrotron radiation for nuclear resonant scattering experiments, *Hyperfine Interactions* **125**, 3 (2000).

[131] Y. V. Shvyd'ko, *X-Ray Optics: High Energy Resolution Applications*, Springer-Verlag Berlin, 2004.

[132] D. W. Susnitzky and C. B. Carter, Surface Morphology of Heat-Treated Ceramic Films, *J. Am. Ceram. Soc.* **75**, 2463 (1992).

[133] C. Revenant, F. Leroy, G. Renaud, R. Lazzari, A. Létoublon, and T. Madey, Structural and morphological evolution of Co on faceted Pt/W(111) surface upon thermal annealing, *Surface Science* **601**, 3431 (2007).

[134] A. Westphalen, H. Zabel, and K. Theis-Bröhl, Magnetic nanowires on faceted sapphire surfaces, *Thin Solid Films* **449**, 207 (2004).

[135] Q. Xu, J. Bao, F. Capasso, and G. M. Whitesides, Surface Plasmon Resonances of Free-Standing Gold Nanowires Fabricated by Nanoskiving, *Anged. Chem. Int. Ed.* **45**, 3631 (2006).

[136] M. Przybylski and U. Gradmann, Ferromagnetic Order in a Fe(110) Monolayer on W(110) by Mössbauer Spectroscopy, *Phys. Rev. Lett.* **59**, 1152 (1987).

[137] M. Przybylski, I. Kaufmann, and U. Gradmann, Mössbauer analysis of ultrathin ferromagnetic Fe(110) films in W(110) coated by Ag, *Phys. Rev. B* **40**, 8631 (1989).

[138] Z. Q. Qiu, J. Pearson, and S. D. Bader, Asymmetry of the Spin Reorientation Transition in Ultrathin Fe Films and Wedges Grown on Ag(100), *Phys. Rev. Lett.* **70**, 1006 (1993).

[139] D. O. Smith, M. S. Cohen, and G. P. Weiss, Oblique-Incidence Anisotropy in Evaporated Permalloy Films, *J. Appl. Phys.* **31**, 1755 (1960).

[140] J. M. Alameda, F. Carmona, F. H. Salas, L. M. Alvarez-Prado, R. Morales, and G. T. Pérez, Effects of the initial stages of film growth on the magnetic anisotropy of obliquely-deposited cobalt thin films, *JMMM* **154**, 249 (1996).

[141] F. Liu, M. T. Umlor, L. Shen, J. Weston, W. Eads, J. A. Barnard, and G. J. Mankey, The growth of nanoscale structured iron films by glancing angle deposition, *J. Appl. Phys.* **85**, 5486 (1999).

[142] C. Tang, E. M. Lennon, G. H. Fredrickson, E. J. Kramer, and C. J. Hawker, Evolution of Block Copolymer Lithography to Highly Ordered Square Arrays, *Science* **322**, 429 (2008).

[143] A. Haryono and W. H. Binder, Controlled Arrangement of Nanoparticle Arrays in Block-Copolymer Domains, *Small* **2**, 600 (2006).

[144] T. Thurn-Albrecht, J. Schotter, G. A. Kästle, N. Emley, T. Shibauchi, L. Krusin-Elbaum, K. Guarini, C. T. Black, M. T. Tuominen, and T. P. Russell, Ultrahigh-Density Nanowire Arrays Grown in Self-Assembled Diblock Copolymer Templates, *Science* **290**, 2126 (2000).

[145] M. Lazzari and C. De Rosa, Methods for the Alignment and the Large-scale Ordering of Block Copolymer Morphologies, in *Block Copolymers in Nanoscience*, edited by M. Lazzari, G. Liu, and S. Lecommandoux, page 191, Wiley-VCH, Weinheim, 2006.

[146] M. J. Fasolka, D. J. Harris, A. M. Mayes, M. Yoon, and S. G. J. Mochrie, Observed Substrate Topography-Mediated Lateral Patterning of Diblock Copolymer Films, *Phys. Rev. Lett.* **79**, 3018 (1997).

[147] T. Xu, H.-C. Kim, J. DeRouchey, C. Seney, C. Levesque, P. Martin, C. M. Stafford, and T. P. Russell, The influence of molecular weight on nanoporous polymer films, *Polymer* **42**, 9091 (2001).

[148] T. Xu, J. Stevens, J. Villa, J. T. Goldbach, K. W. Guarini, C. T. Black, C. J. Hawker, and T. P. Russell, Block Copolymer Surface Reconstruction: A Reversible Route to Nanoporous Films, *Adv. Funct. Mater.* **13**, 698 (2003).

[149] G. D. Fu, Z. Shang, L. Hong, E. T. Kang, and K. G. Neoh, Preparation of Cross-Linked Polystyrene Hollow Nanospheres via Surface-Initiated Atom Transfer Radical Polymerizations, *Macromolecules* **38**, 7867 (2005).

[150] L. Li, Y. Zhong, J. Li, C. Chen, A. Zhang, J. Xu, and Z. Ma, Thermally stable and solvent resistant honeycomb structured polystyrene films via photochemical cross-linking, *J. Mater. Chem.* **19**, 7222 (2009).

[151] C. Wochnowski, M. A. S. Eldin, and S. Metev, UV-laser-assisted degradation of poly(methylmethacrylate), *Polymer Degradation and Stability* **89**, 252 (2005).

[152] M. Park, C. Harrison, P. M. Chaikin, R. A. Register, and D. H. Adamson, Block Copolymer Lithography: Periodic Arrays of 10^{11} Holes in 1 Square Centimeter, *Science* **276**, 1401 (1997).

[153] R. Ruiz, H. Kang, F. A. Detcheverry, E. Dobisz, D. S. Kercher, T. R. Albrecht, J. J. de Pablo, and P. F. Nealey, Density Multiplication and Improved Lithography in Directed Block Copolymer Assembly, *Science* **321**, 936 (2008).

[154] I. Bita, J. K. W. Yang, Y. S. Jung, C. A. Ross, E. L. Thomas, and K. K. Berggren, Grapoexpitaxy of Self-Assembled Block Copolymers on Two-Dimensional Periodic Patterned Templates, *Science* **321**, 939 (2008).

[155] R. A. Segalman, H. Yokoyama, and E. J. Kramer, Graphoepitaxy of Spherical Domain Block Copolymer Films, *Adv. Mater.* **13**, 1152 (2001).

[156] J. Y. Cheng, A. M. Mayes, and C. A. Ross, Nanostructure engineering by templated self-assembly of block copolymers, *Nat. Mater.* **3**, 823 (2004).

[157] J. Y. Cheng, C. A. Ross, H. I. Smith, and E. L. Thomas, Templated Self-Assembly of Block Copolymers: Top-Down Helps Bottom-Up, *Adv. Mater.* **18**, 2505 (2006).

[158] H.-W. Li and W. T. S. Huck, Ordered Block-Copolymer Assembly Using Nanoimprint Lithography, *Nano Lett.* **4**, 1633 (2004).

[159] C. L. Soles and Y. Ding, Nanoscale Polymer Processing, *Science* **322**, 689 (2008).

[160] J. R. Heffelfinger, M. W. Bench, and C. B. Carter, On the faceting of ceramic surfaces, *Surface Science* **343**, L1161 (1995).

[161] L. Rockford, Y. Liu, P. Mansky, T. P. Russell, M. Yoon, and S. G. J. Mochrie, Polymers on Nanoperiodic, Heterogeneous Surfaces, *Phys. Rev. Lett.* **82**, 2602 (1999).

[162] E. Kim, H. Ahn, S. Park, H. Lee, M. Lee, S. Lee, T. Kim, E.-A. Kwak, J. H. Lee, X. Lei, J. Huh, J. Bang, B. Lee, and D. Y. Ryu, Directed Assembly of High Molecular Weight Block Copolymers: Highly Ordered Line Patterns of Perpendicularly Oriented Lamellae with Large Periods, *ACS Nano* **7**, 1952 (2013).

[163] S. Xiao, X. M. Yang, E. W. Edwards, Y.-H. La, and P. F. Nealey, Graphoepitaxy of cylinder-forming block copolymers for use as templates to pattern magnetic metal dot arrays, *Nanotechnology* **16**, S324 (2005).

[164] T. L. Morkved, P. Wiltzius, H. M. Jaeger, D. G. Grier, and T. A. Witten, Mesoscopic self-assembly of Au islands on diblock-copolymer films, *Appl. Phys. Lett.* **64**, 422 (1994).

[165] W. A. Lopes and H. M. Jaeger, Hierarchical self-assembly of metal nanostructures on diblock copolymer scaffolds, *Nature* **414**, 735 (2001).

[166] W. A. Lopes, Nonequilibrium self-assembly of metals on diblock copolymer templates, *Phys. Rev. E* **65**, 031606 (2002).

[167] A. Gopinathan, Kinetic self-assembly of metals on copolymer templates, *Phys. Rev. E* **71**, 041601 (2005).

[168] F. A. Nichols and W. W. Mullins, Morphological Changes of a Surface of Revolution due to Capillarity-Induced Surface Diffusion, *J. Appl. Phys.* **36**, 1826 (1965).

[169] W. W. Mullins, Mass Transport at Interfaces in Single Component Systems, *Metall. Mater. Trans. A* **26**, 1917 (1995).

[170] N. Combe, P. Jensen, and A. Pimpinelli, Changing Shapes in the Nanoworld, *Phys. Rev. Lett.* **85**, 110 (2000).

[171] S. B. Darling and A. Hoffmann, Tuning metal surface diffusion on diblock copolymer films, *J. Vac. Sci. Technol. A* **25**, 1048 (2007).

[172] E. B. Gowd, B. Nandan, M. K. Vyas, N. C. Bigall, A. Eychmüller, H. Schlörb, and M. Stamm, Highly ordered palladium nanodots and nanowires from switchable block copolymer thin films, *Nanotechnology* **20**, 415302 (2009).

[173] B. Nandan, E. B. Gowd, N. C. Bigall, A. Eychmüller, P. Formanek, P. Simon, and M. Stamm, Arrays of Inorganis Nanodots and Nanowires Using Nanotemplates Based On Switchable Block Copolymer Supramolecular Assemblies, *Adv. Funct. Mater.* **19**, 2805 (2009).

[174] Y. S. Jung, J. H. Lee, J. Y. Lee, and C. A. Ross, Fabrication of Diverse Metallic Nanowire Arrays Based on Block Copolymer Self-Assembly, *Nano Lett.* **10**, 3722 (2010).

[175] E. B. Gowd, B. Nandan, N. C. Bigall, A. Eychmüller, P. Formanek, and M. Stamm, Hexaonally ordered arrays of metallic nanodots from thin films of functional block copolymers, *Polymer* **51**, 2661 (2010).

[176] A. Horechyy, N. E. Zafeiropoulos, B. Nandan, P. Formanek, F. Simon, A. Kiriy, and M. Stamm, Highly ordered arrays of magnetic nanoparticles via block copolymer assembly, *J. Mater. Chem.* **20**, 7734 (2010).

[177] K. Schlage, S. Couet, S. V. Roth, U. Vainio, R. Rüffer, M. M. A. Kashem, P. Müller-Buschbaum, and R. Röhlsberger, The formation and magnetism of iron nanostructures on ordered polymer templates, *New Journal of Physics* **14**, 043007 (2012).

[178] E. Metwalli, V. Körstgens, K. Schlage, R. Meier, G. Kaune, A. Buffet, S. Couet, S. V. Roth, R. Röhlsberger, and P. Müller-Buschbaum, Cobalt Nanoparticles Growth on a Block Copolymer Thin Film: A Time-Resolved GISAXS Study, *Langmuir* **29**, 6331 (2013).

[179] S. Kamali-M, T. Ericsson, and R. Wäppling, Characterization of iron oxide nanoparticles by Mössbauer spectroscopy, *Thin Solid Films* **515**, 721 (2006).

[180] R. Röhlsberger, Photon Polarization Precession Spectroscopy for High-Resolution Studies of Spin Waves, *Phys. Rev. Lett.* **112**, 117205 (2014).

[181] K. Haneda and A. H. Morrish, On the hyperfine field of γ-Fe_2O_3 small particles, *Physics Letters* **64A**, 259 (1977).

[182] A. M. van der Kraan, Mössbauer Effect Studies of Surface Ions of Ultrafine α-Fe_2O_3 Particles, *phys. stat. sol. (a)* **18**, 215 (1973).

[183] S. Mørup, Magnetic Hyperfine Splitting in Mössbauer Spectra of Microcrystals, *JMMM* **37**, 39 (1983).

Acknowledgements

Many people have helped me in accomplishing this thesis in their own ways.

I would like to express my thankfulness to my colleagues at DESY:
Lars Bocklage, Stephan Botta, Werner Brefeld, Jade Comfort, Frank-Uwe Dill, Liudmila Dzemiantsova, Birgit Fischer, Hermann Franz, Sergio Funari, Rainer Gehrke, Tatyana Guryeva, Sven Gutschmidt, Hanno Haber, Klaudia Hagemann, Manuel Harder, Brit Heilmann, Didem Ketenoglu, Milena Lippmann, Jan Perlich, Carsten Richter, Ralf Röhlsberger, Wojciech Roseker, André Rothkirch, Jan Rubeck, Kai Schlage, Alexander Scholz, Andreas Schöps, Daniel Schumacher, Matthias Schwartzkopf, Oliver Seeck, Andrey Siemens, Stefan Sonntag, Georg Spiekermann, Manfred Spiwek, Mehran Taherkani, Markus Tischer, Hans-Christian Wille, Christoph Wollschläger, Ulla Vainio, Hasan Yavas, Horst Zink
for being so charming people to be around, for their individuality, their goodheartedness, their commitment, their humor – for making me feel comfortable and appreciated among them.

I am especially grateful to

Ralf Röhlsberger, for welcoming me in his research group and having confidence in my abilities, and for being a great example of a stunningly innovative, hilariously funny, and deeply caring personality.

Kai Schlage, for accompanying and guiding my efforts in sample preparation, data acquisition and analysis, for keeping cool during stressful beamtimes, and for inviting me to relaxed hours here and taking me to exciting tours abroad.

Hans-Christian Wille, Jan Perlich, and Rudolf Rüffer, for all the effort they made to reliably provide their outstanding support at the beamlines P01, BW4 (PETRA III), and ID18 (ESRF).

Daniel Schumacher, for his help with recording the XRD data of the copolymer films at the HZG reflectometer and for his support during beamtimes.

Lars Bocklage, for helping me to get to grips with CONUSS and for his support during beamtimes.

André Rothkirch, for his valuable IT skills (as incomprehensible as his work may be to me).

David Babonneau, for implementing the core-shell ripple form factor in FitGISAXS and for kindly and promptly answering my questions regarding the simulations.

Wolfgang Sturhahn, for replying so very quickly, precisely, and comprehensively to my questions concerning simulations with CONUSS.

Brit Heilmann, Milena Lippmann, Klaudia Hagemann, and Manfred Spiwek, for their excellent technical and infrastructural support, and for always having a smile for me.

Tanya Guryeva, for being such a warmhearted, amiable person, and for inviting me to come to her wedding party and get a glimpse of Russia.

Stephan Botta, Rainer Gehrke, Carsten Richter, and Ulla Vainio, for making lunch breaks so nourishing with their witty conversation, generous helpfulness, and shared humor.

My parents, for letting me know, that what I consider my daily work is actually a rather extraordinary occupation, and – most importantly – that I will always be extraordinary to them, no matter what.

Gregor, for cherishing my strengths and accepting my weaknesses; for knowing whatever I'm in need of and giving it without condition; for taking it completely for granted to be my constant source of love and care, support, comfort, and peace of mind.